V. 120, NO. 4
JULY 2023

ACI MATERIALS JOURNAL

A JOURNAL OF THE AMERICAN CONCRETE INSTITUTE

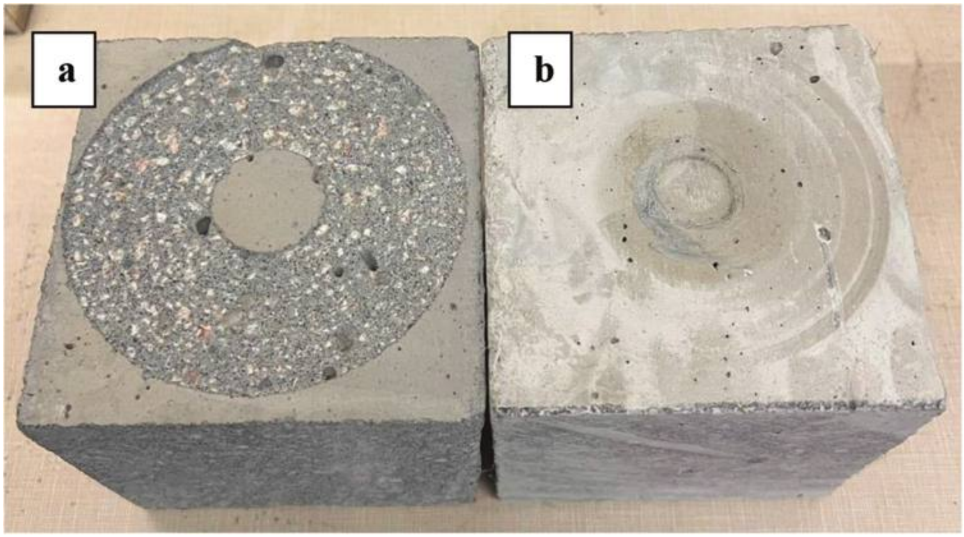

American Concrete Institute

ACI MATERIALS JOURNAL

JULY 2023, V. 120, NO. 4

A JOURNAL OF THE AMERICAN CONCRETE INSTITUTE
AN INTERNATIONAL TECHNICAL SOCIETY

Discussion is welcomed for all materials published in this issue and will appear ten months from this journal's date if the discussion is received within four months of the paper's print publication. Discussion of material received after specified dates will be considered individually for publication or private response. ACI Standards published in ACI Journals for public comment have discussion due dates printed with the Standard.

The *ACI Materials Journal* (ISSN 0889-325x) is published bimonthly by the American Concrete Institute. Publication office: 38800 Country Club Drive, Farmington Hills, MI 48331. Periodicals postage paid at Farmington, MI, and at additional mailing offices. Subscription rates: $192 per year, payable in advance. POSTMASTER: Send address changes to: *ACI Materials Journal*, 38800 Country Club Drive, Farmington Hills, MI 48331.

Canadian GST: R 1226213149.

Direct correspondence to 38800 Country Club Drive, Farmington Hills, MI 48331. Telephone: +1.248.848.3700.
Website: http://www.concrete.org.

MEETINGS

AUGUST

10-12—World of Concrete Asia, Shanghai, China, https://en.wocasia.cn

14-18—The Twelfth International Structural Engineering and Construction Conference (ISEC 12), Chicago, IL, www.isec-society.org/ISEC_12

24-25—2023 PEER Annual Meeting, Berkeley, CA, https://peer.berkeley.edu/home

SEPTEMBER

5-7—Building Innovation 2023, Washington, DC, www.buildinginnovation.org

10-13—Concrete 2023, Perth, WA, Australia, https://concreteinstitute.com.au/concrete-2023

10-14—FraMCoS-XI: 11th International Conference on Fracture Mechanics of Concrete and Concrete Structures, Bangalore, India, https://framcos11.iisc.ac.in/index.php

17-20—17th International Congress on Polymers in Concrete (ICPIC 2023), Warsaw, Poland, https://icpic23.org

17-20—4th Fiber Reinforced Concrete International ACI-*fib*-RILEM Joint Workshop: from Design to Structural Applications, Tempe, AZ, www.rilem.net/agenda/4th-fiber-reinforced-concreteinternational-aci-fib-rilem-joint-workshop-from-design-tostructural-applications-1537

18-22—16th International Congress on the Chemistry of Cement 2023 (ICCC 2023), Bangkok, Thailand, www.iccc2023.org

25-29—2nd Conference of the European Association on Quality Control of Bridges and Structures – EUROSTRUCT 2023, Vienna, Austria, https://eurostruct.org/eurostruct-2023

26-29—Greenbuild 2023: Building Transformation, Washington, DC, https://greenbuild.informaconnect.com/2023

27-30—ASCC 2023 Annual Conference, Grand Rapids, MI, https://ascconline.site-ym.com/event/ac2023

28-30—2023 Concrete NZ Conference, Hamilton, New Zealand, https://confer.eventsair.com/concretenz-conference-2023

OCTOBER

6-9—2023 APA Annual Convention, Delray Beach, FL, www.archprecast.org/annual-convention

9-11—Dni Betonu 2023, Wisła, Poland, www.dnibetonu.com/en

ACI CONCRETE CONVENTION: FUTURE DATES

2023—Oct. 29-Nov. 2, Westin Boston Seaport District & Boston Convention and Exhibition Center, Boston, MA
2024—March 24-28, Hyatt Regency New Orleans, New Orleans, LA
2024—November 3-7, Philadelphia Marriott Downtown, Philadelphia, PA
2025—Mar. 30-Apr. 3, Sheraton Centre Toronto Hotel, Toronto, ON, Canada

For additional information, contact:
Event Services, ACI
38800 Country Club Drive
Farmington Hills, MI 48331
Telephone: +1.248.848.3795
email: conventions@concrete.org

ON FRONT COVER: 120-M44, p. 47, Fig. 3—Mixture M5 samples after 6 minutes of testing under: (a) rotating-cutter abrasion test; and (b) smooth-roller abrasion test.

Contributions to *ACI Materials Journal*

The *ACI Materials Journal* is an open forum on concrete technology and papers related to this field are always welcome. All material submitted for possible publication must meet the requirements of the "American Concrete Institute Publication Policy" and "Author Guidelines and Submission Procedures." Prospective authors should request a copy of the Policy and Guidelines from ACI or visit ACI's website at **www.concrete.org** prior to submitting contributions.

Papers reporting research must include a statement indicating the significance of the research.

The Institute reserves the right to return, without review, contributions not meeting the requirements of the Publication Policy.

All materials conforming to the Policy requirements will be reviewed for editorial quality and technical content, and every effort will be made to put all acceptable papers into the information channel. However, potentially good papers may be returned to authors when it is not possible to publish them in a reasonable time.

Discussion

All technical material appearing in the *ACI Materials Journal* may be discussed. If the deadline indicated on the contents page is observed, discussion can appear in the designated issue. Discussion should be complete and ready for publication, including finished, reproducible illustrations. Discussion must be confined to the scope of the paper and meet the ACI Publication Policy.

Follow the style of the current issue. Be brief—1800 words of double spaced, typewritten copy, including illustrations and tables, is maximum. Count illustrations and tables as 300 words each and submit them on individual sheets. As an approximation, 1 page of text is about 300 words. Submit one original typescript on 8-1/2 x 11 plain white paper, use 1 in. margins, and include two good quality copies of the entire discussion. References should be complete. Do not repeat references cited in original paper; cite them by original number. Closures responding to a single discussion should not exceed 1800-word equivalents in length, and to multiple discussions, approximately one half of the combined lengths of all discussions. Closures are published together with the discussions.

Discuss the paper, not some new or outside work on the same subject. Use references wherever possible instead of repeating available information.

Discussion offered for publication should offer some benefit to the general reader. Discussion which does not meet this requirement will be returned or referred to the author for private reply.

Send manuscripts to:
http://mc.manuscriptcentral.com/aci

Send discussions to:
Journals.manuscripts@concrete.org

ACI MATERIALS JOURNAL TECHNICAL PAPER

Title No. 120-M41

Behavior of Engineered Cementitious Composites with Expanded Glass for Thermal Applications

by Adeyemi Adesina and Sreekanta Das

Expanded glass (EG) made from recycled glass waste was used as an aggregate in the production of engineered cementitious composites (ECCs) to improve their thermal conductivity. The corresponding influence of the EG content on the physical, mechanical, and durability properties was evaluated. The EG was used as up to 100% replacement of the conventional silica sand (SS) in ECCs. The physical properties evaluated are thermal conductivity and density, while the mechanical properties evaluated are the compressive, flexural, and tensile strengths alongside the permeability properties and drying shrinkage. The findings from this study showed that the use of EG as a replacement for SS as aggregate in ECCs resulted in an improvement in the thermal insulation properties and a reduction in density. The 28-day thermal conductivity of ECCs made with EG as 100% replacement of SS is 53.8% lower than that of the ECCs made with only SS as the aggregate.

Keywords: engineered cementitious composites (ECCs); expanded glass (EG); fly ash (FA); portland cement (PC); thermal conductivity.

INTRODUCTION

The operation of infrastructures such as buildings is highly energy-intensive due to the need to maintain a conducive temperature for everyday activities. It has been estimated that the energy consumption by buildings is approximately 30% of the world's energy consumption.[1] The rapid urbanization going on globally coupled with the increase in population is expected to result in the construction of more buildings and a consequential increase in energy use. Thus, it is critical to find innovative and sustainable approaches to improve the thermal efficiency of buildings. One such effective approach is the improvement of the thermal insulation properties of construction materials such as cementitious materials by incorporating various materials with lower thermal conductivity.[2,3] Several studies have been able to successfully reduce the thermal conductivity (that is, improve the thermal insulation properties) of cementitious materials by incorporating various lightweight recycled materials/by-products.[4-6] The use of these lightweight recycled materials/by-products in cementitious materials not only helps improve the thermal insulation properties, but also helps in managing these detrimental wastes effectively and efficiently.

On the other hand, there exists a special type of fiber-reinforced cementitious composite referred to as engineered cementitious composites (ECCs).[7] In contrast to the conventional cementitious composites, ECCs exhibit a high strain capacity and are suitable for the construction of various building envelope elements such as walls, floors, and roofs.[8,9] Several studies[8,10] have been carried out to evaluate the mechanical and durability properties of ECCs, but there is limited knowledge on their corresponding thermal insulation properties, thereby limiting their thermal applications. In addition, there is limited use of lightweight materials with low thermal conductivity in ECCs. Thus, finding suitable sustainable materials with low thermal conductivity to incorporate into ECCs would help to bridge this knowledge gap and improve the thermal insulation properties of ECCs, opening a pathway for more sustainable application of ECCs.

One such sustainable material that can be incorporated into ECCs is expanded glass (EG), which is obtained from recycling waste glass. EG has a thermal conductivity of approximately 0.07 W/m·K and a specific gravity of 0.19,[11] while the conventional aggregates (that is, natural sand) used in cementitious materials have a thermal conductivity and specific gravity of approximately 3.5 W/m·K and 2.65, respectively. Thus, the use of EG to replace the conventional silica sand (SS) in ECCs is expected to result in a reduction in thermal conductivity and density. Some studies have used EG as aggregate in conventional cementitious materials such as mortars.[12,13] However, no study exists on the application of EG as aggregate in ECCs. In addition, the existing studies on the use of EG in mortars (that is, not ECC) primarily focus on the compressive strength, with a limited study on the influence of EG on other mechanical and durability properties.

A recent study by Adewoyin et al.[13] showed that the use of EG to replace natural aggregates in mortar resulted in a reduction in the thermal conductivity of the mortars. The study also showed that the use of EG does not pose any alkali-silica reaction threat. Thus, EG can be deemed a good candidate for an eco-friendly material that can be used to improve the thermal conductivity of ECCs. Moreover, the limited availability of the conventional aggregates used in ECCs (that is, SS) inhibit the large-scale application of ECCs due to their high cost and high embodied carbon.[14] Thus, the use of EG as a replacement for SS would result in a reduction in the cost and embodied carbon of ECCs in addition to reducing the thermal conductivity of the composites.

In addition to the use of lightweight aggregates in cementitious materials, studies have also shown that the use of supplementary cementitious materials (SCMs) such as fly

---

ACI Materials Journal, V. 120, No. 4, July 2023.
MS No. M-2022-035.R5, doi: 10.14359/51738816, received April 27, 2023, and reviewed under Institute publication policies. Pertinent discussion including author's closure, if any, will be published ten months from this journal's date if the discussion is received within four months of the paper's print publication.

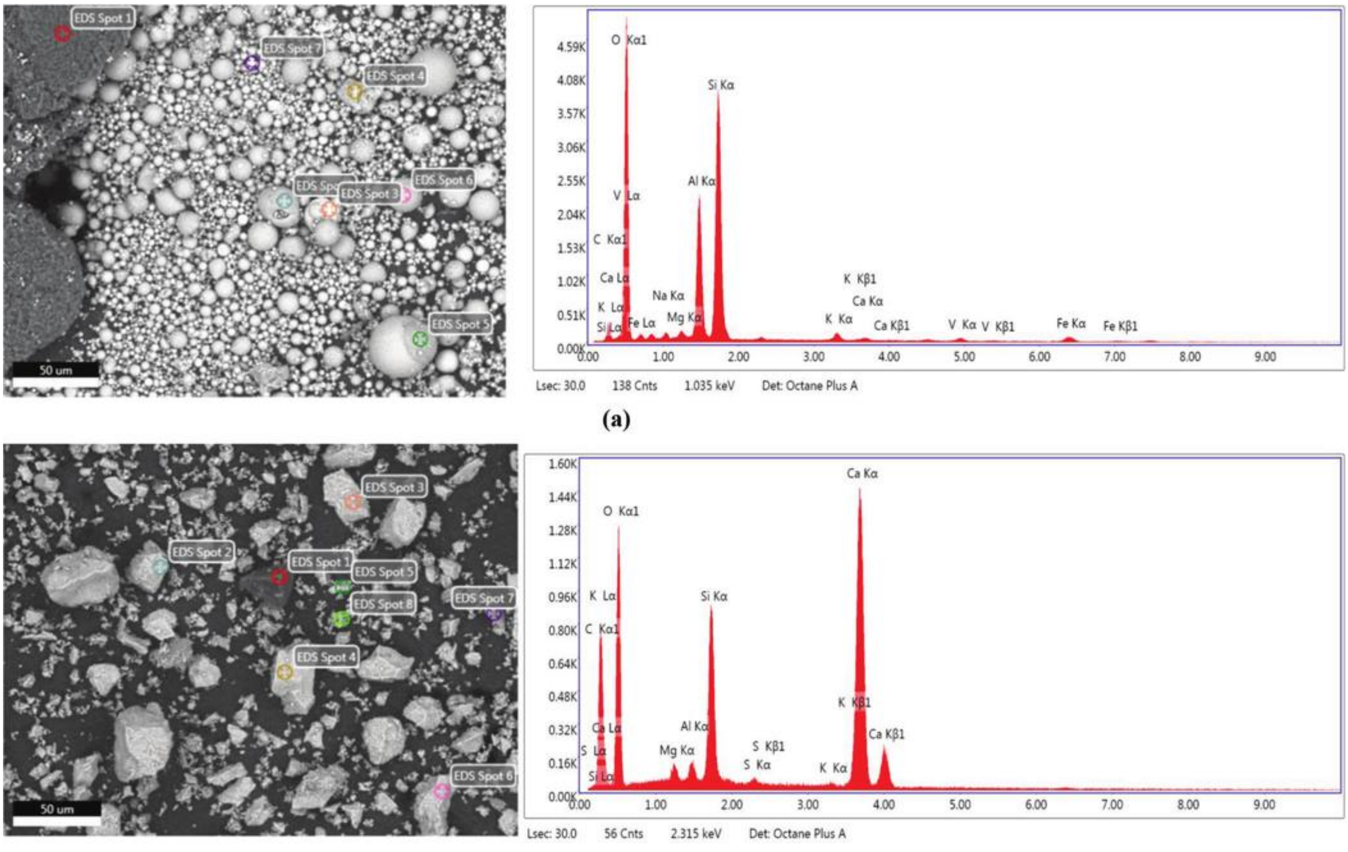

(a)

(b)

Fig. 1—SEM images and energy-dispersive X-ray spectroscopy (EDS) spectra of binders: (a) FA; and (b) PC.

ash (FA) can be used to improve the thermal insulation properties of cementitious materials.[15-17] A significantly high amount of FA is already used in ECC mixtures at an FA-to-portland cement (PC) ratio of 1.2.[18,19] Thus, increasing the FA content used as the replacement of PC in ECCs would result in more improvement in the thermal insulation properties.

RESEARCH SIGNIFICANCE

This study aims to bridge the current knowledge gap by using a high-volume FA (that is, approximately 70% replacement of PC) as a binder component and EG as a replacement for different contents of SS as aggregate in ECCs. The corresponding influence of EG content on the physical, mechanical, and durability properties was evaluated. The physical properties assessed are density and thermal conductivity, while the mechanical properties of the ECCs were evaluated in terms of the compressive, flexural, and tensile strengths. The permeability properties investigated are sorption, water absorption, chloride-ion penetration, and porosity. Microstructural investigations were also carried out on one of the developed mixtures, and the observations correlated with exhibited properties of ECCs. The findings presented in this paper provide more insights into the influence of various contents of EG on the thermal conductivity and other properties of ECCs.

EXPERIMENTAL PROGRAM

Materials

The ECCs produced in this study are made with Type 1 PC and Class F FA as the binders. The scanning electron microscope (SEM) images of the binders alongside their elemental compositions are presented in Fig. 1. More about the chemical composition of the binder is available in a previous study.[20] The primary aggregate used is SS, while EG was used as a partial to total replacement of the SS. The SEM images of the aggregates used are presented in Fig. 2, while the corresponding elemental compositions are presented in Fig. 3. As can be observed from Fig. 2(a), the EG is a very porous material compared to SS. Table 1 shows the properties of the SS and EG. Polyvinyl alcohol (PVA) fibers with a length of 8 mm (0.31 in.) and tensile strength of 1600 MPa (232 ksi) were used as reinforcement. Figure 4 shows the SEM image of the PVA fibers. To improve the workability of the mixtures, a high-range water-reducing admixture (HRWRA) was used as the chemical admixture.

Mixture composition and sample preparation

The FA-to-PC ratio for all the ECC mixtures was kept at 2.2, while the water-binder ratio (*w*/*b*) and sand-binder ratio were fixed at 0.25 and 0.38, respectively. A total of five mixtures were made with varying contents of EG (that is, 0, 25, 50, 75, and 100%) as a replacement for SS up to 100%. PVA fibers at a dosage of 2% were used to reinforce all mixtures. The ECC mixtures were prepared by dry mixing the aggregates and the binder for 3 minutes, followed by the

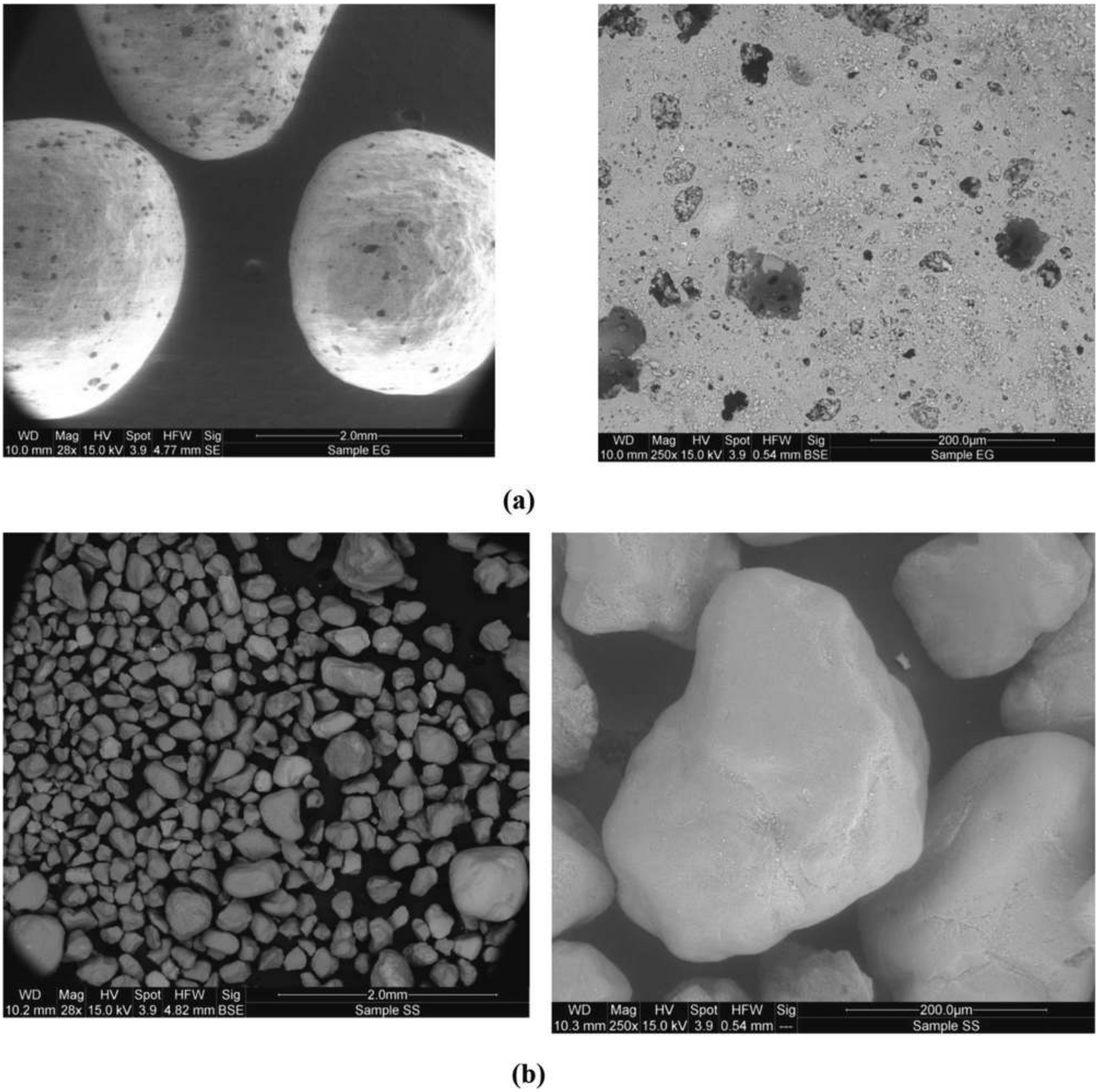

Fig. 2—SEM images of aggregates used at different magnifications: (a) EG; and (b) SS.

addition of water with the chemical admixture pre-added. After a flowable mixture was obtained, the PVA fibers were slowly added to the fresh mixture as the mixing continued to ensure the fibers were properly dispersed. The mixing process was continued for an additional 2 minutes after all the fibers were added to achieve a homogenous mixture. As soon as the mixing was completed, the fresh ECC mixtures were placed in molds for the tests to be evaluated. The molds were covered with a thin plastic sheet to avoid loss of moisture from the samples during curing. At approximately 24 hours after the fresh mixtures were placed, the samples were removed from the molds and cured underwater until the tests were due.

Test methods

Thermal conductivity—The thermal conductivity of the ECC samples was evaluated by using the probe method following the test procedure in ASTM D5334-14.[21] This method involves inserting the probe of the conductivity meter into premade holes in cylindrical samples with a diameter and height of 100 and 200 mm (4 and 8 in.), respectively, as shown in Fig. 5. For each EG content and age, the thermal conductivity of three samples was measured and the average thermal conductivity was reported.

Mechanical properties—The mechanical properties evaluated are compressive strength, flexural strength, and tensile strength. The compressive strength of the ECCs was assessed in accordance with ASTM C109/C109M-16a[22] by using samples with dimensions of 50 x 50 x 50 mm (2 x 2 x 2 in.). The tensile strength of the ECCs was evaluated by using dog-bone samples as recommended by the Japan Society of Civil Engineers[23] and used in previous studies.[14,24]

The flexural properties of the ECCs were evaluated using prism samples with dimensions of 75 x 75 x 350 mm (3 x

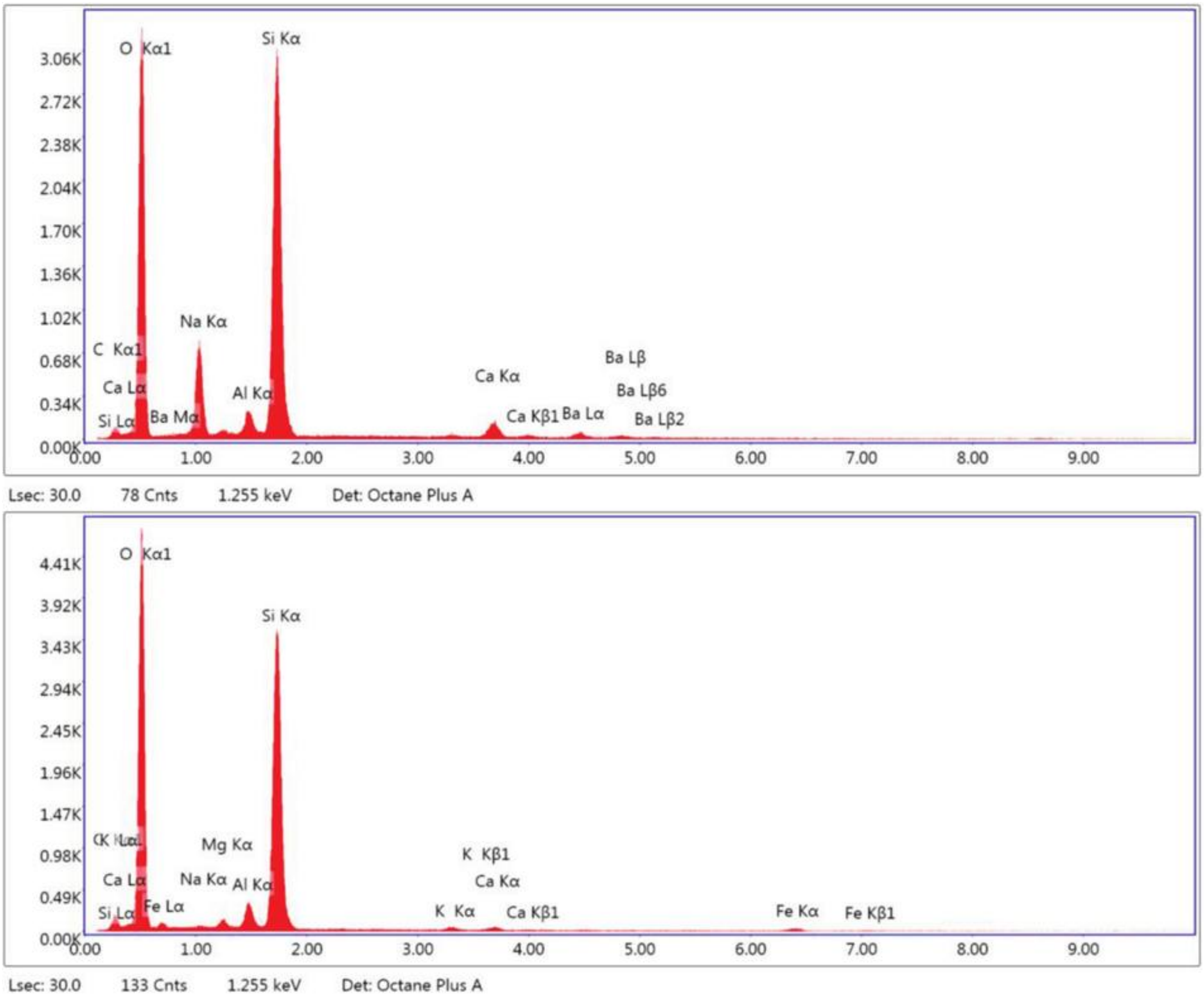

Fig. 3—EDS spectra of aggregates: (a) EG; and (b) SS.

3 x 14 in.) and following the test procedures in ASTM C1609/C1609M-07.[25] For the compressive and tensile strengths, three samples were tested, and the average result was presented. However, for the flexural properties, three samples were also tested but a representative load-deflection curve for each mixture was selected for the flexural properties calculations, as stipulated in ASTM C1609/C1609M.

Permeability properties—The permeability properties of the ECCs were assessed in terms of water absorption, porosity, sorption, sorptivity, and chloride-ion penetration. The test procedures in ASTM C642-13[26] were followed for the water absorption and porosity assessments. Cylindrical samples with a height of 50 mm (2 in.) and a diameter of 100 mm (4 in.) were used. Similar to the water absorption test, cylindrical samples with a height and diameter of 50 mm (2 in.) and 100 mm (4 in.), respectively, were used to assess the sorption of the ECCs as per the test procedures in ASTM C1757-13.[27]

The rate of water absorption (that is, sorptivity) of the ECCs was evaluated in accordance with ASTM C1585-13.[28] Cylindrical samples were also used to evaluate the chloride-ion penetration of the ECCs by carrying out a rapid chloride penetration test in accordance with ASTM C1202-12.[29] For each of the permeability tests, three samples were tested for each mixture and the corresponding average results were presented.

Drying shrinkage—Bar samples with dimensions of 25 x 25 x 250 mm (1 x 1 x 10 in.) were used to evaluate the drying shrinkage of the ECCs. The drying shrinkage of the ECCs was measured in terms of the length change up to 28 days by adhering to the test procedures in ASTM C596-07.[30] A total of three samples were made and evaluated for each mixture. Thus, the results of the drying shrinkage provided represent the average drying shrinkage for each mixture.

Ultrasonic pulse velocity—The presence of pores and deformities in the ECCs was evaluated nondestructively by using the ultrasonic pulse velocity (UPV) method. The test entails measuring the velocity at which a pulse passes through the sample based on the length of the sample and the time it takes the pulse to pass through the sample. Samples with dimensions of 50 x 50 x 50 mm (2 x 2 x 2 in.) were used to evaluate the UPV of the ECCs following the test in ASTM C597-02.[31]

RESULTS AND DISCUSSION

Physical properties

Density—The densities of the ECCs incorporating various contents of EG are presented in Fig. 6. The density of the ECCs ranged between 1654 and 1960 kg/m^3 (103 and 122 lb/ft^3)

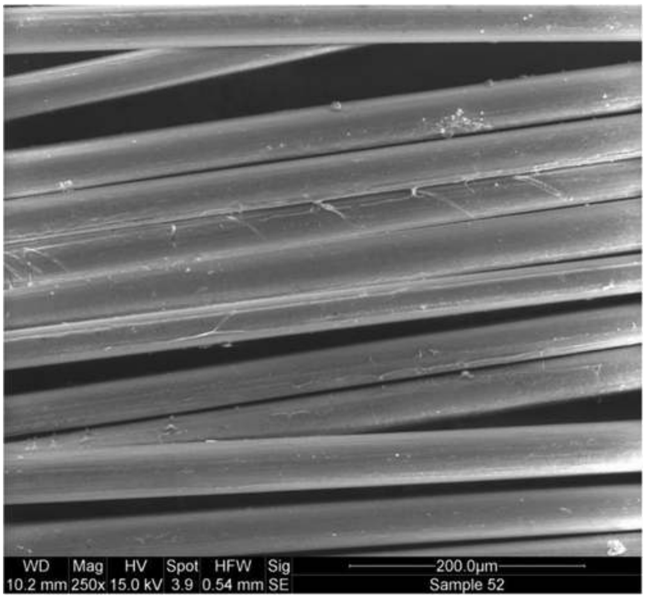

Fig. 4—SEM images of PVA fibers.

Fig. 5—Thermal conductivity measurement of ECCs.

Table 1—Properties of EG

Property	Value	
	EG	SS
Physical		
Particle size, mm	2 to 4	0.11 to 0.20
Bulk density, kg/m^3	190	—
Compressive strength, MPa	1.40	—
Thermal conductivity, W/m·K	0.07	—
Water absorption, %	23	2.71
Specific gravity	0.90	2.57
pH value	9 to 12	—
Softening point, °C	700	—
Color	Creamy white	Brown
Chemical		
Element	Weight, %	
	EG	SS
O	47.36	6.1
Na	11.14	13.6
Al	12.96	—
Si	25.58	68.3
Ca	2.96	6.2
Mg	—	2.7

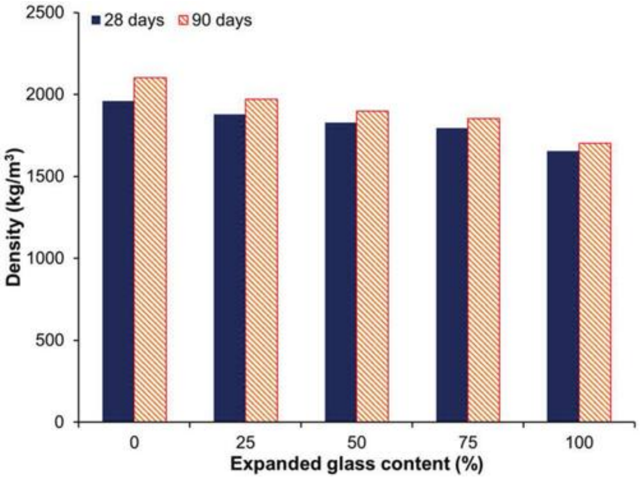

Fig. 6—Influence of EG content on density.

at 28 days, while at 90 days, the density ranged from 1700 to 2101 kg/m^3 (106 to 131 lb/ft^3). The increase in the density of the ECCs with age regardless of the EG content can be ascribed to the continuous pozzolanic reactivity of the FA and hydration of the PC.[32,33] For example, the 90-day density of the ECC made with EG as a 25% replacement of the SS exhibited a density of 4.9% higher than the density at 28 days. It can also be observed from Fig. 6 that the density of the ECCs reduced with increasing content of EG used as the replacement for the SS. The density at 90 days of ECCs made with EG as 25%, 50%, 75%, and 100% replacement of the SS is 6.2%, 9.7%, 11.7%, and 19.1%, respectively, lower compared to that of the ECCs made with only SS as aggregate.

The reduction in the densities of the ECCs with the incorporation of EG can be linked to the lower specific gravity of the EG compared to that of SS. The specific gravity of EG used in this study is 0.9, while that of SS is 2.6. The possible incorporation of air voids into the ECCs with the incorporation of EG could also contribute to the reduction in density.[34] These findings are in agreement with other studies on ECCs where the use of lightweight aggregates such as crumb rubber and FA cenosphere has been reported to result in a lower density of ECCs.[24,35] These findings indicate EG can be incorporated into ECCs to reduce their density. It is well known that lightweight cementitious materials exhibit better thermal conductivity and offer an effective way to reduce the dead load of structures.

In accordance with ASTM C330/C330M-09[36] and ACI 213R-03,[37] cementitious composites with a 28-day density

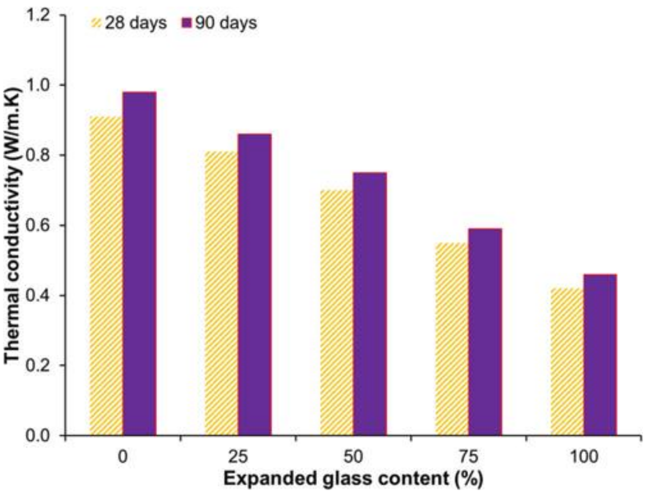

Fig. 7—Influence of EG content on thermal conductivity.

of less than 1850 kg/m^3 (115 lb/ft^3) can be considered to be lightweight composites for structural applications. Thus, ECCs made in this study with EG as 50, 75, and 100% replacement of SS as aggregate can be considered lightweight ECC.

Thermal conductivity—Thermal conductivity is an efficient way to evaluate the thermal properties of cementitious materials. For insulation applications, lower thermal conductivity is better. Thus, the lower the thermal conductivity of cementitious material, the higher its thermal insulation capacity. The influence of the EG content on the thermal conductivity is presented in Fig. 7. The thermal conductivity at 28 days of the ECCs made with 25%, 50%, 75%, and 100% EG is 10.9%, 23.1%, 39.6%, and 53.8%, respectively, lower than that of the control ECC made with only SS as the aggregate. The reduction in the thermal conductivity of the ECCs with the incorporation of EG can be ascribed to the lower thermal conductivity of the EG compared to that of SS. The thermal conductivity of SS used in this study is 3 W/m·K (1.7 BTU/h·ft·°F), while that of the EG used is 0.07 W/m·K (0.04 BTU/h·ft·°F). The possible introduction of air voids into the ECCs coupled with the porous nature of EG (Fig. 2(a)) could also contribute to the lower thermal conductivity of ECCs made with EG. The thermal conductivity of air has been estimated to be 0.025 W/m·K (0.014 BTU/h·ft·°F). Hence, the incorporation of these voids into ECCs with the incorporation of EG would result in a reduction in the thermal conductivity of the ECCs.

From Fig. 7, it can also be observed that the thermal conductivity of the composites increased slightly with age. The 90-day thermal conductivity of the ECCs made with EG as 0, 25, 50, 75, and 100% replacement of SS increased by 7.7, 6.2, 7.1, 7.3, and 9.5% when compared to the corresponding thermal conductivities at 28 days. The slight increase in the thermal conductivity of the composites with age can be linked to the refinement of the microstructure of the ECCs due to the formation of pozzolanic and hydration products with age. Thus, as the microstructure of the ECCs becomes more refined in the long term, a slight increase in the thermal conductivity should be anticipated.

Several studies have indicated that the thermal conductivity of cementitious materials is directly related to their corresponding density.[38-40] Hence, a correlation between the density and thermal conductivity of the ECCs was made and is presented in Fig. 8. It can be observed from Fig. 8 that there is a good linear relationship between the thermal conductivity and the density. The thermal conductivity of the ECCs increases with higher density. These findings confirmed that the reduction in the thermal conductivity and density of the ECCs with the incorporation of EG is due to the physical properties of EG coupled with the possible introduction of air voids into the matrix. Thus, to improve the thermal insulation properties of ECCs in terms of a reduction in thermal conductivity, EG can be incorporated as aggregate.

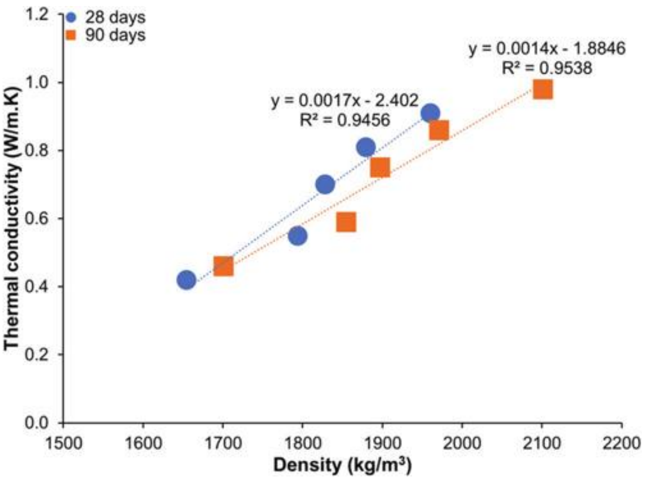

Fig. 8—Correlation between thermal conductivity and density of ECCs.

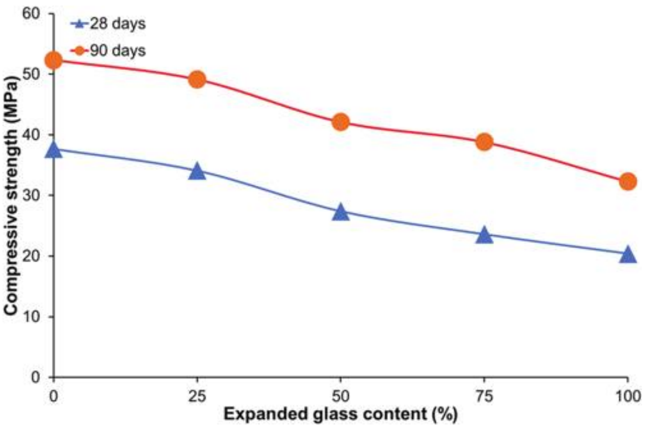

Fig. 9—Influence of EG content on compressive strength.

Mechanical properties

Compressive strength—Figure 9 shows the influence of EG content on the compressive strength of ECCs. The compressive strength of the ECCs reduced with a higher content of EG, as shown in Fig. 9. The compressive strength of ECCs at 28 days is in the range of 20.4 to 37.7 MPa (2.9 to 5.5 ksi), while at 90 days, the compressive strength of the ECCs is in the range of 32.3 to 52.3 MPa (4.7 to 7.6 ksi). The reduction in the compressive strength of the ECCs with higher EG content can be linked to the introduction of air voids into the matrix coupled with the porous nature of EG (Fig. 2(a)) resulting in weak zones. The lower stiffness of

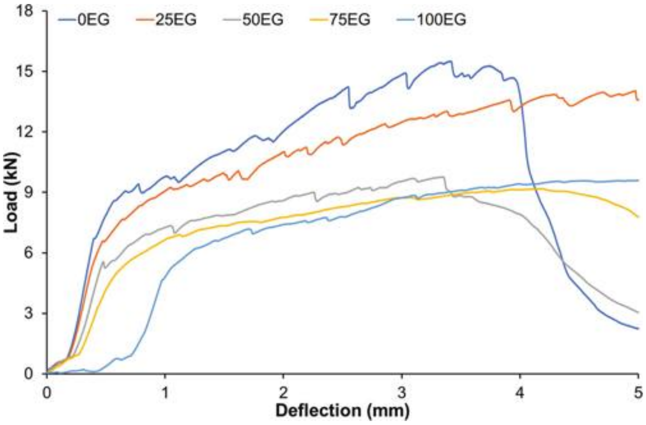

Fig. 10—Load-deflection behavior of ECCs at 90 days.

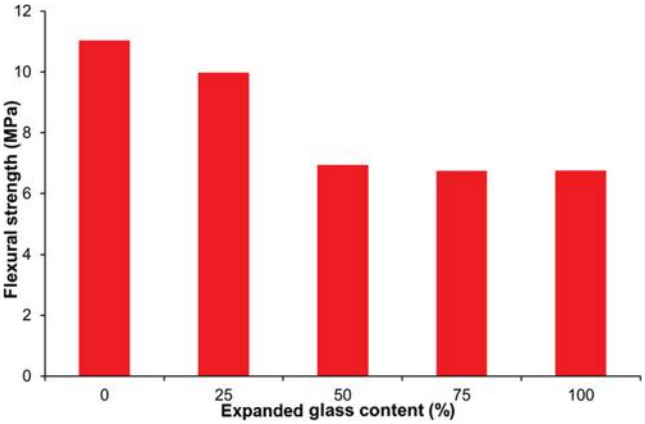

Fig. 11—Influence of EG content on flexural strength.

EG compared to SS could also contribute to the reduction in compressive strength. Similar observations have been reported by various studies, where the incorporation of porous lightweight aggregates into ECCs has been reported to yield lower compressive strength.[10,14,24] Nonetheless, it can be observed that even at 28 days, the compressive strength of ECC made with EG as 100% replacement of the SS is greater than 20 MPa (2.9 ksi). Thus, in accordance with ACI 213R-03,[37] all the ECC mixtures made in this study can be used for structural applications as the compressive strengths are greater than 17.5 MPa (2.5 ksi).

As a result of the progression of the PC hydration and FA pozzolanic reactivity with age, it can be observed that the compressive strength of the ECCs increased with age. For example, the 90-day compressive strength of ECC made with EG as a 50% replacement of the SS is 14.7% higher than that of the similar mixture at 28 days. These findings showed that the incorporation of the EG into the ECCs does not alter the binder reactivity.

Flexural properties—The representative load-deflection curves of the ECCs at 90 days are presented in Fig. 10, while the corresponding flexural strengths are presented in Fig. 11. It can be observed from Fig. 10 that the incorporation of EG into the ECCs does not have any detrimental impact on the strain-hardening behavior of the ECCs. However, there was a reduction in the flexural load capacity and the corresponding flexural strength, as shown in Fig. 11. The reduction in the flexural load capacity with the incorporation of EG can also be linked to the increase in the air voids coupled with the lower stiffness of the EG. On the other hand, the use of EG as aggregate in ECCs does not result in any negative impact on the deflection capacity of the ECCs. In fact, ECCs made with EG exhibited higher deflection capacity compared to the control ECC, which was made with only SS as the aggregate. The improvement in the deflection capacity of the ECCs with the incorporation of EG can be ascribed to the lower stiffness of the EG resulting in a reduction in the matrix fracture toughness.[41] Thus, in applications where higher deflection capacity is required, EG can be incorporated as aggregate provided the load capacity requirements are met. A similar observation has been reported when crumb rubber, which has a low stiffness, was incorporated as aggregate into ECCs.[24,42,43]

Similar to the compressive strength results (Fig. 9), it can be observed that the flexural strength of the ECCs reduced with higher EG content, as shown in Fig. 11. The 90-day flexural strength of the ECCs made with 25%, 50%, 75%, and 100% replacement of the SS is 9.5%, 37.0%, 38.8%, and 38.7%, respectively, lower compared to that of the control with only SS as the aggregate. The reduction in the flexural strength with the incorporation of EG can also be linked to the porous nature of EG and the increase in the weak zone areas in the ECCs due to the incorporation of air voids. These results are in agreement with a similar study by Keskin et al.[41] where perlite was incorporated as lightweight aggregate to replace up to 30% SS in ECCs. The incorporation of perlite by Keskin et al.[41] as 10, 20, and 30% replacement of SS resulted in a decrease in the 90-day flexural strength by 11.8%, 22.8%, and 25.2%, respectively, when compared to the control without perlite. The lower reduction in flexural strength (that is, 9.5%) when EG was used as a 25% replacement of the SS in this study, compared to that of Keskin et al.[41] when a similar content (that is, 30%) of lightweight aggregate was used, can be ascribed to the higher content of FA used in the current study. The ECCs made in this study are composed of an FA-to-PC ratio of 2.2, while that of Keskin et al.[41] is 1.2. The use of a higher content of SCMs such as FA has been found to enhance the properties of cementitious materials in the long term.[44,45]

Tensile strength—Similar to other mechanical properties, the tensile strength of ECCs reduced with the incorporation of EG as a replacement for the conventional sand, as shown in Fig. 12. The reduction in the 90-day tensile strength when EG is used as a replacement for SS up to 100% is in the range of 9.3 to 21.6%. The reduction in the tensile strength when EG is used as aggregate can also be ascribed to the reasons mentioned earlier for compressive and flexural strengths. These observations are consistent with that of Şahmaran et al.,[46] where pumice was used as a lightweight aggregate to replace up to 20% SS in ECC mixtures. A similar observation was also reported by Zhou et al.,[47] where the use of FA cenosphere as up to a 60% replacement for SS resulted in a reduction in the tensile strength. On the other hand, the tensile strength of the ECCs increased with age due to the formation of more reaction products and densification of the cementitious matrix. The 90-day tensile strength of ECCs

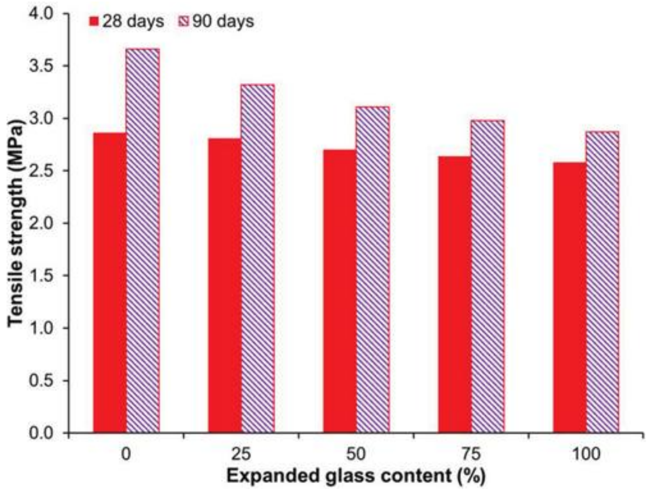

Fig. 12—Influence of EG content on tensile strength.

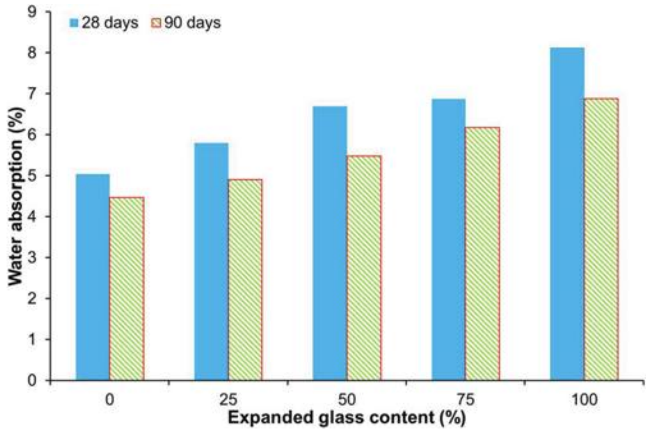

Fig. 13—Influence of EG content on water absorption.

made with 25%, 50%, 75%, and 100% EG is 18.1%, 15.2%, 12.9%, and 11.2%, respectively, greater than their corresponding tensile strength at 28 days.

Durability properties

Water absorption—The water absorption test evaluates the performance of cementitious materials that can be subjected to constant moisture contact or submerged continuously. The influence of the EG content on the water absorption of the ECCs is presented in Fig. 13. It is evident from Fig. 13 that the incorporation of EG into the ECCs as aggregate resulted in an increase in their corresponding water absorption. The incorporation of EG as up to 100% replacement for SS resulted in an increase in the water absorption by up to 35.1% at 90 days. The increase in the water absorption of the ECCs due to the use of EG as aggregate can be linked to the porous nature of the EG coupled with the incorporation of additional air voids into the cementitious matrix. On a positive note, the water absorption of the ECCs reduced with age as a result of the continuous refinement of the cementitious matrix by the additional reaction products formed. For example, the 90-day water absorption of ECC made with EG as 100% replacement of the SS is 15.3% lower than the corresponding water absorption at 28 days.

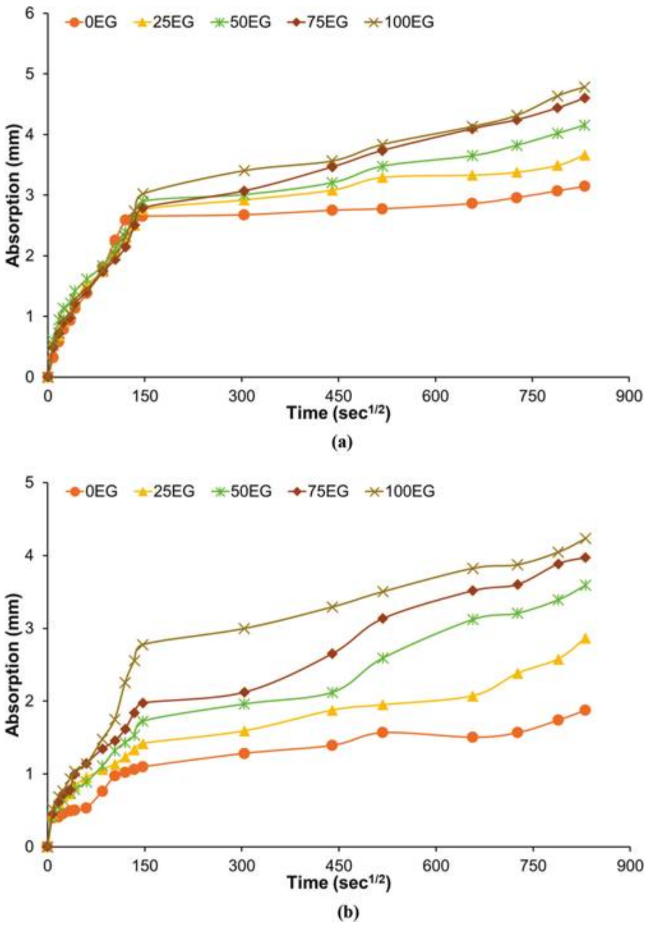

Fig. 14—Sorptivity of ECCs at: (a) 28 days; and (b) 90 days.

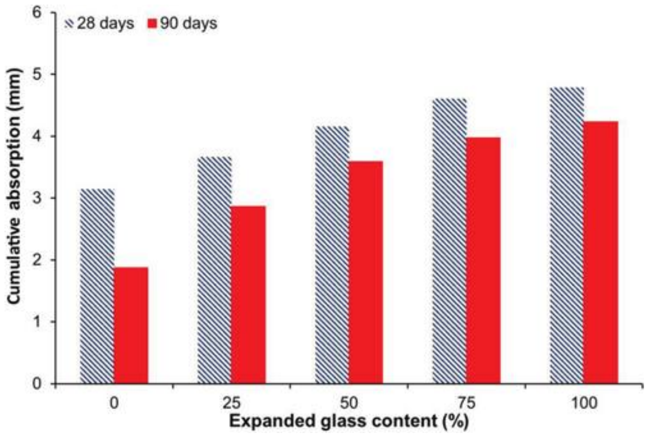

Fig. 15—Influence of EG content on cumulative absorption.

Sorptivity—In contrast to the water absorption and sorption evaluations, the sorptivity evaluates the rate of water absorption. The rate of water absorption (that is, sorptivity) of the ECC mixtures and the cumulative water absorption are presented in Fig. 14 and 15, respectively. It can be observed from the figures that a similar trend to other permeability properties was exhibited by the ECCs. The water absorption of the ECCs increased with higher content of EG. It can also be observed from Fig. 14 that the rate of water absorption of all ECCs was higher during the initial period of the test (that is, up to 6 hours), indicating the ECCs possess higher initial sorptivity. However, after the high initial sorptivity,

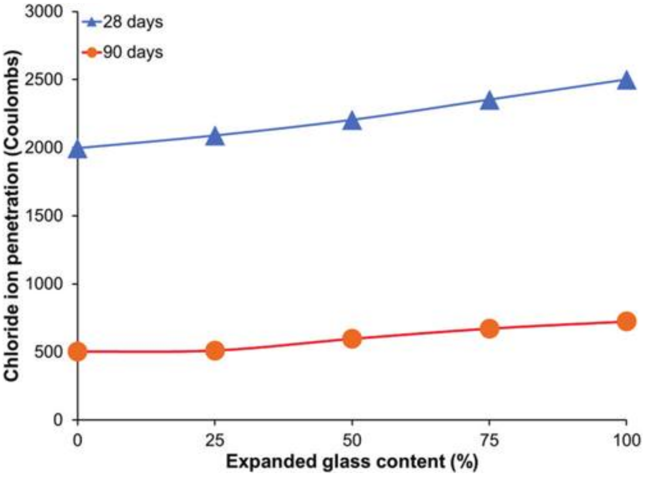

Fig. 16—Influence of EG content on chloride ion penetration.

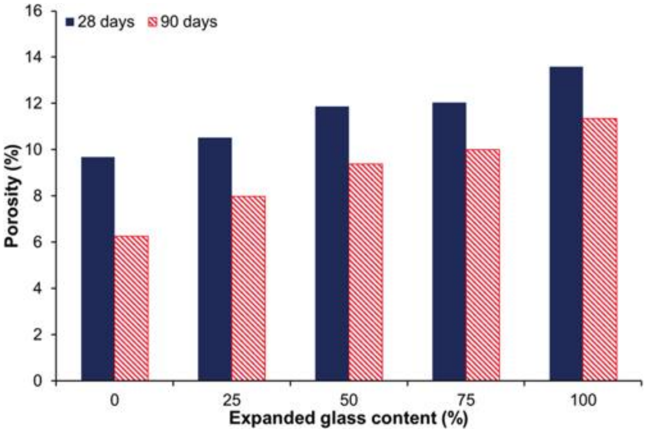

Fig. 17—Influence of EG content on porosity.

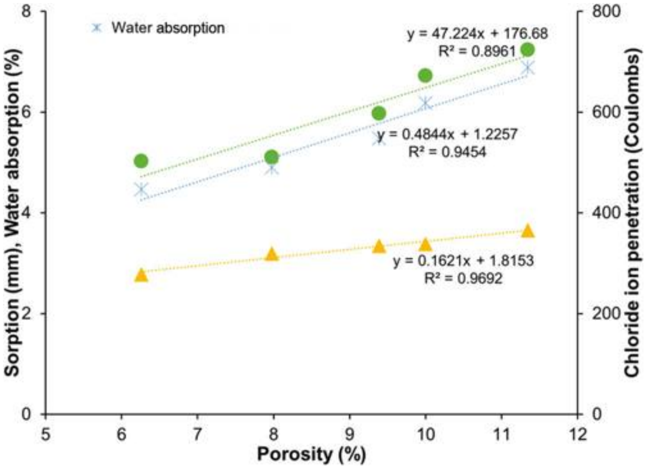

Fig. 18—Correlation between porosity and permeability properties of ECC.

the ECCs exhibited a lower secondary sorptivity due to the pores of the ECCs already filling up during the initial sorptivity. Nonetheless, similar to the water absorption (Fig. 13) of the ECCs, there was an increase in the cumulative water absorption with higher EG content. Similarly, the cumulative absorption of the ECCs reduced with age.

Chloride-ion penetration—The chloride-ion penetration assessed by the rapid chloride penetration test is based on measuring the total charges passed through a sample for a duration of 6 hours. The higher the total charges passed, the more permeable the composites. As per ASTM C1202, composites with total charges passed in the range of 100 to 1000 coulombs can be classified as very low chloride ion penetrability, while those in the range of 1000 to 2000 coulombs can be deemed to have low chloride ion penetrability. On the other hand, composites with total charges passed between 2000 and 4000 coulombs are classified as moderate chloride ion penetrability, while those greater than 4000 coulombs are deemed high chloride permeability. From the results of the total charges passed in the ECCs presented in Fig. 16, it can be observed that the ECCs at 28 days have moderate chloride ion penetrability, while at 90 days, the chloride-ion penetrability was significantly reduced to very low. The higher total charges passed at 28 days (that is, 1996 to 2501 coulombs) compared to 90 days (that is, 503 to 724 coulombs) can be ascribed to the high content of FA used as the replacement of PC coupled with the slow pozzolanic reactivity of the FA.

Similar to other permeability properties, it can be observed from Fig. 16 that the chloride ion penetration of the ECCs increased with higher content of EG. The use of EG to replace 25%, 50%, 75%, and 100% of SS resulted in an increase in the total charges passed at 28 days of 4.7%, 10.4%, 17.9%, and 25.3%, respectively. Similarly, at 90 days, there was an increase in the total charges passed of 1.6%, 18.7%, 33.6%, and 43.9% when EG was used as the replacement of 25%, 50%, 75%, and 100%, respectively, of SS. The increase in the total charges passed in the ECCs with the presence and higher content of EG can be ascribed to the porous nature of the EG, which resulted in an increase in the open porosity in the ECCs. These observations are in agreement with a previous study[48] where the use of a porous aggregate (that is, recycled concrete) in ECCs resulted in an increase in the total charges passed.

Porosity—The porosity (that is, voids) of the ECCs is shown in Fig. 17. The results showed that the use of EG as a partial replacement of SS resulted in an increase in the porosity at all ages. For example, the incorporation of EG as 25%, 50%, 75%, and 100% replacement of SS resulted in an increase in the porosity of the ECCs of 8.7%, 22.5%, 24.3%, and 40.2%, respectively, at 28 days. The increase in the porosity of the ECCs can be linked to both the porous nature of the EG and the incorporation of air voids into the ECCs. Nonetheless, at 90 days, there was a significant reduction in the porosity of the ECCs due to the microstructure refinement by the reaction products resulting in a denser matrix. Similar observations have also been reported by Zhou et al.,[47] where the use of FA cenosphere as up to 60% replacement of the SS in ECCs resulted in an increase in the total porosity of up to 69%.

As the increase in the permeability properties of the ECCs has been linked to an increase in void content, as discussed in previous sections, a correlation between the porosity of the ECCs and the permeability properties was made, as shown in Fig. 18. It can be noted from Fig. 18 that a relationship exists between the porosity and the permeability properties. The permeability properties of the ECCs increased

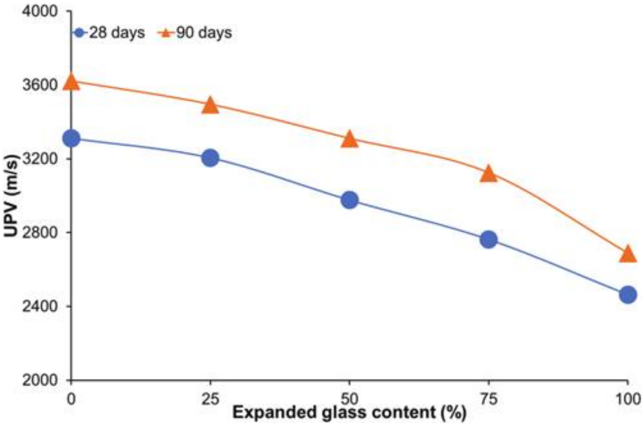

Fig. 19—Influence of EG content on UPV.

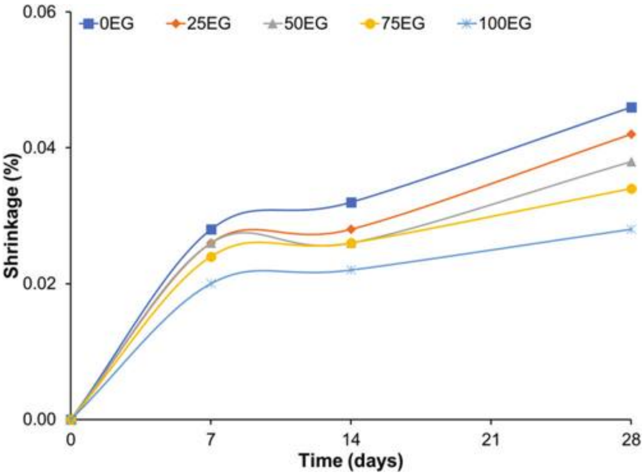

Fig. 20—Influence of EG content on drying shrinkage.

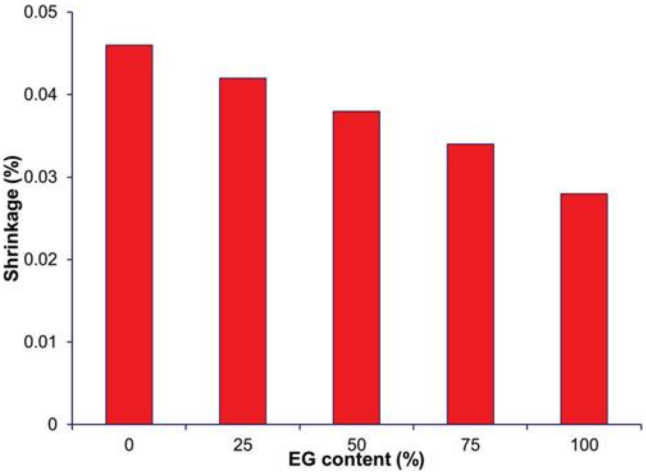

Fig. 21—Cumulative drying shrinkage of ECC.

with higher porosity. Thus, the increase in the permeability properties of the ECCs with higher EG content can be linked to the increase in porosity due to the incorporation of EG as aggregate. Thus, in cases where lower permeability properties are required with higher EG content, various initiatives to reduce the porosity can be implemented.

Ultrasonic pulse velocity—UPV was used as a nondestructive method to evaluate the quality and presence of pores in the ECCs. The lower the UPV value, the higher the presence of voids in the composite. It can be observed from Fig. 19 that the UPV of the ECCs reduced with higher EG content at all ages. For example, the 28-day UPV of ECC made with EG as 75% replacement of the SS is 16.6% lower than that of the ECC mixture made with only SS as the aggregate. The reduction in the UPV of the ECC mixtures with age could be linked to the increase in the porosity of the ECCs due to the incorporation of the EG. These findings further showed that the reduction in the mechanical strength of the ECCs coupled with the increase in permeability can be ascribed to the increased porosity of the ECCs. Nonetheless, at 90 days, the UPV of each ECC mixture was higher due to the refinement of the microstructure by hydration and pozzolanic products. Hence, the improvement in the strength and reduction in the permeability of the ECCs can be linked to the reduction in the porosity with age.

Drying shrinkage—The influence of the EG content on the drying shrinkage of the mixtures with time is presented in Fig. 20, while the corresponding cumulative shrinkage of the mixtures at 28 days is presented in Fig. 21. It can be observed from the figures that, in contrast to the detrimental impact of the EG on the permeability properties, there is an improvement in the resistance of the ECCs to drying shrinkage. The drying shrinkage of the ECCs reduced with higher content of EG. The cumulative drying shrinkage of ECCs made with EG as 25%, 50%, 75%, and 100% replacement of SS is 8.7%, 17.4%, 26.1%, and 39.1%, respectively, lower compared to when only SS was used as the aggregate. The reduction in the drying shrinkage of the ECCs could be linked to the higher particle size of EG, which embodied it with an ability to act as a better restraint against the volumetric change in the cementitious matrix. The porous nature of the EG also means the EG could absorb some of the mixing water and act as an internal curing agent for the cementitious matrix during the drying process. Similar observations have been reported by Şahmaran et al.,[46] where the use of pumice as a lightweight aggregate to replace 10% and 20% of SS in ECCs resulted in a reduction in the drying shrinkage of 28% and 37%, respectively. Xuan and Jun[49] also reported a significant reduction in the drying shrinkage of ECCs when high-volume zeolite was used as lightweight aggregate in ECCs. Thus, in addition to the reduction in the thermal conductivity and density of ECCs, EG can be incorporated to reduce drying shrinkage.

CONCLUSIONS

Expanded glass (EG) was used as an aggregate to produce engineered cementitious composites (ECCs) for thermal applications, and the corresponding effect of different EG contents on the properties of ECCs was investigated. Based on the outcome of this study, the following conclusions can be made:

1. The use of EG as a replacement for silica sand (SS) as aggregate in ECCs resulted in an improvement in the thermal insulation properties and a reduction in density. The 28-day thermal conductivity of ECCs made with EG as 100% replacement of SS is 53.8% lower than that of the ECCs made with only SS as the aggregate. Similarly, a reduction in

the density of ECCs of up to 19.1% was achieved when EG was used to replace SS by up to 100%. Thus, a significant enhancement of the thermal insulation properties of ECCs can be achieved with the incorporation of EG as aggregate.

2. On the other hand, the incorporation of EG into ECCs resulted in a decrease in the strength performance and an increase in the permeability properties due to the porous nature of the EG and the consequential increase in the porosity when EG is used. Nevertheless, ECCs incorporating EG as 100% replacement of the SS exhibited 90-day compressive, flexural, and tensile strengths of 32.3, 2.9, and 6.8 MPa (4.7, 0.4, and 1.0 ksi), respectively. Thus, ECCs incorporating a high content of EG can still be used for various structural applications.

3. The use of EG as aggregate in ECCs is beneficial to improving the resistance of the ECCs to drying shrinkage. The use of EG as 25%, 50%, 75%, and 100% replacement of SS resulted in a reduction in drying shrinkage of 8.7%, 17.4%, 26.1%, and 39.1%, respectively.

AUTHOR BIOS

Adeyemi Adesina *is an Adjunct Professor at the University of Windsor, Windsor, ON, Canada. His research interests include sustainable building materials, sustainable energy, and eco-friendly construction processes.*

Sreekanta Das *is a Professor of civil engineering at the University of Windsor. His research interests include full-scale testing of rehabilitated structures, masonry structures, and steel modular structures.*

ACKNOWLEDGMENTS

The authors acknowledge the Natural Sciences and Engineering Research Council of Canada for the financial support provided. The first author appreciates the internship with Facca Incorporated under the Mitacs Accelerate program and the scholarship received from the Natural Sciences and Engineering Research Council of Canada.

REFERENCES

1. Martínez-Molina, A.; Tort-Ausina, I.; Cho, S.; and Vivancos, J.-L., “Energy Efficiency and Thermal Comfort in Historic Buildings: A Review,” *Renewable and Sustainable Energy Reviews*, V. 61, Aug. 2016, pp. 70-85. doi: 10.1016/j.rser.2016.03.018

2. Agoudjil, B.; Benchabane, A.; Boudenne, A.; Ibos, L.; and Fois, M., “Renewable Materials to Reduce Building Heat Loss: Characterization of Date Palm Wood,” *Energy and Buildings*, V. 43, No. 2-3, Feb.-Mar. 2011, pp. 491-497. doi: 10.1016/j.enbuild.2010.10.014

3. Wu, Y.; Krishnan, P.; Yu, L. E.; and Zhang, M.-H., “Using Lightweight Cement Composite and Photocatalytic Coating to Reduce Cooling Energy Consumption of Buildings,” *Construction and Building Materials*, V. 145, Aug. 2017, pp. 555-564. doi: 10.1016/j.conbuildmat.2017.04.059

4. Coppola, B.; Courard, L.; Michel, F.; Incarnato, L.; Scarfato, P.; and Di Maio, L., “Hygro-Thermal and Durability Properties of a Lightweight Mortar Made with Foamed Plastic Waste Aggregates,” *Construction and Building Materials*, V. 170, May 2018, pp. 200-206. doi: 10.1016/j.conbuildmat.2018.03.083

5. Asasutjarit, C.; Hirunlabh, J.; Khedari, J.; Charoenvai, S.; Zeghmati, B.; and Shin, U. C., “Development of Coconut Coir-Based Lightweight Cement Board,” *Construction and Building Materials*, V. 21, No. 2, Feb. 2007, pp. 277-288. doi: 10.1016/j.conbuildmat.2005.08.028

6. Almeshal, I.; Tayeh, B. A.; Alyousef, R.; Alabduljabbar, H.; Mustafa Mohamed, A.; and Alaskar, A., “Use of Recycled Plastic as Fine Aggregate in Cementitious Composites: A Review,” *Construction and Building Materials*, V. 253, Aug. 2020, Article No. 119146. doi: 10.1016/j.conbuildmat.2020.119146

7. Li, V. C.; Wang, S.; and Wu, C., “Tensile Strain-Hardening Behavior of Polyvinyl Alcohol Engineered Cementitious Composite (PVA-ECC),” *ACI Materials Journal*, V. 98, No. 6, Nov.-Dec. 2001, pp. 483-492. doi: 10.14359/10851

8. Hisseine, O. A., and Tagnit-Hamou, A., “Development of Ecological Strain-Hardening Cementitious Composites Incorporating High-Volume Ground-Glass Pozzolans,” *Construction and Building Materials*, V. 238, Mar. 2020, Article No. 117740. doi: 10.1016/j.conbuildmat.2019.117740

9. Zhang, Z.; Yang, F.; Liu, J.-C.; and Wang, S., “Eco-Friendly High Strength, High Ductility Engineered Cementitious Composites (ECC) with Substitution of Fly Ash by Rice Husk Ash,” *Cement and Concrete Research*, V. 137, Nov. 2020, Article No. 106200. doi: 10.1016/j.cemconres.2020.106200

10. Xu, L.-Y.; Huang, B.-T.; and Dai, J.-G., “Development of Engineered Cementitious Composites (ECC) Using Artificial Fine Aggregates,” *Construction and Building Materials*, V. 305, Oct. 2021, Article No. 124742. doi: 10.1016/j.conbuildmat.2021.124742

11. Kralj, D., “Experimental Study of Recycling Lightweight Concrete with Aggregates Containing Expanded Glass,” *Process Safety and Environmental Protection*, V. 87, No. 4, July 2009, pp. 267-273. doi: 10.1016/j.psep.2009.03.003

12. Adewoyin, O.; Adesina, A.; and Das, S., “Physico-Thermal and Microstructural Properties of Thermal-Efficient Mortars Made with Low Cement Content,” *Construction and Building Materials*, V. 325, Mar. 2022, Article No. 126850. doi: 10.1016/j.conbuildmat.2022.126850

13. Adewoyin, O.; Adesina, A.; and Das, S., “Performance Evaluation of Thermal-Efficient Lightweight Mortars Made with Expanded Glass as Aggregates,” *Journal of Materials in Civil Engineering*, ASCE, V. 34, No. 5, May 2022, p. 04022068. doi: 10.1061/(ASCE)MT.1943-5533.0004208

14. Adesina, A., and Das, S., “Sustainable Utilization of Recycled Asphalt as Aggregates in Engineered Cementitious Composites,” *Construction and Building Materials*, V. 283, May 2021, Article No. 122727. doi: 10.1016/j.conbuildmat.2021.122727

15. Lu, D.; Tang, Z.; Zhang, L.; Zhou, J.; Gong, Y.; Tian, Y.; and Zhong, J., “Effects of Combined Usage of Supplementary Cementitious Materials on the Thermal Properties and Microstructure of High-Performance Concrete at High Temperatures,” *Materials (Basel)*, V. 13, No. 8, Apr. 2020, Article No. 1833. doi: 10.3390/ma13081833

16. Sargam, Y.; Wang, K.; and Alleman, J. E., “Effects of Modern Concrete Materials on Thermal Conductivity,” *Journal of Materials in Civil Engineering*, ASCE, V. 32, No. 4, Apr. 2020, p. 04020058. doi: 10.1061/(ASCE)MT.1943-5533.0003026

17. Huang, X.; Ranade, R.; Zhang, Q.; Ni, W.; and Li, V. C., “Mechanical and Thermal Properties of Green Lightweight Engineered Cementitious Composites,” *Construction and Building Materials*, V. 48, Nov. 2013, pp. 954-960. doi: 10.1016/j.conbuildmat.2013.07.104

18. Özbay, E.; Karahan, O.; Lachemi, M.; Hossain, K. M. A.; and Atis, C. D., “Dual Effectiveness of Freezing-Thawing and Sulfate Attack on High-Volume Slag-Incorporated ECC,” *Composites Part B: Engineering*, V. 45, No. 1, Feb. 2013, pp. 1384-1390. doi: 10.1016/j.compositesb.2012.07.038

19. Özbay, E.; Karahan, O.; Lachemi, M.; Hossain, K. M. A.; and Atiş, C. D., “Investigation of Properties of Engineered Cementitious Composites Incorporating High Volumes of Fly Ash and Metakaolin,” *ACI Materials Journal*, V. 109, No. 5, Sept.-Oct. 2012, pp. 565-571. doi: 10.14359/51684088

20. Adesina, A., and Das, S., “Mechanical Performance of Engineered Cementitious Composite Incorporating Glass as Aggregates,” *Journal of Cleaner Production*, V. 260, July 2020, Article No. 121113. doi: 10.1016/j.jclepro.2020.121113

21. ASTM D5334-14, “Standard Test Method for Determination of Thermal Conductivity of Soil and Soft Rock by Thermal Needle Probe Procedure,” ASTM International, West Conshohocken, PA, 2014, 8 pp.

22. ASTM C109/109M-16a, “Standard Test Method for Compressive Strength of Hydraulic Cement Mortars (Using 2-in. or [50-mm] Cube Specimens),” ASTM International, West Conshohocken, PA, 2016, 10 pp.

23. JSCE Concrete Committee, “Recommendations for Design and Construction of High Performance Fiber Reinforced Cement Composites with Multiple Fine Cracks (HPFRCC),” Japan Society of Civil Engineers, Tokyo, Japan, 2008, 113 pp.

24. Adesina, A., and Das, S., “Performance of Engineered Cementitious Composites Incorporating Crumb Rubber as Aggregate,” *Construction and Building Materials*, V. 274, Mar. 2021, Article No. 122033. doi: 10.1016/j.conbuildmat.2020.122033

25. ASTM C1609/C1609M-07, “Standard Test Method for Flexural Performance of Fiber-Reinforced Concrete (Using Beam With Third-Point Loading),” ASTM International, West Conshohocken, PA, 2007, 9 pp.

26. ASTM C642-13, “Standard Test Method for Density, Absorption, and Voids in Hardened Concrete,” ASTM International, West Conshohocken, PA, 2013, 3 pp.

27. ASTM C1757-13, “Standard Test Method for Determination of One-Point, Bulk Water Sorption of Dried Concrete (Withdrawn 2022),” ASTM International, West Conshohocken, PA, 2013, 3 pp.

28. ASTM C1585-13, “Standard Test Method for Measurement of Rate of Absorption of Water by Hydraulic-Cement Concretes,” ASTM International, West Conshohocken, PA, 2013, 6 pp.

29. ASTM C1202-12, “Standard Test Method for Electrical Indication of Concrete’s Ability to Resist Chloride Ion Penetration,” ASTM International, West Conshohocken, PA, 2012, 8 pp.

30. ASTM C596-07, “Standard Test Method for Drying Shrinkage of Mortar Containing Hydraulic Cement,” ASTM International, West Conshohocken, PA, 2007, 3 pp.

31. ASTM C597-02, “Standard Test Method for Pulse Velocity Through Concrete,” ASTM International, West Conshohocken, PA, 2002, 4 pp.

32. Shi, C., “Pozzolanic Reaction and Microstructure of Chemical Activated Lime-Fly Ash Pastes,” *ACI Materials Journal*, V. 95, No. 5, Sept.-Oct. 1998, pp. 537-545. doi: 10.14359/396

33. Vance, K.; Aguayo, M.; Oey, T.; Sant, G.; and Neithalath, N., “Hydration and Strength Development in Ternary Portland Cement Blends Containing Limestone and Fly Ash or Metakaolin,” *Cement and Concrete Composites*, V. 39, May 2013, pp. 93-103. doi: 10.1016/j.cemconcomp.2013.03.028

34. Wu, Y.; Wang, J.-Y.; Monteiro, P. J. M.; and Zhang, M.-H., “Development of Ultra-Lightweight Cement Composites with Low Thermal Conductivity and High Specific Strength for Energy Efficient Buildings,” *Construction and Building Materials*, V. 87, July 2015, pp. 100-112. doi: 10.1016/j.conbuildmat.2015.04.004

35. Jin, Q., and Li, V. C., “Development of Lightweight Engineered Cementitious Composite for Durability Enhancement of Tall Concrete Wind Towers,” *Cement and Concrete Composites*, V. 96, Feb. 2019, pp. 87-94. doi: 10.1016/j.cemconcomp.2018.11.016

36. ASTM C330/C330M-09, “Standard Specification for Lightweight Aggregates for Structural Concrete,” ASTM International, West Conshohocken, PA, 2009, 4 pp.

37. ACI Committee 213, “Guide for Structural Lightweight-Aggregate Concrete (ACI 213R-03),” American Concrete Institute, Farmington Hills, MI, 2003, 38 pp.

38. Kaze, C. R.; Lemougna, P. N.; Alomayri, T.; Assaedi, H.; Adesina, A.; Das, S. K.; Lecomte-Nana, G.-L.; Kamseu, E.; Chinje Melo, U.; and Leonelli, C., “Characterization and Performance Evaluation of Laterite Based Geopolymer Binder Cured at Different Temperatures,” *Construction and Building Materials*, V. 270, Feb. 2021, Article No. 121443. doi: 10.1016/j.conbuildmat.2020.121443

39. Abdel Tawab, O. F.; Amin, M. R.; Ibrahim, M. M.; Abdel Wahab, M.; Abd El Rahman, E. N.; Hassanien, R. H.; Hatem, M. H.; and Ghaly, A. E., “Recycling Waste Plastic Bags as a Replacement for Cement in Production of Building Bricks and Concrete Blocks,” *Journal of Waste Resources and Recycling*, V. 2, No. 1, 2020, 13 pp.

40. Adesina, A., “Overview of the Influence of Waste Materials on the Thermal Conductivity of Cementitious Composites,” *Cleaner Engineering and Technology*, V. 2, June 2021, Article No. 100046. doi: 10.1016/j.clet.2021.100046

41. Keskin, S. B.; Sulaiman, K.; Sahmaran, M.; and Yaman, I. O., “Effect of Presoaked Expanded Perlite Aggregate on the Dimensional Stability and Mechanical Properties of Engineered Cementitious Composites,” *Journal of Materials in Civil Engineering*, ASCE, V. 25, No. 6, June 2013, pp. 763-771. doi: 10.1061/(ASCE)MT.1943-5533.0000553

42. Zhang, Z.; Ma, H.; and Qian, S., “Investigation on Properties of ECC Incorporating Crumb Rubber of Different Sizes,” *Journal of Advanced Concrete Technology*, V. 13, No. 5, 2015, pp. 241-251. doi: 10.3151/jact.13.241

43. Huang, X.; Ranade, R.; Ni, W.; and Li, V. C., “On the Use of Recycled Tire Rubber to Develop Low E-Modulus ECC for Durable Concrete Repairs,” *Construction and Building Materials*, V. 46, Sept. 2013, pp. 134-141. doi: 10.1016/j.conbuildmat.2013.04.027

44. Yang, E.-H.; Yang, Y.; and Li, V. C., “Use of High Volumes of Fly Ash to Improve ECC Mechanical Properties and Material Greenness,” *ACI Materials Journal*, V. 104, No. 6, Nov.-Dec. 2007, pp. 620-628. doi: 10.14359/18966

45. Li, G., and Zhao, X., “Properties of Concrete Incorporating Fly Ash and Ground Granulated Blast-Furnace Slag,” *Cement and Concrete Composites*, V. 25, No. 3, Apr. 2003, pp. 293-299. doi: 10.1016/S0958-9465(02)00058-6

46. Şahmaran, M.; Lachemi, M.; Hossain, K. M. A.; and Li, V. C., “Internal Curing of Engineered Cementitious Composites for Prevention of Early Age Autogenous Shrinkage Cracking,” *Cement and Concrete Research*, V. 39, No. 10, Oct. 2009, pp. 893-901. doi: 10.1016/j.cemconres.2009.07.006

47. Zhou, Y.; Xi, B.; Sui, L.; Zheng, S.; Xing, F.; and Li, L., “Development of High Strain-Hardening Lightweight Engineered Cementitious Composites: Design and Performance,” *Cement and Concrete Composites*, V. 104, Nov. 2019, Article No. 103370. doi: 10.1016/j.cemconcomp.2019.103370

48. Adesina, A., and Das, S., “Evaluation of the Durability Properties of Engineered Cementitious Composites Incorporating Recycled Concrete as Aggregate,” *Journal of Materials in Civil Engineering*, ASCE, V. 33, No. 2, Feb. 2021, p. 04020439. doi: 10.1061/(ASCE)MT.1943-5533.0003563

49. Xuan, Z., and Jun, Z., “Influence of Zeolite Addition on Mechanical Performance and Shrinkage of High Strength Engineered Cementitious Composites,” *Journal of Building Engineering*, V. 36, Apr. 2021, Article No. 102124. doi: 10.1016/j.jobe.2020.102124

ACI MATERIALS JOURNAL TECHNICAL PAPER

Title No. 120-M42

Kappaphycus alvarezii Seaweed as Novel Viscosity-Modifying Admixture for Cement-Based Materials

by Asma Boukhatem, Kamal Bouarab, and Ammar Yahia

The effect of different conditioning and processing parameters of Kappaphycus alvarezii *(*K. alvarezii*) seaweed solutions—such as their dosage, heating temperature, and pre-hydration method on the rheological behavior, hydration kinetics, and compressive strength of cement suspensions—was evaluated. The use of marine* K. alvarezii *seaweed in fluid cement matrixes could be an excellent alternative for a wide range of existing viscosity-modifying admixtures (VMAs) given its environmental and economic advantages. The use of* K. alvarezii *increased the yield stress, plastic viscosity, and rigidity of cement suspensions. This was not always the case when conventional VMAs were used, which shows the effectiveness of* K. alvarezii *as a VMA. On the other hand, incorporating a 0.5% dosage of* K. alvarezii *resulted in comparable yield stress and plastic viscosity values compared to (κ)-carrageenan, which confirms the feasibility of using* K. alvarezii *instead of (κ)-carrageenan as a VMA. Unlike (κ)-carrageenan, the use of* K. alvarezii *did not increase the dormant period of cement suspensions, which is very interesting in terms of compatibility between this new VMA and cement. The use of* K. alvarezii *generally showed no significant effect on the strength development of the cement suspensions compared to the reference mixture. This validates the feasibility of using* K. alvarezii *seaweed as a VMA.*

Keywords: cement suspensions; compressive strength; hydration kinetics; kappa (κ)-carrageenan; *Kappaphycus alvarezii* (*K. alvarezii*); rheology; viscosity-modifying admixtures (VMAs).

INTRODUCTION

Carrageenan biopolymers are a new generation of seaweed-based viscosity-modifying admixtures (VMAs) that are used to increase the viscosity and improve the stability of flowable cement suspensions, such as self-consolidating concrete (SCC).[1-3] SCC is prone to bleeding and segregation due to its low yield stress.[4-8] Incorporating a VMA into SCC can prevent separation between the liquid and solid phases during the transport, placement, and consolidation processes, ensuring adequate mechanical performance and durability. VMAs are high-molecular-weight water-soluble polymeric admixtures mainly used to increase the viscosity and cohesion of fresh cement-based materials. Most VMAs come from organic or inorganic materials. Organic VMAs can be categorized as natural (such as polysaccharides like starch, alginates, agar, welan gum, xanthan gum, diutan gum, as well as vegetable proteins)[7] or semi-synthetic (such as decomposed starch and its derivatives; derivatives of cellulose ether, such as hydroxypropyl methylcellulose [HPMC], hydroxyethyl cellulose [HEC], and carboxymethyl cellulose [CMC]; as well as electrolytes and synthetic polymers, such as ethylene-based polymers).[9] Inorganic VMAs are silica-based materials, such as nanosilica, amorphous colloidal silica, and fine calcareous fillers.[7,10]

The most widely used VMAs in SCC are cellulose ethers, starch derivatives, and gums.[5,7] Although the use of VMAs such as HPMC, welan gum, starch ether, and so on has proven very effective in improving the rheology and stability of cement-based materials, their cost is high compared to other concrete ingredients, especially in the case of microbial-based VMAs such as welan gum, which requires a time-consuming and energy-intensive extraction and recovery process. Moreover, most synthetic VMAs have negative impacts on the environment due to their petrochemical origins, which contribute to the emission of toxic elements into the environment. Furthermore, using them in combination with a high-range water reducer (HRWR) can delay the setting time and strength development, especially at high HRWR dosages. Considering these limitations, and in particular the rising prices of raw materials and increased CO_2 emissions, the current development of VMAs for use in concrete should be economically and ecologically sound. Various types of "biopolymer" VMAs that have a low environmental footprint and are inexpensive compared to synthetic VMAs are currently being investigated. The applications of biopolymers in the construction field today are widespread and diverse because they are available locally and they offer distinct advantages in terms of quality, performance, and cost compared to synthetic polymers.

Although natural polymers have other advantages such as biodegradability, nontoxicity, and water-retention capacity, some of them show poor mechanical properties[7] and chemical instability. Considering these limitations, the current trend is to use new plant-based biopolymers, in particular carrageenans, which are obtained from red seaweeds, due to their abundant availability. The seaweed cell wall is composed of cellulose fibers,[11] a fibrillar skeleton, and a hydrocolloid matrix made up of sulfated polysaccharides.[12,13] Seaweed polysaccharides are a very interesting group of phycocolloids, which are used in different industries—such as the food, pharmaceutical, textile, paper, medical, and biotechnology industries—as stabilizers, thickeners, emulsifiers, and fillers.[14-16]

ACI Materials Journal, V. 120, No. 4, July 2023.
MS No. M-2022-083.R2, doi: 10.14359/51738805, received September 29, 2022, and reviewed under Institute publication policies. Pertinent discussion including author's closure, if any, will be published ten months from this journal's date if the discussion is received within four months of the paper's print publication.

Carrageenan is a mixture of sulfated galactans belonging to the linear sulfated polysaccharide family.[17] It is found in the cell wall of many species of marine red seaweed,[15,18-21] especially *Kappaphycus alvarezii* (*K. alvarezii*), representing between 30 and 80% of its dry weight.[22,23] From a chemical point of view, natural carrageenan consists of a repetition of disaccharide subunits of two galactoses, incompletely sulfated at specific positions of carbon number 2 (C_2) and/or C_4, C_3, and C_6. Specifically, the repeating disaccharide unit has alternating residues of β(1,4)-D-galactose-4-sulfate and α(1,3)-3,6-anhydro-D-galactose.[24] Depending on the number and position of the sulfate ester groups presenting on the basic digalactan and the presence or absence of the 3,6-anhydrogalactose bridge, carrageenan can be found in different forms. The most well-known types are kappa (κ)-, iota (ι)-, and lambda (λ)-carrageenans. For example, (κ)-carrageenan has a 3,6-anhydrogalactose bridge, but only one sulfate ester per disaccharide unit.[25] On the other hand, (ι)- and (λ)-carrageenans contain one and zero 3,6-anhydrogalactose bridge, as well as two and three groups of sulfate esters, respectively. The presence of the 3,6-anhydro bridge is responsible for the gelation of carrageenan.[26-28] Therefore, only (κ)- and (ι)-carrageenans can produce gels, while (λ)-carrageenan simply acts as a thickening admixture.

The use of seaweed polysaccharides in concrete technology mainly targets alginates as new VMAs[29] and carrageenans as superabsorbent fillers[30-34] and new VMAs.[1-3] The (κ)- and (ι)-carrageenans modify the rheology and improve the stability of flowable cement suspensions by providing suitable cohesion even in the presence of HRWRs.[1-3] Carrageenans increase the rigidity of cement suspensions and accelerate their buildup kinetics over time. Carrageenans form a three-dimensional (3-D) network in the cement matrix by cross-linking between chains. This is due to the presence of potassium (K^+) and calcium (Ca^{2+}) ions in the pore solution, as well as carrageenan sulfate ester groups. Furthermore, cement-based mixtures containing low dosages of carrageenan exhibited relatively higher compressive strength compared to those containing conventional VMAs.[1-3] However, the saccharide nature of the main chain of carrageenan can affect the setting time of cement considerably.[1-3] For example, Boukhatem et al.[2] reported that the addition of 1.5% (κ)-carrageenan delays the setting time of cement paste by increasing the dormant period to up to 21 hours. Therefore, high dosages of carrageenan can significantly affect the development of mechanical properties at early ages.[1-3]

The carrageenans used in previous studies[1-3] include food-grade (in the case of (κ)-carrageenan) and commercial Type II (in the case of (ι)-carrageenan). These carrageenans are pure, refined products that are more expensive than the polymers generally used in construction. According to a commercial chemical and biotechnology company, the price of 1 kg of refined (ι)-carrageenan is $500 CAD, while (κ)-carrageenan is $2500 CAD. The high cost compared to other ingredients used in concrete can limit, to a large extent, the use and commercialization of carrageenan as a building biomaterial. The extraction of carrageenans from red seaweed often involves multi-step energy-intensive and time-consuming industrial processes.[35] In addition, the extraction of carrageenans requires a large amount of organic and inorganic reagents and solvents. These solvents are highly toxic and can have a considerable negative impact on human health and the quality of ecosystems.[36] Moreover, some solvents are expensive due to the high cost of distilling and recovering alcohol, as well as purchasing explosion-proof equipment.[36] Therefore, it is necessary to establish a trade-off between the quality, economic, and environmental aspects to produce sustainable cement-based mixtures.

Carrageenans are produced by several species of red seaweed, including *K. alvarezii*, which are among the most commonly used seaweeds to produce polysaccharides. Interestingly, dried-seaweed powders can modify the rheological properties of aqueous solutions similarly to purified polysaccharides.[37-39] Therefore, *K. alvarezii* seaweed powder may potentially exhibit characteristics comparable to those of (κ)-carrageenan and be used as a VMA in cement-based suspensions. Moreover, the use of *K. alvarezii* seaweed powder as a VMA could greatly reduce the production cost of SCC associated with the use of (κ)-carrageenan, reducing the cost from $2500 CAD/kg in the case of commercial (κ)-carrageenan to $3.96 CAD/kg in the case of dried *K. alvarezii* seaweed,[40] which is almost 600 times cheaper than using a refined food product. The native (κ)-carrageenan may have lower 3,6-anhydrogalactose bridge content, which promotes its viscous behavior but weakens its gelling properties (that is, rigidity) when it is dissolved in aqueous solution,[39] unlike commercial (κ)-carrageenan extracted from *K. alvarezii* seaweeds by means of alkaline treatment with potassium hydroxide (KOH). This consists of subjecting it to a temperature of 194°F (90°C) in KOH solution for several hours. The alkaline extraction can induce desulfation of the polysaccharide and, consequently, the 3,6-anhydro-D-galactose bridge formation.[27,28] The formation of the 3,6-anhydro-D-galactose bridge increases the rigidity of the gel. However, the (κ)-carrageenan extraction process is expensive and has a substantial environmental impact.

It is known in the literature that the rheological properties (that is, the viscosity and rigidity) of aqueous solutions containing *K. alvarezii* seaweed may be improved using certain conditioning and treatment processes at a temperature of 80°C for several hours.[39] Therefore, to maximize the effect of the native (κ)-carrageenan as a VMA without alkaline extraction, various *K. alvarezii* conditioning and processing parameters should be optimized. In particular, the efficiency of *K. alvarezii* grinding (that is, the fineness of the powder), the heating time and temperature of solutions containing the *K. alvarezii*, as well as the mode of introduction (that is, powder form or pre-hydrated solution) should be investigated. This study aims to evaluate the potential replacement of pure and refined extracted (κ)-carrageenan by *K. alvarezii* in cement-based suspensions. This contributes to the development of a cost-effective and eco-friendly VMA by eliminating the negative environmental impacts and additional costs associated with the extraction process of semi-refined or refined (κ)-carrageenan.

Table 1—Chemical and physical characteristics of GU cement used

SiO_2, %	TiO_2, %	Al_2O_3, %	Fe_2O_3, %	MgO, %	CaO, %	Na_2O, %	K_2O, %	SO_3, %	BET, in.^{2}/lb (m^2/kg)	Blaine fineness, in.^{2}/lb (m^2/kg)	Gs, lb/yd^3 (g/cm^3)
20.4	0.2	4.4	2.5	2.1	62.0	0.0	0.8	3.8	1,094,679 (1557)	312,163 (444)	5309 (3.15)

Note: BET is Brunauer-Emmett-Teller surface area measurement; Gs is specific gravity.

RESEARCH SIGNIFICANCE

Carrageenan-based VMAs are expensive, and their extraction process is energy-intensive and time-consuming, requiring large amounts of costly and extremely toxic organic solvents. Furthermore, (κ)-carrageenan can delay setting time and strength development, especially at higher dosages. This study aims to highlight the benefits and limitations of incorporating *K. alvarezii* seaweed instead of (κ)-carrageenan and its impact on various rheological properties that directly influence the performance of cement suspensions. The performance of *K. alvarezii* seaweed was compared with that of (κ)-carrageenan.

EXPERIMENTAL PROGRAM

The rheology, hydration kinetics, and compressive strength of cement suspensions containing *K. alvarezii* seaweed and refined (commercial) (κ)-carrageenan were investigated. The yield stress and plastic viscosity of aqueous solutions were first evaluated. This was carried out to identify the required dosage of *K. alvarezii* seaweed and the necessary cooking conditions to ensure comparable rheological properties to those observed with solutions containing (κ)-carrageenan. Therefore, different *K. alvarezii* dosages, times, and cooking temperatures were evaluated. Obtaining comparable rheological behaviors confirms the feasibility of using *K. alvarezii* seaweed as a VMA instead of refined (κ)-carrageenan in cement-based materials. After identifying the *K. alvarezii* dosage and the cooking conditions that ensure comparable rheological behavior to that of (κ)-carrageenan solutions, the effect of *K. alvarezii* solutions on the properties of cement-based suspensions made with a water-cement ratio (*w/c*) of 0.43 was evaluated. The rheological and viscoelastic properties, the structural buildup kinetics at rest, the cement hydration kinetics, and compressive strength were evaluated. A comparison between the effect of *K. alvarezii* and (κ)-carrageenan on the previously cited parameters was also carried out.

Materials

A general-use (GU) cement that complies with ASTM C150 specifications was used. The cement had a density of 3.15 and a specific surface area of 312,163 in.^{2}/lb (444 m^2/kg). The chemical and physical properties of the cement are summarized in Table 1. The mixture proportions of the investigated mixtures are presented in Table 2.

Different varieties of commercial *K. alvarezii* seaweed were obtained.[40] Food-grade (κ)-carrageenan was obtained from a commercial supplier and used as a reference VMA.[1-3] The properties of the native *K. alvarezii* seaweed were compared with those of the reference commercial (κ)-carrageenan. The physical properties of *K. alvarezii* seaweed powder and commercial (κ)-carrageenan are summarized in Table 3.

Table 2—Proportions of cement-paste mixtures made with different dosages of *K. alvarezii* powder

w/c	*K. alvarezii* dosage, by weight of water, % w/w	VMA type
0.43	0	—
	0.25	*K. alvarezii*
	0.50	*K. alvarezii*
	0.75	*K. alvarezii*

Table 3—Physical properties of commercial κ-carrageenan and *K. alvarezii* powders

	Density, lb/yd^3 (g/cm^3)	Blaine fineness, in.^{2}/lb (m^2/kg)
Commercial (κ)-carrageenan	2797 (1.66)	142,723 (203)
K. alvarezii—160 μm	2730 (1.62)	262,948 (374)
K. alvarezii—100 μm	2730 (1.62)	305,835 (435)

Test methods

Treatment and conditioning of K. alvarezii *seaweed*—*K. alvarezii* seaweed was sun-dried to reduce its moisture content to less than 36% and then mixed with sea salt. Sea salt is a natural preservative that protects seaweed against microbial contamination. First, the dried *K. alvarezii* seaweed was carefully washed with tap water to remove salt and impurities such as epiphytes (other seaweeds), mollusk shells, small stones, sand, and so on. The wet seaweed was then dried in an oven at 140°F (60°C) for 72 hours to remove the excess moisture. The dried seaweed was minced using a blender, then ground in a ball mill for 1 hour. After grinding, the resulting seaweed powder was sieved through 315, 160, and 100 μm sieves and then stored until their characterization. Particles greater than 160 μm were discarded in this experimental study. Two powder fractions of particles that passed through sieves of 160 and 100 μm were selected to carry out rheological measurements.

To avoid variability in the particle-size distribution, the *K. alvarezii* powder was carefully homogenized using a V-blender. The V-blender consists of two hollow cylinders joined at a typical angle of 1.31 to 1.57 rad (75 to 90 degrees). As the V-blender rotated, the material continuously divided and recombined. The powder was properly mixed inside the container, resulting in a homogeneous mixture.[41] The powder's homogenization was carried out at a rotational speed of 12 rpm for 30 minutes. These parameters were carefully selected to avoid powder segregation due to the high centrifugal forces.

Preparation of aqueous solutions—An exhaustive experimental program (72 experiments) was carried out to evaluate the effect of *K. alvarezii* seaweed powder on the rheological properties of aqueous solutions. The investigated mixtures were prepared by dissolving either 1.5 or 3 g of *K. alvarezii* seaweed powder in 100 mL of distilled water that was subjected to continuous magnetic stirring for 30 and 60 minutes at 73.4, 104, and 176°F (23, 40, and 80°C). *K. alvarezii* seaweed powder was not added to the water until the desired temperature was reached, and time zero corresponds to the introduction time of the powder. The solutions were then cooled for 15 minutes and were either immediately tested or stored at room temperature (~73.4°F [23°C])[42] or in the refrigerator (46.4 ± 3.6°F [8 ± 2°C])[43] for approximately 24 hours before performing the rheological measurements. In addition, aqueous solutions containing different dosages of (κ)-carrageenan corresponding to 0.5, 1.0, and 1.5% by weight of water were prepared by dispersing the required amount of (κ)-carrageenan powder in distilled water that was kept at room temperature. These solutions were magnetically stirred until the powder dissolved.

Mixing sequence of cement-paste mixtures—The investigated cement-paste mixtures were prepared in 0.26 gal. (1 L) batches using a high-shear blender and the mixing procedure described in the ASTM C1738/C1738M specifications and in the previous studies by Boukhatem et al.,[2,3] Yahia et al.,[1] and Mostafa and Yahia.[44]

Rheological measurements—The rheological properties were assessed using a high-precision coaxial cylinder rheometer equipped with a Peltier system capable of adequately controlling the temperature during testing. In this study, the sample temperature was kept at 73.4°F (23°C) for all rheological measurements. A profiled inner cylinder connected to a motor that measures the torque through the application of different rotational speeds while the outer cylinder remains stationary was used. The profiled cylinders were used to reduce wall slip. The inner and outer cylinders have 1.050 and 1.138 in. (26.660 and 28.911 mm) diameters, respectively, which provide a narrow gap of 0.044 in. (1.126 mm) and ensure a constant shear rate across the gap.

The flow curves, the viscoelastic properties, and the structural buildup kinetics at rest of the investigated cement suspensions were determined. The test procedures used for the determination of these measurements are described in the previous studies by Boukhatem et al.,[2,3] Yahia et al.,[1] Mostafa and Yahia,[44] and Mezger.[45]

Hydration kinetics of cement—The evolution of the heat release was determined using the test procedure described in the previous studies by Boukhatem et al.,[2,3] Yahia et al.,[1] and Mostafa and Yahia.[44] The resulting heat flow curve reflects the cement hydration process as well as the different hydration phases.

Compressive strength of cement suspensions—Various 0.003 in. (50 mm) cubic molds were prepared to determine the compressive strength of cement suspensions containing *K. alvarezii* seaweed. The molds were made according to ASTM C39/C39M specifications. After 24 hours, the cubes were demolded and moist cured. The compressive strength tests were performed at 1 and 7 days, following ASTM C109/C109M recommendations.

Statistical analysis—Analysis of variance (ANOVA) was performed to evaluate significant differences between the investigated mixtures. This analysis was carried out considering a confidence interval of 95%. The significance of the control factors was assessed by calculating the degree of freedom (DDL), the sum of squares (SS), and the mean of squares (MS). This analysis permits the identification of the most significant factors impacting the rheology of the investigated mixtures. Multiple pairwise comparisons were carried out to determine which of the means are significantly different from each other. The Tukey-Kramer method was used in this study to perform this comparison. The letters A, B, C, and D presented above or beside each average help identify the significant differences between the means. Two means with at least one letter in common are not significantly different. In contrast, two means with no letters in common are significantly different.

RESULTS AND DISCUSSION

In this study, the conditioning and treatment parameters, such as dosage, finesse, heating time, temperature, and the pre-hydration method, of *K. alvarezii* solutions were investigated. The effect of *K. alvarezii* and (κ)-carrageenan on rheological behavior, including flow curves and viscoelastic properties, structural buildup kinetics, hydration heat, and compressive strength of cement suspensions was also evaluated.

Rheology of aqueous solutions containing *K. alvarezii* seaweed powder

The effect of conditioning and treatment parameters on the rheology of the aqueous solution was evaluated. Different dosages (1.5 and 3%, by weight of water), particle sizes (≤160 and ≤100 μm), stirring times (30 and 60 minutes), heating temperatures (ambient, 104°F [40°C], and 176 ± 3.6°F [80 ± 2°C]), and storage modes (without storage or stored for 24 hours at room temperature or at 46.4 ± 3.6°F [8 ± 2°C]) were evaluated.

Effect of storage mode of aqueous solutions containing K. alvarezii *on rheological parameters*—The yield stress and plastic viscosity values of aqueous solutions containing different dosages of *K. alvarezii*—unheated or heated at 104 and 176°F (40 and 80°C), tested immediately or stored for 24 hours at room temperature or at 46.4°F (8°C)—are presented in Fig. 1, 2, and 3, respectively. As can be seen, storing the sample for 24 hours at room temperature significantly increased the yield stress and plastic viscosity values of solutions that contain 3.0% *K. alvarezii* powder compared to solutions that contain the same dosage and were immediately tested without storage or were stored at 46.4°F (8°C), regardless of the particle size, stirring time, or heating temperature. However, the yield stress values of unheated solutions that contain 3.0% *K. alvarezii*, stored at room temperature or not, appeared to be significantly affected by the stirring time, regardless of the particle size. In addition, with a similar dosage of 3.0% *K. alvarezii* and similar conditioning, the use of the fine fraction (particles

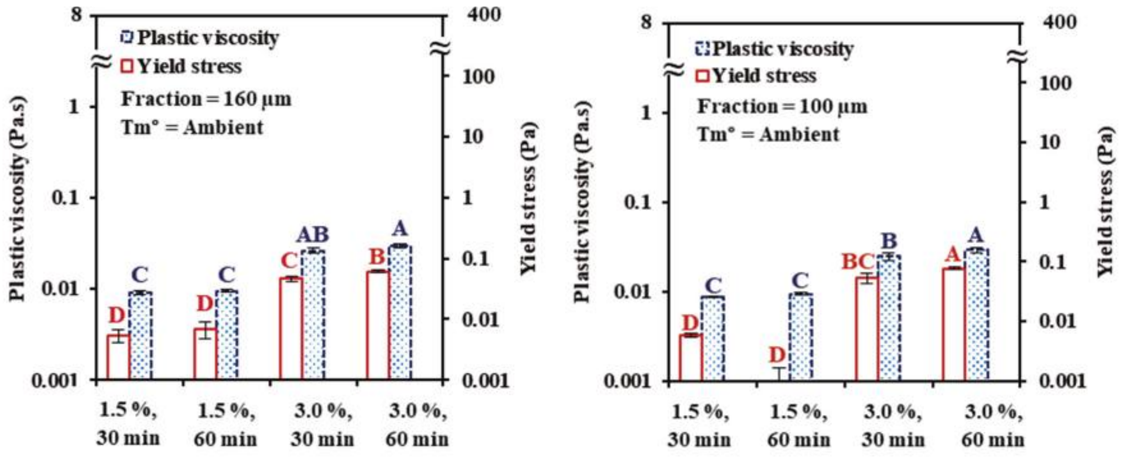

(a) Coarse and fine fractions of *K. alvarezii* immediately tested

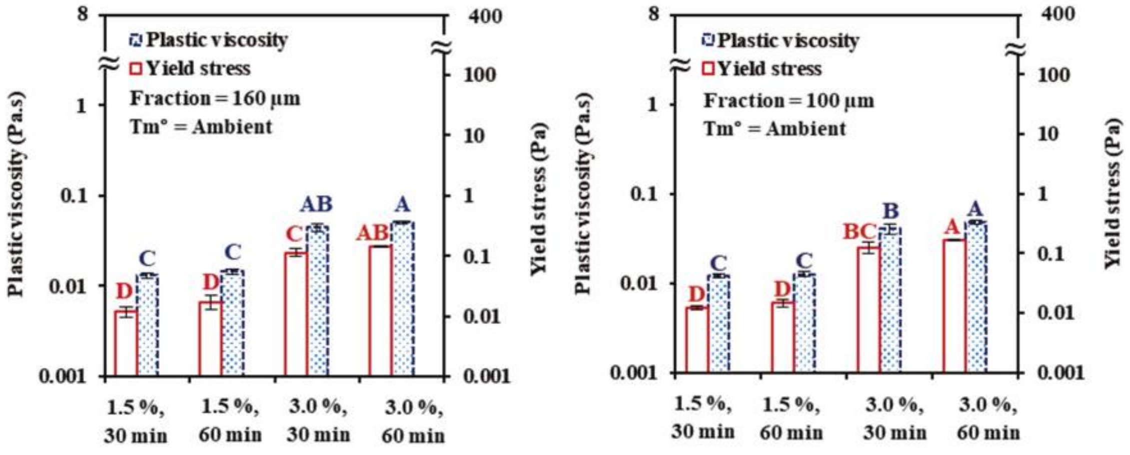

(b) Coarse and fine fractions of *K. alvarezii* tested after storage at room temperature

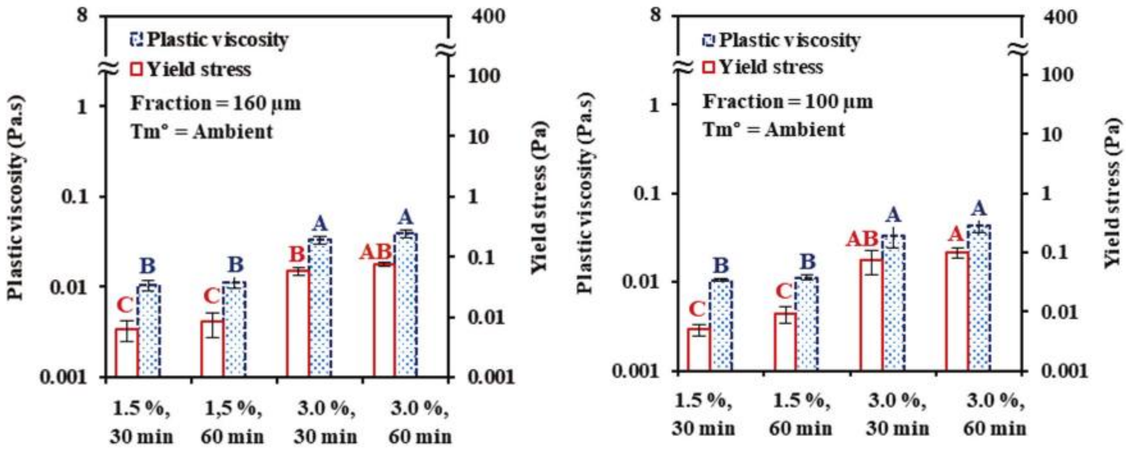

(c) Coarse and fine fractions of *K. alvarezii* tested after storage at 46.4 °F (8 °C)

Fig. 1—Variation in plastic viscosity and yield stress of unheated aqueous solutions containing K. alvarezii *seaweed powder: (a) immediately tested; (b) tested after storage at room temperature; and (c) at 46.4°F (8°C). (Note: 1 Pa = 0.02* lb/ft^2*; 1 Pa·s = 0.67* lb/ft^{-s}*.)*

≤100 μm) significantly increased the yield stress compared to the coarse fraction (particles ≤160 μm). However, these claims are only valid for solutions that were tested immediately without storage. This may be due to the fact that *K. alvarezii* powder did not properly dissolve in cold water. Therefore, cooling may inhibit the pre-hydration of the particles of *K. alvarezii* powder. Because the particle size of *K. alvarezii* powder did not show a significant effect on the

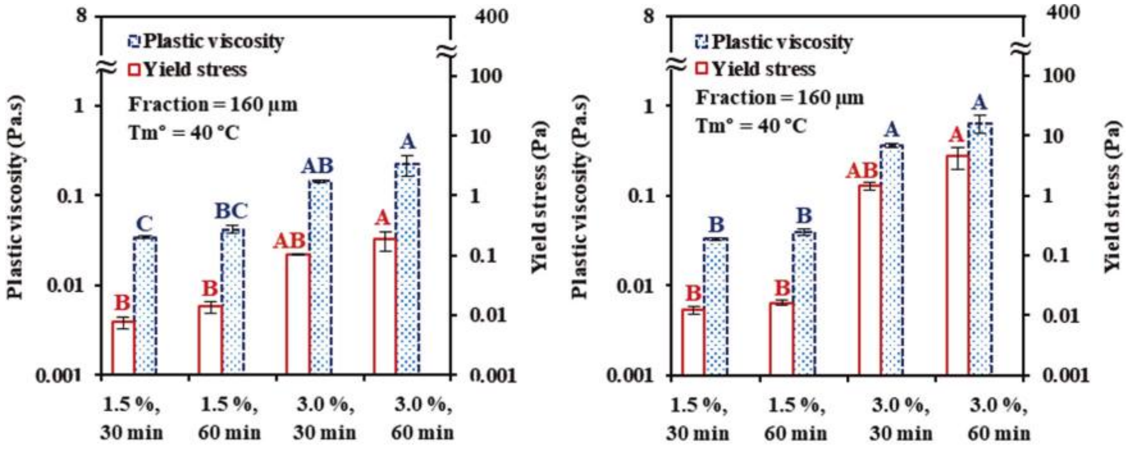

(a) *K. alvarezii* immediately tested

(b) *K. alvarezii* tested after storage at room temperature

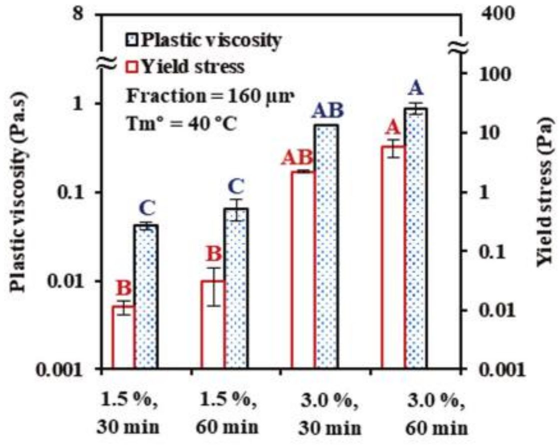

(c) *K. alvarezii* tested after storage at 46.4 °F (8 °C)

Fig. 2—Variation in plastic viscosity and yield stress of aqueous solutions containing K. alvarezii *seaweed powder heated at 104°F (40°C): (a) immediately tested; (b) tested after storage at room temperature; and (c) at 46.4°F (8°C). (Note: 1 Pa = 0.02 lb/ft^2; 1 Pa·s = 0.67 lb/ft^{-s}.)*

plastic viscosity and yield stress of the stored aqueous solutions, the coarse fraction of 160 µm was used to carry out the rheological measurements.

Effect of K. alvarezii *dosage on rheological parameters of aqueous solutions*—As can be observed in Fig. 1 to 3, the dosage of *K. alvarezii* was the most influential parameter on the yield stress and plastic viscosity values, regardless of the stirring time, storage mode, or heating temperature. The highest yield stress and plastic viscosity values were observed in solutions that contain 3.0% *K. alvarezii* powder, regardless of the stirring time, storage mode, or heating temperature. The yield stress values increased drastically to 1.8170 lb/ft^2 (87 Pa) in the case of solutions that contain 3.0% *K. alvarezii* (fraction ≤160 µm), heated at 176°F (80°C) for 60 minutes and in non-stored conditions (Fig. 3). However, it is not possible to use these solutions in cement suspensions due to their high yield stress values.

Effect of heating temperature of aqueous solutions containing K. alvarezii *on rheological parameters*—Heating *K. alvarezii* aqueous solutions to 104 and 176°F

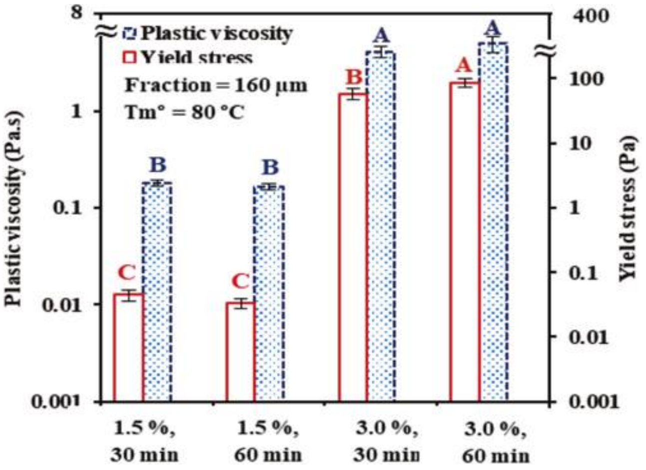

Fig. 3—Variation in plastic viscosity and yield stress of aqueous solutions containing K. alvarezii *seaweed powder heated at 176°F (80°C) immediately tested. (Note: 1 Pa = 0.02 lb/ft^2; 1 Pa·s = 0.67 lb/ft^{-s}.)*

(40 and 80°C) significantly increased the yield stress and plastic viscosity values, especially at high dosages of 3.0% *K. alvarezii*, regardless of the storage mode, as can be observed in Fig. 2 and 3. However, no significant increase was observed in the case of solutions that contain 1.5% *K. alvarezii* powder compared to that of water, regardless of the storage mode and stirring time. Moreover, no significant difference in the yield stress was observed between the heated and unheated solutions that were immediately tested. It is well-known in the literature that the aqueous extraction of (κ)-carrageenan (that is, heating aqueous solutions that contain *K. alvarezii* without treating them with KOH) increases the yield, but solutions that contain 1.5% native (κ)-carrageenan could not form a gel.[28] This means that the native (κ)-carrageenan extracted with distilled water exhibits poor gelation properties at a dosage of 1.5%. Distantina et al.[28] hypothesized that these observations were due to the lower cation content in native (κ)-carrageenan.

Effect of (κ)-carrageenan dosage on rheological parameters of aqueous solutions—The variation in yield stress and plastic viscosity values of aqueous solutions that contain different dosages of (κ)-carrageenan corresponding to 0.5, 1.0, and 1.5% by weight of water is shown in Fig. 4. As can be observed, the yield stress and plastic viscosity values increased from 0.0015 lb/ft^2 (0.07 Pa) and 0.0015 lb/ft^{-s} (0.071 Pa·s) to 0.5430 lb/ft^2 (26 Pa) and 0.8 Pa·s, respectively, in the case of solutions that contain 0.5 and 1.5% (κ)-carrageenan.

Based on the statistical analysis carried out on the yield stress and plastic viscosity values of aqueous solutions containing (κ)-carrageenan and *K. alvarezii* powders, any solution with a particle fraction of less than 160 μm and a dosage of less than 3.0% that is stirred for 30 minutes and heated to 104°F (40°C), and is immediately tested or stored for 24 hours at room temperature or at 46.4°F (8°C), can be used as a VMA in cement suspensions.

Effect of *K. alvarezii* on rheology and viscoelastic properties of cement suspensions

The rheology and viscoelastic properties of cement-paste mixtures that contain different *K. alvarezii*-based solutions were evaluated. These solutions were prepared based on the aforementioned processing and treatment optimization results. Heated (104°F [40°C]) solutions containing 0.25, 0.50, and 0.75%, by weight of water, of *K. alvarezii* powder (particle fraction ≤160 μm) were prepared by stirring them for 30 minutes. After cooling (51.8 ± 3.6°F [11 ± 2°C]), these solutions were used as mixing water to prepare cement suspensions that were immediately tested. Pre-hydration for 24 hours at room temperature or at 46.4°F (8°C) for solutions that contain similar dosages of *K. alvarezii* powder was also carried out to formulate other cement suspensions.

The flow curves presented in Fig. 5 show that mixtures containing *K. alvarezii* exhibited a shear-thinning behavior (characteristic of cement suspensions), in which the apparent viscosity decreases significantly with the increase in the shear rate, regardless of the dosage of *K. alvarezii* or the pre-hydration method. At low shear rates, the attractive forces between cement particles predominate over the hydrodynamic forces, leading to the formation of flocs. As the shear rate increases, the hydrodynamic forces become greater than the attractive forces. Therefore, the flocs are broken down into smaller units, which frees the water trapped in the flocs and decreases the viscosity of the system. However, the shear stress increased significantly in tandem with the dosage of *K. alvarezii*, regardless of the pre-hydration method. For example, in the case of cement suspensions made with solutions containing 0.25, 0.50, and 0.75%, by weight of water, of *K. alvarezii* directly tested without pre-hydration, the shear stress at 150 s^{-1} increased from 0.7936 lb/ft^2 (38 Pa) in the case of the reference cement-paste mixture to 1.4411, 1.9632, and 2.4854 lb/ft^2 (69, 94, and 119 Pa), respectively. However, the pre-hydration of solutions containing *K. alvarezii* powder did not lead to significant differences in the shear stress, regardless of the dosage.

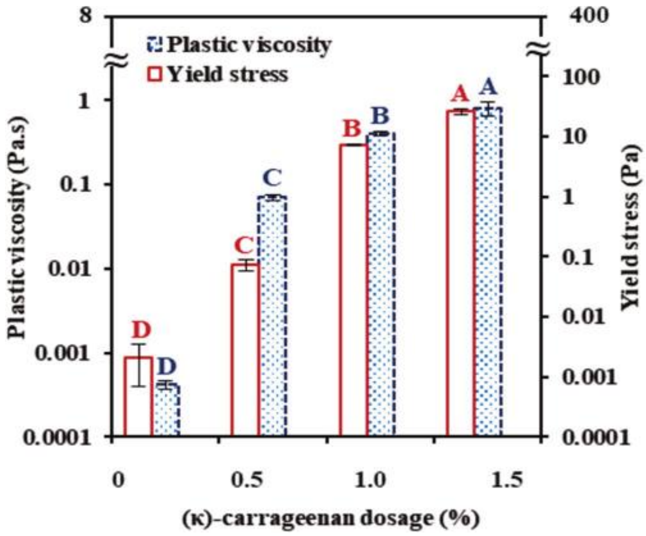

Fig. 4—Variation in plastic viscosity and yield stress of aqueous solutions containing (κ)-carrageenan powder corresponding to 0.5, 1.0, and 1.5%, by weight of water. (Note: 1 Pa = 0.02 lb/ft^2; 1 Pa·s = 0.67 lb/ft^{-s}.)

As can be observed in Table 4, for a given dosage of 0.5%, the shear stress values at 150 s^{-1} of cement suspensions that contain (κ)-carrageenan are higher than those that contain *K. alvarezii* (almost double). This means that the shear-thinning effect is more pronounced in the case of (κ)-carrageenan, which is probably due to the chemical composition of each powder. Indeed, the native (κ)-carrageenan contained in the *K. alvarezii* seaweed is devoid of the 3,6-anhydrogalactose bridge and consequently contains more sulfate ester groups than the commercial (κ)-carrageenan.[46] Therefore, when incorporated into a cement suspension, the native (κ)-carrageenan may act like a thickening admixture (that is, it helps increase the viscosity) but not like a gelling admixture (that is, it did not help increase rigidity).

As can be observed in Fig. 6, the use of *K. alvarezii* powder increased both yield stress and plastic viscosity values of cement-paste mixtures. For example, in the case of mixtures containing non-pre-hydrated *K. alvarezii* solutions, the use of 0.25% increased the yield stress from 0.2297 to

0.3551 lb/ft^2 (11 to 17 Pa) and plastic viscosity from 0.2957 to 0.5779 lb/ft^{-s} (0.44 to 0.86 Pa·s). An increase in the dosage of *K. alvarezii* to 0.50 and 0.75% resulted in higher yield stress of 0.4595 and 0.5430 lb/ft^2 (22 and 26 Pa), and plastic viscosity of 0.7862 and 0.9139 lb/ft^{-s} (1.17 and 1.36 Pa·s), respectively. However, the pre-hydration of *K. alvarezii* did not lead to significant differences in the yield stress and plastic viscosity, regardless of the dosage of *K. alvarezii*.

Table 4—Rheological parameters of mixtures containing 0.5% (κ)-carrageenan and *K. alvarezii*[1-3]

	Shear stress at 150 s^{-1}, lb/ft^2 (Pa)	Plastic viscosity, lb/ft^{-s} (Pa·s)	Yield stress, lb/ft^2 (Pa)
0%	0.79 (37.6)	0.30 (0.44)	0.23 (10.95)
0.5% (κ)-carrageenan	2.21 (106)	0.88 (1.31)	0.63 (30)
0.5% *K. alvarezii*	1.96 (93.82)	0.79 (1.17)	0.46 (22.16)

As can be observed in Table 4, at an equal dosage of 0.5% of (κ)-carrageenan and *K. alvarezii*, the use of (κ)-carrageenan did not increase the yield stress and plastic viscosity values compared to *K. alvarezii*. This confirms that the 3,6-anhydrogalactose bridge is not responsible for the viscosity increase of cement suspensions but rather their rigidity.

The viscoelastic behavior of cement-paste mixtures was also evaluated by performing strain sweep measurements, in which the sample is subjected to increasing shear strain from 0.0001 to 100% at a constant angular frequency of 10 rad/s. This aims to characterize the flocculated microstructure of the investigated suspensions in the region where the rigidity of the system is independent of the imposed shear strain (that is, in the linear viscoelastic domain [LVED]). As can be observed in Fig. 7, increasing the dosage of *K. alvarezii* to 0.75% increased the critical shear strain from 0.0055% (reference mixture) to 0.0174% in the case of mixtures that contain non-pre-hydrated solutions,

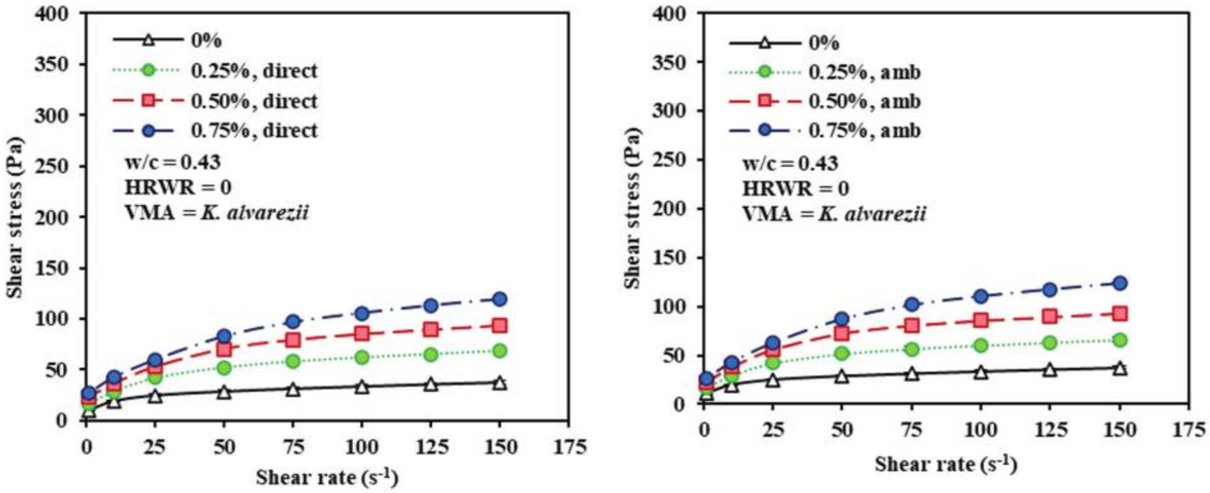

(a) Immediately tested (b) Pre-hydrated for 24 h at room temperature

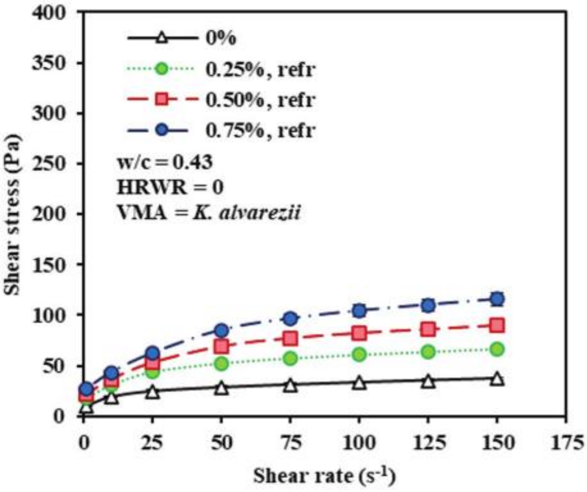

(c) Pre-hydrated for 24 h at 8 °C

Fig. 5—Flow curves of cement-paste mixtures proportioned with different solutions containing K. alvarezii*: (a) immediately tested or pre-hydrated for 24 hours; (b) at room temperature; or (c) at 46.4°F (8°C). (Note: 1 Pa = 0.02 lb/ft^2.)*

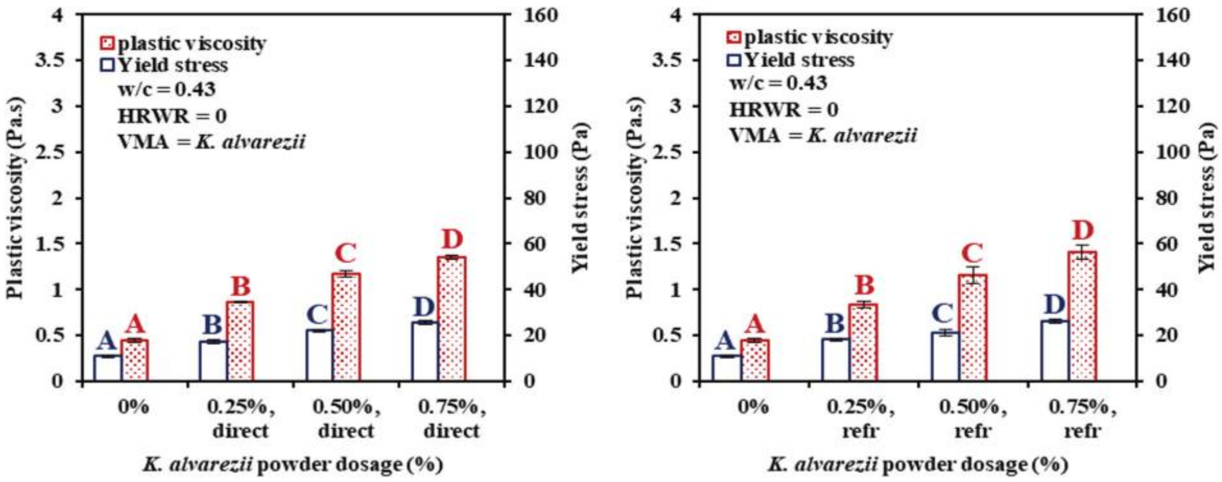

(a) Immediately tested

(b) Pre-hydrated for 24 h at room temperature

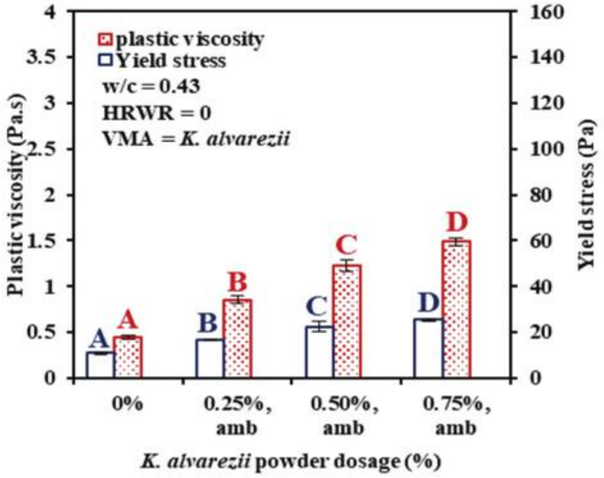

(c) Pre-hydrated for 24 h at 8 °C

Fig. 6—Variation in plastic viscosity and yield stress values of cement-paste mixtures proportioned with different solutions containing K. alvarezii*: (a) immediately tested or pre-hydrated for 24 hours; (b) at room temperature; or (c) at 46.4°F (8°C). (Note: 1 Pa = 0.02 lb/ft^2; 1 Pa·s = 0.67 lb/ft^{-s}.)*

and 0.0175% in the case of mixtures that contain pre-hydrated solutions at room temperature or at 46.4°F (8°C). However, dosages of 0.25 and 0.50% *K. alvarezii* did not significantly increase the critical shear strain compared to the reference mixture, regardless of the pre-hydration method, except in the mixture prepared with a non-pre-hydrated solution containing 0.50% *K. alvarezii*. In addition, the pre-hydration did not lead to significant differences in the values of the critical shear strain. Nevertheless, it is worth mentioning that there were no significant differences in the critical shear strain values between the mixtures prepared from a non-pre-hydrated solution containing 0.25% *K. alvarezii* and those containing a solution of 0.50% *K. alvarezii*, regardless of the method of pre-hydration.

The maximum value of G', referring to $G_{max.}'$, in the LVED was also determined. As shown in Fig. 7, the use of *K. alvarezii* generally increased the rigidity of cement-paste mixtures, regardless of the dosage of *K. alvarezii* or the pre-hydration method. However, in this case, the pre-hydration method significantly increased the rigidity of cement-paste mixtures prepared from solutions containing 0.50% *K. alvarezii*. Indeed, the $G_{max.}'$ increased from 585 lb/ft^2 (28,000 Pa) to 764, 916, and 922 lb/ft^2 (36,600, 43,867, and 44,167 Pa) when using 0.50% *K. alvarezii*, non-pre-hydrated, and pre-hydrated solutions at room temperature or at 46.4°F (8°C), respectively. On the other hand, the pre-hydration of solutions containing 0.25 or 0.75% of *K. alvarezii* did not lead to significant differences in the $G_{max.}'$ values of the investigated mixtures.

Although the use of *K. alvarezii* increased the rigidity of cement-paste mixtures, it is important to mention that increasing the dosage of *K. alvarezii* from 0.25 to 0.75% generally decreased the values of $G_{max.}'$, regardless of the pre-hydration method.

As shown in Table 5, for a given dosage of 0.5%, the use of *K. alvarezii* resulted in a higher critical shear strain value compared to (κ)-carrageenan. However, the mixture containing 0.5% (κ)-carrageenan exhibited lower initial

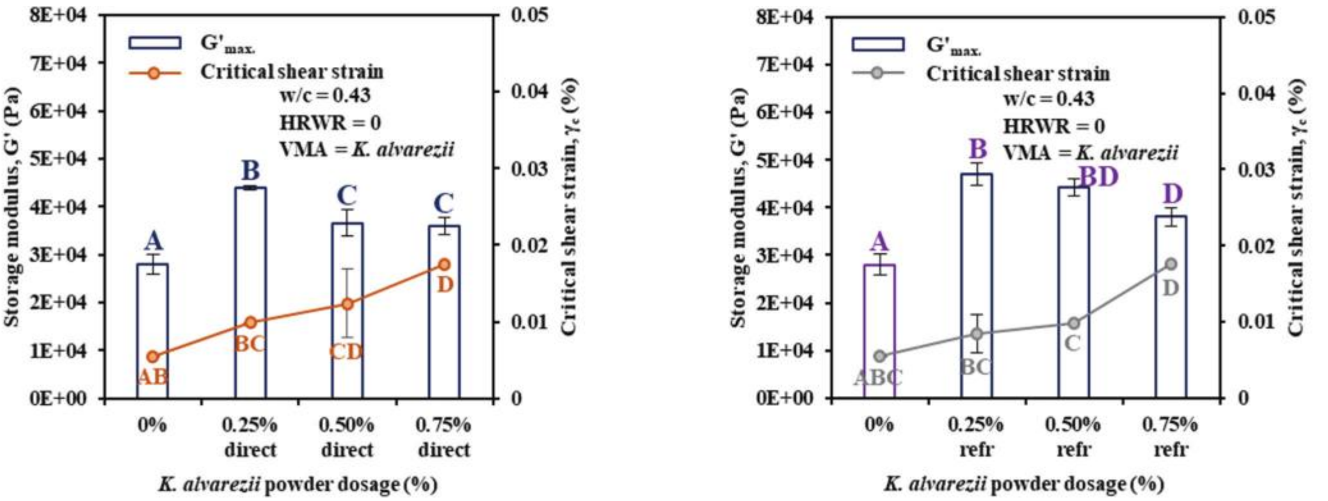

(a) Immediately tested

(b) Pre-hydrated for 24 h at room temperature

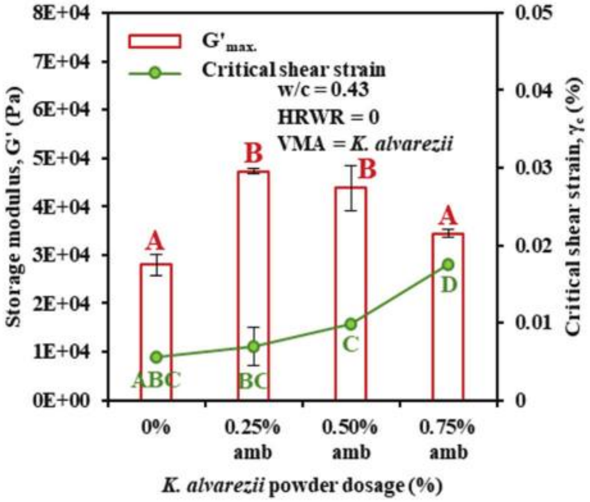

(c) Pre-hydrated for 24 h at 8 °C

Fig. 7—Variation in maximum rigidity ($G_{max.}'$*) and critical shear strain (*γ_c*) of cement-paste mixtures proportioned with different solutions containing* K. alvarezii*: (a) immediately tested or pre-hydrated for 24 hours; (b) at room temperature; or (c) at 46.4°F (8°C). (Note: 1 Pa = 0.02 lb/ft*^{2}*.)*

Table 5—Variation in critical shear strain, rigidity, and rigidification rate of mixtures containing 0.5% (κ)-carrageenan and *K. alvarezii*$^{1-3}$

	0%	0.5% (κ)-carrageenan	0.5% *K. alvarezii*
γ_c, %	0.0030	0.0098	0.0123
G', lb/ft^2 (Pa)	585 (28,000)	503 (24,100)	764 (36,600)
$G_{rigid.}$, lb/ft^2 (Pa/min)	34 (1623)	72.41 (3467)	41 (1968)

rigidity (that is, $G_{max.}'$) compared to the mixture containing *K. alvarezii*.

It is known in the literature that the aqueous gelation of carrageenans depends on the type of carrageenan, the temperature, and the type of cations dissolved in the solution and its concentrations. The ability to form a gel is mainly due to the presence of the 3,6-anhydro bridge of the 4-linked-α-D-galactose unit, which adopts a $^1C_4$ conformation, thereby forming a helical structure. The aqueous extraction of carrageenan from red seaweed using hot water allows it to retain the original structure of carrageenan, unlike when it is extracted using chemical treatment with alkalis (such as KOH), which may cause the structure of the carrageenan chains to lack 3,6-anhydro bridges. This is due to the presence of sulfate at the C_6 of α-L-galactose residues in the precursor units, which acts as a "kink," preventing the formation of the double helix. The alkaline base is used due to its double action. The hydroxyl transforms the biological (κ)-carrageenan form found in the thallus of red seaweeds into commercial-quality (κ)-carrageenan,[28] while potassium plays an essential role in gel formation.[26] Indeed, alkalis can induce desulfation of the polysaccharide by causing the formation of the 3,6-anhydrogalactose bridge between

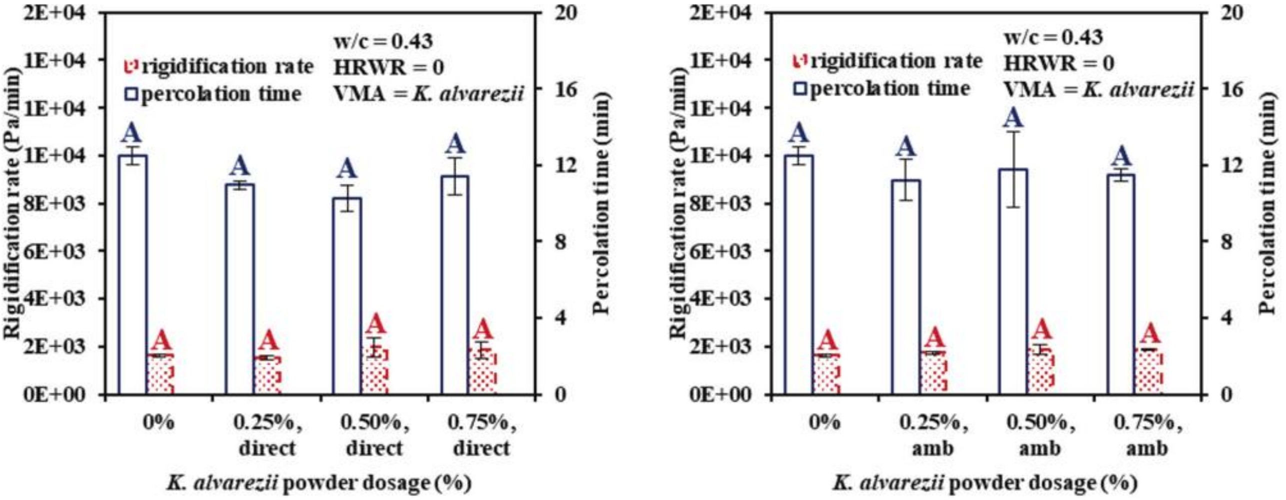

(a) Immediately tested

(b) Pre-hydrated for 24 h at room temperature

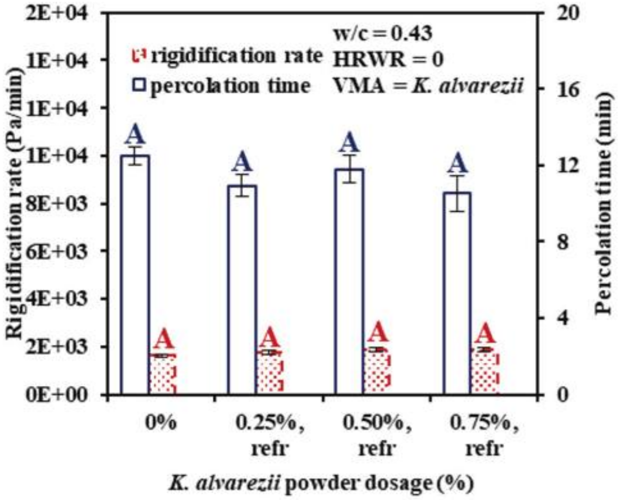

(c) Pre-hydrated for 24 h at 8 °C

Fig. 8—Values of $G_{rigid.}$ *and* $t_{perc.}$ *of cement-paste mixtures proportioned with different solutions containing* K. alvarezii*: (a) immediately tested or pre-hydrated for 24 hours; (b) at room temperature; or (c) at 46.4°F (8°C). (Note: 1 Pa = 0.02 lb/ft*^{2}*.)*

C_3 and C_6 in 4-linked-α-L-galactose units by changing the conformation of the 4-linked-α-L-galactose unit from $^4C_1$ to $^1C_4$, which leads to the formation of the 3,6-anhydro-D-galactose unit. The formation of this unit increases the gel strength.[27,28,36] When this sulfate group is removed, the chain becomes flexible, which leads to regularity in the polymer. Therefore, the native (κ)-carrageenan contained in *K. alvarezii* seaweed may present a high sulfate ester and probably low 3,6-anhydro bridge contents, thus exhibiting high viscosity but low rigidity,[27,35,46,47] which influences the rigidity of cement-paste mixtures. On the other hand, the electrostatic repulsion between the negatively charged sulfate groups can contribute to increasing the distance between chains, which leads to a greater distance between cement particles, hence longer LVED.

Effect of *K. alvarezii* on kinetics of structural buildup of cement suspensions

The percolation time ($t_{perc.}$) and rigidification rate ($G_{rigid.}$) were determined to assess the structural buildup kinetics of cement suspensions containing *K. alvarezii* seaweed. Although the use of *K. alvarezii* significantly increased the viscosity and rigidity of cement-paste mixtures, no significant effect was observed on the structural buildup kinetics. Indeed, the addition of *K. alvarezii* did not lead to any significant change in the $t_{perc.}$ and $G_{rigid.}$ values (Fig. 8), which agrees with the strain sweep measurements. The neutral effect of *K. alvarezii* on the structural buildup kinetics of cement suspensions can limit its use in certain construction applications, in particular 3-D concrete printing.

Moreover, these results confirm that the native (κ)-carrageenan present in *K. alvarezii* seaweed did not help increase the rigidity of cement suspensions over time. This is probably due to the lack of 3,6-anhydro bridges, which are

Table 6—Values of dormant period durations of mixtures containing 0.5% (κ)-carrageenan and *K. alvarezii*[1-3]

	Dormant period
0%	1 hour, 32 minutes
0.5% (κ)-carrageenan	6 hours, 12 minutes
0.5% *K. alvarezii*	1 hour, 31 minutes

responsible for the gel formation and the thixotropic effect reported in previous studies[1-3] (Table 5). Therefore, an alkaline extraction should be required to maintain the thixotropic effect of (κ)-carrageenan in cement suspensions.

Based on the rheological results and statistical analysis previously presented, it can be stated that the effect of the pre-hydrated *K. alvarezii* on the rheological behavior of the cement suspensions was not significant. Only the cement suspensions containing non-pre-hydrated aqueous solutions of *K. alvarezii* were chosen for use in subsequent tests. This was done to optimize the testing duration and reduce the energy used in the case of solutions stored at 46.4°F (8°C).

Effect of *K. alvarezii* on cement hydration kinetics

The effect of *K. alvarezii* on cement hydration is necessary because most conventional VMAs interfere with the kinetics of cement hydration. This is due to the adsorption of the VMAs' polymer chains onto cement particles, which then form a film around the clinker particles and delay their reaction by preventing the rate of solubilization of mineral species in the pore solution. In addition, it has been observed in previous studies[1-3] that the refined (κ)-carrageenan significantly slows the hydration of cement (Table 6). This has been attributed to the capture of the Na^+, Ca^{2+}, and K^+ ions necessary to initiate the acceleration period of the polymer of (κ)-carrageenan to stabilize its junction sites and form a rigid gel.[1-3] This decreases the ions' concentrations in the pore solution, thus delaying the hydration of the cement.[1-3]

The evolution of the heat flow of cement-paste mixtures prepared from aqueous solutions containing different dosages of *K. alvarezii* corresponding to 0.25, 0.50, and 0.75%, by weight of water, is shown in Fig. 9. The heat flow of each of the studied mixtures is determined for 72 hours after mixing. As can be observed, despite the increase in the viscosity of the cement paste, the addition of the *K. alvarezii* seaweed did not show any significant effect on the hydration of cement compared to the reference mixture, regardless of the dosage of *K. alvarezii*, which is unusual for a VMA. The time required to reach the silicates-hydration peak was comparable to that of the reference mixture, as shown in Fig. 9. In addition, the hydration heat corresponding to the silicates-hydration peak was generally comparable for all the investigated mixtures. However, adding 0.75% of *K. alvarezii* slightly decreased the intensity of this heat peak. The silicates-hydration peak is often followed by a period of deceleration, in which a final peak of hydration related to the transformation of ettringite into monsulfoaluminate appears. This peak was slightly higher for mixtures containing *K. alvarezii*.

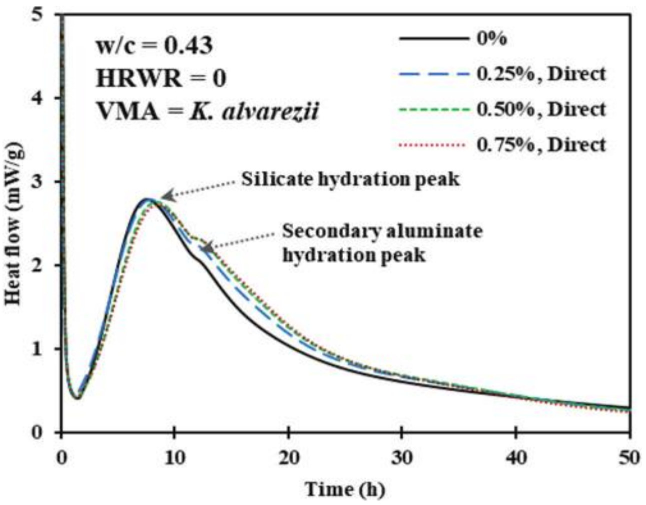

Fig. 9—Effect of K. alvarezii *on hydration kinetics of cement-paste mixtures. (Note: 1 mW/g = 3.38 × 10^{-5} hp/oz.)*

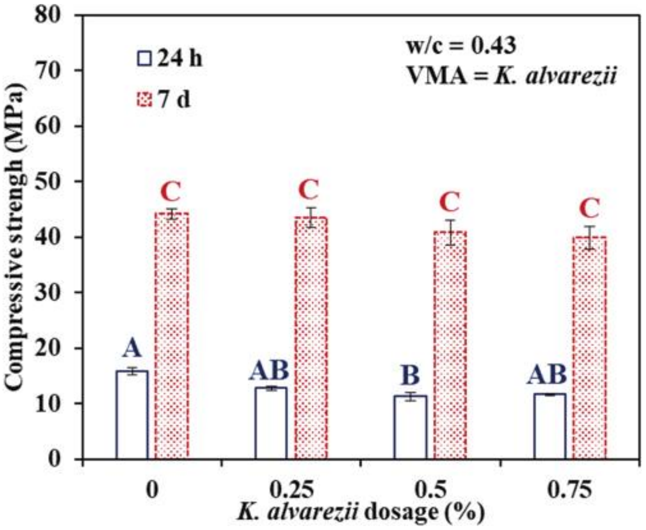

Fig. 10—Compressive strength of cement suspensions containing K. alvarezii *after: (a) 24 hours; and (b) 7 days. (Note: 1 MPa = 0.145 ksi.)*

Overall, considering the results presented previously, it can be concluded that the use of *K. alvarezii* as a VMA did not significantly affect the cement's hydration kinetics. This is particularly advantageous because most common VMAs, such as cellulose ether and welan gum, have adverse effects on hydration kinetics, especially at high dosages.

Effect of *K. alvarezii* seaweed on compressive strength of cement suspensions

The compressive strengths of cement suspensions containing different dosages of *K. alvarezii*, corresponding to 0.25, 0.5, and 0.75%, by weight of water, after 24 hours and 7 days of wet curing are shown in Fig. 10. As can be observed, the use of *K. alvarezii* generally showed no significant effect (positive/negative) on the strength development of cement suspensions compared to the reference mixture, regardless of the dosage of *K. alvarezii* or the curing time. This validates the feasibility of using *K. alvarezii* seaweed as a VMA. Indeed, most VMAs reduce the mechanical

Table 7—Values of compressive strength of cement suspensions containing 0.5% (κ)-carrageenan at 24 hours and 7 days of age[1-3]

Compressive strength at 24 hours, ksi (MPa)	
(κ)-carrageenan dosage, %	Neat
0.5	4.0 ± 0.1 (27.5 ± 0.5)
Compressive strength at 7 days, ksi (MPa)	
(κ)-carrageenan dosage, %	Neat
0.5	6.1 ± 0.3 (42.0 ± 1.8)

resistance development of cement systems, especially at high VMA dosages.[1,2,7] This reduction is mainly due to the delay in cement setting time observed when a VMA is incorporated into these cement systems. The use of *K. alvarezii* did not delay the setting time of cement suspensions; its use increased the adhesion mechanism between cement particles due to its viscous properties without having a negative effect on the compressive strength development of cement suspensions.

At a given dosage of 0.5%, the use of (κ)-carrageenan significantly increased the compressive strength of cement suspensions after 24 hours of hardening compared to the use of *K. alvarezii* (Table 7). This is probably due to the intrinsic mechanisms of the (κ)-carrageenan polymer. Indeed, when (κ)-carrageenan is used as a VMA in cement systems, its gelling properties and ability to form a rigid gel allow for an increase in the adhesion between the cement particles by filling the pores while reinforcing the performance of cement paste.[31] The (κ)-carrageenan also increases the ability of the cement system to retain the free water available in the cement matrix, which improves its internal curing,[1,2] unlike *K. alvarezii*.[1] However, after 7 days of wet curing and with the same dosage of 0.5%, cement suspensions containing *K. alvarezii* showed a compressive strength comparable to those of suspensions containing (κ)-carrageenan (Table 7). This confirms the possibility of using *K. alvarezii* as a VMA in cement systems.

CONCLUSIONS

The effect of different dosages and pre-hydration methods of *Kappaphycus alvarezii* (*K. alvarezii*) on the rheological behavior, viscoelastic properties, structural buildup kinetics, hydration kinetics, and compressive strength of cement-paste mixtures proportioned with a water-cement ratio (w/c) of 0.43 was evaluated. Based on the results presented herein, the following conclusions can be drawn:

1. The cement-paste mixtures containing *K. alvarezii* showed a pseudoplastic (shear-thinning) behavior, in which the shear stress increases with the increase of the *K. alvarezii* dosage, regardless of the pre-hydration method.

2. The pre-hydration method of aqueous solutions had no significant effect on the rheological behavior of cement pastes. This confirms the stability of *K. alvarezii* under various conditions (concreting work in hot/cold weather).

3. The use of *K. alvarezii* enhanced the plastic viscosity, yield stress, initial rigidity, and linear viscoelastic domain (LVED) values of cement pastes more than the use of kappa (κ)-carrageenan, regardless of the pre-hydration method, which is highly recommended for the preparation of grouts intended for underwater applications. However, it did not increase the structural buildup kinetics of cement suspensions compared to (κ)-carrageenan. Moreover, *K. alvarezii* did not affect the cement hydration kinetics compared to (κ)-carrageenan, which makes it more efficient than the current viscosity-modifying admixtures (VMAs) and confirms the compatibility of this VMA with cement.

4. The use of *K. alvarezii* seaweed showed no significant effect (positive/negative) on the strength development of the cement suspensions compared to the reference mixture, regardless of the dosage of *K. alvarezii* or the curing time. This validates the feasibility of using *K. alvarezii* seaweed as a VMA.

5. *K. alvarezii* seaweed can be used as a VMA to improve the viscosity of flowable cement matrixes without changing either their hydration kinetics or their mechanical strength. This is consistent with the definition of a VMA cited in the Experts for Specialised Construction and Concrete Systems (EFNARC) specifications. However, the neutral effect of *K. alvarezii* on the structural buildup kinetics of cement suspensions restricts its use in concrete three-dimensional (3-D) printing.

AUTHOR BIOS

Asma Boukhatem *is a PhD Candidate at the Université de Sherbrooke, Sherbrooke, QC, Canada. She received her bachelor's degree from the University of Chlef, Ouled Farès, Chlef, Algeria, and her MSc from the Université de Sherbrooke. Her research interests include the use of biopolymers as viscosity-modifying admixtures (VMAs) and multifunctional molecules in cement-based materials.*

Kamal Bouarab *is a Professor of biology at the Université de Sherbrooke. His research interests include the mechanisms of plant immunity as well as the strategies used by certain pathogens to divert this immunity.*

ACI member **Ammar Yahia** *is a Professor at the Université de Sherbrooke. He is a member of ACI Committees 237, Self-Consolidating Concrete, and 552, Cementitious Grouting. His research interests include the rheology of cement-based materials, the use of VMAs in cement-based materials, innovative materials with adapted structural buildup for three-dimensional (3-D) printing, self-consolidating concrete, and high-performance grouting.*

REFERENCES

1. Yahia, A.; Bouarab, K.; Boukhatem, A.; and Mostafa, A., "Use of Carrageenan as a Viscosity-Modifying Admixture in a Flowable Cementitious Suspensions," International Patent No. WO 2022/104469 A1, 2022, 137 pp.

2. Boukhatem, A.; Bouarab, K.; and Yahia, A., "Kappa (κ)-Carrageenan as a Novel Viscosity-Modifying Admixture for Cement-Based Materials – Effect on Rheology, Stability, and Strength Development," *Cement and Concrete Composites*, V. 124, Nov. 2021, Article No. 104221. doi: 10.1016/j.cemconcomp.2021.104221

3. Boukhatem, A.; Bouarab, K.; and Yahia, A., "Effect of (κ)- and (ι)-Carrageenans on Rheology and Strength Development of Cement-Based Materials," *ACI Materials Journal*, V. 119, No. 1, Jan. 2022, pp. 207-219.

4. ACI Committee 237, "Self-Consolidating Concrete (ACI 237R-07) (Reapproved 2019)," American Concrete Institute, Farmington Hills, MI, 2007, 30 pp.

5. Khayat, K. H., "Effects of Antiwashout Admixtures on Fresh Concrete Properties," *ACI Materials Journal*, V. 92, No. 2, Mar.-Apr. 1995, pp. 164-171.

6. Khayat, K. H., "Viscosity-Enhancing Admixtures for Cement-Based Materials – An Overview," *Cement and Concrete Composites*, V. 20, No. 2-3, 1998, pp. 171-188. doi: 10.1016/S0958-9465(98)80006-1

7. Khayat, K. H., and Yahia, A., "Effect of Welan Gum-High-Range Water Reducer Combinations on Rheology of Cement Grout," *ACI Materials Journal*, V. 94, No. 5, Sept.-Oct. 1997, pp. 365-372.

8. Yahia, A., and Khayat, K. H., "Analytical Models for Estimating Yield Stress of High-Performance Pseudoplastic Grout," *Cement and Concrete Research*, V. 31, No. 5, May 2001, pp. 731-738. doi: 10.1016/S0008-8846(01)00476-8

9. Kawai, T., "Non-Dispersible Underwater Concrete Using Polymers," *The Production, Performance & Potential of Polymers in Concrete: ICPIC 87: 5th International Congress on Polymers in Concrete*, B. W. Staynes, ed., Brighton, UK, 1987, pp. 385-390.

10. Nehdi, M., "Why Some Carbonate Fillers Cause Rapid Increases of Viscosity in Dispersed Cement-Based Materials," *Cement and Concrete Research*, V. 30, No. 10, Oct. 2000, pp. 1663-1669. doi: 10.1016/S0008-8846(00)00353-7

11. Cronshaw, J.; Myers, A.; and Preston, R. D., "A Chemical and Physical Investigation of the Cell Walls of Some Marine Algae," *Biochimica et Biophysica Acta*, V. 27, 1958, pp. 89-103. doi: 10.1016/0006-3002(58)90295-6

12. Davis, T. A.; Volesky, B.; and Mucci, A., "A Review of the Biochemistry of Heavy Metal Biosorption by Brown Algae," *Water Research*, V. 37, No. 18, Nov. 2003, pp. 4311-4330. doi: 10.1016/S0043-1354(03)00293-8

13. Kloareg, B., and Quatrano, R. S., "Structure of the Cell Walls of Marine Algae and Ecophysiological Functions of the Matrix Polysaccharides," *Oceanography and Marine Biology: An Annual Review*, V. 26, H. Barnes, ed., CRC Press, London, UK, 1988, pp. 259-315.

14. Kraan, S., "Algal Polysaccharides, Novel Applications and Outlook," *Carbohydrates: Comprehensive Studies on Glycobiology and Glycotechnology*, first edition, C.-F. Chang, ed., InTech, Rijeka, Croatia, 2012, pp. 489-532.

15. Imeson, A. P., ed., *Thickening and Gelling Agents for Food*, Blackie Academic and Professional Publisher, Glasgow, UK, 1992, pp. 1-24.

16. Mishra, V. K.; Temelli, F.; Ooraikul, B.; Shacklock, P. F.; and Craigie, J. S., "Lipids of the Red Alga, *Palmaria palmata*," *Botanica Marina*, V. 36, No. 2, 1993, pp. 169-174. doi: 10.1515/botm.1993.36.2.169

17. Painter, T. J., "Algal Polysaccharides," *The Polysaccharides*, G. O. Aspinall, ed., Academic Press, New York, NY, 1983, pp. 195-285.

18. Rees, D. A., "Structure, Conformation, and Mechanism in the Formation of Polysaccharide Gels and Networks," *Advances in Carbohydrate Chemistry and Biochemistry*, V. 24, 1969, pp. 267-332. doi: 10.1016/S0065-2318(08)60352-2

19. Rochas, C.; Rinaudo, M.; and Landry, S., "Relation between the Molecular Structure and Mechanical Properties of Carrageenan Gels," *Carbohydrate Polymers*, V. 10, No. 2, 1989, pp. 115-127. doi: 10.1016/0144-8617(89)90061-1

20. van de Velde, F.; Pereira, L.; and Rollema, H. S., "The Revised NMR Chemical Shift Data of Carrageenans," *Carbohydrate Research*, V. 339, No. 13, Sept. 2004, pp. 2309-2313. doi: 10.1016/j.carres.2004.07.015

21. Pereira, L., and van de Velde, F., "Portuguese Carrageenophytes: Carrageenan Composition and Geographic Distribution of Eight Species (*Gigartinales, Rhodophyta*)," *Carbohydrate Polymers*, V. 84, No. 1, Feb. 2011, pp. 614-623. doi: 10.1016/j.carbpol.2010.12.036

22. Whistler, R. L., and BeMiller, J. N., *Carbohydrate Chemistry for Food Scientists*, Egan Press, St. Paul, MN, 1997, pp. 65.

23. McHugh, D. J., ed., "Production and Utilization of Products from Commercial Seaweeds," FAO Fisheries Technical Paper No. 288, FAO Fisheries and Aquaculture, Rome, Italy, 1987.

24. Stevenson, T. T., and Furneaux, R. H., "Chemical Methods for the Analysis of Sulphated Galactans from Red Algae," *Carbohydrate Research*, V. 210, Mar. 1991, pp. 277-298. doi: 10.1016/0008-6215(91)80129-B

25. Knutsen, S. H.; Myslabodski, D. E.; Larsen, B.; and Usov, A. I., "A Modified System of Nomenclature for Red Algal Galactans," *Botanica Marina*, V. 37, No. 2, 1994, pp. 163-169. doi: 10.1515/botm.1994.37.2.163

26. van de Velde, F.; Knutsen, S. H.; Usov, A. I.; Rollema, H. S.; and Cerezo, A. S., "^{1}H and ^{13}C High Resolution NMR Spectroscopy of Carrageenans: Application in Research and Industry," *Trends in Food Science & Technology*, V. 13, No. 3, Mar. 2002, pp. 73-92. doi: 10.1016/S0924-2244(02)00066-3

27. Rees, D. A., "Structure, Conformation, and Mechanism in the Formation of Polysaccharide Gels and Networks," *Advances in Carbohydrate Chemistry and Biochemistry*, V. 24, 1969, pp. 267-332. doi: 10.1016/S0065-2318(08)60352-2

28. Distantina, S.; Wiratni; Fahrurrozi, M.; and Rochmadi, "Carrageenan Properties Extracted from *Eucheuma cottonii*, Indonesia," *World Academy of Science, Engineering and Technology*, V. 78, 2011, pp. 738-742.

29. León-Martínez, F. M.; Cano-Barrita, P. F. D. J.; Lagunez-Rivera, L.; and Medina-Torres, L., "Study of Nopal Mucilage and Marine Brown Algae Extract as Viscosity-Enhancing Admixtures for Cement Based Materials," *Construction and Building Materials*, V. 53, Feb. 2014, pp. 190-202. doi: 10.1016/j.conbuildmat.2013.11.068

30. Aday, A. N.; Osio-Norgaard, J.; Foster, K. E. O.; and Srubar, W. V. III, "Carrageenan-Based Superabsorbent Biopolymers Mitigate Autogenous Shrinkage in Ordinary Portland Cement," *Materials and Structures*, V. 51, No. 2, Apr. 2018, Article No. 37. doi: 10.1617/s11527-018-1164-5

31. Susilorini, R. M. I. R.; Hardjasaputra, H.; Tudjono, S.; Hapsari, G.; Wahyu, S. R.; Hadikusumo, G.; and Sucipto, J., "The Advantage of Natural Polymer Modified Mortar with Seaweed: Green Construction Material Innovation for Sustainable Concrete," *Procedia Engineering*, V. 95, 2014, pp. 419-425. doi: 10.1016/j.proeng.2014.12.201

32. Abdollahnejad, Z.; Kheradmand, M.; and Pacheco-Torgal, F., "Mechanical Properties of Hybrid Cement Based Mortars Containing Two Biopolymers," *International Scholarly and Scientific Research & Innovation*, V. 11, No. 9, 2017, pp. 1242-1245.

33. Abdollahnejad, Z.; Kheradmand, M.; and Pacheco-Torgal, F., "Short-Term Compressive Strength of Fly Ash and Waste Glass Alkali-Activated Cement-Based Binder Mortars with Two Biopolymers," *Journal of Materials in Civil Engineering*, ASCE, V. 29, No. 7, July 2017, p. 04017045. doi: 10.1061/(ASCE)MT.1943-5533.0001920

34. Majid, N. B.; Ibrahim, I. S. B.; Sarbini, N. N. B.; Zakaria, Z. A. B.; and Osman, M. H. B., "The Chemical Properties of Seaweed for Modify Concrete," *IOP Conference Series: Earth and Environmental Science*, V. 220, 2019, Article No. 012026.

35. Normah, O., and Nazarifah, I., "Production of Semi-Refined Carrageenan from Locally Available Red Seaweed, *Eucheuma cottonii* on a Laboratory Scale," *Journal of Tropical Agriculture and Food Science*, V. 31, No. 2, 2003, pp. 207-213.

36. Hernández-Carmona, G.; Freile-Pelegrín, Y.; and Hernández-Garibay, E., "Conventional and Alternative Technologies for the Extraction of Algal Polysaccharides," *Functional Ingredients from Algae for Foods and Nutraceuticals*, H. Domínguez, ed., Woodhead Publishing, Sawston, UK, 2013, pp. 475-516.

37. Sjamsiah; Ramli, N.; Daik, R.; and Yarmo, M. A., "Determination of the Functional Properties of *Kappaphycus alvarezii* Seaweed Powder," *The Malaysian Journal of Analytical Sciences*, V. 17, No. 2, 2013, pp. 236-243.

38. Ajithkumar, S.; Krishnaraj, G.; Abdul Haleem, M. I.; Manivasagan, V.; Ramesh Babu, N. G.; and Pandi Durai, S., "Optimization of Carrageenan Extraction Process from Seaweed," *World Journal of Pharmacy and Pharmaceutical Sciences*, V. 6, No. 4, Apr. 2017, pp. 2205-2213.

39. Moses, J.; Anandhakumar, R.; and Shanmugam, M., "Effect of Alkaline Treatment on the Sulfate Content and Quality of Semi-refined Carrageenan Prepared from Seaweed *Kappaphycus alvarezii* Doty (Doty) Farmed in Indian Waters," *African Journal of Biotechnology*, V. 14, No. 18, May 2015, pp. 1584-1589. doi: 10.5897/AJB2014.14203

40. PT. Alamindo Makmur Cemerlang, "Website," 2020, https://picbabun.com/pt_amc.

41. Lemieux, M.; Bertrand, F.; Chaouki, J.; and Gosselin, P., "Comparative Study of the Mixing of Free-Flowing Particles in a V-Blender and a Bin-Blender," *Chemical Engineering Science*, V. 62, No. 6, Mar. 2007, pp. 1783-1802. doi: 10.1016/j.ces.2006.12.012

42. Thrimawithana, T. R.; Young, S.; Dunstan, D. E.; and Alany, R. G., "Texture and Rheological Characterization of Kappa and Iota Carrageenan in the Presence of Counter Ions," *Carbohydrate Polymers*, V. 82, No. 1, Aug. 2010, pp. 69-77. doi: 10.1016/j.carbpol.2010.04.024

43. Webber, V.; de Carvalho, S. M.; Ogliari, P. J.; Hayashi, L.; and Barreto, P. L. M., "Optimization of the Extraction of Carrageenan from *Kappaphycus alvarezii* Using Response Surface Methodology," *Ciência Tecnologia Alimentos Campinas*, V. 32, No. 4, Dec. 2012, pp. 812-818. doi: 10.1590/S0101-20612012005000111

44. Mostafa, A. M., and Yahia, A., "New Approach to Assess Build-Up of Cement-Based Suspensions," *Cement and Concrete Research*, V. 85, July 2016, pp. 174-182. doi: 10.1016/j.cemconres.2016.03.005

45. Mezger, T. G., *The Rheology Handbook: For Users of Rotational and Oscillatory Rheometers*, Vincentz Network, Hanover, Germany, 2011, 432 pp.

46. Bono, A.; Anisuzzaman, S. M.; and Ding, O. W., "Effect of Process Conditions on the Gel Viscosity and Gel Strength of Semi-Refined Carrageenan (SRC) Produced from Seaweed (*Kappaphycus alvarezii*)," *Journal of King Saud University - Engineering Sciences*, V. 26, No. 1, Jan. 2014, pp. 3-9. doi: 10.1016/j.jksues.2012.06.001

47. Heriyanto, H.; Kustiningsih, I.; and Sari, D. K., "The Effect of Temperature and Time of Extraction on the Quality of Semi Refined Carrageenan (SRC)," *MATEC Web of Conferences*, V. 154, 2018, Article No. 01034.

ACI MATERIALS JOURNAL TECHNICAL PAPER

Title No. 120-M43

Influence of Activated Coal Gangue Powder on Compressive Strength of Coal Gangue Coarse Aggregate Concrete

by J. Yan, D. Shan, X. Wang, Y. Luo, W. Weng, L. Wang, J. Xie, C. Lu, Z. Lai, X. Yu, G. Xing, and X. Liu

Coal gangue is one of the largest industrial solid wastes, and the application of coal gangue to cement-based materials is an effective way of resourcing the use of coal gangue. The optimum activation temperature of coal gangue was determined by X-ray diffraction (XRD), thermogravimetric-differential (TG-DSC) analysis, and cement mortar strength testing, and then the optimal temperature-activated coal gangue powder (CGP) was mixed into coal gangue coarse aggregate concrete (CGC) as an admixture to form the double-admixture CGC. The compressive strength testing of CGC was carried out by selecting different CGP contents and coal gangue aggregate (CGA) replacement rates as variables. On the microscopic scale, the pore structure of the CGC could be analyzed by the physical adsorption analyzer technique and scanning electron microscopy (SEM). The results indicate that: 1) the optimal activation temperature of raw coal gangue in the Xuanhua Mine, Zhangjiakou, China, is 500°C; 2) with the increased replacement rate of CGA, the compressive strength of CGC indicates a decreased tendency. With the CGP content rise, the compressive strength of CGC increases first and then declines. In the case of total substitution of CGA, selecting 10% CGP to replace cement makes the compressive strength of CGC reach the maximum value; and 3) the chloride penetration resistance property of CGC could be significantly improved by mixing CGP (within 20%) into CGC.

Keywords: coal gangue; compressive strength; hydration reaction; microscopic analysis; thermal activation.

INTRODUCTION

Coal gangue is a solid waste discharged in coal washing and choosing, accounting for 10 to 25% of coal production.[1] According to statistics, China's coal industry has emitted more than 5 billion tons of coal gangue, an increase of 300 million tons per year.[2] Not only is a large amount of land wasted by dealing with coal gangue, but it also causes environmental pollution. Nowadays, solving the environmental problems caused by coal gangue have become very urgent.

On the other hand, with the rapid economic development in China, a large amount of concrete is consumed to promote the urbanization process. During this process, the large amount of consumed concrete raw materials such as clay and natural gravel impose a heavy burden on the environment. Thus, there is an urgent requirement to find a high-quality replacement concrete material. The mineral composition of coal gangue aggregate (CGA) is similar to natural aggregate (NA), and has a certain elasticity modulus and strength that allow it to be used as coarse concrete aggregate.[3-5] It is an effective way to use coal gangue to prepare concrete with high added value. However, compared with NA, CGA has lower physical properties—it is more porous and has lower strength and water absorption. Therefore, mixing coal gangue will harm concrete performance. Ma et al.[6] found that the strength of raw coal gangue coarse aggregate concrete (CGC) had a negative linear relationship with the amount of CGA. Yi et al.[7] found that with the increase of coal gangue replacement rates and carbonation time, the raw CGA concrete's carbonation depth increased as well. Qiu et al.[8] found that the increase of CGA content will significantly reduce the frost resistance performance of concrete, mainly because the pore and water absorption of CGA were larger than NA, and the pore water produced larger water-swelling and frost-heaving stresses.[9,10]

The previously mentioned literature suggests that CGA as the coarse aggregate can partially replace natural gravel in concrete, but will decrease the mechanical and durability properties of CGC. To improve the performance of CGC, many scholars and experts have done a lot of research. Many papers have proven that the mechanical properties of CGC could be improved by mixing with high-quality mineral admixtures. Coal gangue is poorly activated in cement materials compared with other mineral admixtures. Fortunately, many measures could improve its pozzolanic activity, such as using thermal, mechanical, and microwave activation or compound activation methods. Cao et al.[11] studied the coal gangue's pozzolanic activity, which was calcined at different temperatures. The results show that the pozzolanic activity of coal gangue increases first and then decreases when calcined at high temperatures from 400 to 1000°C. In this process, kaolin, the mineral component of coal gangue, is dehydroxylated under high-temperature calcination to produce metakaolin, which has high pozzolanic activity.[12,13] Wang et al.[14] explored the influence mechanism of activated coal gangue powder (CGP) on the mechanical performance of cement mortar. The results show that the pozzolanic activity of activated CGP is improved, which positively influences the mechanical performance of cement mortar. Therefore, coal gangue, after activation treatment, can be used as a concrete admixture.[15] Furthermore, Zhou and Chen[16] found that concrete's chloride ion penetration resistance

---

ACI Materials Journal, V. 120, No. 4, July 2023.
MS No. M-2022-131.R6, doi: 10.14359/51738821, received January 19, 2023, and reviewed under Institute publication policies. Pertinent discussion including author's closure, if any, will be published ten months from this journal's date if the discussion is received within four months of the paper's print publication.

performance can be improved by mixing activated CGP. Ju[17] found that the appropriate replacement rate of activated CGP can improve the frost resistance of concrete. Zhao et al.[18] found that activated CGP can improve the sulfate resistance of concrete.

RESEARCH SIGNIFICANCE

Activated CGP as an admixture is mostly used in ordinary concrete. There is little research on how using activated CGP improves the performance of CGC. Based on the research foundation of CGA and CGP in cement-based materials, activated CGP as admixture and coal gangue coarse aggregate are mixed into concrete simultaneously to form a double-admixture CGC. Then, conducting a macro-experiment and using micro-methods simultaneously, the influence mechanism of CGP on CGA is observed and analyzed. Finally, the two-way high-value-added use of coal gangue is realized.

EXPERIMENT AND MATERIALS

Materials

Cement—The cement selected in this test is P·O42.5.

Admixture—The raw coal gangue sampled from the Xuanhua Mine in Zhangjiakou, China, was calcined and ground to produce activated CGP. Table 1 lists the main chemical composition of the CGP and cement; Table 2 lists the physical performance of cement.

Fine aggregate—The medium sand in Zone II has a fineness modulus of 2.71 and a mud content of 1.42%. The sieve analysis curve is shown in Fig. 1(a).

Coarse aggregate—Natural coarse aggregate uses 5 to 20 mm continuous-graded limestone crushed stone; raw coal gangue coarse aggregate is selected from the Xuanhua Mine to obtain coarse aggregate with continuous grading of 5 to 20 mm diameter after crushing, screening, and assembly. The physical properties of coarse aggregate are shown in Table 3. The sieve analysis curve is shown in Fig. 1(b).

Water—Ordinary tap water.

Testing methods

Preparation of activated CGP—The CGP was made of raw coal gangue from the Xuanhua Mine, and a jaw crusher was used to break and sieve the coal gangue. The coal gangue with a particle size of less than 5 mm was placed in a rapid-heating box electric furnace and calcined for 2 hours at 400, 500, 600, and 700°C. Out of the oven, the air cools rapidly to room temperature, then the CGP made at different temperatures was obtained by grinding it to 350 mesh size with a ball mill.

X-ray diffraction analysis—The raw coal gangue, which was calcined at five different temperature points, was tested with an X-ray diffractometer (XRD). The instrument's parameters of operation were 40 kW, 100 mA, and Cu target; the scanning speed was 4 deg/min and the scanning range was 10 to 70 degrees.

Thermogravimetric-differential analysis (TG-DSC)—The thermogravimetric differential test of raw coal gangue, which was ground, was carried out under an argon environment using a thermogravimetric differential analyzer; the temperature curve was from 26 to 1000°C, and the heating rate was 10°C/min.

Cement mortar strength test—Thirty percent of P·O42.5 cement was replaced by the CGP, which was calcined at four different temperature points and room temperature points with a water-cement ratio and lime-sand ratio of 0.5:1:3, and the size of the test specimen was 40 x 40 x 160 mm. Under the condition of temperature 20 ± 1°C and relative humidity $\geq$ 90%, the specimens were demolded after standard curing for 24 hours and then cured in water to different ages. At 3 and 28 days, the specimens' flexural and compressive strength were tested, respectively.

Concrete compressive strength test—The CGP at the optimum activation temperature was used as the admixture of CGC. In this test, the water-binder ratio was 0.5. The additional water consumption is considered as 78% of the saturated water absorption rate of CGA,[19] and two factors, cement replacement rates and coarse aggregate replacement rates, were considered. The replacement rates of CGP were 0, 10, 15, and 20%, and those of CGA were 0, 30, 50, and 100%. The proportion of CGA is shown in Table 4. Based on GB/T 50081-2019[20] requirements, the compressive strength samples were prepared and tested with a universal testing machine. (The range of error is ±1% and the effective measurement range is 2 to 100%.) All the tests were repeated at least three times and the final test results were averaged.

Chloride penetration resistance of CGC—The rapid chloride migration (RCM) method was selected to research the average of CGC's chloride penetration resistance performance. The sample size is a cylinder with a radius of 50 mm and a thickness of 50 mm, cured for 28 days underwater in the standard curing condition. Every test group was repeated three times at least, choosing the average value as the final

Table 1—Chemical composition of coal gangue and cement, %

Chemical composition	SiO_2	Al_2O_3	Fe_2O_3	CaO	MgO	Loss
Cement	20.32	6.14	3.56	62.03	1.71	6.24
Coal gangue	53.65	14.19	7.31	4.61	2.07	13.25

Table 2—Physical performance of cement

Fineness 0.08, %	Specific surface area, m^2/kg	Density, g/cm^3	Standard consistency, %	Setting time, min		Flexural strength, MPa		Compressive strength, MPa	
				Initial	Final	3 days	28 days	3 days	28 days
0.5	355	3.12	25.4	99	158	6.4	93	27.0	53.2

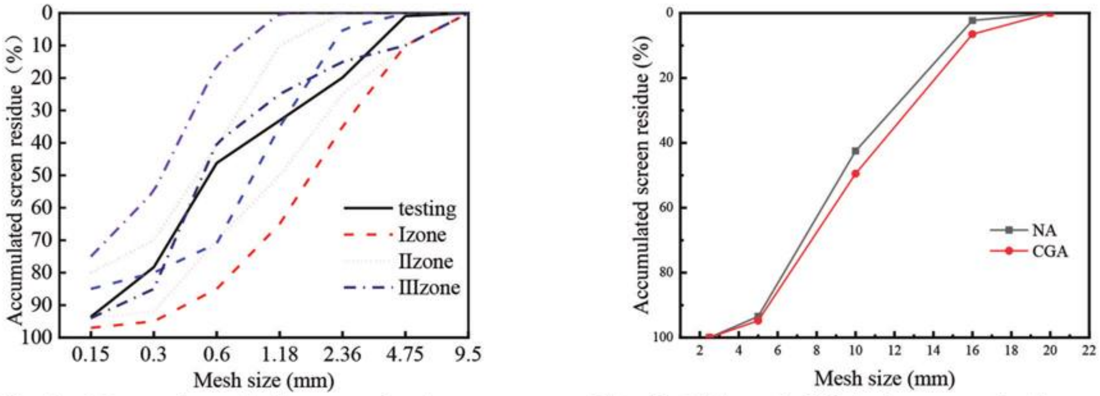

Fig.1a Natural sand sieve analysis curve

Fig.1b NA and CGA sieve analysis curve

Fig. 1—Sieve analysis curve.

Table 3—Performance index of coarse aggregate

Material	Apparent density, kg/m^3	Bulk density, kg/m^3	Water absorption, %	Crushing index, %
Crushed stone	2780	1546	0.5	6.9
Coal gangue	2530	1452	3.7	15.4

Table 4—Mixture proportion design and workability of CGC

Sample No.	CGP replacement rate, %	CGA replacement rate, %	CGP, kg	Cement, kg	Sand, kg	CGA, kg	Crushed stone, kg	Water, kg	Workability, mm
A-0-0	0	0	0	375	642	0	1193	185	88
A-0-30	0	30	0	375	642	357.9	835.1	185	99
A-0-50	0	50	0	375	642	596.5	596.5	185	103
A-0-100	0	100	0	375	642	1193	0	185	115
B-10-0	10	0	37.5	337.5	642	0	1193	185	85
B-10-30	10	30	37.5	337.5	642	357.9	835.1	185	96
B-10-50	10	50	37.5	337.5	642	596.5	596.5	185	99
B-10-100	10	100	37.5	337.5	642	1193	0	185	111
C-15-0	15	0	56.25	318.75	642	0	1193	185	81
C-15-30	15	30	56.25	318.75	642	357.9	835.1	185	91
C-15-50	15	50	56.25	318.75	642	596.5	596.5	185	96
C-10-100	15	100	56.25	318.75	642	1193	0	185	106
D-20-0	20	0	75	300	642	0	1193	185	78
D-20-30	20	30	75	300	642	357.9	835.1	185	87
D-20-50	20	50	75	300	642	596.5	596.5	185	94
D-20-100	20	100	75	300	642	1193	0	185	103

Note: As an example, A-10-30 expresses CGC with 10% CGP and 30% CGA.

chloride diffusion coefficient. A concrete vacuum-saturating machine and an apparatus to determine the RCM coefficient of concrete (voltage accuracy: ±0.1 V; temperature accuracy: ±0.1°C; running time accuracy: <10 seconds) were used in the test.

Specific surface area and micropore analysis—A high-performance specific surface area and micropore analyzer was used to study the specific surface area of concrete with different CGP and CGA replacement rates by the Brunauer-Emmett-Teller (BET) multi-point method. The Barrett-Joyner-Halenda (BJH) method was selected to analyze the pore-size distribution average.

Scanning electron microscopy (SEM)—The morphology of CGC (curing age of 28 days) with different CGP and CGA replacement rates is observed by scanning electron microscopy (SEM). The samples were selected from concrete mixtures containing CGP, which underwent calcination at different temperatures. Before observing the microstructures, the samples need to be sprayed with gold.

RESULTS AND DISCUSSION

Influence of calcination temperature on activity of coal gangue

XRD analysis of coal gangue—Figure 2 shows the XRD spectrum of calcined coal gangue at different temperatures. Through the analysis of its phases, the main phase composition of the raw coal gangue from the Xuanhua Mine are kaolinite, quartz, dolomite, albitite, and microcline. With increasing calcination temperature, the peak value of each phase of samples changes. When the temperature is 400°C, the characteristic peak (*D*-value of approximately 0.289 nm) of dolomite disappears and a new diffraction peak appears. The hematite peak (*D*-value of approximately 0.252 nm) and illite peak (*D*-value of approximately 0.284 nm), which indicate that the characteristic peak (*D*-value of approximately 0.448 nm) of kaolinite is weakened, indicate that the crystal structure that accompanies the hydroxyl of kaolinite begins to break down.[21] When the temperature is 500°C, the characteristic peak of the characterization of kaolinite completely disappears, suggesting that all kaolinite has been transformed into metakaolinite, representing lower crystallinity and higher activity. The enhancement of the characteristic peak of quartz (*D*-value of approximately 0.335 nm) indicates that the transformation of amorphous SiO_2 occurs in coal gangue, resulting in an increase in the relative content of quartz. In addition, due to the existence of hematite, the coal gangue has a yellow-brown appearance (Fig. 3). When the temperature is 600°C, the characteristic peaks of albite (*D*-value of approximately 0.319 nm) and microcline (*D*-value of approximately 0.325 nm) weaken, indicating that albite and microcline begin to decompose at this temperature point. When the temperature is 700°C, the characteristic peaks of hematite, illite, and microcline disappear completely, and the characteristic peak of characteristic quartz weakens. This is because the decomposition of microcline promotes the melting of quartz, resulting in the reduction of the relative content of SiO_2, and the appearance of collapse of coal gangue is black vitreous (Fig. 3).

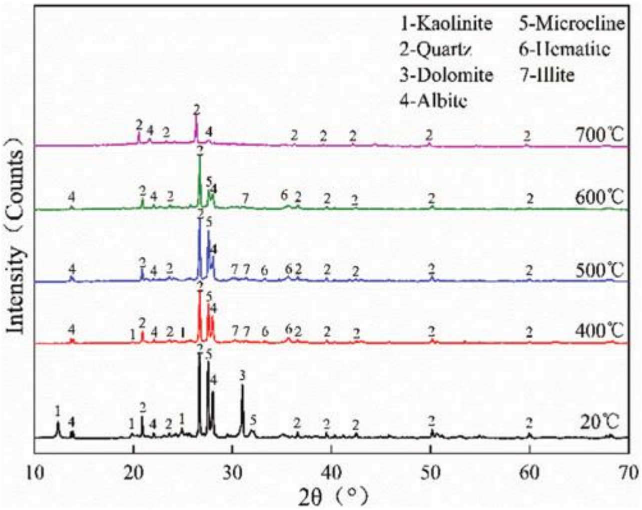

Fig. 2—XRD patterns of coal gangue calcined at different temperatures.

TG-DSC of coal gangue—Figure 4 shows the thermogravimetric differential diagram of raw coal gangue; according to the diagram, the mass loss is 13.32% after heating up to 700°C in an argon environment. The mass loss is mainly caused by the hydroxyl release of kaolinite and a small amount of organic volatilizing. At approximately 500 and 700°C, the coal gangue has a larger mass loss, indicating that strong phase changes take place at these two temperature points. It can be seen from the thermogravimetric differential diagram of raw coal gangue that the difference is not obvious before 400°C. With the formation of new-phase hematite and illite, the endothermic and exothermic peaks are mainly caused by the loss of water adsorption by coal gangue and heat release

Fig. 3—Appearance of coal gangue calcined at different temperatures.

from the combustion of carbonaceous organic matter. As the temperature continues to rise, a strong endothermic peak appears at approximately 488°C, corresponding to the phase-changing peak of kaolinite. Combined with XRD analysis, at this temperature, kaolinite transforms into metakaolinite in a thermodynamically metastable state, and the layered structure is gradually destroyed.[11] When the temperature is 510°C, kaolinite completely transforms into metakaolinite and its layered structure completely transforms into a porous, amorphous structure. When the temperature is 679°C, a strong endothermic peak appears, corresponding to the decomposition reaction of the coal gangue phase. According to XRD analysis, hematite, illite, and microcline decompose at this temperature. When the temperature is approximately 700°C, the characteristic peaks of the three phases disappear and the phases completely decompose, which may be accompanied by the transformation process of metakaolinite into amorphous SiO_2 and Al_2O_3. According to the previous analysis, in the temperature range of 400 to 700°C, the atomic arrangement of the kaolinite layered structure is irregular, showing a thermodynamically metastable state. Coal gangue in this temperature range has pozzolanic activity, and 500°C is the most likely optimal activation temperature point of coal gangue.

Strength analysis of cement mortar—The macro-mechanical properties can reflect the pozzolanic activity of the CGP. Thus, 30% cement is replaced by thermal-activated CGP to prepare mortar, and compressive and flexural strength testing was carried out; Fig. 5 lists the results. Both compressive and flexural strength increase first and then decrease, which reached maximums at 500°C. Based on the XRD and TG-DSC analyses, kaolinite was transformed into metakaolin by dehydroxylation at this temperature. During this process, amorphous SiO_2 and Al_2O_3 were generated; Qiu et al.[22] found that both SiO_2 and Al_2O_3 consume CH in the hydration process and generate calcium silicate hydrate (C-S-H) gel, thus improving the strength of mortar. However, the mechanical properties of all samples showed a descent tendency gradually when the calcination temperature exceeded 500°C. One possible reason is that the decomposition of microcline at this temperature point promotes the melting of quartz and leads to the collapse of coal gangue into the vitreous body. Finally, the pozzolanic activity decreased. In conclusion, the optimal activation temperature of raw coal gangue from the Xuanhua Mine is 500°C.

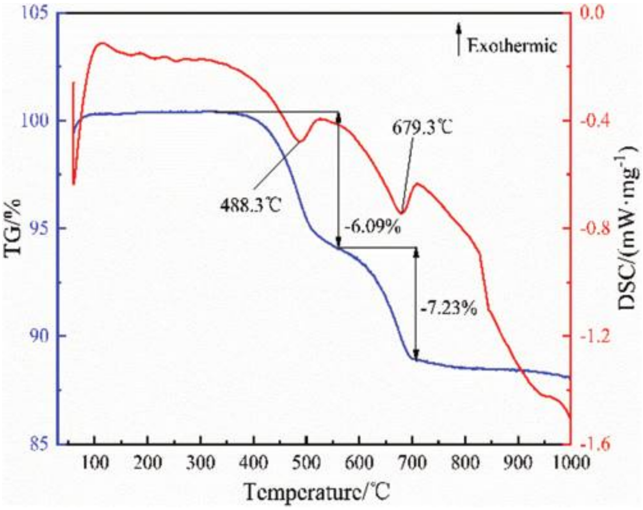

Fig. 4—Thermogravimetric-differential curve of coal gangue.

Influence of CGP on compressive strength of CGC

Compressive strength analysis—Figure 6(a) shows the concrete compressive strength at a cured age of 7 days. Compared with that at a 0% CGP replacement rate, the compressive strength of the specimen with a 10% CGP replacement rate declines by 11.2%, 7.4%, 12.9%, and 4.8%, respectively. At the cured age of 28 days, compared with those with a 0% CGP replacement rate, the compressive strength of specimens with a 10% CGP replacement rate decreased by 3.1%, 2.3%, 6.5%, and –21.1%, respectively. This phenomenon could be explained by the fact that the chemical reaction activity of CGP cement clinker in the early hydration stage could not fully hydrate, leading to the lower early strength of CGP. With the hydration process, the active metakaolinite in CGP consumes CH through secondary hydration. During this process, more C-S-H gel is generated,[23,24] which improves the late strength of CGC. When the cured age is 28 days, with the different CGP and CGA content, the compressive strength of CGC has a different value. When the CGA replacement rate is 0% and mixing 15% CGP compared with no CGP added, the compressive strength of the specimen decreases by 1.4%, and the reduction strength is the least. When CGP content is 20% compared with 0%, the compressive strength of specimens decreases by 14.4%, the highest strength decrease. When the replacement rate of CGP is less than 15%, the compressive strength of concrete decreases slightly, mainly because there are still more clinker minerals in the hydration reaction system after mixing the appropriate amount of CGP and the active metakaolinite in CGP react with CH in the hydration system to form C-S-H gel, resulting in reduced strength loss caused by the reduction of clinker. When the CGP content is more than 15%, the compressive strength drops sharply, mainly because the clinker minerals in the hydration reaction system are reduced after the addition of excessive CGP, and the C-S-H gel generated by the secondary hydration of CGP is not enough to supplement the decrease in the number of the primary hydration products of clinker minerals, so the strength of concrete decreases significantly. When the CGA replacement rate is less than 50%, the more CGP mixed, the lower the compressive strength of CGC; specimen D-20-50 shows a higher compressive strength than D-20-30, indicating that with a 20% replacement rate of CGP, increasing the replacement rate of CGA in an appropriate range can improve the compressive strength. When the CGA replacement rate is 100%, the compressive strength of the specimen with the replacement rate of 10% CGP is the highest, which is 21.1% higher than that of the specimen with 0% CGP. Because the mixing of CGP changes the damage mode of CGC, the compressive strength of concrete with different CGA replacement rates varies.

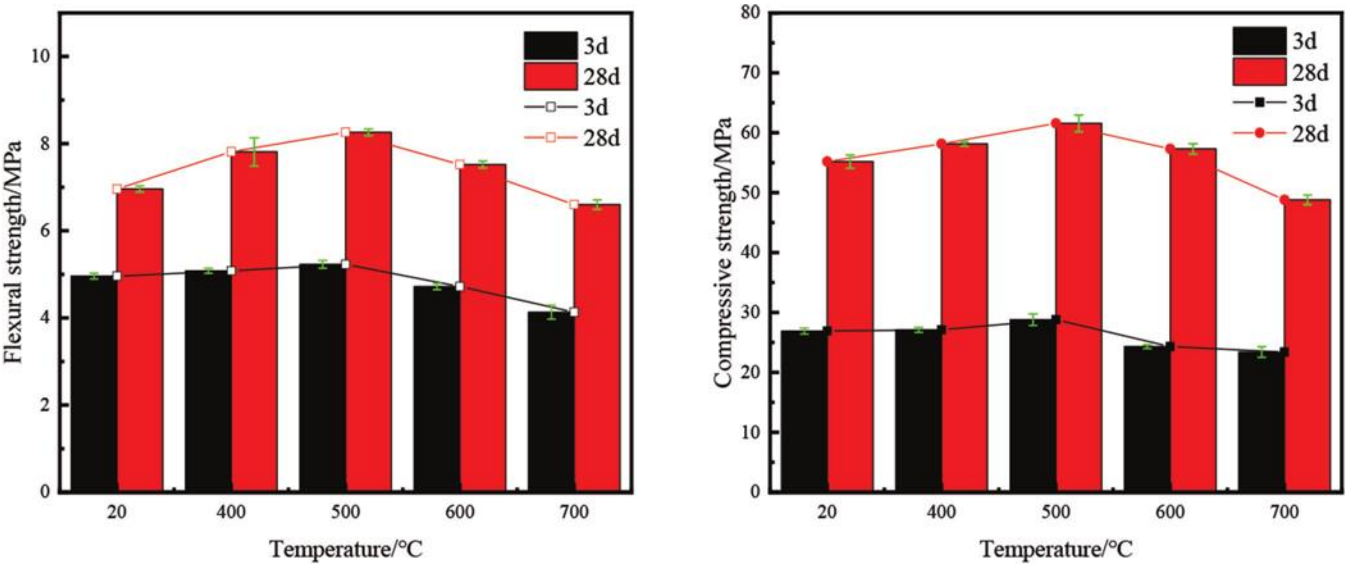

Fig. 5—Strength of cement mortar mixed with CGP at different activation temperatures.

Damage mode analysis of CGC—Figure 7 shows the pressure resistance test phenomenon of CGC at 28 days hydration age; according to the phenomenon from Fig. 7, the damage modes of A-0-0 are mainly manifested as the cracking of cement mortar and the damage of the contact interface between NA and mortar. After mixing 15% CGP, the cracking of C-15-0 is less than that of A-0-0 cement mortar, and the damage of the contact interface between cement mortar and natural coarse aggregate is increased. It indicates that the mixing of CGP reduces the degree of bonding of the interfacial transition zone (ITZ) between cement mortar and NA, leading to a reduction in the compressive strength. Compared with A-0-100, C-15-100 shows more self-fracture damage modes of CGA, indicating that adding CGP improves the degree of bonding of the cement mortar and coarse aggregate ITZ, increasing compressive strength. The damage modes of D-20-30 and D-20-50 are mainly manifested as the damage of the contact interface between NA and cement mortar and the fracture of coal gangue coarse aggregate itself. However, compared with D-20-50, D-20-30 shows more fractures and pores, thus showing lower compressive strength. When the CGP content is 20%, it shows that appropriately increasing the CGA replacement rate had a positive effect on the compressive strength of CGC.

The previously mentioned damage mode can be divided into two types: the ITZ between the cement mortar and NA is damaged, and the failure of the CGA itself. Two reasons can explain this phenomenon. On the one hand, compared with the NA, the CGA is more porous and has a lower strength; on the other hand, the addition of CGP provides more SiO_2 and Al_2O_3, which consume more CH, promote the secondary hydration, and generate more C-S-H gel, which filled the cracks in CGA. Thus, the bonding strength between the aggregate and mortar is enhanced.[25] The changing of the damage mode and compressive strength of the specimens is affected by the changing of the internal pore structure of concrete, which requires further analysis based on the characteristics of the pore structure.

Chloride ion penetration analysis of CGC

Figure 8 shows the D_{RCM} of CGC at 28 days for different CGA replacement rates and CGP content. At the same CGP content, the D_{RCM} gradually increased as the CGA replacement rates increased. It indicates that the CGA decreased the performance of CGC resistance against chloride ion penetration. This phenomenon presents the same tendency as in the study by Ma et al.[26] The reason for this phenomenon is as follows: compared to the NA, the CGA is in a loose and porous state, leading to a lower chloride ion penetration resistance performance.

At the same CGA substitution rates, the D_{RCM} decreases as the content of CGP increases. It indicates that incorporating CGP can significantly improve the performance of CGC resistance against chloride ion penetration. Two reasons lead to these results. On the one hand, the CGP particles are tiny, which fill the microcracks and reduce the pores inside the concrete. Thus, the concrete structure is optimized. On the other hand, the pozzolanic activity of CGP promotes secondary hydration and makes concrete more compact, resulting in improved impermeable concrete ability. In conclusion, the chloride ion permeability of concrete will decrease with the increase of the substitution rate of CGA. It will increase with the improvement of the substitution rate of activated CGP. When the substitution rate of CGA is 100% and the replacement rate of CGP is 20%, the increase is the largest.

Influence of CGP on microporous structure of CGC

Adsorption-desorption isotherm analysis—Figure 9 is the adsorption-desorption isotherm diagram of contained and uncontained CGP concrete at 28 days hydration age when the CGA replacement rate is 0%. It can be seen from Fig. 9(a) that the adsorption-desorption curve of CGC has the phenomenon of a “hysteresis loop” caused by the capillary pores’ condensation.[27] At the low partial pressure point, the adsorption and desorption curves basically coincide, indicating that the micropore morphology of the specimen is closed at one end. There is an obvious inflection

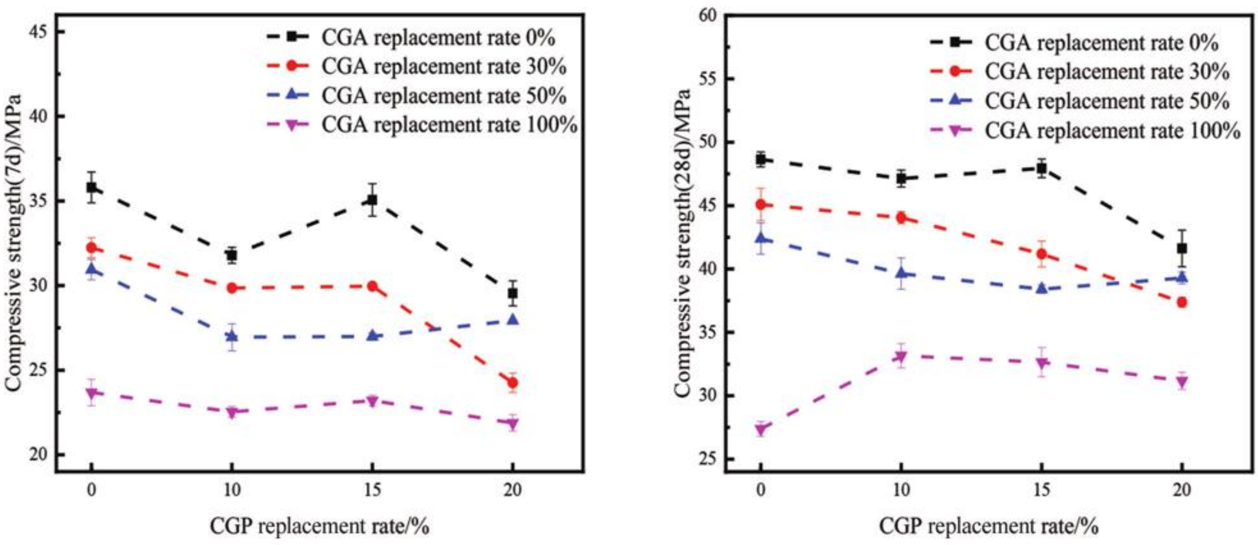

（a）7d hydration age （b）28d hydration age

Fig. 6—Compressive strength of CGC with different CGP content.

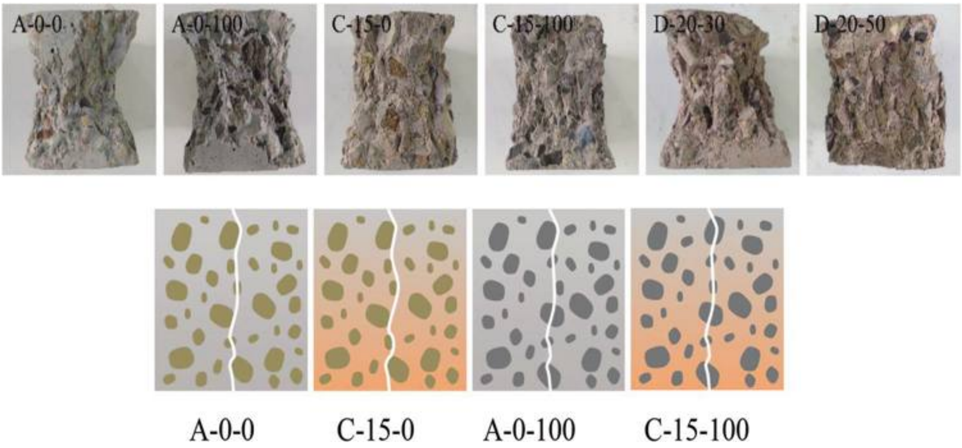

Fig. 7—Experimental phenomena of compressive strength of CGC.

point at the middle pressure point, indicating that there is a connected mesopore in the specimen. The large separation of adsorption and desorption curves at high partial pressure points indicate that there are large connected macropores in the specimen. As can be seen from Fig. 9(b) and (c), this phenomenon indicates that compared to concrete specimens without CGP, the specimens with CGP exhibit an increased adsorption capacity and a larger specific surface area. When the replacement rates of CGP are greater than 15%, the isotherm of contained CGP concrete located on the isotherm curve, which represents uncontained CGP concrete, and the adsorption capacity of the specimen increase, resulting in a larger specific surface area than uncontained CGP concrete. Combined with these changes in compressive strength of CGC, it shows that controlling the replacement rates of CGP within 15% is the first choice to improve the mechanic properties of concrete.

Pore structure analysis—Table 5 shows the pore-size distribution and specific surface area of the specimen; it can be seen from Table 5 that the specific surface area and macropore volume of C-15-0 decreased by 1.3% and 5.4%, respectively, and the micropore volume increased by 4.6% compared with A-0-0. Compared with A-0-100, the specific surface area and macropore volume of C-15-100 decreased by 2.4% and 14.2%, respectively, while the microporous volume increased by 3.3%. Combined with the compressive strength results, the mixing of CGP (15%) reduced the specific surface area and macropore volume of concrete specimens; however, the compressive strength of C-15-0 is reduced by 1.4% compared with A-0-0. This is because the mixing of CGP reduces the gel amount of the hydration system and fewer pores are formed between NA and the cement mortar, which cannot be fully supplemented by the secondary hydration reaction, resulting in the bond strength between the mortar and NA declining. The damage of the interface structure increases and the compressive strength decreases. The compressive strength of C-15-100 is 21.1% higher than that of A-0-100. This is due to coal gangue being a porous material; the C-S-H gel generated by CGP through the secondary hydration reaction fills the pores between the cement mortar and CGA, improves the bond strength between the mortar and CGA, reduces the damage

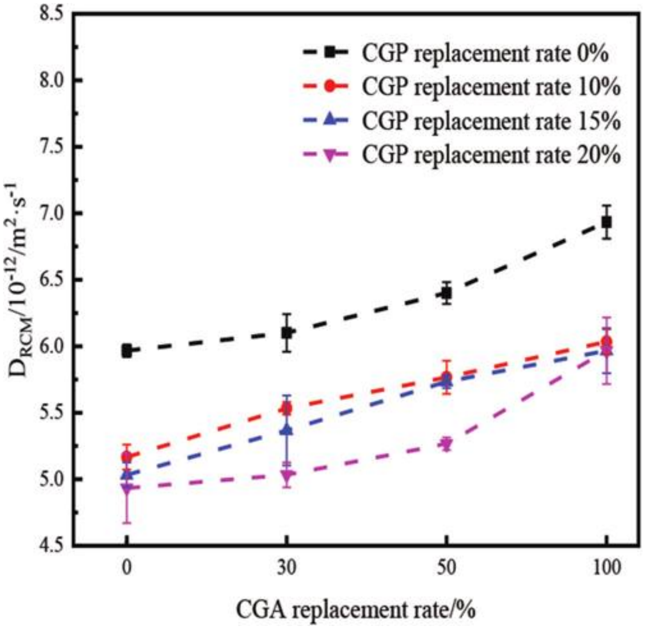

Fig. 8—Chloride diffusion coefficients at different CGA and CGP replacement rates (28 days).

at the ITZ, and increases the compressive strength.[28] As the replacement rates of CGP continue to increase (20%), the volume of micropores decreases, the volume of macropores increases, and the compressive strength of CGC declines. This is mainly due to the dilution effect[29] of CGP, which results in the insufficient quantity of gel generated through the secondary hydration process of C-S-H facilitated by CGP to compensate for the reduction in gel caused by the decrease in cement content. Therefore, the compressive strength of D-20-30 is 9.2% lower than that of C-15-30. In addition, with a 20% CGP replacement rate, the specific surface area and macropore volume of D-20-50 decrease by 8.1% and 0.9%, respectively, compared with D-20-30, while the micropore volume increases by 2.5%, indicating that the replacement rates of CGA are nonlinear with the specific surface area and pore-size distribution of CGC under this replacement rate. The substitution rate of CGA can be appropriately increased to optimize the microporous structure of CGC and then affect the strength development of CGC. Therefore, D-20-50 shows higher compressive strength than D-20-30.

Figure 10 shows the pore volume-pore differential integral distribution curves of the specimen at a 28-day hydration age. It can be seen from Fig. 10 that the peak value of the differential distribution curve of the specimen is stronger at 2 to 4 nm, indicating that there are many pores of 2 to 4 nm in the specimen. The pore volume of 2 to 4 nm in Fig. 10(a) to (d) of CGC specimens accounts for 14.2%, 10.8%, 9.3%, and 11.3% of the total pore volume, respectively, indicating that the pore-size distribution range of specimens is relatively wide. Combined with the analysis results of the pore structure, the total pore volume and macropore volume of A-0-100 increased 1.5% and 14.78%, respectively, compared with A-0-0, and the total pore volume and macropore volume of C-15-100 increased 1.3% and 6.63%, respectively, compared with A-15-0. It shows that increasing the replacement rates of coal gangue coarse aggregate will increase the internal pore fractures of concrete, resulting in a sharp decrease in compressive strength. Compared with A-0-0, the total pore volume and macropore volume of C-15-0 decreased by 23.7% and 5.4%, respectively, and the total pore volume and macropore volume of C-15-100 decreased by 23.9% and 14.2%, respectively, indicating that the addition of 15% CGP can optimize the internal pore fractures of concrete. As a result, the volume of macropores decreases and the volume of micropores and mesopores increases. Wu and Lian[30] pointed out in the literature that reducing the proportion of large pore volume in the total pore volume of concrete can improve the strength of concrete. Combined with the results of compressive strength, the compressive strength of A-0-100 is 43.7% lower than that of A-0-0, and the compressive strength of C-15-100 is 21.1% higher than that of A-0-100. The main reason is that the thermal-activated CGP can promote the early hydration of cement and consume CH; the product of hydration is C-S-H, which can fill the pore fractures at the junction between cement slurry and CGA and improve the bond strength at the interface structure of CGC, thereby greatly improving the compressive strength and the resistance of the chloride permeability.[31]

Analysis of microscopic appearance of CGC—The internal microstructure of a CGC test block is observed by SEM. The test specimens selected were A-0-0, A-0-100, C-15-0, and C-15-100. The test specimens are taken from the central part of the test block and a cube with a side length of approximately 10 mm, and the specimens are vacuum-degassed and then gilded in the vacuum coating equipment for observation.

Compared with Fig. 11(e) and (f), the filling amount of pore fractures in C-15-100 is denser than that in A-0-100, indicating that when the CGA replacement rate is 100%, mixing CGP can also optimize the pore structure in the inner part of CGC. By comparison with Fig. 11(g) and (h), the interface of mortar and coarse aggregate of coal gangue in C-15-100 is denser than that in A-0-100. It can be seen from Fig. 9(h) that many reticular and granular C-S-H gels are wrapped at the interface, while there are obvious fractures in the ITZ of the A-0-100 mortar and CGA. Combined with the pore analysis results, the volume of macropores of A-0-100 increases by 23.9% compared with C-15-100, which also leads to the sharp decrease in the compressive strength of A-0-100. After CGP is mixed, the specific surface area and total pore volume of CGC decrease, the volume of macropores decreases, and the volume of small pores increases. Furthermore, Yi et al.[7] found that the C-S-H generated by the cement secondary hydration not only refined the microstructure of CGC but also promoted chloride binding, which increased the chloride ion permeability of CGC.

As a result, the number of fractures and macropores are reduced and the bond strength between the cementation material and CGA is improved; the mechanical properties of C-15-100 are strengthened, and the compressive strength is increased by 21.1% compared with A-0-100.

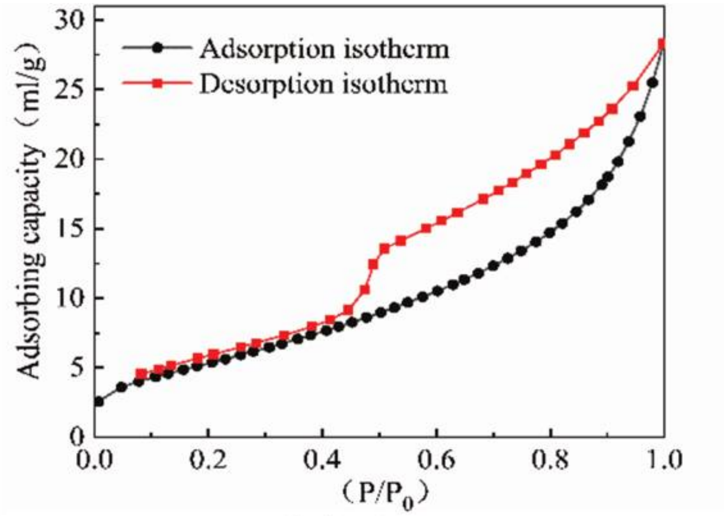

（a）A-0-0

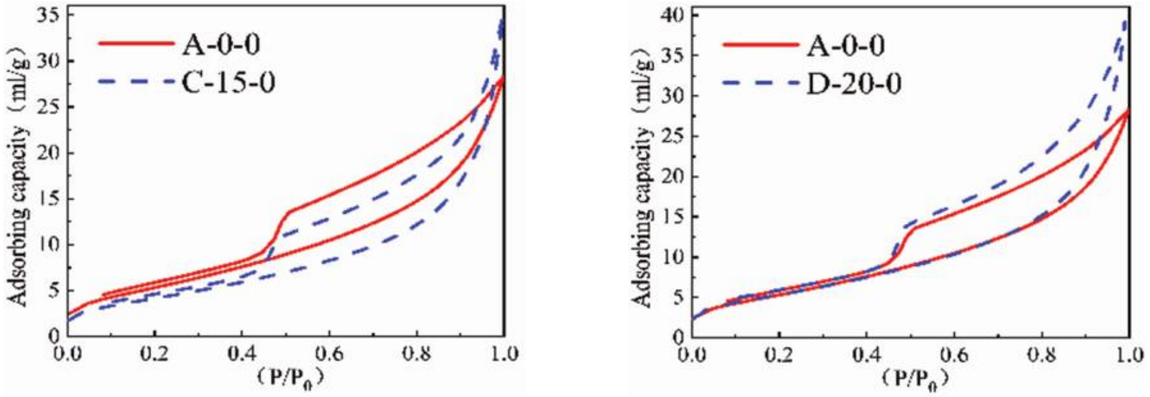

（b）A-0-0 and C-15-0

（c）A-0-0 and D-20-0

Fig. 9—Adsorption-desorption isotherm of CGC.

Table 5—Pore-size distribution and specific surface area of CGC

Sample No.	Cumulative pore volume fraction, %			Total pore volume, mL·g^{-1}	Specific surface area, m^2·g^{-1}
	<2 nm	2 to 50 nm	>50 nm		
A-0-0	15.44	68.92	15.64	0.0518	20.4407
A-0-100	10.46	59.13	30.42	0.0526	14.944
C-15-0	20.00	70.38	9.62	0.0395	20.1831
C-15-100	13.75	70.00	16.25	0.0400	14.5802
D-20-30	12.47	61.18	15.06	0.0425	15.362
D-20-50	14.93	59.95	14.18	0.0402	14.1122

CO_2 calculation and cost analysis

The premise of using coal gangue instead of cement as a cementitious material is that the carbon dioxide emissions of CGP are lower than those of ordinary cement. The carbon dioxide emitted in the stage of calcining clinker accounts for most of the total emissions.[32] The following formula is used to calculate the carbon dioxide emissions for the production of ordinary cement and the carbon dioxide required for the production of CGP; the formula is derived from Zhang et al.'s[33] research

$$BE_1 = C_c \times \frac{44}{56} + C_m \times \frac{44}{40} \qquad (1)$$

where BE_1 is the ordinary cement CO_2 emissions per kg; C_c and C_m are the percentage of CaO and MgO content, respectively; 44/56 is the molecular weight conversion between CO_2 and CaO; and 44/40 is the molecular weight conversion between CO_2 and MgO. According to Eq. (1), the carbon dioxide emissions of cement in this paper can be calculated as 0.48 kg/kg, and the value of coal gangue is 0.06 kg/kg.

On the other hand, the cost plays a role in the production process of concrete. The price of natural gravel is 87.86 yuan/t in Jiangxi, China; however, the price of coal gangue gravel is 65 to 70 yuan/t and the price of ordinary cement is 467.96 yuan/t. In conclusion, compared with the

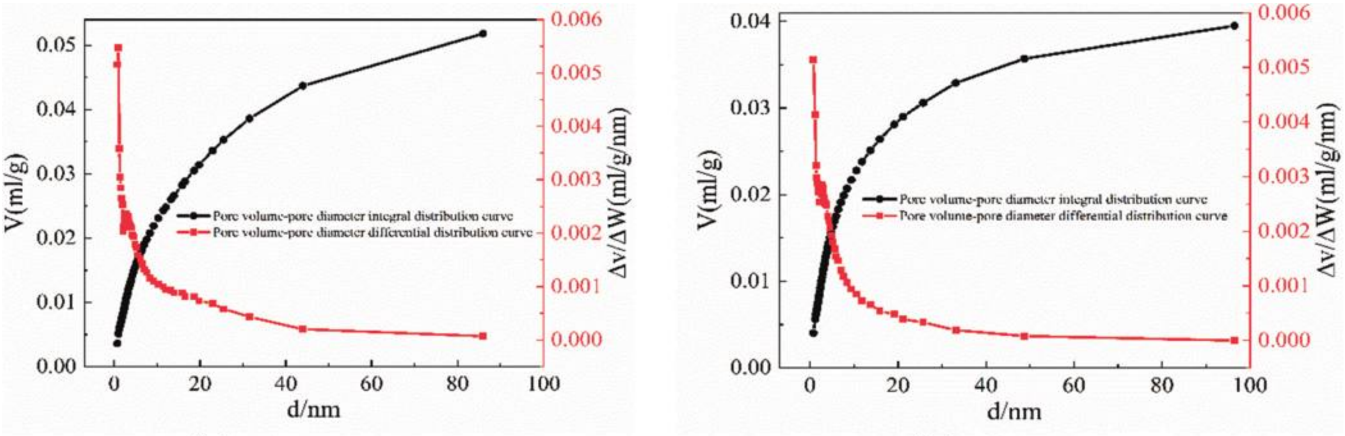

(a) A-0-0 (b) C-15-0

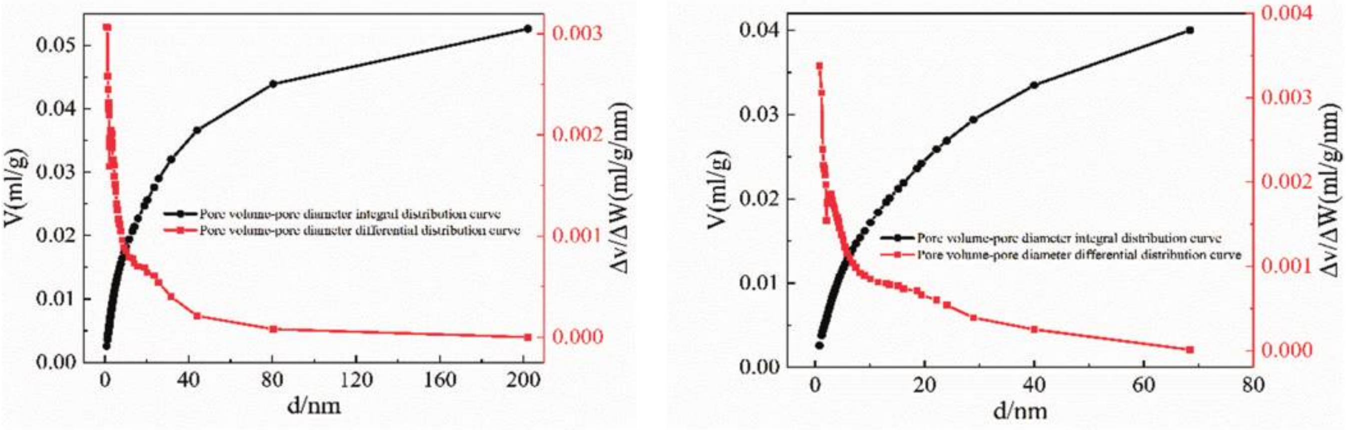

(c) A-0-100 (d) C-15-100

Fig. 10—Pore volume-pore diameter differential and integral distribution curves.

ordinary concrete, the CGC has lower CO_2 emissions and price.

CONCLUSIONS

1. According to the results of X-ray diffraction (XRD), thermogravimetric-differential (TG-DSC) analysis, and cement mortar strength analysis, the raw coal gangue from the Xuanhua Mine in Zhangjiakou, China, belongs to claystones containing kaolinite, illite, and other mineral components, which have the potential value of pozzolanic activity. The optimal activation temperature is 500°C.

2. The compressive strength of coal gangue coarse aggregate concrete (CGC) will decrease as the replacement rate of coal gangue aggregate (CGA) increases. However, with increasing CGA substitution rates, the contribution of coal gangue powder (CGP) to the compressive strength of the specimen gradually increases. This is because CGP consumes the CH and promotes secondary hydration; lots of calcium-silicate-hydrate (C-S-H) gel is generated in this process, which refined the microstructure. Therefore, in the case of total substitution of CGA, the compressive strength of concrete reaches the maximum value when the content of CGP is 10%.

3. The chloride penetration resistance of CGC could be significantly improved by mixing the CGP into CGC. Under the same CGA substitution rate, with the increase of CGP content, the chloride penetration resistance of CGC increases and reaches the maximum when the content is at 20%. Combined with the pore structure analysis, mixing CGP can optimize the pore structure and reduce the amount of macropores. Thus, adding a moderate amount of CGP could increase the chloride penetration resistance of CGC.

AUTHOR BIOS

Jie Yan *works at Hebei Key Laboratory of Diagnosis, Reconstruction, and Anti-Disaster of Civil Engineering, Zhangjiakou, Hebei, China. They attended the College of Civil Engineering, Hebei University of Architecture, Zhangjiakou, Hebei, China.*

Doudou Shan *works at Hebei Key Laboratory of Diagnosis, Reconstruction, and Anti-Disaster of Civil Engineering. They attended the College of Civil Engineering, Hebei University of Architecture.*

Xiaotian Wang *works at Hebei Key Laboratory of Diagnosis, Reconstruction, and Anti-Disaster of Civil Engineering. They attended the College of Civil Engineering, Hebei University of Architecture.*

Yan Luo *works at Hebei Key Laboratory of Diagnosis, Reconstruction, and Anti-Disaster of Civil Engineering. They attended the College of Civil Engineering, Hebei University of Architecture.*

Weisu Weng *works at Hebei Key Laboratory of Diagnosis, Reconstruction, and Anti-Disaster of Civil Engineering. They attended the College of Civil Engineering, Hebei University of Architecture.*

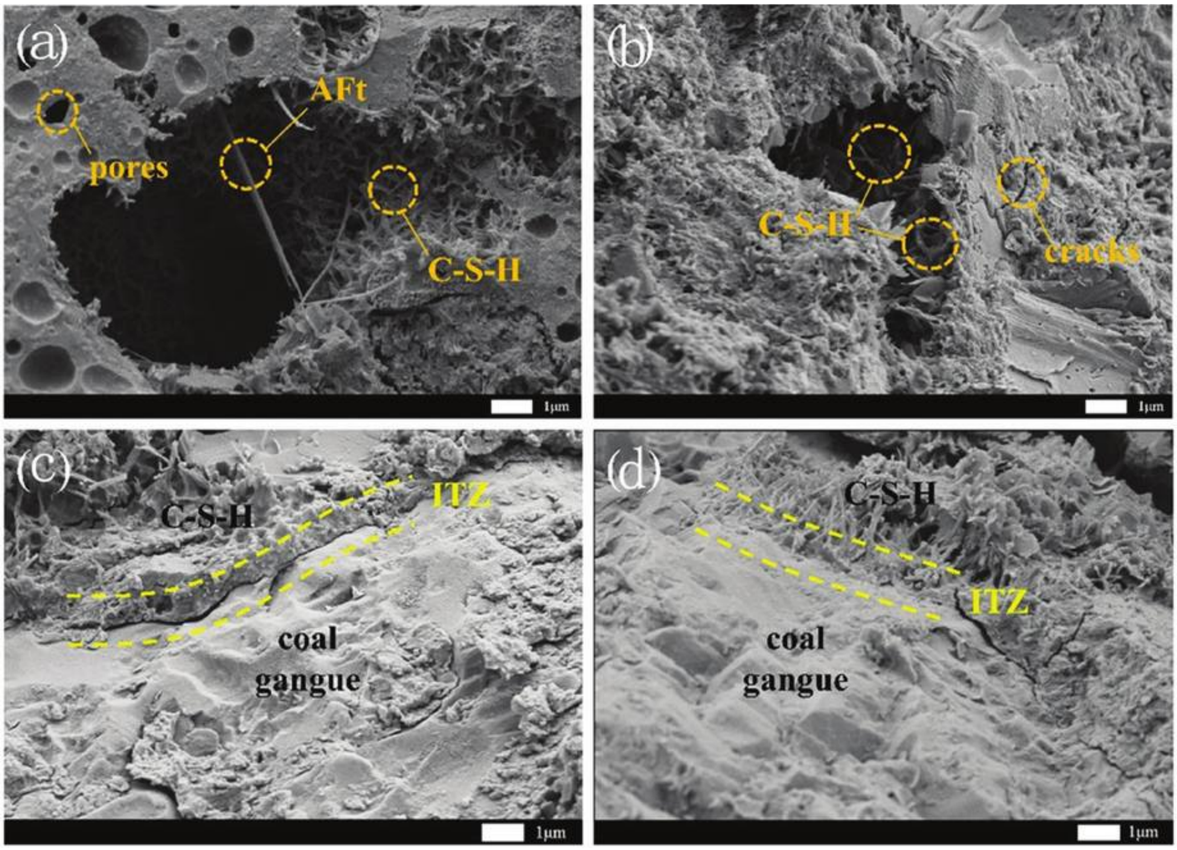

Fig. 11—Microstructure appearance of CGC.

Lijun Wang *works at Hebei Key Laboratory of Diagnosis, Reconstruction, and Anti-Disaster of Civil Engineering. They attended the College of Civil Engineering, Hebei University of Architecture.*

Jun Xie *works at Hebei Key Laboratory of Diagnosis, Reconstruction, and Anti-Disaster of Civil Engineering. They attended the College of Civil Engineering, Hebei University of Architecture.*

Chao Lu *works at Hebei Key Laboratory of Diagnosis, Reconstruction, and Anti-Disaster of Civil Engineering. They attended the College of Civil Engineering, Hebei University of Architecture.*

Zhenquan Lai *works at Hebei Key Laboratory of Diagnosis, Reconstruction, and Anti-Disaster of Civil Engineering. They attended the College of Civil Engineering, Hebei University of Architecture.*

Xutao Lu *works at Hebei Key Laboratory of Diagnosis, Reconstruction, and Anti-Disaster of Civil Engineering. They attended the College of Civil Engineering, Hebei University of Architecture.*

Guobin Xing *works at Hebei Key Laboratory of Diagnosis, Reconstruction, and Anti-Disaster of Civil Engineering. They attended the College of Civil Engineering, Hebei University of Architecture.*

Xinglong Liu *works at Hebei Key Laboratory of Diagnosis, Reconstruction, and Anti-Disaster of Civil Engineering. They attended the College of Civil Engineering, Hebei University of Architecture.*

REFERENCES

1. Huang, G.; Ji, Y.; Li, J.; Hou, Z.; and Dong, Z., "Improving Strength of Calcinated Coal Gangue Geopolymer Mortars via Increasing Calcium Content," *Construction and Building Materials*, V. 166, 2018, pp. 760-768. doi: 10.1016/j.conbuildmat.2018.02.005

2. Chen, X., and Wang, F., "Research Progress of the Synthesis of Sialon Ceramic Materials by Coal Gangue," *Multipurpose Utilization of Mineral Resources*, V. 4, 2017, pp. 16-20.

3. Wang, C.-L.; Ni, W.; Zhang, S.-Q.; Wang, S.; Gai, G.; and Wang, W., "Preparation and Properties of Autoclaved Aerated Concrete Using Coal Gangue and Iron Ore Tailings," *Construction and Building Materials*, V. 104, 2016, pp. 109-115. doi: 10.1016/j.conbuildmat.2015.12.041.

4. Wang, Q.; Li, Z.; Zhang, Y.; Zhang, H.; Zhou, M.; and Fang, Y., "Influence of Coarse Coal Gangue Aggregates on Elastic Modulus and Drying Shrinkage Behaviour of Concrete," *Journal of Building Engineering*, V. 32, 2020, p. 32. doi: 10.1016/j.jobe.2020.101748

5. Zhou, M.; Dou, Y.; Zhang, Y.; Zhang, Y.; and Zhang, B., "Effects of the Variety and Content of Coal Gangue Coarse Aggregate on the Mechanical Properties of Concrete," *Construction and Building Materials*, V. 220, 2019, pp. 386-395. doi: 10.1016/j.conbuildmat.2019.05.176

6. Ma, H.; Yi, C.; and Zhu, H., "Compressive Strength and Durability of coal gangue Aggregate Concrete," *Materials Reports*, V. 32, No. 14, 2018, pp. 2390-2395.

7. Yi, C.; Ma, H.; Zhu, H.; Li, W.; Xin, M.; Liu, Y.; and Guo, Y., "Study on Chloride Binding Capability of Coal Gangue Based Cementitious Materials," *Construction and Building Materials*, V. 167, 2018, pp. 649-656. doi: 10.1016/j.conbuildmat.2018.02.071

8. Qiu, J.; Zhou, Y.; Vatin, N. I.; Guan, X.; Sultanov, S.; and Khemarak, K., "Damage Constitutive Model of Coal Gangue Concrete Under Freeze-Thaw Cycles," *Construction and Building Materials*, V. 264, 2020, p. 264. doi: 10.1016/j.conbuildmat.2020.120720

9. Zhang, J., and Chen, W. L., "Research on Durability of Coal Gangue Aggregate Concrete," *Journal of Beijing University of Technology*, V. 37, 2011, pp. 116-125.

10. Li, Y. J.; Han, J. J.; and Xing, Y., "Research on the Freezing and Thawing Cycle Test of Coal Gangue Aggregate Concrete," *Concrete (London)*, No. 12, 2013, pp. 100-103.

11. Cao, Z.; Cao, Y.; Dong, H.; Zhang, J.; and Sun, C., "Effect of Calcination Condition on the Microstructure and Pozzolanic Activity of Calcined Coal Gangue," *International Journal of Mineral Processing*, V. 146, 2016, pp. 23-28. doi: 10.1016/j.minpro.2015.11.008

12. Jiu, S.; Cheng, S.; Li, H.; and Wang, L., "Reaction Mechanism of Metakaolin Materials Prepared by Calcining Coal Gangue," *Materials Research Express*, V. 8, No. 1, 2021, p. 015508. doi: 10.1088/2053-1591/abd907

13. Liu, Q.; Jin, H.; Zhu, M.; Li, H.; and Wang, M., "Study on Phase Transformation and Aluminum-Silicon Activity of Coal Gangue During Roasting," *Hydrometallurgy of China*, V. 33, 2014, pp. 222-225.

14. Wang, A.; Liu, P.; Mo, L.; Liu, K.; Ma, R.; Guan, Y.; and Sun, D., "Mechanism of Thermal Activation On Granular Coal Gangue And Its Impact On The Performance Of Cement Mortars," *Journal of Building Engineering*, V. 45, 2022, p. 45. doi: 10.1016/j.jobe.2021.103616

15. Zhang, C.; Yang, X.; and Li, Y., "Mechanism and Structural Analysis of the Thermal Activation of Coal-Gangue," *Advanced Materials Research*, V. 356-360, 2011, pp. 1807-1812. doi: 10.4028/www.scientific.net/AMR.356-360.1807

16. Zhou, S., and Chen, Y., "Effect of Mixing Activated Coal Gangue Fine Powder on Chloride Ion Permeability Resistance of Concrete," *China Concrete and Cement Products*, 2007, pp. 4-6.

17. Ju, X., "Effect of Thermal Activated Coal Gangue Mineral Admixtures on Impermeability and Frost Resistance of Concrete," *Bulletin of the Chinese Ceramic Society*, V. 34, No. 9, 2015, pp. 2696-2701.

18. Zhao, X.; Liu, K.; Chen, J.; Qin, Y.; Chen, Y.; Zhao, Y.; Xiao, X.; and Shui, Z., "Long-Term Performance and Hydration Characteristics of Activated Coal Gangue Ecological Concrete," *Bulletin of the Chinese Ceramic Society*, V. 39, 2020, pp. 1757-1764.

19. Zhou, M.; Wang, Q.; and Mou, S., "The Effects on Workability of Concrete Mixture of Spontaneous Combustion Coal Gangue Coarse Aggregate Characteristics," *Non-Metallic Mines*, V. 36, No. 1, 2013, pp. 8-11.

20. GB/T 50081-2019, "Standard of Test Methods of Concrete Physical and Mechanical Properties," Ministry of Housing and Urban-Rural Development of the People's Republic of China, Beijing, China, 2019.

21. Park, J.; Lee, K.-M.; Kwon, S.-O.; Bae, S.-H.; Jung, S.-H.; and Yoo, S.-W., "Diffusion Decay Coefficient for Chloride Ions of Concrete Containing Mineral Admixtures," *Advances in Materials Science and Engineering*, V. 2016, 2016, Article No. 2042918.

22. Qiu, G.; Luo, Z.; Shi, Z.; and Ni, M., "Utilization of Coal Gangue and Copper Tailings as Clay for Cement Clinker Calcinations," *Journal of Wuhan University of Technology-Materials Science Edition*, V. 26, No. 6, 2011, pp. 1205-1210. doi: 10.1007/s11595-011-0391-1

23. Zhou, S.; Dong, J.; Yu, L.; Xu, C.; Jiao, X.; and Wang, M., "Effect of Activated Coal Gangue in North China on the Compressive Strength and Hydration Process of Cement," *Journal of Materials in Civil Engineering*, ASCE, V. 31, No. 4, 2019, p. 04019022. doi: 10.1061/(ASCE)MT.1943-5533.0002643

24. Liu, X.; Wang, P.; and Ding, M., "Hydration Process in Portland Cement Blended with Activated Coal Gangue," *Journal of Zhejiang University-SCIENCE A*, V. 12, No. 7, 2011, pp. 503-510. doi: 10.1631/jzus.A1000479

25. Yu, L.; Xia, J.; Xia, Z.; Chen, M.; Wang, J.; and Zhang, Y., "Study on the Mechanical Behavior and Micro-Mechanism of Concrete with Coal Gangue Fine and Coarse Aggregate," *Construction and Building Materials*, V. 338, 2022, p. 338. doi: 10.1016/j.conbuildmat.2022.127626

26. Ma, H.; Zhu, H.; Wu, C.; Chen, H.; Sun, J.; and Liu, J., "Study on Compressive Strength and Durability of Alkali-Activated Coal Gangue-Slag Concrete and its Mechanism," *Powder Technology*, V. 368, 2020, pp. 112-124. doi: 10.1016/j.powtec.2020.04.054

27. Yuan, C., and Gao, D., "Research of the Pore Structure of Polypropylene Fiber Concrete After High Temperature," *Journal of Huazhong University of Science and Technology*, V. 42, No. 4, 2014, pp. 122-126.

28. Chen, Y.; Zhou, S.; and Zhang, W., "Effect of Coal Gangue with Different Kaolin Content Son Compressive Strength and Pore," *Journal of Wuhan University of Technology-Materials Science Edition*, V. 23, 2008, pp. 12-15.

29. Yang, J.; Su, Y.; He, X.; Tan, H.; Jiang, Y.; Zeng, L.; and Strnadel, B., "Pore Structure Evaluation of Cementing Composites Blended with Coal By-Products: Calcined Coal Gangue and Coal Fly Ash," *Fuel Processing Technology*, V. 181, 2018, pp. 75-90. doi: 10.1016/j.fuproc.2018.09.013

30. Wu, Z. W., and Lian, H. Z., *High Performance Concrete*, China Railway Publishing House, Beijing, China, 1999, 306 pp.

31. Guo, W.; Zhu, J.; Li, D.; Chen, J.; and Yang, N., "Early Hydration of Composite Cement With Thermal Activated Coal Gangue," *Journal of Wuhan University of Technology-Materials Science Edition*, V. 25, 2010, pp. 162-166.

32. Sun, C.; Zhang, J.; Yan, C.; Yin, L.; Wang, X.; and Liu, S., "Hydration Characteristics of Low Carbon Cementitious Materials with Multiple Solid Wastes," *Construction and Building Materials*, V. 322, 2022, p. 322. doi: 10.1016/j.conbuildmat.2022.126366

33. Zhang, J.; Liu, G.; Chen, B.; Song, D.; Qi, J.; Liu, X., "Analysis of CO_2 Emission for the Cement Manufacturing with Alternative Raw Materials: A LCA-based Framework," *Energy Procedia*, V. 61, 2014, pp. 2541-2545. doi: 10.1016/j.egypro.2014.12.041

ACI MATERIALS JOURNAL TECHNICAL PAPER

Title No. 120-M44

Assessment of Abrasion Resistance of Fiber-Reinforced Concrete at Cold Temperatures through Acoustic Emission Analysis

by Omar A. Kamel, Ahmed A. Abouhussien, Assem A. A. Hassan, and Basem H. AbdelAleem

This study investigated using acoustic emission (AE) monitoring to assess the abrasion performance of fiber-reinforced self-consolidating concrete at cold temperatures (–20°C). In addition, the study targeted correlating the abrasion damage to AE data through AE intensity analysis parameters. Seven concrete mixtures were developed with variable water-binder ratios (w/b) *(0.4 and 0.55), fiber types (steel and polypropylene synthetic fibers), fiber lengths (19 and 38 mm), and fiber volumes (0.2 and 1%). Tests on 100 mm cubic samples were conducted at –20 and 25°C, for comparison, according to the rotating-cutter technique in conjunction with AE monitoring. Characteristics of the AE signals such as signal amplitudes, number of hits, and signal strength were collected and underwent* b*-value and intensity analyses, resulting in three subsidiary parameters:* b*-value, severity* (S_r)*, and the historic index* (H*(t)*)*. A clear correlation between abrasion damage progress and AE parameters was noticed. Analyzing AE parameters along with experimental measurements generally revealed a better abrasion resistance for all mixtures when tested at –20°C compared to those at room temperature. The mixtures with steel fibers, lower* w/b *values, shorter fibers, and higher fiber volume showed improved abrasion resistance irrespective of temperature. Noticeably, the mixtures containing longer fibers, higher* w/b *values, or lower fiber dosages experienced a more pronounced enhancement ratio in the abrasion resistance when cooled down to sub-zero temperatures. Two damage classification charts were developed to infer the mass loss percentage and wear depth due to abrasion using intensity analysis parameters:* S_r *and* H*(t)*.

Keywords: abrasion resistance; acoustic emission analysis; *b*-value analysis; cold temperature; fiber-reinforced self-consolidating concrete; intensity analysis; structural health monitoring.

INTRODUCTION

Core infrastructure such as harbors, bridges, and roads inevitably suffer from abrasive erosion. The high wind speed, severe wave hits, and ship/iceberg collisions further aggravate the situation in the Arctic region, which is also characterized by extremely low temperatures. Such circumstances may lead to premature aging and could decrease the predicted service life of concrete structures in these areas. Therefore, the abrasion performance of concrete in such structures should be given great attention.[1]

Abrasion resistance is defined as the materials' ability to resist being rubbed off due to friction. To evaluate the abrasion resistance of concrete, various standard destructive techniques by ASTM International are available. These methods included the rotating-desk test,[2] sandblasting test,[3] and the rotating-cutter test.[4] Selecting the proper standard test method mainly depends on simulating the configuration of forces that the structure is exposed to. Many factors contribute to the abrasion performance of concrete, such as the percentage of coarse aggregate in mixture[5] and the cement paste/aggregate quantity.[6] Hence, engineers can mitigate the abrasion damage by selecting the proper concrete type and constituents. For instance, self-consolidating concrete (SCC), which usually has a low coarse aggregate fraction and high fine materials volume,[7] was found to have a better abrasion resistance over normal vibrated concrete (NVC).[8]

SCC is a highly flowable and non-segregating concrete type. It can flow and enclose reinforcing bars without any vibration effort.[9] Using SCC has gained wide acceptance in Japan since the late 1980s, and its use in North America has grown drastically since 2000, especially in the precast industry.[9] In an attempt to improve the mechanical performance of SCC, previous studies investigated adding steel fibers (SFs) and/or synthetic fibers (SynFs) to the mixture.[10-13] The inclusion of fibers in concrete allows omnidirectional crack control by transferring tensile stresses over crack faces, which adds extra strength to cementitious composites.[14-16] Fibers also increase the ductility of concrete, which in turn makes it harder for parts of the concrete to be pulled off by abrasion action. Ridgley et al.[17] reported that adding polypropylene SynFs to SCC generally enhanced the abrasion performance in terms of percentage of weight loss and wearing depth. Their results also indicated that flexible and short fibers exhibited better abrasion performance on average than rigid and longer ones.

At below-freezing temperatures, the performance of fibrous concretes could be quite different than at room temperature. Previous studies supported that exposure to cold temperatures increased compressive strength, tensile strength, flexural toughness, and impact resistance with more brittle failure for various types of fiber-reinforced concretes.[18-21] Omar et al.[22] investigated the impact and mechanical performance of developed lightweight fiber-reinforced SCC mixtures at varying temperatures (+20, 0, and –20°C). Their study showed an enhancement in the mechanical and impact performance of all mixtures when

---

ACI Materials Journal, V. 120, No. 4, July 2023.

MS No. M-2022-192.R2, doi: 10.14359/51738806, received January 9, 2023, and reviewed under Institute publication policies. Pertinent discussion including author's closure, if any, will be published ten months from this journal's date if the discussion is received within four months of the paper's print publication.

Table 1—Mixture proportions

Mixture No.	Mixture type	Cement, kg/m^3	MK, kg/m^3	FA, kg/m^3	C/F	w/b	C.A., kg/m^3	F.A., kg/m^3	Water content, kg/m^3	V_f, %	HRWRA, kg/m^3
M1	500-0.55w/b	500	—	—	0.7	0.55	606.24	866.1	275	—	—
M2	500-0.4w/b	500	—	—	0.7	0.4	686.54	980.77	200	—	2.13
M3	550-control	275	110	165	0.7	0.4	620.3	886.1	220	—	3.43
M4	550-SynF19	275	110	165	0.7	0.4	620.3	886.1	220	0.2	4.35
M5	550-SynF38	275	110	165	0.7	0.4	620.3	886.1	220	0.2	4.69
M6	550-1%SynF38	275	110	165	0.7	0.4	620.3	886.1	220	1	5.8
M7	550-SF35	275	110	165	0.7	0.4	620.3	886.1	220	0.2	4.6

Note: Regarding mixtures designations, 500-0.55 w/b means concrete mixture with binder content of 500 kg/m^3 and 0.55 w/b; 550-SynF38 means concrete mixture with binder content of 550 kg/m^3 and reinforced with synthetic fibers 38 mm in length; MK is metakaolin; FA is fly ash; C/F is coarse-to-fine aggregates ratio; C.A. is coarse aggregate; F.A. is fine aggregate; HRWRA is high-range water-reducing admixture.

decreasing the temperature. They also found that the inclusion of fibers in the mixture compensated for the brittle behavior of concrete that resulted from decreasing the temperature. They attributed this behavior to the fact that water in pores freezes at subzero temperatures, leading to an increase in strength because the capillary pores will be filled with a solid substance that has an extra load capacity. They also attributed the improved strength of fiber-reinforced SCC to the increased bond between the fibers and the hardened cementitious matrix due to shrinkage of concrete at low temperatures.

Nondestructive techniques (NDT) such as visual inspection, ultrasonic waves, and eddy-current methods are of high importance for the ongoing condition assessment of concrete structures, especially in harsh environments. Meanwhile, for hard-to-reach areas and continuous monitoring cases, acoustic emission (AE) monitoring was proven to be a more convenient candidate, taking advantage over other traditional forms of NDT.[23] AE is a phenomenon that occurs in a solid material under stress when it is cracked or damaged. This event emits strain energy waves that can be collected by attached AE sensors. The sensors convert the picked-up waves into electrical signals and then feed them into a data acquisition system for recording and processing to detect and quantify the damage.[24,25] AE has been successfully employed in many concrete-related studies—for instance, to classify the fracture process of SF-reinforced concrete[26]; monitor alkali-silica reaction expansion damage[27]; evaluate the performance of a simple-span prestressed concrete bridge during a proof test[28]; assess abrasion damage of SCC containing SynFs or rubberized materials under room temperature[17,29]; and to identify initial yielding and the failure onset of bonded post-tensioned concrete elements.[30]

Preliminary studies were performed by Ridgley et al.[17,29] to assess the abrasion damage of different concrete types by means of AE analysis. The outcomes of these studies demonstrated the capability of AE parameters to state the extent of abrasion damage in terms of both mass loss and wear depth when samples were tested at room temperature. To date, there are no studies in the literature that used AE monitoring to assess the abrasion performance of concrete under sub-zero temperatures. It is anticipated that the changes in the microstructure of concrete as a result of exposure to sub-zero temperatures could lead to an impact on the AE wave propagation and spread following the behavior of ultrasonic waves.[31] Consequently, further investigations are warranted to examine this effect and confirm the validity of the AE analysis in evaluating the abrasion resistance of concrete at cold temperatures. This study examined the use of AE continuous monitoring as a potential NDT technique to assess the cold-temperature abrasion performance of fiber-reinforced concrete containing various types, lengths, and dosages of fibers. The study also aimed to provide a method to roughly infer the abrasion mass loss and wearing depth using AE intensity analysis parameters.

RESEARCH SIGNIFICANCE

Concrete in Arctic regions is subjected to various abrasive forces under sub-freezing temperatures. To ensure the long-term integrity of these structures, investigating the ongoing abrasion performance is a high priority. Physical inspection of structures in Arctic regions can be very difficult and expensive due to the challenge of reaching specific areas. The AE technique is considered a great solution to overcome this challenge. However, the information regarding the ability of AE in monitoring the abrasion damage in concrete at sub-freezing temperatures is limited. Especially, cold temperatures may have some effects on the AE wave propagation and spread, which need to be investigated and considered when analyzing AE parameters. In addition, cold temperatures may change the stiffness of SynFs in the mixture, which can also affect the AE wave attenuation. This study attempts to cover this knowledge gap by providing comprehensive experimental work and analysis regarding the use of AE in monitoring the abrasion damage of concrete at cold temperatures. The results of this study will potentially contribute to enriching the validity of using AE monitoring as an NDT tool for structural health monitoring (SHM) applications of concrete structures in Arctic regions.

EXPERIMENTAL INVESTIGATION

Materials and mixture design

A total of seven mixtures were prepared and tested. The full details of all mixture proportions tested in this study are shown in Table 1. Mixtures include two SCC mixtures with 500 kg/m^3 binder (cement) content (M1 and M2) but

Table 2—Physical and mechanical properties of fibers

Fiber type	Material	Length, mm	Diameter, mm	Specific gravity	Tensile strength, MPa	Fiber shape
SF-35	Steel	35	0.55	7.85	1150	Hooked end
SynF-19	Polypropylene	19	0.66	0.91	300	Straight
SynF-38	Polypropylene	38	0.64	0.91	515	Straight

Table 3—Average values of L-box ratio, T_{50}, V-funnel time, compressive strength, and wear depth of all samples at room and cold temperatures

Mixture No.	Mixture type	Testing temperature	L-box (H_2/H_1)	T_{50}, sec	V-funnel time, sec	Compressive strength, MPa	Wear depth, mm	Rate of mass loss, g/min	Weight loss/ compressive strength, g/MPa
M1	500-0.55w/b	Room	0.75	3.8	15	61.63	1.21	1.63	0.16
		Cold				76.55	1.02	1.27	0.10
M2	500-0.4w/b	Room	0.89	2.1	8	66.54	1.04	1.41	0.13
		Cold				79.74	0.98	1.23	0.09
M3	550-control	Room	0.92	2.0	7.2	74.56	0.82	1.29	0.10
		Cold				89.73	0.72	1.17	0.08
M4	550-SynF19	Room	0.88	2.3	8.5	78.85	0.57	0.96	0.07
		Cold				90.97	0.46	0.89	0.06
M5	550-SynF38	Room	0.82	2.6	11.4	76.26	0.62	1.12	0.09
		Cold				88.11	0.54	0.97	0.07
M6	550-1%SynF38	Room	—	—	—	51.92	0.52	1.08	0.12
		Cold				63.85	0.46	0.88	0.08
M7	550-SF35	Room	0.79	2.5	10.9	78.96	0.46	0.81	0.06
		Cold				89.74	0.40	0.69	0.05

different water-binder ratios (*w*/*b*). The behavior of AE waves is related to the properties of the transfer medium. Upon this, Mixtures M1 and M2 were implemented to check the effect of turning a high amount of water (Mixture M1 had a *w*/*b* of 0.55, compared to Mixture M2 with a *w*/*b* of 0.4) into ice on the propagation of AE waves at –20°C and to evaluate AE's ability to detect the change in abrasion performance. In addition, five mixtures were made with 550 kg/m^3 binder content. The five mixtures are as follows: one SCC mixture without fibers (control) (M3); two SCC mixtures with 0.2% polypropylene SynFs (19 and 38 mm lengths); one normal vibrated mixture with 1% polypropylene SynFs (38 mm length); and one SCC mixture with 0.2% SFs (35 mm length). The geometrical and mechanical characteristics of these fibers are described in Table 2. Mixtures M2 to M5 were adopted from a previous study performed by the authors.[17] Meanwhile, various trial mixtures were performed to develop Mixtures M1, M6, and M7. The fresh properties of the mixtures were evaluated by conducting V-funnel, L-box, and T_{50} tests, and the results are summarized in Table 3. The SFs and SynFs included in this study are the most commercially common in the market and were implemented to evaluate the change in the AE parameters due to changing fiber type. The volume of fibers (V_f) was set as 0.2% for all mixtures, except for mixture M6, where V_f was taken as 1%. In SCC mixtures, 0.2% was found to be the maximum possible dosage of fibers that satisfied the requirements of fresh properties for SCC, while the 1% fiber in Mixture M6 was the maximum percentage of fibers that ensured a homogeneous mixture with no fiber balling. Mixtures M5 with 38 mm long polypropylene SynFs and M7 with 35 mm long SFs have the same fiber content of 0.2% and almost the same fiber length. Comparing the parameters of the AE waves emitted in both mixtures could address the effect of fiber material on the AE wave characteristics. Mixture M6 was included to study the effect of increasing fiber content on the behavior of the AE parameters and to assess the AE monitoring ability to detect the variation in abrasion performance. Besides, the high dose of polypropylene SynFs is anticipated to have some attenuation effect on signal amplitudes because the fiber's material (polypropylene) has some acoustic absorption properties.

All tested mixtures contained type general-use (GU) cement, which was in compliance with ASTM Type I[32] and had a specific gravity of 3.15. Two supplementary cementitious materials (SCMs): fly ash (FA) and metakaolin (MK), were used in five mixtures. These SCMs had a specific gravity of 2.5 and 2.27, respectively. Both coarse aggregate (C.A.) and fine aggregate (F.A.) used in this investigation had a specific gravity of 2.6 and water absorption of 1%. The coarse-to-fine aggregate ratio was taken as 0.7 in all mixtures to achieve acceptable fresh properties of the SCC mixtures. The *w*/*b* was kept constant at 0.4 in all mixtures, except for one mixture (M2), where a *w*/*b* of 0.55 was used to study the effect of increasing water content (that will turn into ice after freezing) on the abrasion performance and the characteristics

Fig. 1—AE and rotating-cutter abrasion test setup.

of the emitted AE waves at –20°C. To obtain successful SCC mixtures (in terms of fresh properties), a high-range water-reducing admixture (HRWRA) was added to all SCC mixtures to achieve the desired slump flow of 700 ± 50 mm, as per ASTM C1611.[33] The HRWRA used was similar to that described in ASTM Type F,[34] and had a specific gravity of 1.2 and a pH level of 9.5.

Test setup

For each mixture, six cylinders (100 mm height and 200 mm diameter) and four prisms (100 mm square cross section and 400 mm length) were cast to test the compressive strength and abrasion resistance, respectively. All specimens were cured in a moisture curing room at approximately 25°C for 28 days. When samples reached 28 days of maturity, the prisms were cut into 100 mm cubes (to obtain six cubes from each mixture) for abrasion testing. A group of three cylinders and three cubes from each mixture was kept at ambient room temperature, and another group was kept in a freezer at –20°C for at least 48 hours before testing to reach a steady-state temperature before testing.[1] The compressive strength was determined for each mixture by testing three cylinders at both room temperature and –20°C according to ASTM C39.[35] For the abrasion test, the rotating-cutter standard ASTM C944 method[4] was implemented on three faces (one from each cubic specimen). This ASTM standard abrasion test uses a drill press with a rotating chuck that carries 10 kg applied directly on the chosen face of cubic samples.[4]

Table 4—AE system details

AE hardware setup	
Threshold	40 dB$_{AE}$
Sample rate	1 MSPS
Pre-trigger	256 µs
Length	1 k point
Preamp gain	40 dB
Preamp voltage	28
Analog filter	1 to 50 kHz
Digital filter	100 to 400 kHz
Peak definition time	200 µs
Hit definition time	800 µs
Hit lockout time	1000 µs
Maximum duration	1000 µs

The used abrasion test setup is shown in Fig. 1. In this study, each face was tested for six intervals (1 minute each) and the weight loss was measured after each interval. Besides, the wear depth due to abrasion was measured for each face at the end of the test (after 6 minutes) using electronic calipers having a sensitivity of 0.01 mm.

In this study, piezoelectric AE sensors with an integral preamplifier were used.[36] During the abrasion tests, one piezoelectric sensor was attached to each cube specimen using a two-part epoxy adhesive. The AE system monitored and recorded the signals being emitted during the abrasion testing (refer to Fig. 1 for AE system setup). These sensors have high sensitivity and low resonant frequency, making them more convenient for multiple applications, including metals, fiber-reinforced polymers, and concrete structures.[37] The sensors attached to the specimens were connected to a cable and then to a data acquisition system.

AE data filtering

AE data acquisition software was used to record the AE data and control the data acquisition system during the tests. An amplitude threshold of 40 dB was set to record different AE signal parameters emitted during the abrasion testing period. A full list of the AE parameters determined in the system can be seen in Table 4. The pre-testing analog and digital filter ranges shown in Table 4 were selected based on a preliminary study completed by the authors to evaluate the abrasion damage in concrete using AE analysis.[17,29] The AE data acquisition setup shown in Table 4 has also been implemented in other previous studies conducted by the authors and allowed the detection of various damage mechanisms in concrete.[37,38] The collected AE parameters included signal amplitude, signal strength, duration, absolute energy, number of hits, rise time, average frequency, and peak frequency. A full description of these parameters is discussed in ASTM E1316.[39]

AE data analysis

b-*value analysis*—The signal amplitudes and number of hits of AE signals were collected, filtered, and underwent a *b*-value analysis to evaluate abrasion damage progress for all samples. The *b*-value is based on seismic equations in the first place and was effectively used in many studies to indicate the changes in the frequency level of the AE waves to assess several damage mechanisms in concrete.[40-43] The *b*-value was calculated throughout the abrasion tests for all specimens according to Eq. (1)

$$\log N_A = a - b \log A \quad (1)$$

where N_A is the number of hits prior to the specific time having amplitudes larger than A; A is the signal amplitude of the specific hit at the specific time (dB); a is an empirically derived constant; and b is the *b*-value.[41-44]

The constant a was determined for each specimen by plotting $\log A$ against $\log N_A$, and the average value of the $\log N_A$ axis intercept was taken as the value of a.

Intensity analysis—In addition to the *b*-value analysis, an intensity analysis was performed on the signal strength of the collected AE signals to calculate more parameters that could be correlated to the damage and to study the effects of varying temperatures, *w*/*b*, and fiber type, length, and dosage on the AE data characteristics variation. The intensity analysis included calculating two additional AE parameters: the historic index ($H(t)$) and severity (S_r). These two parameters are very sensitive to the progress of damage, making them convenient for the quantifiable assessment of the different damage mechanisms of concrete in several different studies.[36,43-46] The $H(t)$ could measure any sudden peaks or troughs in the cumulative signal strength (CSS) versus time and was calculated using Eq. (2)

$$H(t) = \frac{N}{N-K} \frac{\sum_{i=K+1}^{N} S_{oi}}{\sum_{i=1}^{N} S_{oi}} \quad (2)$$

where N is the cumulative number of hits until time (t); and S_{oi} is the signal strength of the i-th event. On the other hand, the severity (S_r) was calculated according to Eq. (3)

$$S_r = \sum_{i=1}^{J} \frac{S_{oi}}{J} \quad (3)$$

The S_r value measures any changes in the recorded signal strengths, hence highlighting any severe damage or excessive cracking damage. The S_r value was based on the average signal strength of the J number of hits. The constants (K and J) in Eq. (2) and (3) used in this study were determined based on previous studies concerning AE analysis in concrete.[44-47]

Constant K used in Eq. (2) may affect the magnitude of $H(t)$ and subsequently highlight the damage progression in terms of capturing any pronounced AE activity. In this analysis, K was calculated as follows

a) $K = 0$: if $N \leq 50$; b) $K = N - 30$: if $51 \leq N \leq 200$;
c) $K = 0.85\ N$: if $201 \leq N \leq 500$; and d) $K = N - 75$: if $N \geq 501$

The previously mentioned ranges of K are dependent on the type of the material under testing[43-45] and were adapted from the first standard AE intensity analysis made by Fowler et al.[46]

The values of J have a similar effect on the S_r that K has on $H(t)$. A range of values of J of 25 to 75 has been studied to calculate S_r, which was also followed in previous studies.[27,45,47] In this study, J was set to an average constant value of 50 based on an analysis performed in preliminary studies conducted by the authors.[17,29]

EXPERIMENTAL RESULTS AND DISCUSSION

The experimental measurements regarding abrasion weight loss and the associated AE parameters collected during the abrasion tests are analyzed and discussed in further detail in the following sections to assess the abrasion performance and reliability of AE analysis. It is worth noting that the values of abrasion weight loss measured at both room and cold temperatures were found to be close to another similar study that adopted the same abrasion test.[17] The implications of the studied AE parameters are as follows: the cumulative number of hits indicates the number of cracks induced in concrete, CSS implies both the number and width of cracks induced in concrete, the intensity analysis parameters (S_r and $H(t)$) are sensitive to damage and cracks progression, and the *b*-value implies the change in the frequency of the AE events (cracks) emitted in concrete, hence addressing damage progression.

Validity of built-in and post-processing filters to eliminate noise data

A smooth-roller abrasion test was performed on sample 1 from Mixture 550-SynF38 (M5) at 25°C while being monitored with an AE sensor, as shown in Fig. 2. The smooth rollers were adopted to simulate the test conditions and eliminate abrasion action to check the validity of the filter's ranges adopted in this study. The sample's weight loss for sample 1 from Mixture M5 was measured after each 1-minute interval at both the rotating-cutter and smooth-roller abrasion tests (as shown in Table 5). Figure 3 shows two samples "a" and "b" of Mixture M5 after 6 minutes of abrasion testing under the rotating-cutter and the smooth-roller abrasion test, respectively. The figure shows the significant abrasion damage due to the rotating-cutter effect on sample "a". Meanwhile, sample "b" has barely been affected by any abrasion damage due to the smooth-roller abrasion test. The associated AE parameters emitted at both tests were collected and analyzed, as shown in Table 6. As can be noticed in Table 6, the abrasion damage induced under the smooth-roller test was negligible compared to the damage induced under the effect of the rotating-cutter test. For instance, after 6 minutes of abrasion, the sample experienced 0.0031% weight loss under the smooth-roller test compared to 0.29% under the rotating-cutter test. The AE parameters collected by the AE monitoring system experienced the same pattern. For example, the signal amplitude for the hits emitted under the smooth-roller test was approximately 43 dB, barely exceeding the amplitude threshold in the adopted filters (40 dB). Besides, under the smooth-roller abrasion test, the collected total number of hits was 24 compared to 336 in the case of the rotating-cutter abrasion test. Moreover, the CSS recorded by the end of the test was 0.063 mV.s in the case of the smooth-roller test compared to 1.39 mV.s in the case of the rotating-cutter test. These results manifest the validity of the adopted filter range to eliminate most of the AE noise data induced throughout the abrasion test.

Table 5—Percentage of weight loss after testing sample 2 of mixture 550-SynF38 (M5) at 25°C under smooth-roller and rotating-cutter test

	Average weight loss, %					
Test type	1 min	2 min	3 min	4 min	5 min	6 min
Smooth-roller test	0.0	0.001	0.0018	0.002	0.0024	0.0031
Rotating-cutter test	0.05	0.12	0.17	0.22	0.26	0.29

Table 6—Average percentage of weight after testing sample 2 of mixture 550-SynF38 at 25°C under smooth-roller and rotating-cutter test

	Average signal amplitude, dB		Number of hits		CSS × 10^{12}, mV.s		$H(t)$		S_r, mV.s	
Test type	1 min	6 min	1 min	6 min	1 min	6 min	1 min	6 min	1 min	6 min
Smooth-roller test	42	44	8	24	0.014	0.063	0.11	0.21	0.11	0.24
Rotating-cutter test	84	81	68	336	0.18	1.39	1.13	1.23	2.06	3.27

Fig. 2—Verification abrasion test setup using smooth roller.

Correlation between abrasion damage and AE parameters at cold temperatures

After checking the validity of the adopted filter ranges to eliminate most of the noise data, any AE hit and its signal strength (energy) recorded by the sensors should be related to a crack or damage induced inside the testing sample. Hence, the cumulative number of hits or CSS should imply the damage severity in the tested samples. It has been concluded in a previous study performed by the authors that AE parameters can be correlated to abrasion damage of fiber-reinforced concrete at room temperature.[17,29]

Figures 4(a) and (b) show the percentage of weight loss throughout the 6-minute rotating-cutter abrasion tests at 25 and –20°C, respectively. The AE parameters emitted throughout the test were collected and analyzed to find a pattern that correlates abrasion damage to the corresponding emitted AE signals. Sample S2 (SCC-500-0.55*w*/*b* mixture) is presented in Fig. 5 as an example of all other tested mixtures. Figure 5 shows the changes in the number of hits, CSS, *b*-value, $H(t)$, and S_r versus time of the selected sample (S2) tested at –20°C. The change in the percentage of weight loss due to abrasion versus time was also displayed on each graph for comparison. The sections with smaller slopes or that are flat in the graphs of Fig. 5(a) and (b) represent the time between tests when the abrasion was stopped and resumed after each minute to measure the weight loss following each 1-minute interval. The graph shows that the abrasion damage follows a semi-linear trend in the average percentage of weight loss versus time in contrast to the variations in some of the studied AE parameters.

Figure 5(a) (for the selected S2 sample tested at –20°C) shows that the cumulative number of hits increased over time throughout the test period. For this sample, the number of hits after 1 minute was 68 and increased to reach 376 after 6 minutes. This AE activity coincided with an increase in the percentage of weight loss from 0.09% to reach 0.37% during the same period. CSS followed a similar trend to that of the number of hits versus time, as seen in Fig. 5(b). Specifically, CSS values linearly increased from 161 to 1311 mV.s as the abrasion damage increased from 0.09 to 0.37%. In contrast, the *b*-value curve fluctuated over the test and followed an overall descending trend as the abrasion weight loss increased. For instance, the *b*-value decreased from 1.8 to 1.0 in accordance with an increase in the weight loss for the same sample from 0.09 to 0.37%, as seen in Fig. 5(c). It is worth noting that the locations of the higher fluctuations in the *b*-value chart (Fig. 5(c)) corresponded to the times that have higher AE activity (linear increase in the number of hits and CSS) and greater abrasion damage.

Similarly, the $H(t)$ magnitudes experienced slightly sudden peaks and drops throughout the test while constantly

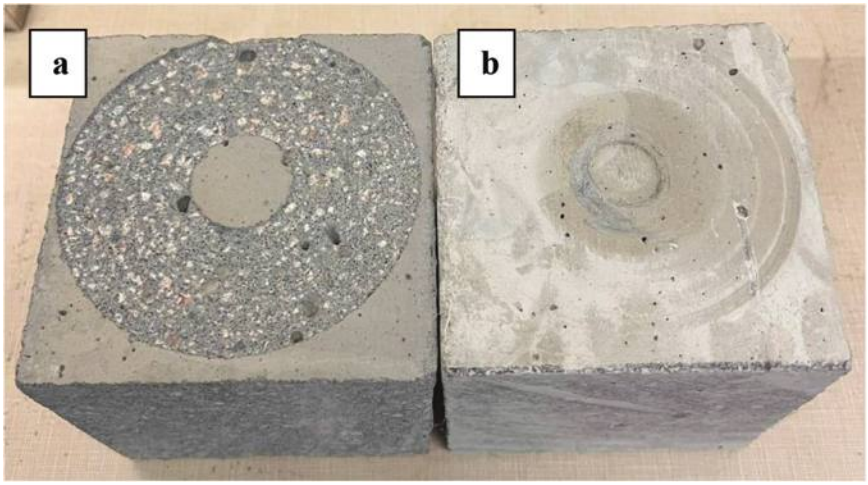

Fig. 3—Mixture M5 samples after 6 minutes of testing under: (a) rotating-cutter abrasion test; and (b) smooth-roller abrasion test.

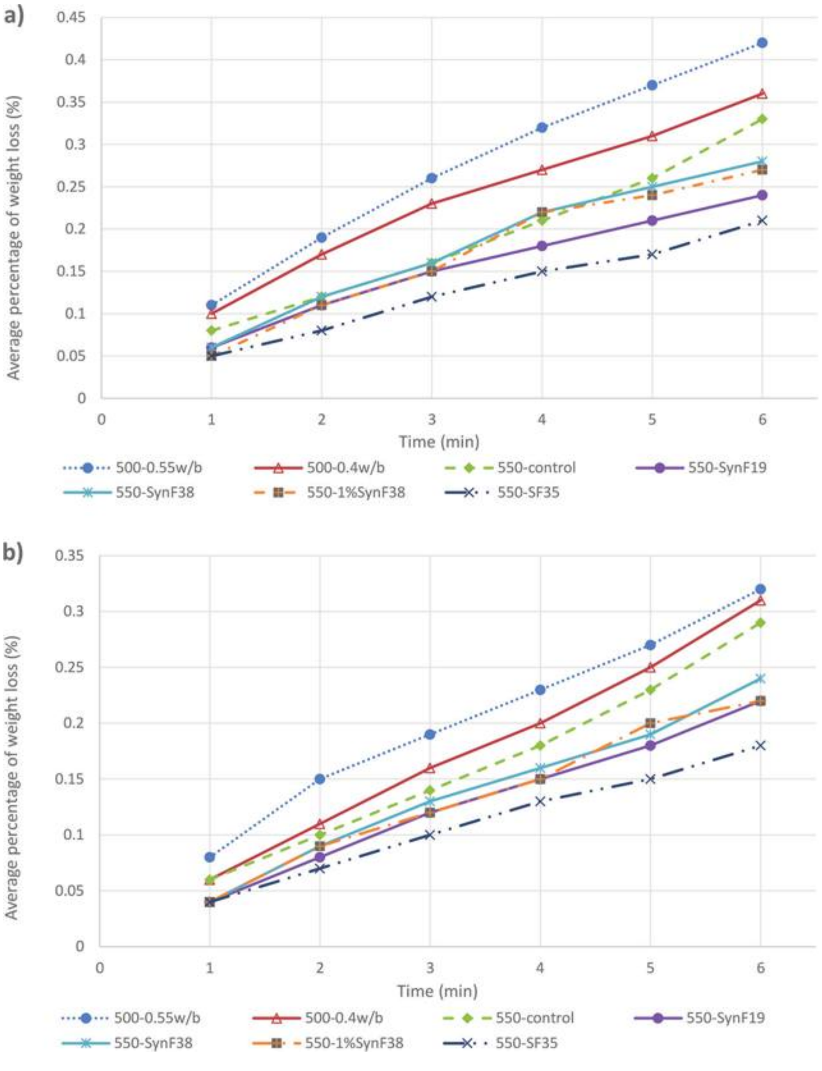

Fig. 4—Average percentage of weight loss of all mixtures at: (a) room temperature (25°C); and (b) cold temperature (–20°C).

fluctuating at a value of approximately 1.8 with a maximum value of 1.92, as seen in Fig. 5(d). The sudden increases in the $H(t)$ values coincided with an increased AE activity corresponding to the locations of the slope change in the CSS variation. All these previous events can be related to the rising linear trend in the abrasion damage after each test interval. This increased AE activity (in terms of variation of the values of $H(t)$) can be attributed to the particle exfoliation associated with abrasion damage.[17] In contrast, S_r spiked in the first testing interval to reach a value of

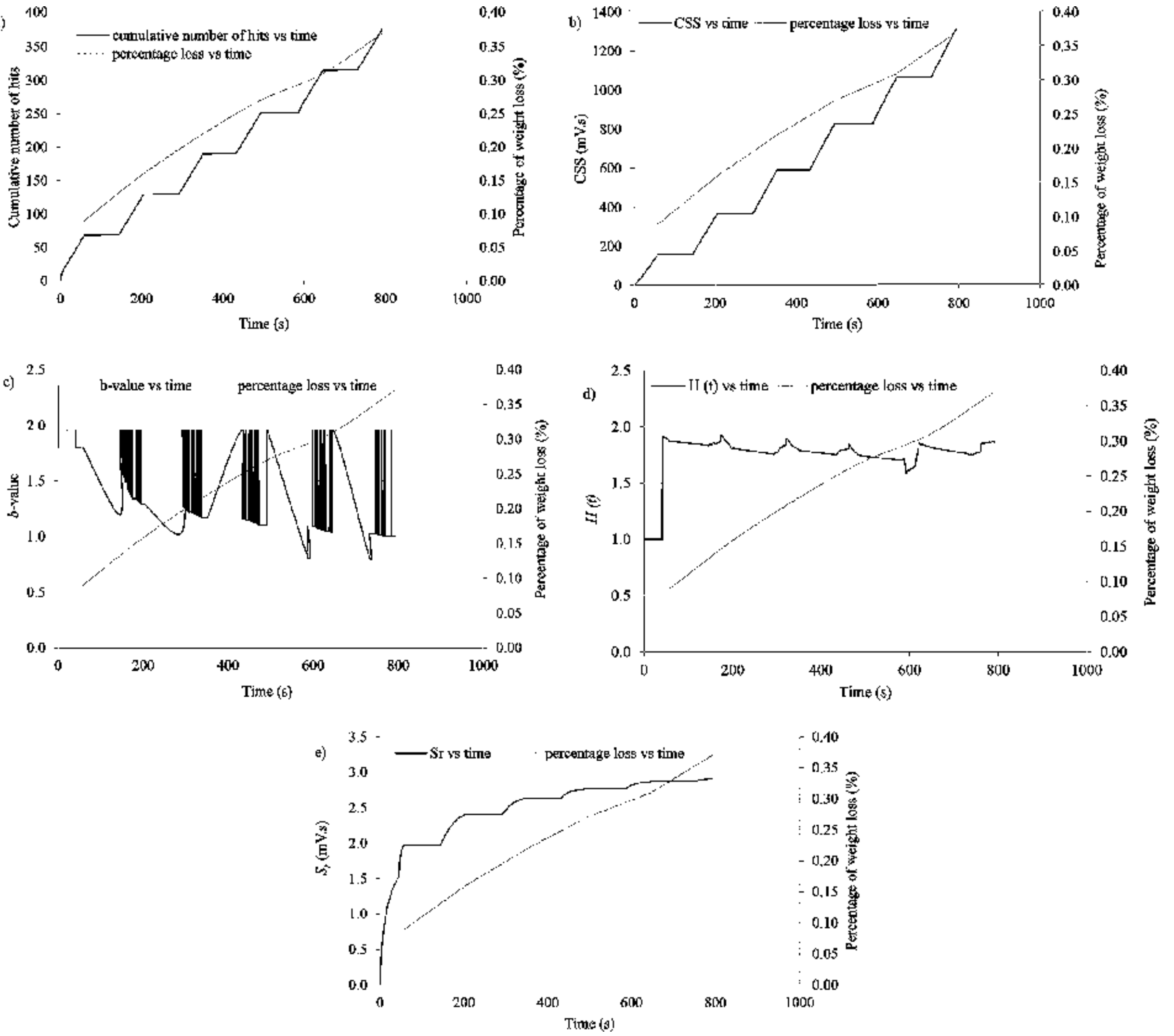

*Fig. 5—Variations in AE parameters for 500-0.55*w/b *(S2) tested at cold temperature: (a) number of hits; (b) CSS; (c)* b*-value; (d)* H(t)*; and (e)* S_r.

1.9 mV.s and showed a gradual increase for the rest of the test, reaching its peak value of 2.9 mV.s at the end of the test, as seen in Fig. 5(e). The continual increase in the S_r during the test could be attributed to the abrasion damage progression leading to more cracks and AE strain energy release.

Figure 6 displays the *b*-values obtained by the end of each testing interval, at which the *b*-value almost reached the minimum value. The figure displays the relationship between *b*-value and weight loss percentage for the same mixture (S2) tested at room and –20°C. It is shown that the increase in the weight loss due to abrasion was accompanied by an almost linear decline in the *b*-value. These relationships of the S2 sample (presented in Fig. 6) also indicate the existence of a correlation between abrasion damage and *b*-value at both cold and room temperatures.

On the other hand, the values of signal amplitudes for the same sample (S2 sample tested at –20°C) throughout the test were analyzed and found to experience insignificant changes in accordance with the damage progression, except for a slight increase in the amplitude values for samples tested at cold temperature compared to those tested at room temperature. For example, for sample SCC-500-0.55*w*/*b*-S2, the average amplitude values corresponding to each testing interval from 1 to 6 minutes were 87, 88, 88, 86, 87, and 88 dB, respectively. Other samples tested in this study showed a similar trend in the variations in the previously noted AE parameters, as the sample graphed in Fig. 5 and 6 demonstrates. Subsequently, it can be concluded that the analysis of these AE parameters could be used as a tool to identify the abrasion damage progress in the tested mixtures regardless of temperature. The values of the selected AE parameters (number of hits, CSS, *b*-value, $H(t)$, S_r) at the end of the first and last 1-minute intervals were summarized in Table 7. The AE parameters in Table 7 were used on a comparative basis to assess the abrasion resistance of the tested SCC mixtures, as discussed in the following sections.

Effect of cold temperature on abrasion performance and AE data

Lab measurements and the collected AE parameters supported that cold temperature generally enhanced the compressive strength and abrasion resistance of all mixtures, as displayed in Fig. 7 and Tables 3, 7, and 8. For example, experimental measurements showed that Mixture M1

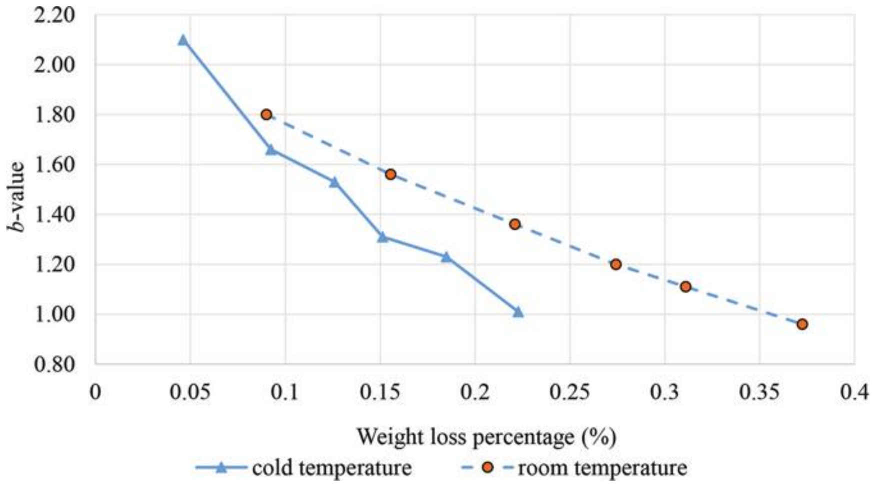

Fig. 6—Relation between b-*value and weight loss for 550-0.55*w/b *(S2) at cold and room temperatures.*

Table 7—Average values of AE parameters after 1- and 6-minute abrasion testing of all samples at room and cold temperatures

Mixture No.	Mixture type	Testing temperature	Average signal amplitude, dB		Number of hits		CSS × 10^{12}, mV.s		*H*(*t*)		S_r, mV.s		*b*-value	
			1 min	6 min	1 min	6 min	1 min	6 min	1 min	6 min	1 min	6 min	1 min	6 min
M1	500-0.55*w*/*b*	Room	85	85	104	604	0.29	1.91	1.77	2.72	2.62	4.08	1.43	0.94
		Cold	87	86	95	532	0.21	1.29	1.52	2.55	2.45	3.73	1.88	1.07
M2	500-0.4*w*/*b*	Room	87	83	96	519	0.26	1.85	1.70	2.51	2.55	3.85	1.8	1.15
		Cold	84	86	83	506	0.15	1.11	1.56	2.0	2.40	3.41	1.85	1.63
M3	550-control	Room	81	82	81	381	0.24	1.8	1.49	1.45	2.14	3.81	1.88	1.32
		Cold	84	86	66	367	0.14	1.28	1.54	1.29	2.25	3.35	2.0	1.39
M4	550-SynF19	Room	80	78	68	341	0.17	1.21	0.95	1.05	1.94	3.22	2.83	1.91
		Cold	86	87	57	327	0.13	1.06	0.92	1.03	1.83	2.72	2.97	1.99
M5	550-SynF38	Room	84	79	61	345	0.2	1.37	1.09	1.2	2.05	3.29	2.42	1.71
		Cold	83	85	60	337	0.18	1.13	1.03	1.17	1.94	3.11	2.71	1.83
M6	550-1%SynF38	Room	87	84	55	321	0.18	1.29	1.39	1.18	2.75	2.92	2.48	1.83
		Cold	87	85	47	309	0.14	1.09	0.98	1.14	1.79	2.83	2.81	1.95
M7	550-SF35	Room	87	85	54	336	0.17	1.11	0.96	1.14	1.92	2.69	2.60	1.85
		Cold	87	85	51	318	0.13	1.07	1.01	1.13	1.66	2.37	2.71	1.91

experienced 24% less weight loss when tested at –20°C compared to room temperature (25°C) after 6 minutes of abrasion. Similarly, the reduction in weight loss was 14% for M2, 13.7% for M3, 8.3% for M4, 14.3% for M5, 7.4% for M6, and 14.3% for M7 compared with room temperature. In terms of wear depth, as expected, lab testing showed a decrease of 16% for M1, 6% for M2, 12% for M3, 19.3% for M4, 13% for M5, 11.5% for M6, and 13% for M7 at cold temperature versus room temperature. The values of abrasion mass loss rate (g/min) listed in Table 3 confirm the same observations. For instance, the rate of mass loss for the mixtures when tested at cold temperature compared to room temperature dropped from 1.63 to 1.27 g/min for Mixture M1 and from 1.29 to 1.17 g/min for Mixture M3. This behavior could be attributed to the fact that when water in pores began to freeze, the strength increased because the capillary pores were filled with a solid substance, which added an extra load-bearing capacity.[1] The effect of variation in the compressive strength of the tested mixtures was also considered by presenting the values of normalized mass loss with respect to the compressive strength in Table 3.

Another reason is that the ice may have bridged the cracks and limited crack growth in the matrix, which can add more strength to the concrete matrix. The shrinkage of concrete at –20°C may also have positively affected the bond between the fibers and the hardened cementitious matrix,[1] which is another reason that may have contributed to increasing the strength at cold temperatures. The aforementioned reasons could be further confirmed by the result of mixture 500-0.55*w*/*b* (M1), which had the highest *w*/*b* compared to all other tested mixtures. This mixture experienced the most pronounced enhancement ratio in the abrasion resistance when frozen (24% reduction in weight loss and 16% reduction in wear depth).

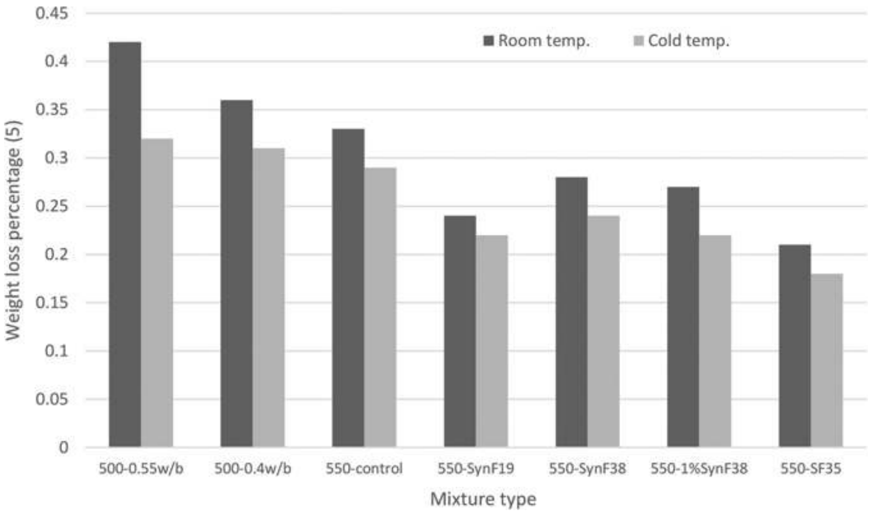

Fig. 7—Average percentage of weight loss of all samples after 6 minutes of abrasion at room and cold temperatures.

Table 8—Average percentage of weight loss after testing at room and cold temperatures for all samples

Mixture No.	Mixture type	Average weight loss, %											
		1 min		2 min		3 min		4 min		5 min		6 min	
		Room	Cold	Room	Cold	Room	Cold	Room	Cold	Room	Cold	Room	Cold
M1	500-0.55*w*/*b*	0.11	0.08	0.19	0.15	0.26	0.19	0.32	0.23	0.37	0.27	0.42	0.32
M2	500-0.4*w*/*b*	0.10	0.06	0.17	0.11	0.23	0.16	0.27	0.20	0.31	0.25	0.36	0.31
M3	550-control	0.08	0.06	0.12	0.10	0.16	0.14	0.21	0.18	0.26	0.23	0.33	0.29
M4	550-SynF19	0.06	0.04	0.11	0.08	0.15	0.12	0.18	0.15	0.21	0.18	0.24	0.22
M5	550-SynF38	0.06	0.04	0.12	0.09	0.16	0.13	0.22	0.16	0.25	0.19	0.28	0.24
M6	550-1%SynF38	0.05	0.04	0.11	0.09	0.15	0.12	0.22	0.20	0.24	0.20	0.27	0.22
M7	550-SF35	0.05	0.04	0.08	0.07	0.12	0.10	0.15	0.13	0.17	0.15	0.21	0.18

The same behavior could be found from the AE collected parameters shown in Table 7. For example, the reduction in weight loss due to freezing of the 500-0.55*w*/*b* mixture (M1) was accompanied by an average reduction of 12% in the number of hits, 32.5% in CSS, 43% in *H*(*t*), and 13.5% in S_r, and an average increase of 13.8% in *b*-value. Concerning the signal amplitudes, there was a slight increase in the average signal amplitudes for samples tested at –20°C compared with those at room temperature, as shown in Fig. 8. This amplitude trend could be attributed to the fact that water inside the pores turned into ice and decreased signal attenuation. Another reason could be that cooling down samples to –20°C was accompanied by higher strength and more brittle behavior, resulting in higher values of strain energy released during damage progress.

Effect of *w*/*b* on abrasion performance and AE data at room and cold temperatures

Two SCC mixtures were developed with two different *w*/*b*, 0.4 and 0.55 (M1 and M2). The results in Table 3 indicated that increasing the *w*/*b* negatively affected the abrasion wear depth at normal temperatures. The cold temperature, however, alleviated these reductions. Samples with a higher *w*/*b* (0.55) experienced a more pronounced enhancement ratio in the abrasion resistance when cooled down to –20°C. For instance, Mixture M2 (0.4 *w*/*b*) experienced a weight loss of 0.36% compared to 0.42% for Mixture M1 (0.55 *w*/*b*) when tested at room temperature, while Mixture M2 (0.4 *w*/*b*) experienced weight loss of 0.31% compared to 0.32% for Mixture M1 (0.55 *w*/*b*) when tested at cold temperature. Regarding wear depth, Mixture M2 (0.4 *w*/*b*) experienced 1.04 mm compared to 1.21 mm for Mixture M1 (0.55 *w*/*b*) when tested at room temperature. On the other hand, Mixture M2 (0.4 *w*/*b*) experienced 0.98 mm compared to 1.02 mm for Mixture M1 (0.55 *w*/*b*) when tested at cold temperature. This enhancement ratio in the abrasion resistance of mixtures with a higher *w*/*b* at cold temperature could be related to the fact that more water converted to ice in higher *w*/*b* mixtures, which filled the microcracks in the matrix. This led to a relatively higher strength, as discussed in the previous section, "Effect of cold temperature on abrasion performance and AE data."

The same behavior in the abrasion performance could be noticed from the AE parameters values (refer to Table 7). For example, when testing at room temperature, increasing the *w*/*b* from 0.4 (M2) to 0.55 (M1) yielded an average increase of 16% in the number of hits, 3% in CSS, 8% in *H*(*t*) values, and 6% in S_r, and a decrease of 18% in *b*-value, indicating lower abrasion resistance. On the other hand, increasing the *w*/*b* at –20°C resulted in an increase in the number of hits of 5%, 16% in CSS, 27% in *H*(*t*), 6% in S_r,

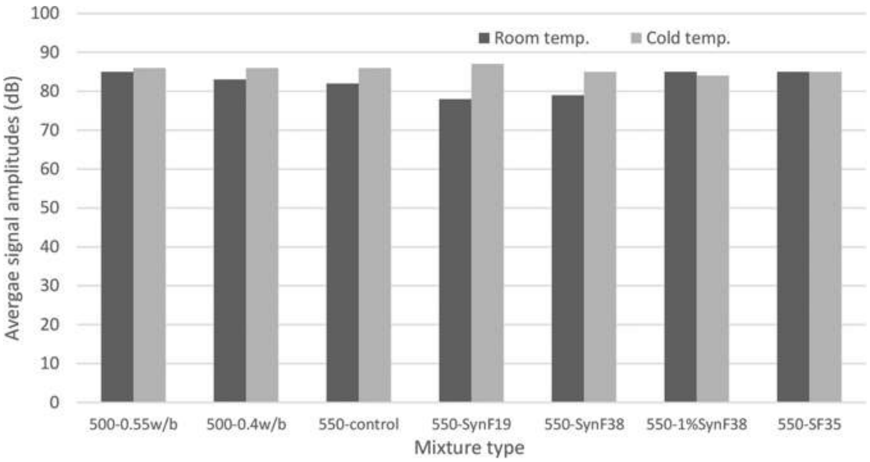

Fig. 8—Average signal amplitude values of all samples at room and cold temperatures.

and a decrease in *b*-value of 34%, indicating slightly lower abrasion resistance.

Effect of fibers on abrasion performance and AE data at room and cold temperatures

A control SCC mixture without fibers (M3) was developed, and four other mixtures (M4 to M7) including different types, lengths, and volumes of fibers were included and tested at room and cold temperatures for comparison. The results in Tables 7 and 8 showed an overall improvement in the abrasion performance for the different fiber-reinforced mixtures compared to the control mixture, irrespective of temperature. For instance, the control mixture without fibers (M3) experienced an average weight loss of 0.33% and 0.29% at room and cold temperatures, respectively, while these numbers were 0.27% and 0.23% (on average) in mixtures containing fibers (M4 to M7). Similarly, the control mixture without fibers (M3) showed average wear depths of 0.82 and 0.72 mm at room and cold temperatures, respectively, and these numbers were 0.52 and 0.42 mm (on average) in mixtures containing fibers (M4 to M7).

The same enhancement in the abrasion performance could be noticed from the AE parameter values (refer to Table 7). For example, incorporating fibers in the mixtures (M4 to M7) yielded an average decrease of 13.4% in the number of hits, 30.5% in CSS, 21.4% in *H*(*t*) values, and 20.4% in S_r, and an increase of 37% in *b*-value for fiber-reinforced mixtures compared to the results of the control mixture (M3) at –20°C. This result could be attributable to the fact that fibers provide more crack control and prevent particles from pulling out as a result of abrasion. Besides, the shrinkage of concrete under cold temperature promoted the bond between fibers and the surrounding matrix.[1]

Effect of fiber volume on abrasion and AE data at room and cold temperatures

The study included two mixtures containing the same fiber type and length at different dosages: 0.2 and 1% (M5 and M6, respectively). The results in Tables 3 to 8 indicate that increasing the fiber volume yielded slightly lower values of weight loss and wearing depth under both cold and room temperatures, indicating better abrasion resistance. For example, Mixture M5 with 0.2% fibers experienced mass losses of 0.28% and 0.24%, and wear depths of 0.62 and 0.54 mm at room and cold temperatures, respectively. Alternatively, Mixture M6 (with 1% fibers) showed 0.27% and 0.22% mass loss, as well as 0.52 and 0.46 mm wear depths at room and cold temperatures, respectively. This enhancement in the abrasion resistance could be attributed to the additional crack control accompanied by using higher fiber volumes.

The previous experimental results were further confirmed by analyzing the calculated AE parameters shown in Table 7. For example, when tested at –20°C, increasing the fiber volume from 0.2 to 1% was accompanied by a reduction in the number of hits from 337 to 309, in CSS from 1130 to 1090 mV.s, in *H*(*t*) from 1.17 to 1.14, and in S_r from 3.11 to 2.83, and an increase in *b*-value from 1.83 to 1.95 (which indicates an improved abrasion resistance when a higher volume of fibers was used).

Effect of fiber type on abrasion and AE data at room and cold temperatures

Two types of fibers were used in this investigation: 38 mm polypropylene SynFs (M5) and 35 mm SFs (M7). For Mixture M5, the average percentages of abrasion weight loss at room and cold temperatures were 0.28% and 0.24%, respectively. These numbers dropped to 0.21% and 0.18%, respectively, when using SFs (M7), indicating better abrasion resistance. Similarly, in the mixture with polypropylene SynFs (M5) the average wear depths were 0.62 and 0.54 mm at room and cold temperature, respectively, and these numbers also dropped to 0.46 and 0.40 mm, respectively, in the mixture with SFs (Table 3). These results show that the SF mixture encouraged better abrasion resistance than polypropylene SynF at both room and subzero temperatures.

The calculated AE parameters showed a similar trend to that observed from the experimental results for the two mixtures. For example, in the case of the SF mixture, the average values of the number of hits, CSS, *H*(*t*), and S_r were lower, and the average *b*-values were higher than in the case of the polypropylene SynF mixture. The average magnitudes of these parameters in the same order were 336, 1110 mV.s, 1.14, 3.65, and 1.85 at room temperature and 318,

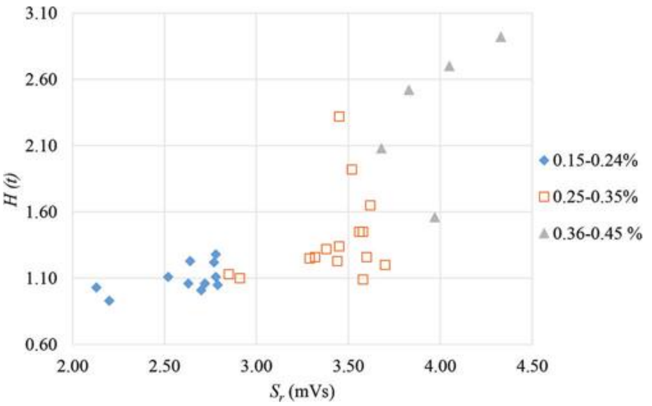

Fig. 9—Percentage of weight loss quantification chart.

1070 mV.s, 1.13, 3.11, and 1.91 at –20°C for the SF mixture compared to 345, 1370 mV.s, 1.2, 3.81, and 1.71 at room temperature and 337, 1130 mV.s, 1.17, 3.31, and 1.83 at –20°C for the polypropylene SynF mixture, as seen in Table 7. Unlike other AE parameters, the signal amplitude did not show a significant difference when fiber materials changed from steel to polypropylene, and hence no attenuation effect was detected. This conclusion is limited to the fiber content used in this study (0.2%).

Effect of fiber length on abrasion and AE data under different temperatures

Two SCC mixtures were developed with two different lengths of polypropylene SynF (19 and 38 mm). Experimental measurements showed that shorter fiber enhances the abrasion resistance compared to longer fiber, irrespective of sample temperature. At room and cold temperatures, the 19 mm fiber mixture (M4) experienced an average percentage of weight loss of 0.24% and 0.22%, respectively, compared to 0.28% and 0.24% in the mixture with 38 mm fibers (M5). Also, at room and cold temperatures, the 19 mm fiber mixture (M4) had average wear depths of 0.57 and 0.46 mm, respectively, compared to 0.62 and 0.54 mm, respectively, in the 38 mm fiber mixture (Tables 3 and 8). This result could be attributed to the increased value of compressive strength as a result of decreasing the fiber length, as can be seen in Table 3. Another significant reason could be that, at the same volume of fiber (0.2%), increasing the fiber length reduces the number of fibers distributed in the mixture, which leads to a lower effect on controlling the crack growth or confining the concrete.

The analyzed AE parameters, including the number of hits, CSS, *b*-value, $H(t)$, and S_r showed a similar trend, as expected (Table 7). For instance, changing the fiber length from 19 to 38 mm yielded a 4% higher average number of hits, 13% higher average CSS, 14% higher average $H(t)$, 3% higher average S_r, and 11% lower average *b*-value at room temperature (which matched an increase in the mass loss due to abrasion). At –20°C, the collected AE parameters of the 38 mm mixture reported a 3% average increase in the number of hits, 7% average increase in CSS, 13% average increase in $H(t)$, 2% average increase in S_r, and 8% average decrease in *b*-value, compared to the 19 mm fiber counterpart mixture. It is worth noting that the 38 mm fiber mixture witnessed a more pronounced enhancement ratio in the abrasion resistance when frozen compared to the 19 mm mixture. For instance, the 38 mm mixture witnessed a 14.3% decrease in the mass loss compared to an 8% decrease for the 19 mm fiber mixture when decreasing the sample temperature to –20°C. This result could be attributed to the improved bond strength between the fibers and cement matrix due to concrete shrinkage at freezing temperature, and this effect is more pronounced in longer fibers compared to shorter ones. The AE signals amplitude witnessed no significant change as a result of changing the fiber length in the polypropylene SynF mixtures, as can be seen in Fig. 8.

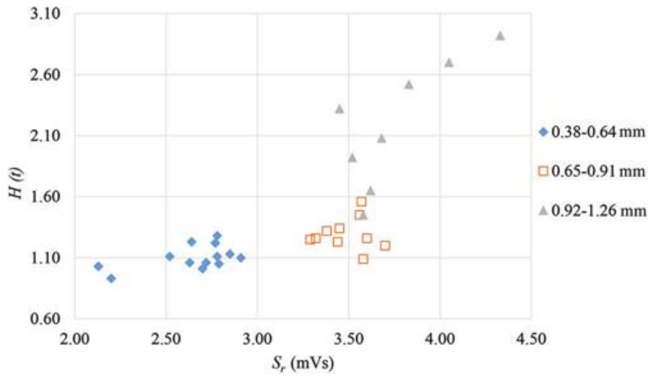

Fig. 10—Wear depth quantification chart.

Damage quantification charts using AE intensity analysis parameters

One of the major targets of this study was to evaluate the extent of abrasion damage in various fiber-reinforced concrete mixtures through the analysis of AE characteristics throughout the tests. Two damage quantification charts were developed in terms of weight loss and wear depth (Fig. 9 and 10, respectively) using the $H(t)$ and S_r values at the end of the abrasion test for all mixtures. These charts were developed by combining the calculated AE intensity analysis parameters and experimental results presented in Tables 3, 7, and 8 at both cold and room temperatures. Using the pair of values of the $H(t)$ and S_r, resulting from the intensity analysis, the user can predict the range of mass loss percentage as well as the wear depth from the charts in Fig. 9 and 10. The mass loss attained from all tested mixtures falls into three ranges: 0.15 to 0.24%, 0.25 to 0.34%, and 0.35 to 0.45%, as seen in Fig. 7. Likewise, the wear depth values in Fig. 10 were classified into three groups: 0.38 to 0.64, 0.65 to 0.91, and 0.92 to 1.26 mm. For example, if the calculated values of $H(t)$ and S_r were 1.6 and 3.5 mV.s, respectively, the predicted mass loss would be in the range of 0.25 to 0.35%, and the predicted wear depth would be 0.65 to 0.91 mm (Fig. 9 and 10). It is worth noting that these charts are limited to the range of mixture compositions used in this study tested at room temperature (25°C) and –20°C. Further studies on various SCC mixtures reinforced with other types, lengths, and volumes of fibers are recommended to refine the abrasion damage prediction charts presented herein.

CONCLUSIONS

The scope of this study was to evaluate the abrasion performance at subzero temperatures of various concrete mixtures reinforced with different types, lengths, and dosages of fibers and different water-binder ratios (*w*/*b*). Cubic samples were tested using the rotating-cutter abrasion method along with piezoelectric sensors to collect the acoustic emission (AE) signals generated during the tests. It should be noted that the scope of the current paper focused on the laboratory examination of the application of AE monitoring. For the potential implementation in the field, further verifications are warranted to confirm the effectiveness of the studied AE parameters for the condition evaluation of existing structures undergoing continuous structural health monitoring (SHM) using the AE technique.

1. The AE parameters, including the number of hits, cumulative signal strength (CSS), $H(t)$, S_r, and *b*-value, were found to be directly correlated to the abrasion damage at both cold and room temperatures. Upon comparing the experimental and AE results, it was noticed that the increase in both mass loss and wear depth was accompanied by an overall increase in the number of hits, CSS, and S_r and by an overall decrease in the *b*-values. The values of $H(t)$ fluctuated over the test period at a specific value as an indication of the propagation of the abrasion damage.

2. Adding different types, lengths, or volumes of fibers or changing the *w*/*b* did not seem to significantly affect the AE signal amplitude as they fluctuated with no recognizable pattern at both subzero and room temperatures. However, it was noticed that the signals collected at subzero temperatures seemed to have slightly higher average amplitudes than those obtained at room temperature. The other studied AE parameters (number of hits, CSS, $H(t)$, S_r, and *b*-value) were found to be more sensitive to the abrasion damage progression regardless of concrete mixture design or testing temperature.

3. All tested mixtures experienced an overall enhancement in their abrasion performance when tested at cold temperature (–20°C) compared to their abrasion performance at room temperature. In addition, the improvement of the abrasion resistance due to cold temperature was more pronounced in mixtures with a higher *w*/*b* (0.55) compared to ones with a lower *w*/*b* (0.4).

4. Using a higher volume of fibers in the mixture resulted in a slight increase in the abrasion resistance in terms of mass loss and wear depth at both cold and room temperatures compared to the counterpart mixture with a lower volume. This could be attributed to the enhanced crack control in the higher-fiber-volume mixture compared to the lower-fiber-volume mixture.

5. Using steel fibers in the mixture improved the abrasion performance (lower values of mass loss and wear depth) compared with using polypropylene synthetic fibers at both cold and room temperatures. The analysis of the values of the calculated AE parameters throughout the tests supported the same outcome.

6. Increasing the length of fibers led to higher average values of mass loss and wear depth compared to mixtures with shorter fibers at both cold and room temperatures, indicating lower abrasion resistance. The retrogression in the abrasion resistance of mixtures with longer fibers versus those with shorter fibers matched an increase in the values of the number of hits, CSS, $H(t)$, and S_r, and a decrease in the *b*-value. On the other hand, the mixture with longer fibers experienced a more significant enhancement in the abrasion performance when cooled down to –20°C compared to that with shorter fibers.

7. The results of this study supported the sensitivity of the AE analysis to assess the abrasion damage of various mixtures with and without fibers at cold temperatures. This study also proposed damage prediction charts that could facilitate the application of AE monitoring to classify the abrasion wear extent. The charts were developed based on the AE intensity analysis parameters together with the abrasion mass loss and wear depth of all samples tested at room and cold temperatures.

AUTHOR BIOS

Omar A. Kamel *is a Graduate Research and Teaching Assistant in the Faculty of Engineering and Applied Science at Memorial University of Newfoundland, St. John's, NL, Canada. He received his BSc in civil engineering from Alexandria University, Alexandria, Egypt, in 2017. His research interests include fiber-reinforced concrete, green concrete, service life prediction, and structural health monitoring of concrete structures.*

Ahmed A. Abouhussien *is a Civil/Structural Engineer at GE-Hitachi Nuclear Energy International, LLC, in Markham, ON, Canada. He received his bachelor's degree from Menoufia University, Shebin El-Kom, Egypt, in 2008, and his master's degree and PhD in civil engineering from Memorial University of Newfoundland in 2013 and 2017, respectively, all in civil engineering. His research interests include durability, reinforcing steel corrosion, service life prediction, structural health monitoring of concrete structures; acoustic emission monitoring; and self-consolidating concrete.*

Assem A. A. Hassan *is a Professor in the Faculty of Engineering and Applied Science at Memorial University of Newfoundland. His research interests include the development and use of self-consolidating, high-performance, and high-strength concretes; rheology of cement paste and concrete mixtures; durability (porosity, diffusivity, and chloride permeability) of concrete structures; corrosion monitoring and accelerated corrosion testing of reinforced concrete structures; service life prediction of concrete structures; and performance of large-scale structural members under loading.*

Basem H. AbdelAleem *is an Assistant Professor in the Faculty of Engineering, Cairo University, Giza, Egypt, and a Postdoctoral Fellow in the Faculty of Engineering and Applied Science, Memorial University of Newfoundland. He received his BSc in civil engineering and his MSc in structural engineering from Cairo University in 2012 and 2015, respectively, and his PhD in civil engineering from Memorial University of Newfoundland in 2019. His research interests include structural applications of self-consolidating, rubberized, and fiber-reinforced concretes; and the structural performance of beam-column joints under reversed cyclic loading.*

REFERENCES

1. Zaki, R. A.; AbdelAleem, B. H.; Hassan, A. A. A.; and Colbourne, B., "Abrasion Resistance of Fiber-Reinforced Concrete under Cold Temperatures," *ACI Materials Journal*, V. 117, No. 5, Sept. 2020, pp. 221-232.

2. ASTM C779/C779-12, "Standard Test Method for Abrasion Resistance of Horizontal Concrete Surfaces," ASTM International, West Conshohocken, PA, 2012.

3. ASTM C418-12, "Standard Test Method for Abrasion Resistance of Concrete by Sandblasting," ASTM International, West Conshohocken, PA, 2012.

4. ASTM C944/C944M-12, "Standard Test Method for Abrasion Resistance of Concrete or Mortar Surfaces by the Rotating-Cutter Method," ASTM International, West Conshohocken, PA, 2012.

5. Pyo, S.; Abate, S. Y.; and Kim, H. K., "Abrasion Resistance of Ultra High Performance Concrete Incorporating Coarser Aggregate," *Construction and Building Materials*, V. 165, 2018, pp. 11-16. doi: 10.1016/j.conbuildmat.2018.01.036

6. Horszczaruk, E., "Abrasion Resistance of High-Strength Concrete in Hydraulic Structures," *Wear*, V. 259, No. 1-6, 2005, pp. 62-69. doi: 10.1016/j.wear.2005.02.079

7. Lachemi, M.; Hossain, K. M.; Lambros, V.; and Bouzoubaa, N., "Development of Cost-Effective Self-Consolidating Concrete Incorporating Fly Ash, Slag Cement, or Viscosity-Modifying Admixtures," *ACI Materials Journal*, V. 100, No. 5, Sept.-Oct. 2003, pp. 419-425.

8. Ghafoori, N.; Najimi, M.; and Aqel, M. A., "Abrasion Resistance of Self-Consolidating Concrete," *Journal of Materials in Civil Engineering*, ASCE, V. 26, No. 2, 2014, pp. 296-303. doi: 10.1061/(ASCE)MT.1943-5533.0000847

9. ACI Committee 237, "Self-Consolidating Concrete (ACI 237R-07) (Reapproved 2019)," American Concrete Institute, Farmington Hills, MI, 2007, 30 pp.

10. Ismail, M. K., and Hassan, A. A. A., "Impact Resistance and Mechanical Properties of Self-Consolidating Rubberized Concrete Reinforced with Steel Fibers," *Journal of Materials in Civil Engineering*, ASCE, V. 29, No. 1, 2017, p. 04016193. doi: 10.1061/(ASCE)MT.1943-5533.0001731

11. AbdelAleem, B. H.; Ismail, M. K.; and Hassan, A. A., "Properties of Self-Consolidating Rubberised Concrete Reinforced with Synthetic Fibres," *Magazine of Concrete Research*, V. 69, No. 10, 2017, pp. 526-540. doi: 10.1680/jmacr.16.00433

12. Khayat, K. H.; Kassimi, F.; and Ghoddousi, P., "Mixture Design and Testing of Fiber-Reinforced Self-Consolidating Concrete," *ACI Materials Journal*, V. 111, No. 2, Mar.-Apr. 2014, pp. 143-152. doi: 10.14359/51686722

13. AbdelAleem, B. H.; Ismail, M. K.; and Hassan, A. A. A., "The Combined Effect of Crumb Rubber and Synthetic Fibers on Impact Resistance of Self-Consolidating Concrete," *Construction and Building Materials*, V. 162, 2018, pp. 816-829. doi: 10.1016/j.conbuildmat.2017.12.077

14. AbdelAleem, B. H., and Hassan, A. A. A., "Cyclic Behavior of Rubberized Beam-Column Joints Reinforced with Synthetic Fibers," *ACI Materials Journal*, V. 116, No. 2, Mar. 2019, pp. 105-118. doi: 10.14359/51714456

15. Li, J. J.; Niu, J. G.; Wan, C. J.; Jin, B.; and Yin, Y. L., "Investigation on Mechanical Properties and Microstructure of High Performance Polypropylene Fiber Reinforced Lightweight Aggregate Concrete," *Construction and Building Materials*, V. 118, 2016, pp. 27-35. doi: 10.1016/j.conbuildmat.2016.04.116

16. Li, J. J.; Wan, C. J.; Niu, J. G.; Wu, L. F.; and Wu, Y. C., "Investigation on Flexural Toughness Evaluation Method of Steel Fiber Reinforced Lightweight Aggregate Concrete," *Construction and Building Materials*, V. 131, 2017, pp. 449-458. doi: 10.1016/j.conbuildmat.2016.11.101

17. Ridgley, K. E.; Abouhussien, A. A.; Hassan, A. A. A.; and Colbourne, B., "Assessing Abrasion Performance of Self-Consolidating Concrete Containing Synthetic Fibers Using Acoustic Emission Analysis," *Materials and Structures*, V. 51, No. 5, 2018, pp. 1-17. doi: 10.1617/s11527-018-1247-3

18. Pigeon, M., and Cantin, R., "Flexural Properties of Steel Fiber-Reinforced Concretes at Low Temperatures," *Cement and Concrete Composites*, V. 20, No. 5, 1998, pp. 365-375. doi: 10.1016/S0958-9465(98)00017-1

19. Zaki, R. A.; AbdelAleem, B. H.; Hassan, A. A. A.; and Colbourne, B., "Impact Resistance of Steel Fiber Reinforced Concrete in Cold Temperatures," *Cement and Concrete Composites*, V. 122, 2021, p. 104116. doi: 10.1016/j.cemconcomp.2021.104116

20. Duthil, P., "Material Properties at Low Temperature," *Proceedings of the CAS-CERN Accelerator School: Superconductivity for Accelerators*, Erice, Italy, R. Bailey, ed., 2015, 18 pp.

21. Lee, G. C.; Shih, T. S.; and Chang, K. C., "Mechanical Properties of Concrete at Low Temperature," *Journal of Cold Regions Engineering*, ASCE, V. 2, No. 1, 1988, pp. 13-24. doi: 10.1061/(ASCE)0887-381X(1988)2:1(13)

22. Omar, A. T.; Sadek, M. M.; and Hassan, A. A. A., "Impact Resistance and Mechanical Properties of Lightweight Self-Consolidating Concrete under Cold Temperatures," *ACI Materials Journal*, V. 117, No. 5, Sept. 2020, pp. 81-91. doi: 10.14359/51725975

23. Vidya Sagar, R.; Raghu Prasad, B. K.; and Sharma, R., "Evaluation of Damage in Reinforced Concrete Bridge Beams Using Acoustic Emission Technique," *Nondestructive Testing and Evaluation*, V. 27, No. 2, 2012, pp. 95-108. doi: 10.1080/10589759.2011.610452

24. Ziehl, P. H.; Galati, N.; Nanni, A.; and Tumialan, J. G., "In-Situ Evaluation of Two Concrete Slab Systems. II: Evaluation Criteria and Outcomes," *Journal of Performance of Constructed Facilities*, ASCE, V. 22, No. 4, 2008, pp. 217-227. doi: 10.1061/(ASCE)0887-3828(2008)22:4(217)

25. Zaki, A.; Chai, H. K.; Aggelis, D. G.; and Alver, N., "Non-Destructive Evaluation for Corrosion Monitoring in Concrete: A Review and Capability of Acoustic Emission Technique," *Sensors (Basel)*, V. 15, No. 8, 2015, pp. 19069-19101. doi: 10.3390/s150819069

26. Aggelis, D. G.; Soulioti, D. V.; Sapouridis, N.; Barkoula, N. M.; Paipetis, A. S.; and Matikas, T. E., "Acoustic Emission Characterization of the Fracture Process in Fibre Reinforced Concrete," *Construction and Building Materials*, V. 25, No. 11, 2011, pp. 4126-4131. doi: 10.1016/j.conbuildmat.2011.04.049

27. Abdelrahman, M.; ElBatanouny, M. K.; Ziehl, P.; Fasl, J.; Larosche, C. J.; and Fraczek, J., "Classification of Alkali-Silica Reaction Damage Using Acoustic Emission: A Proof-of-Concept Study," *Construction and Building Materials*, V. 95, 2015, pp. 406-413. doi: 10.1016/j.conbuildmat.2015.07.093

28. Anay, R.; Cortez, T. M.; Jáuregui, D. V.; ElBatanouny, M. K.; and Ziehl, P., "On-Site Acoustic-Emission Monitoring for Assessment of a Prestressed Concrete Double-Tee-Beam Bridge without Plans," *Journal of Performance of Constructed Facilities*, ASCE, V. 30, No. 4, 2016, p. 04015062. doi: 10.1061/(ASCE)CF.1943-5509.0000810

29. Ridgley, K. E.; Abouhussien, A. A.; Hassan, A. A. A.; and Colbourne, B., "Evaluation of Abrasion Resistance of Self-Consolidating Rubberized Concrete by Acoustic Emission Analysis," *Journal of Materials in Civil Engineering*, ASCE, V. 30, No. 8, 2018, p. 04018196. doi: 10.1061/(ASCE)MT.1943-5533.0002402

30. Salamone, S.; Veletzos, M. J.; Lanza di Scalea, F.; and Restrepo, J. I., "Detection of Initial Yield and Onset of Failure in Bonded Posttensioned Concrete Beams," *Journal of Bridge Engineering*, ASCE, V. 17, No. 6, 2012, pp. 966-974. doi: 10.1061/(ASCE)BE.1943-5592.0000311

31. Shang, H.; Yi, T.; and Guo, X., "Study on Strength and Ultrasonic Velocity of Air-Entrained Concrete and Plain Concrete in Cold Environment," *Advances in Materials Science and Engineering*, V. 2014, 2014, pp. 1-7. doi: 10.1155/2014/706986

32. ASTM C150/C150M-12, "Standard Specification for Portland Cement," ASTM International, West Conshohocken, PA, 2012.

33. ASTM C1611/C1611M-09, "Standard Test Method for Slump Flow of Self-Consolidating Concrete," ASTM International, West Conshohocken, PA, 2009.

34. ASTM C494/C494M-13, "Standard Specification for Chemical Admixtures for Concrete," ASTM International, West Conshohocken, PA, 2013.

35. ASTM C39/C39M-12, "Standard Test Method for Compressive Strength of Cylindrical Concrete Specimens," ASTM International, West Conshohocken, PA, 2012.

36. Physical Acoustics Corp, "PCI-2 Based AE System User's Manual," MISTRAS Group Inc., Princeton Junction, NJ, 2009. 4 pp.

37. Abouhussien, A. A., and Hassan, A. A. A., "Acoustic Emission Monitoring for Bond Integrity Evaluation of Reinforced Concrete under Pull-Out Tests," *Advances in Structural Engineering*, V. 20, No. 9, 2017, pp. 1390-1405. doi: 10.1177/1369433216678864

38. Abouhussien, A. A., and Hassan, A. A. A., "Application of Acoustic Emission Monitoring for Assessment of Bond Performance of Corroded Reinforced Concrete Beams," *Structural Health Monitoring*, V. 16, No. 6, 2017, pp. 732-744. doi: 10.1177/1475921716681460

39. ASTM E1316-14, "Standard Terminology for Nondestructive Examinations," ASTM International, West Conshohocken, PA, 2014.

40. Colombo, I. S.; Main, I. G.; and Forde, M. C., "Assessing Damage of Reinforced Concrete Beam Using '*b*-value' Analysis of Acoustic Emission Signals," *Journal of Materials in Civil Engineering*, ASCE, V. 15, No. 3, 2003, pp. 280-286. doi: 10.1061/(ASCE)0899-1561(2003)15:3(280)

41. Ohtsu, M., and Tomoda, Y., "Phenomenological Model of Corrosion Process in Reinforced Concrete Identified by Acoustic Emission," *ACI Materials Journal*, V. 105, No. 2, Mar.-Apr. 2008, pp. 194-199.

42. Vidya Sagar, R., and Raghu Prasad, B. K., "Laboratory Investigations on Cracking in Reinforced Concrete Beams Using On-Line Acoustic Emission Monitoring Technique," *Journal of Civil Structural Health Monitoring*, V. 3, No. 3, 2013, pp. 169-186. doi: 10.1007/s13349-013-0036-5

43. ElBatanouny, M. K.; Mangual, J.; Ziehl, P. H.; and Matta, F., "Early Corrosion Detection in Prestressed Concrete Girders Using Acoustic Emission," *Journal of Materials in Civil Engineering*, ASCE, V. 26, No. 3, 2014, pp. 504-511. doi: 10.1061/(ASCE)MT.1943-5533.0000845

44. Vélez, W.; Matta, F.; and Ziehl, P., "Acoustic Emission Monitoring of Early Corrosion in Prestressed Concrete Piles," *Structural Control and Health Monitoring*, V. 22, No. 5, 2015, pp. 873-887. doi: 10.1002/stc.1723

45. Nair, A., and Cai, C. S., "Acoustic Emission Monitoring of Bridges: Review and Case Studies," *Engineering Structures*, V. 32, No. 6, 2010, pp. 1704-1714. doi: 10.1016/j.engstruct.2010.02.020

46. Fowler, T.; Blessing, J.; and Conlisk, P., "New Directions in Testing," *Proceedings, International Conference of Acoustic Emission from Composite Materials*, K. Ono, ed., Acoustic Emission Working Group, Memphis, TN, 1989, pp. 16-27.

47. Abdelrahman, M.; ElBatanouny, M. K.; and Ziehl, P. H., "Acoustic Emission Based Damage Assessment Method for Prestressed Concrete Structures: Modified Index of Damage," *Engineering Structures*, V. 60, 2014, pp. 258-264. doi: 10.1016/j.engstruct.2013.12.037

ACI MATERIALS JOURNAL TECHNICAL PAPER

Title No. 120-M45

Study of Environmental Concrete with Algerian Limestone Dust at Late Age

by Saida Kitouni

The aim of this study was to determine the effect of different amounts of filler on concrete properties. An experimental approach has made it possible to develop a construction product made from limestone dust, which is considered waste. This paper presents an experimental study on the prospects of using a mixture of waste limestone powder for the manufacture of an economical and lightweight composite as a building material.

This paper also presents the results of research on the possibility of using limestone dust as an aggregate in the production of concrete with lightweight aggregates. In this way, different amounts of limestone dust were used. Tests were conducted on concrete to replace 30, 50, and 70% by weight of coarse aggregate. The mechanical properties of concrete mixtures with high proportions of limestone dust were examined. The achieved compressive strength, flexural strength, and unit weight correspond to current international standards.

Keywords: compressive strength; lightweight aggregate concrete; limestone powder wastes; unit weight.

INTRODUCTION

Concrete is a three-phase composite material made of cement paste, aggregates, and an aggregate/cement paste interface.[1] Lightweight concretes (LWCs) are cementitious conglomerates with a bulk density ranging between 300 and 2000 kg/m^3, sensibly inferior to that of an ordinary concrete (usually among 2200 and 2600 kg/m^3). LWC is classified by ACI Committee 213 into three categories according to its strength and density (Table 1).

Lightweight aggregate concrete (LWAC) reduces building costs, eases construction, and has the advantage of being a relatively green building material.[1] These concretes are used in the manufacture of low-density reinforced structures. The reduced bulk density of a LWC is due to the addition of a void pattern in the concrete mixture. To achieve this result, three different methods are followed:

1. Replacing the aggregates with natural or artificial lightweight inert matter characterized by high porosity;
2. Using an inert matter constituted by small polystyrene balls; and
3. Adding pre-formed foam or substances that can release gases in an alkaline environment.[2]

A wide variety of natural and artificial lightweight aggregates are used in the manufacture of mortar and concrete. The use of natural lightweight aggregates instead of processed artificial aggregates can significantly reduce the cost of such concretes.[3] Aggregates are the weakest component of the concrete composite. The higher the strength of the aggregate, the higher the strength of concrete.[1]

The advantages of using lightweight aggregate in concrete include:

1. Reduction in dead weight resulting in small foundation sizes and a lighter and smaller upper structure, which can lead to a reduction in the amount of cement and possibly a reduction in reinforcement;
2. Lighter and smaller prefabricated elements requiring smaller and more expansive handling and transport equipment;
3. Reduced dimensions of pillars and slabs, and beams with consequently better accessibility to spaces;
4. High thermal insulation; and
5. Greater fire resistance. In addition, offshore structures used for oil production require lightweight components.

The incorporation of lightweight aggregates in concrete conserves natural resources and increases the use of industrial by-products, making the most significant potential benefit of lightweight aggregates for concrete its environmental impact. These benefits include the following:

1. Efficient use of lightweight materials[4,5];
2. Assisting with protecting natural and rare raw materials of coarse aggregates and sand;
3. Protection of the landscape, riverbeds, and beaches from the destructive activities of rock quarrying;
4. Manufacturing of aggregates much lighter than natural ones; and
5. Development of an industry with export potential to other countries.

Much research has been done on the reuse of many types of wastes that damage the environment and create complex problems. Important research efforts have been devoted to industrial by-products (fly ash, blast furnace slag, microsilica, and so on) and natural resources (limestone, pozzolana, and so on) as fractional replacements for coarse aggregates.[6-11] These materials can help protect the environment by recycling by-products and reducing the use of natural aggregates. Lime powders are plentiful and can be used in many applications as they are cheaper and less polluting.

Limestone dust is described by its chemical properties (grain size, $CaCO_3$ content). Impurities such as clay, sulphate, quartz, and dolomite can affect the properties of mortars and concrete.[12] At the moment, limestone blocks extracted from

---

ACI Materials Journal, V. 120, No. 4, July 2023.

MS No. M-2022-222.R2, doi: 10.14359/51738807, received February 24, 2023, and reviewed under Institute publication policies. Pertinent discussion including author's closure, if any, will be published ten months from this journal's date if the discussion is received within four months of the paper's print publication.

Table 1—Spectrum of lightweight concrete

	Low strength	Moderate strength	Structural
Density, kg/m^3	250, 500, and 700	1000, 1250, and 1400	1500, 1750, and 2000
Strength, N/mm^2	0.7 to 2	2 to 14	17 to 41

Table 2—Mixture proportions by weight

	Mixture proportion by weight				
Fraction of limestone, %	Cement, kg	Sand (0/3), kg	Limestone dust (20 m), kg/m^3	Coarse aggregates (3/8), kg/m^3	*w/c*
30	350	691.60	311.22	726.18	0.57
50	350	691.60	518.70	518.70	0.65
70	350	691.60	726.18	311.22	0.73

quarries are cut into smaller, suitable sizes that can be used as building materials. Limestone processing, which includes the manufacture of quarried limestone, generates 20% of limestone dust (LPW). Disposal of LPW causes dust, environmental problems, and pollution due to its fine nature. It pollutes the air during summer and spring storms, leading to serious health risks such as asthma. The industry suffers from the accumulation of LPW due to storage costs.

For ultra-lightweight LPW concretes, it makes sense to vary the proportion in the mortar or concrete for structural and non-structural applications.[13] The use of limestone dust in concrete has increased in recent years. A further increase in the use of limestone for these purposes is to be expected. Limestone is used for low- and high-performance concrete.[14] The use of limestone dust as an aggregate in its natural form has made it possible to tolerate a new cheap, lightweight, and environmentally friendly composite material. The influence of limestone dust on fresh concrete and hardened concrete properties has already been reported.[15,16] This paper presents the research work carried out on the properties of this new composite material containing different concentrations of 30, 50, and 70% at 28, 90, and 180 days. Substituting limestone dust as aggregate in test samples reduces unit weight. The tests determined compressive strength, flexural strength, Young's modulus, density, and Poisson's ratio of the limestone dust samples. Because LWC represents a cost-effective alternative to other construction methods, its use can become economical.

RESEARCH SIGNIFICANCE

This work examined the LPW mixture to produce a cheap and lightweight composite as a building material. The tests were conducted on concrete to replace 30, 50, and 70% by weight of coarse aggregate. The mechanical properties of the concrete comply with international standards.

This work is significant in that it will show how waste disposal technology can convert the cause of social and environmental disasters into a natural resource for use in post-construction projects. It has been confirmed that LPW can be used as a raw material to produce cement and concrete. LPW is available and can be used in Algeria as a natural lightweight aggregate. A research program was undertaken to study the comparative properties of concrete using LPW as a lightweight coarse aggregate.

Table 3—Density, compressive strength, flexural strength, modulus of elasticity, and Poisson's ratio results

Properties	Fraction of limestone, %	28 days	90 days	180 days
Density, kg/m^3	30	2075	2027	2020
	50	2027	2020	1951
	70	2013	1942	1936
Compressive strength, MPa	30	31	23	19
	50	30	19	17
	70	27	16	13
Flexural strength, MPa	30	6.39	6.12	6.02
	50	5.89	5.75	5.61
	70	5.61	5.44	5.24
Modulus of elasticity (E), GPa	30	36	26	25
	50	26	24	20
	70	22	20	17
Poisson's ratio (γ)	30	0.18	—	—
	50	0.16	—	—
	70	0.15	—	—

EXPERIMENTAL PROCEDURE

The materials used in the prepared concrete mixtures are Algerian materials. The physical properties of materials are presented in References 15 and 16. The LPW coming from the quarry in East Algeria is subject to the NF P18-508 standard.[17] Its $CaCO_3$ content is higher than 98%. The specific surface is approximately 3000 cm^2/g and the characteristic size of the particle is 29 μm on average.

Three mixtures were used (Table 2); in all mixtures, the proportions by weight of cement and sand were constant. Aggregates are used dry (without prior impregnation). The order of introduction of the different materials follows the NF P18-404 standards.[18] Three 16 x 32 cm cylindrical samples were melted for each fraction. The samples remained in the molds for the first 24 hours and were then removed and air dried.

Development of compressive strength, flexural strength, Young's modulus, and Poisson's ratio of LPW concrete were tested up to approximately 180 days (Table 3).

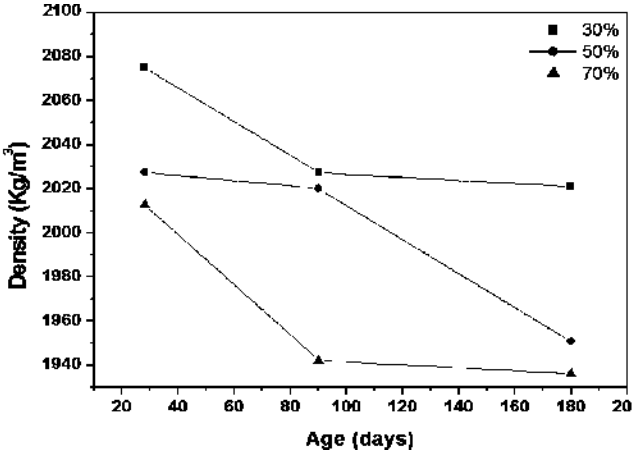

Fig. 1—Density of hardened concrete versus age.

RESULTS AND DISCUSSIONS

Dry density

In addition to the density of the aggregates, the density of the concrete also depends on the grain size of the aggregates, their moisture content, mixing ratios, cement content, water-binder ratio (*w*/*b*), mineral admixtures, and so on. Besides the material, it also depends on the compaction method, curing conditions, and so on.[19]

The 28-day density range for dry limestone dust was 2075 kg/m^3 for 30%, 2027 kg/m^3 for 50%, and 2013 kg/m^3 for 70% of coarse aggregates replacement (Fig. 1). These values correspond to LWC bulk densities between 550 and 2200 kg/m^3 for the replacement of limestone dust with normalweight aggregate[13] or structural LWC bulk densities between 1400 and 2100 kg/m^3.[20] The excellent properties of LWAC can be attributed to the physical and chemical interactions between the cement mortar and aggregate. The porous structure of the lightweight aggregates particles allows the cement gel to grow on the surface of the aggregate and improves its physical bonding.[21] The chemical reaction strengthens the bond. These interfacial physical and chemical processes between the cement mixture and aggregate surface contribute to the overall strength of the LWAC.

The identified physical process was densification of the interfacial transition zone after absorption of the aggregate. The internal moisture of the LWAC is maintained at a higher level for a longer period, resulting in a fully hydrated cement mixture. Thus, under less-favorable conditions, the properties of LWAC would be at least as good if not better than a similar class of ordinary concrete. In addition, the modulus of elasticity of lightweight aggregates is largely compatible with that of cement mortar; this reduces the tendency for microcracks. In addition, the combination of low thermal expansion and high resistance to deformation means that LWAC is significantly less prone to cracking under thermal stress conditions. Considering this, the long-term strength and durability development of LWAC is expected to be equal to, if not better than, that of normalweight concrete.[21]

The weight savings are approximately 14% at 30%, 15% at 50%, and 16% at 70% by replacing coarse aggregate compared to normal 2400 kg/m^3 concrete. This means that seismic forces are reduced by 14, 15, and 16%.[22] The reduced bulk density of a LWC is due to the addition of a void pattern in the concrete mixture.

The density decreased with increasing water-cement ratio (*w*/*c*) (increasing limestone dust content) (Fig. 1). The water content increases with the increasing *w*/*c* value. In addition, the amount of free water trapped in the pores of the paste evaporates; the effect is to increase the pore size and porosity of the cement mixture and thus reduce the weight of the resulting concrete.[22] The decrease in density with increasing age is due to the targeted opening of the pores with a slight increase in total porosity. The increased water absorption uptake is due to the increased permeability of the pore space, which provides a space to be filled with water, and the increased permeability of the hardened paste. Drying is a phenomenological process to which most concrete structures are subjected during use, the mechanism of which forces the water contained in the pores to move the drying surface. The moisture content of concrete therefore varies both spatially and temporally.

Compressive strength

LWCs are classically characterized by their density. This parameter depends on both the porosity and density of the matrix; the density gives inaccurate information about the quantitative aspect of the porosity.

The relationship between density and mechanical properties is a common approach used for lightweight concretes. The change in strength as well as the change in the composition parameters results from the porosity.[23] In general, the lower the density (Fig. 1), the lower the strength (Fig. 2).

Figure 2 shows the compressive strength results. With increasing LPW content, the compressive strengths decreased in all test ages. The compressive strengths at 28 days were 12 to 82% higher than the required minimum strength of 17 MPa for structural LWC.[24] In some structural applications, such as tall buildings and long-span bridges, the unit weight of concrete is almost as important as its strength. Reducing unit weight without reducing strength, or increasing strength without increasing unit weight, allows reduced cross sections and spans, increasing the percentage of space in structures and reducing the amount of concrete required.

LWC is typically 25 to 35% lighter but comparable in strength to ordinary concrete.[25] The 28-day compressive strength (Fig. 2) decreases as the proportion of LPW increases, because the coarse gravel aggregate is replaced by LPW.

All series with LPW developed strength more than 15 MPa. The values range from 19 to 31 MPa and meet the criteria for semi-lightweight structural concrete.[26] The greater relative strength gain of the 30% substitution is due to better bonding between lightweight aggregates and the binder paste. A lower *w*/*c* is typically required for lightweight aggregates to achieve sufficient strength.[27]

However, LPW of lower strength can be used to manufacture lightweight building blocks.[3] Much lighter LPW concrete can be obtained by partial or full replacement of fine aggregates as well as full replacement of coarse aggregates

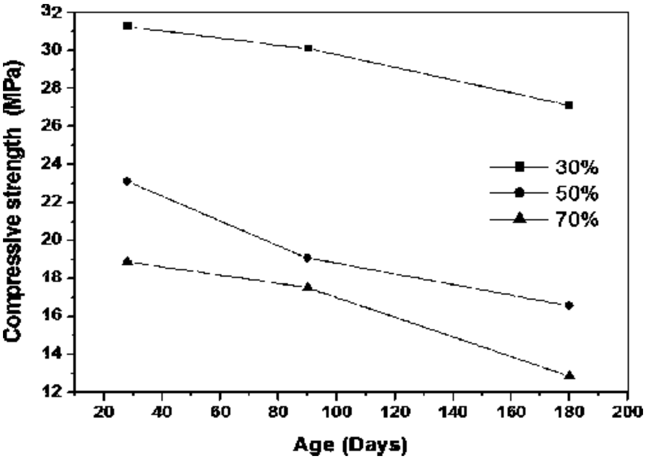

Fig. 2—Compressive strength of hardened concrete versus age.

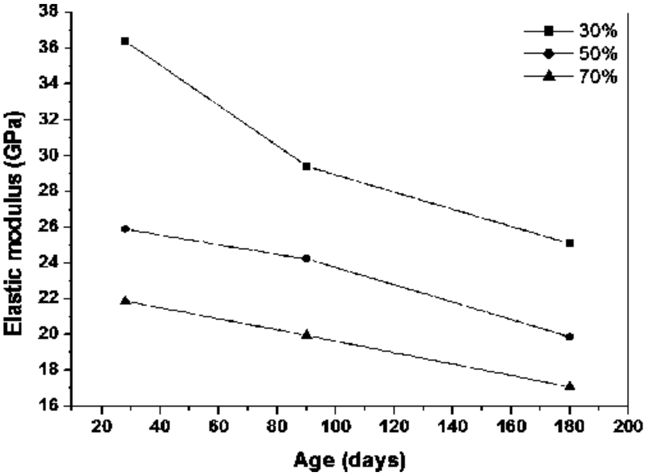

Fig. 3—Elastic modulus of hardened concrete versus age.

by using a combination of fine and coarse LPW,[28] according to the particle size requirements suggested by ASTM C330.

Figure 2 shows the development of compressive strength with LPW content at 28, 90, and 180 days of concrete age. As expected, a decrease in compressive strength was observed, with increasing limestone dust exchange rate. An increase of LPW leads to the formation of an excess of fine-grained fraction, which begins to displace cement grains, which leads to unpacking and leads to a significant decrease in strength. The cement paste is trapped in the pores on the surface of the lightweight aggregates. The pores surface allows the cement slurry to interlock to form a better interfacial bond between the aggregate and mortar at the interface.[29]

Concrete is a three-phase composite whose properties depend on the properties of the lightweight aggregate, hardened cement paste, and the interface zone. In the interface zone, the surface area of the pores increases while the strength of concrete decreases. It has been found that an increase of lightweight aggregate leads to the formation of an additional porous interfacial zone, which influences the strength of the concrete.[30]

On the other hand, it has been found that the lightweight air-dried aggregates incorporated into the concrete mixture can absorb more than 20% of the mixture water. So, the high absorbency after air-drying of a lightweight aggregate reduces the free *w*/*c* for the initial phase of the hydration reaction resulting in higher strength development, which would occur at an early age,[15] while the long aging strength is unfavorable (Fig. 2).[31] In practice, an increase in the *w*/*c* may be necessary, which can affect the porosity, mechanical properties, and durability.[12]

Elastic modulus

The modulus of elasticity of concrete is a basic mechanical parameter for the design and assessment of concrete structures. Figure 3 presents the results of the Young's modulus elasticity *E* tests. Each value presented is the average of three measurements. The results confirmed that the modulus of elasticity for concrete with 30% LPW is 36 GPa, while it is 26 GPa for concrete with 50% LPW and 22 GPa for concrete with 70% LPW (Fig. 3). LWC would have lower elastic modulus values. This is because the elastic modulus value depends on the elastic modulus of the aggregates.

This is by no means an undesirable property, as reducing the *E*-value allows large deflections in vibration or earthquakes, giving the structure greater ductility. The use of LWC allows for greater design flexibility and significant cost savings, reduced dead load, improved structural response to cyclic loading, longer spans, better fire ratings, thinner sections, smaller structural members, and lower foundation costs.[25] On the other hand, these values should not be too small as to cause extreme deviations under normal operating.[32] For the same strength, LWAC *E* is generally between 40 and 80% of ordinary concrete.[28]

The improvement of *E* is influenced by the type of coarse aggregate, the type of cement, the *w*/*c* of the mixture, and the curing age. *E* values vary from 22 to 36 GPA at 28 days (Fig. 3) when compressive strength varies from 27 to 31 MPa (Fig. 2). Concrete *E* is a compressive strength property and increases with increasing compressive strength. Various building codes have provided empirical equations for *E* and compressive strength. The *E*-value of concrete depends on the stiffness of the coarse aggregate, the interface between aggregates and paste, and the elastic properties of the materials.[28]

Due to the negligible Young's modulus of lightweight aggregates, increasing the aggregates content in the mixture increases the elastic incompatibility between the inclusion and the matrix and thus increases the contact interface of the stress concentration bond. This significantly reduces the modulus of elasticity.[20]

Unfortunately, the aggregates used to reduce the unit weight of concrete tend to degrade its elastic properties, modulus of elasticity, and strength. For a given type of aggregate, there is a strong relationship between the cement content, the volume fraction of the aggregate, and the compressive strength and elastic properties. The elastic properties of the aggregate have a large influence on the elastic modulus due to the relatively good bonding of the aggregate to the cementitious material.[33]

The modulus of elasticity of limestone dust LWC depends on the *w*/*c*, the strength of the concrete, and its density. It can be observed that *E* decreases with increasing *w*/*c* value

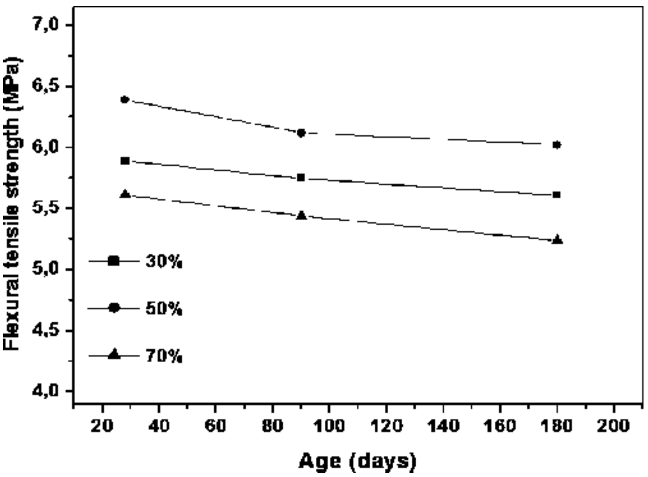

Fig. 4—Flexural tensile strength of hardened concrete versus age.

(increase in limestone dust content) (Fig. 3). The modulus values vary with *w/c* and strength and their relationship is typical of LWC. Due to the high water absorption of the limestone dust and the resulting large fluctuations in moisture content, the water addition is not easy to control. This situation worsens when the concrete is semi-dry.[34]

The *E*-value changes are shown in Fig. 3, which shows that there was slight deterioration in LWC stiffness between 90 and 180 days. The *E* value underwent a significant change from 28 to 180 days and the deterioration of its value is evident. This decrease in modulus can be attributed to the initiation of microcracks and introduction of tensile stresses due to drying shrinkage of the samples.

It is important to note that comparing the development of compressive strength in LWC leaves no doubt that compressive strength, in this case, is not synonymous with durability. Also, changing in modulus with time seems to be a better indicator of durability in this case. Within the ingress of moisture into the concrete, which triggers reinforcement corrosion and other degradation mechanisms, water extent penetrability is a better indicator of durability.[35]

In summary, the *E*-values of concrete decrease with increasing limestone dust content (Fig. 3). This is attributed to[36]:

1. Limestone dust having a lower modulus of elasticity than the cement paste; and

2. The compressive strengths of mixtures having been significantly reduced. It is commonly known that concretes with low compressive strengths (Fig. 2) have lower *E*-values.

Flexural tensile strength

Flexural strength and modulus of elasticity are important properties in concrete structural design as they affect bond strength, shear strength, brittleness ratio, and flexural cracking.[24]

Figure 4 illustrates flexural strength and percentage replacement of LPW. The flexural strengths of the samples with 30, 50, and 70% LPW were 6.39, 5.89, and 5.61 MPa. Similar to the compressive strength results (Fig. 2), the flexural strength samples were reduced. According to the literature, the flexural tensile strength of concrete is influenced by the properties of the interfacial transition zone (ITZ).[37]

Strength and cracking of concrete are influenced by the shape of the aggregate. With high-strength concrete, the strength of concrete is based on the strength of the aggregate and the bond at the interfaces.[38]

Lightweight aggregates have higher water absorption than normal concrete due to their porosity, and have a self-curing function in the interface zone. The water collected in the ITZ migrates through the surface pores to the lightweight aggregate. As the cement hydrates, this localized water is released into the interface. Therefore, the strength of the LWAC depends on the strength of the lightweight aggregate-cement paste and the aggregate/cement paste interface. The water that collects through the aggregate does not penetrate the lightweight aggregate as it does with porous aggregates. Therefore, as with ordinary concrete, walling occurred, resulting in a porous ITZ.

This result is consistent with previous studies showing that the interface of a lightweight aggregate depends on its surface porosity. As the *w/c* of the concrete increases, the pores both increase in the cement paste and the aggregate/cement paste interface. Pores have a significant impact on the strength of concrete. An increase in the number of pores leads to a proportionally lower strength. The use of high-strength lightweight aggregates takes advantage of the wall effect, together with the high porosity at the aggregate/cement paste interface, as found in ordinary concrete.[39]

The flexural strength at 28 days for the different mixtures showed similar compressive strength results. As the amount of LPW increased, the flexural strength decreased, as shown in Fig. 4.

Flexural strength is influenced by the same factors as compressive strength, namely the *w/c*, which in turn influences the bond between aggregates and cement.[36,40] The smooth surface of the LPW and free water that accumulates on the surface of LPW grains can make the limestone particles bond more weakly with the cement pastes.[36]

Flexural strength is more sensitive to internal structure features (such as porosity and microcracks) than compressive strength. The minimum allowable flexural strength (0.65 MPa), which meets the requirements of the specification, was met for all samples.[41]

In the case of lightweight concrete, the lightweight aggregate is weaker than the bond strength between the aggregate and the cement paste, causing cracks in the aggregate. With increasing lightweight aggregate content, the number of lightweight aggregate particles per unit cross section increases, which leads to a decrease in strength.[42] Figure 4 shows the development of flexural strength with the proportion of LPW. The flexural strength decreased with increasing age in all concrete samples. The effect of LPW on the flexural strength of concrete was similar to its effect on compressive strength.

Increasing the flexural strength of concrete has the advantage that the corrosion resistance of this concrete is improved. The flexural strength of concrete is one of the parameters affecting the corrosion rate of reinforcement. The increase in

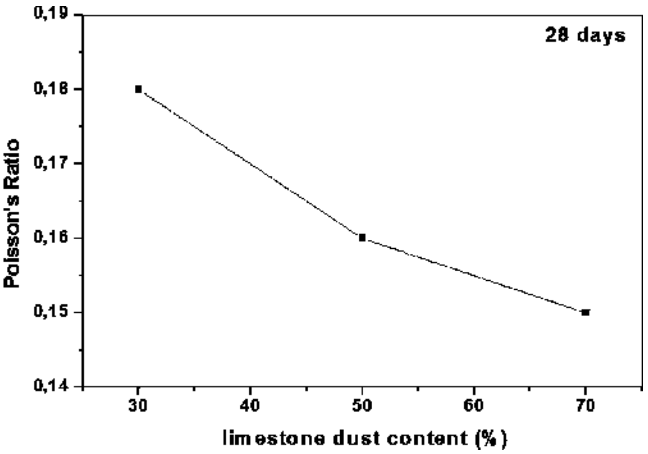

Fig. 5—Poisson's ratio of hardened concrete versus LPW content.

flexural strength indicates a potential increase in the service life of concrete structures.[29]

Normally, for a given compression resistance, LWC has a lower tensile strength than conventional concrete. In general, the compressive strength is greater than 15 MPa and the flexural strength is greater than 3 MPa.[43] Due to the good adhesion of porous aggregates to the matrix of LWC mixtures, they resemble ordinary concrete. However, using a finely porous material to make the LWC mixture reduces the flexural tensile strength of the LWC.

Poisson's ratio

Poisson's ratios of mixtures are shown in Fig. 5; each value presented is the average of three measurements. The value of the mixtures (0.11 to 0.18) is similar to that reported by others.[36]

CONCLUSIONS

This paper shows how waste disposal technology can convert the cause of social and environmental disasters into a natural resource, and then be used in post-construction projects. It has been confirmed that limestone dust (LPW) can be used as a raw material to manufacture cement and concrete production. Replacing LPW in a batch of concrete reduces all its properties such as the strength. The decreases are also visible in the unit weight. The unit weights of concrete with 30% LPW are approximately 2075 kg/m^3 and 14% lighter than ordinary concrete. It may be appropriate to use 30% in concretes where compression and tensile are important. Consequently, from the concrete mixture with a cement dosage of 350 kg/m^3, it can be seen that it would be possible to produce a structural lightweight concrete (LWC) with a unit weight of 2075 kg/m^3 and a compressive strength of 36 MPa. The flexural tensile strength at 28 days decreases from 6.39 to 5.61 MPa with an increase in the LPW from 30 to 70%. The 28-day Young's modulus *E* decreases from 36 to 22 GPa with an increase in the LPW content from 30 to 70%.

Based on the experimental results obtained so far, the following observations and conclusions can be drawn:

1. LPW can be used as a substitute for the conventional coarse aggregates in concrete production.
2. Limestone concrete easily meets the compressive strength requirements of LWC structures.

AUTHOR BIOS

Saida Kitouni *is a Lecturer in the Department of Process Engineering - Constantine 3, University of Constantine, Constantine, Algeria, where she received her PhD in physics in 2013. Her research interests include porcelains and lightweight concretes.*

ACKNOWLEDGMENTS

This study was conducted under the guidance of H. Houari in the Laboratoire Matériaux ET Durabilité des Constructions (LMDC), Department of Civil Engineering, University of Constantine, Constantine, Algeria.

REFERENCES

1. Vali, K. S., and Murugan, S. B., "Effect of Different Binders on Cold-Bonded Artificial Lightweight Aggregate Properties," *Advances in Concrete Construction*, V. 9, No. 2, 2020, pp. 183-193.
2. Hanif, S.; Lu, Z.; Cheng, Y.; Diao, S.; and Li, Z., "Effects of Different Lightweight Functional Fillers for Use in Cementitious Composites," *International Journal of Concrete Structures and Materials*, V. 11, No. 1, 2017, pp. 99-113. doi: 10.1007/s40069-016-0184-1
3. Turk, K., and Demirhan, S., "The Mechanical Properties of Engineered Cementitious Composites Containing Limestone Powder Replaced by Microsilica Sand," *Canadian Journal of Civil Engineering*, V. 40, No. 2, 2013, pp. 151-157. doi: 10.1139/cjce-2012-0281
4. Zorić, D.; Lazar, D.; Rudic, O.; Radeka, M.; Ranogajec, J.; and Hirsenberger, H., "Thermal Conductivity of Lightweight Aggregate Based on Coal Fly Ash," *Journal of Thermal Analysis and Calorimetry*, V. 110, No. 1, 2012, pp. 489-495. doi: 10.1007/s10973-012-2339-x
5. Malenšek, N.; Ducman, V.; and Mirtič, B., "Recycled Granulate Obtained from Waste Alumina-Rich Refractory Powder by the Cold Bonding Process," *Ceramics International*, V. 41, No. 7, 2015, pp. 8996-9002. doi: 10.1016/j.ceramint.2015.03.214
6. Tafheem, Z.; Rakib, R. I.; Esharuhullah, M. D.; Reduanul Alam, S. M.; and Mashfiqul Islam, M., "Experimental Investigation on the Properties of Concrete Containing Post-Consumer Plastic Waste as Coarse Aggregate Replacement," *Journal of Materials and Engineering Structures*, V. 5, No. 1, 2018, pp. 23-31.
7. Nadeem, M., and Pofale, A. D., "Utilization of Industrial Waste Slag as Aggregate in Concrete Applications by Adopting Taguchi's Approach for Optimization," *Open Journal of Civil Engineering*, V. 2, No. 3, 2012, pp. 96-105. doi: 10.4236/ojce.2012.23015
8. Nwafor, E. O., and Aho, M. I., "Partial Replacement of River Gravel with Crushed Granite to Determine the Optimum Compressive Strength of Concrete," *International Journal of Civil Engineering and Construction Science*, V. 5, No. 1, 2018, pp. 1-6.
9. Winsley, B., and Muthukannan, M., "Expanded Fly Ash Clay Aggregate a Sustainable Alternative Coarse Aggregate for Concrete," *Journal of Materials and Engineering Structures*, V. 5, No. 4, 2018, pp. 347-353.
10. Sharkawi, A. M.; Almofty, S. M.; and Abbass, S. M., "Performance of Green Aggregate Produced by Recycling Demolition Construction Wastes (Case Study of Tanta City)," *Engineering*, V. 8, No. 2, 2016, pp. 52-59. doi: 10.4236/eng.2016.82006
11. Salau, M. A.; Ikponmwosa, E. E.; and Adeyemo, A. O., "Shrinkage Deformation of Concrete Containing Recycled Coarse Aggregate," *British Journal of Applied Science and Technology*, V. 4, No. 12, 2014, pp. 1791-1807. doi: 10.9734/BJAST/2014/3950
12. Michel, F., and Courard, L., "Natural Limestone Filler: Physical and Chemical Properties with Regard to Cement Based Materials Properties," International Congress on Durability of Concrete (ICDC) 2012, Trondheim, Norway, June 2012, pp. 1-12.
13. Sadrmomtazi, A.; Sobhani, J.; Mirgozar, A.; and Najimi, M., "Properties of Multi-Strength Grade EPS Concrete Containing Silica Fume and Rice Husk Ash," *Construction and Building Materials*, V. 35, 2012, pp. 211-219. doi: 10.1016/j.conbuildmat.2012.02.049
14. Tanyildizi, H., "Prediction of Compressive Strength of Lightweight Mortar Exposed to Sulfate Attack," *Computers and Concrete*, V. 19, No. 2, 2017, pp. 217-226. doi: 10.12989/cac.2017.19.2.217
15. Kitouni, S., and Houari, H., "Lightweight Concrete with Algerian Limestone Dust: Part I: Study on 30% Replacement to Normal Aggregate at Early Age," *Cerâmica*, V. 59, No. 352, 2013, pp. 600-608. doi: 10.1590/S0366-69132013000400017

16. Kitouni, S., and Houari, H., "Lightweight Concrete with Algerian Limestone Dust. Part II: Study on 50% and 100% Replacement to Normal Aggregate at Timely Age," *Cerâmica*, V. 61, No. 360, 2015, pp. 462-468. doi: 10.1590/0366-69132015613601957

17. NF P18-508, "Additions for Concrete - Limestone Additions - Specifications and Conformity Criteria," Association Française de Normalisation, Paris, France, 2012.

18. NF P18-404, "Concretes. Study, Suitability and Control Tests. Manufacture and Storage of Test Specimens," Association Française de Normalisation, Paris, France, 1982.

19. Spiesz, P.; Rouvas, S.; and Brouwers, H. J. H., "Utilization of Waste Glass in Translucent and Photocatalytic Concrete," *Construction and Building Materials*, V. 128, 2016, pp. 436-448. doi: 10.1016/j.conbuildmat.2016.10.063

20. Li, C.; Miao, L.; You, Q.; Hu, S.; and Fang, H., "Effects of Viscosity Modifying Admixture (VMA) on Workability and Compressive Strength of Structural EPS Concrete," *Construction and Building Materials*, V. 175, 2018, pp. 342-350. doi: 10.1016/j.conbuildmat.2018.04.176

21. Al-Khaiat, H., and Haque, N., "Strength and Durability of Lightweight and Normal Weight Concrete," *Journal of Materials in Civil Engineering*, ASCE, V. 11, No. 3, 1999, pp. 231-235. doi: 10.1061/(ASCE)0899-1561(1999)11:3(231)

22. Tang, W. C.; Fan, K. H.; Tsai, W. P.; and Chen, H. J., "Properties of Lightweight Concrete Masonry Units Made from Lightweight Aggregates," *Advanced Materials Research*, V. 150-151, 2010, pp. 1588-1594. doi: 10.4028/www.scientific.net/AMR.150-151.1588

23. Cabrillac, R.; Fiorio, B.; Beaucour, A.; Dumontet, H.; and Ortola, S., "Experimental Study of the Mechanical Anisotropy of Aerated Concretes and of the Adjustment Parameters of the Introduced Porosity," *Construction and Building Materials*, V. 20, No. 5, 2006, pp. 286-295. doi: 10.1016/j.conbuildmat.2005.01.023

24. Teo, D. C. L.; Mannan, M. A.; Kurian, V.; and Ganapathy, C., "Lightweight Concrete Made from Oil Palm Shell (OPS): Structural Bond and Durability Properties," *Building and Environment*, V. 42, No. 7, 2007, pp. 2614-2621. doi: 10.1016/j.buildenv.2006.06.013

25. Lo, T. Y., and Cui, H. Z., "Properties of Green Lightweight Aggregate Concrete," International Workshop on Sustainable Development and Concrete Technology, Beijing, China, May 2004, pp. 113-118.

26. Abouhussien, A. A.; Hassan, A. A. A.; and Ismail, M. K., "Properties of Semi-Lightweight Self-Consolidating Concrete Containing Lightweight Slag Aggregate," *Construction and Building Materials*, V. 75, 2015, pp. 63-73. doi: 10.1016/j.conbuildmat.2014.10.028

27. Lo, T. Y.; Tang, W. C.; and Nadeem, A., "Comparison of Carbonation of Lightweight Concrete with Normal Weight Concrete at Similar Strength Levels," *Construction and Building Materials*, V. 22, No. 8, 2008, pp. 1648-1655. doi: 10.1016/j.conbuildmat.2007.06.006

28. Hossain, K. M. A., "Properties of Volcanic Pumice Based Cement and Lightweight Concrete," *Cement and Concrete Research*, V. 34, No. 2, 2004, pp. 283-291. doi: 10.1016/j.cemconres.2003.08.004

29. Mouli, M., and Khelafi, H., "Performance Characteristics of Lightweight Aggregate Concrete Containing Natural Pozzolan," *Building and Environment*, V. 43, No. 1, 2008, pp. 31-36. doi: 10.1016/j.buildenv.2006.11.038

30. Lo, T. Y.; Cui, H. Z.; Tang, W. C.; and Leung, W. M., "The Effect of Aggregate Absorption on Pore Area at Interfacial Zone of Lightweight Concrete," *Construction and Building Materials*, V. 22, No. 4, 2008, pp. 623-628. doi: 10.1016/j.conbuildmat.2006.10.011

31. Yang, K. H.; Song, J. K.; and Lee, J. S., "Properties of Alkali-Activated Mortar and Concrete Using Lightweight Aggregates," *Materials and Structures*, V. 43, No. 3, 2010, pp. 403-416. doi: 10.1617/s11527-009-9499-6

32. Kayali, O., "Fly Ash Lightweight Aggregates in High Performance Concrete," *Construction and Building Materials*, V. 22, No. 12, 2008, pp. 2393-2399. doi: 10.1016/j.conbuildmat.2007.09.001

33. Kurugöl, S.; Tanacan, L.; and Ersoy, H. Y., "Young's Modulus of Fibber-Reinforced and Polymer-Modified Lightweight Concrete Composites," *Construction and Building Materials*, V. 22, No. 6, 2008, pp. 1019-1028. doi: 10.1016/j.conbuildmat.2007.03.017

34. Gündüz, L., "The Effects of Pumice Aggregate/Cement Ratios on the Low-Strength Concrete Properties," *Construction and Building Materials*, V. 22, No. 5, 2008, pp. 721-728. doi: 10.1016/j.conbuildmat.2007.01.030

35. Haque, M. N.; Al Khaiat, H.; and Kayali, O., "Long-Term Strength and Durability Parameters of Lightweight Concrete in Hot Regime: Importance of Initial Curing," *Building and Environment*, V. 42, No. 8, 2007, pp. 3086-3092. doi: 10.1016/j.buildenv.2006.10.032

36. Kou, S. C.; Lee, G.; Poon, C. S.; and Lai, W. L., "Properties of Lightweight Aggregate Concrete Prepared with PVC Granules Derived From Scraped PVC Pipes," *Waste Management (New York, N.Y.)*, V. 29, No. 2, 2009, pp. 621-628. doi: 10.1016/j.wasman.2008.06.014

37. Tang, C. W., "Uniaxial Bond Stress-Slip Behaviour of Reinforcing Bars Embedded in Lightweight Aggregate Concrete," *Structural Engineering and Mechanics*, V. 62, No. 5, 2017, pp. 651-661.

38. Zhang, C.; Zhou, W.; Ma, G.; Hu, C.; and Li, S., "A Meso-Scale Approach to Modelling Thermal Cracking of Concrete Induced by Water-Cooling Pipes," *Computers and Concrete*, V. 15, No. 4, 2015, pp. 485-501. doi: 10.12989/cac.2015.15.4.485

39. Wongkvanklom, A.; Posi, P.; Khotsopha, B.; Ketmala, C.; Pluemsud, N.; Lertnimoolchai, S.; and Chindaprasirt, P., "Structural Lightweight Concrete Containing Recycled Lightweight Concrete Aggregate," *KSCE Journal of Civil Engineering*, V. 22, No. 8, 2018, pp. 3077-3084. doi: 10.1007/s12205-017-0612-z

40. Sabau, M., and Vargas, J. R., "Use of E-Plastic Waste in Concrete as A Partial Replacement of Coarse Mineral Aggregate," *Computers and Concrete*, V. 21, No. 4, 2018, pp. 377-384.

41. Turgut, P., "Masonry Composite Material Made of Limestone Powder and Fly Ash," *Powder Technology*, V. 204, No. 1, 2010, pp. 42-47. doi: 10.1016/j.powtec.2010.07.004

42. Domagała, L., "Modification of Properties of Structural Lightweight Concrete with Steel Fibres," *Journal of Civil Engineering and Management*, V. 17, No. 1, 2011, pp. 36-44. doi: 10.3846/13923730.2011.553923

43. Hong, J.; Chen, Z.; Huang, Y.; Cao, Y.; Geng, S.; Zhang, Y.; Zou, X.; and Lu, X., "Fabrication and Characterization of Lightweight Aggregate Prepared From Steel Mill Sludge in one Step," *Journal of Material Cycles and Waste Management*, V. 24, No. 3, 2022, pp. 1072-1082. doi: 10.1007/s10163-022-01385-x

ARE YOU A RESEARCHER?

SIGN UP FOR ORCID TODAY!

ORCID provides a persistent digital identifier that distinguishes you from every other researcher and, through integration in key research workflows such as manuscript and grant submission, supports automated linkages between you and your professional activities, ensuring that your work is recognized.

Individuals may use ORCID services freely and it's as easy as **1-2-3**:

1. REGISTER
2. ADD YOUR INFO
3. USE YOUR ORCID ID

For more information and to register, visit:

WWW.ORCID.ORG

ACI MATERIALS JOURNAL TECHNICAL PAPER

Title No. 120-M46

Pozzolanic Reactivity of Supplementary Cementitious Materials

by Keshav Bharadwaj, O. Burkan Isgor, and W. Jason Weiss

As the number of potential supplementary cementitious materials (SCMs) increase, there is a need to determine their reactivity. Most recent methods to assess pozzolanic reactivity are based on measuring certain outputs such as heat release (Q), calcium hydroxide (CH) consumption, and nonevaporable water. This paper uses thermodynamic modeling to aid in the interpretation of these tests and the quantification of reactivity. It is shown that pozzolanic reactivity should be interpreted based on the SCM type. The presence of sulfates and carbonates during reactivity quantification alter the reaction of the Al_2O_3 *phases, making the interpretation of the reactivity test results challenging. The reactivity of commercial SCMs should be interpreted specific to the type of SCM as described by ASTM International/AASHTO. A proposed interpretation for commercial SCMs is provided in this paper.*

Keywords: pozzolanic reactivity test (PRT); reactivity; supplementary cementitious materials (SCMs); thermodynamic modeling.

INTRODUCTION

The concrete industry has been actively working toward reducing the carbon footprint of concrete. One approach that is widely used to reduce the carbon footprint is to replace a portion of the ordinary portland cement (OPC) in concrete with supplementary cementitious materials (SCMs), which can also improve the performance of concrete. For example, the replacement of OPC with SCMs such as fly ash and silica fume in concrete have been shown to improve compressive strength,[1,2] reduce transport of deleterious ions by refining the pore structure,[1-5] control alkali-silica reaction (ASR) damage,[6,7] and mitigate the potential for calcium oxychloride formation and damage.[8-11] While questions exist regarding the future availability of some SCMs such as fly ash, partly due to the closure of coal combustion plants,[12] there are several other new sources for SCMs such as harvested ashes, agricultural/forest waste ash, municipal waste ash, and natural pozzolans that may be used in concrete.[12-19] However, there is a need for tests to screen and evaluate the performance of SCMs obtained from the new or modified sources for their appropriate use in concrete.[20]

The performance of concrete containing SCMs depends on the: 1) chemical and physical composition of the SCM[21,22]; 2) the reactivity of the SCM (that is, fraction of the phases in the SCM that can react)[1,23]; and 3) the kinetics of reaction of these phases.[24] Standards such as ASTM C618[25] or AASHTO M 295[26] (in the case of fly ash and natural pozzolans) specify the compositional and physical requirements for SCMs, but they do not provide a reliable method to assess how reactive these materials are. Over the years, various approaches have been used to try to ascertain the amount of SCM that can replace OPC, such as by predicting strengths using k-factors.[27,28] These empirical factors were used as a surrogate for the SCM reactivity. Some researchers have assumed the amorphous content as the reactive component of SCM.[29,30] Over the years, several test methods were developed to directly measure reactivity of SCMs for their use in concrete. Some of these are relatively old (for example, the Frattini test[31] or the Chapelle test[32]) and have documented limitations.[33-35] Newer methods to assess pozzolanic reactivity such as the ASTM C1987 test[36] (also known as the "R3 test"[37,38]) and the pozzolanic reactivity test (PRT)[23,33,39] are based on measuring certain outputs of the test to provide a better understanding of SCM reactivity. For example, the primary output of the R3 test is the weight of bound water when heated up to 400°C or the ultimate heat released, which can be used to provide a relative reactivity to compare SCMs of the same type. The outputs of the PRT are heat release (Q) and calcium hydroxide (CH) consumption, which are then used to obtain a numerical value of maximum degree of reactivity (DOR*) of an SCM.[39] The DOR* can also be used as an input to perform thermodynamic calculations and can be used to predict concrete properties for assessing performance.[3,20,40-45] The DOR* serves as a key parameter for performance-based concrete mixture design.[20]

In recent years, the use of Q and CH consumption as an indicator for pozzolanic reactivity has been extensively studied using experimental investigations.[3,23,29,33,37,39,41,46-60] It can be noted that examining these values as a function of time can provide information on the kinetics of SCM reactions. However, these experimental studies are limited by the types, chemical compositions, and reactivities of tested SCMs; therefore, it is not always possible to generalize their conclusions. Thermodynamic modeling of cementitious systems has been a powerful tool that can aid in interpreting experimental studies and has been shown to provide supporting insight to experiments. In this paper, the authors use thermodynamic modeling to explore various aspects of pozzolanic reactivity of SCMs.

The first question that this paper addresses is if the pozzolanic reactivity should be measured and/or interpreted differently for different types of SCMs. For example, in the present form, the PRT quantifies the reactivity of SCMs

---

ACI Materials Journal, V. 120, No. 4, July 2023.

MS No. M-2022-277.R1, doi: 10.14359/51738817, received August 26, 2022, and reviewed under Institute publication policies. Pertinent discussion including author's closure, if any, will be published ten months from this journal's date if the discussion is received within four months of the paper's print publication.

(DOR*) by comparing the measured Q and CH consumption with the theoretical values of Q and CH consumed by pure SiO_2 and pure Al_2O_3 at various degrees of reaction. This approach implies that the DOR* of siliceous materials such as silica fume and fly ash can be quantified accurately. However, the applicability of this approach to quantify the DOR* of silico-aluminous SCMs (for example, calcined clays) or those showing hydraulic properties (for example, slag) needs further investigation. Silico-aluminous SCMs contain comparable portions of silica and alumina, and alumina reactions could affect the interpretation of the Q and CH consumption output.[39] Hydraulic SCMs typically contain the reactions of CaO in the system, which affect the measured Q and CH consumption, while these reactions are not considered pozzolanic in nature. Therefore, in this paper, the effect of SCM type on the measurement and interpretation of pozzolanic reactivity is explored. The second question that this paper addresses is if the presence of sulfates and carbonates in the system affect the measurement and/or interpretation of the pozzolanic reactivity of SCMs. It is clear that the presence of sulfates and carbonates would induce additional reactions in the cementitious mixture, but whether or not these reactions should be considered as part of the measurement and interpretation of pozzolanic reactivity of SCMs need to be investigated further.

These questions are answered though the thermodynamic modeling of the PRT using various SCMs in different chemical conditions. The PRT is selected as a test method because it provided a numerical value of pozzolanic reactivity (that is, DOR*), and the measured outputs in the PRT (that is, Q and CH consumption) could be modeled through thermodynamic modeling. First, ideal SCMs comprising of only a combination of SiO_2 and Al_2O_3 were studied. The SiO_2:Al_2O_3 in the SCM is varied and the phases that form in the PRT (reaction products), Q, and CH consumed are examined. This investigation is intended to understand the interpretation of the reactivity of aluminous SCMs more accurately. Second, ideal SCMs that are combinations of SiO_2, Al_2O_3, and CaO were studied. The influence of CaO on the reaction products, Q, and CH consumed is examined. This investigation is intended to understand the interpretation of the reactivity of SCMs that show hydraulic properties better. Third, it was studied whether the presence of sulfates and carbonates affect the interpretation of the reactivity of SCMs containing SiO_2, Al_2O_3, and CaO. Finally, the first three modeling studies to commercially available SCMs with typical chemistries were expanded. The knowledge generated in this study allows for a more accurate quantification of the SCM reactivity, which can be used to improve the performance of concrete by allowing for the selection of the appropriate SCMs for use in concrete.[20]

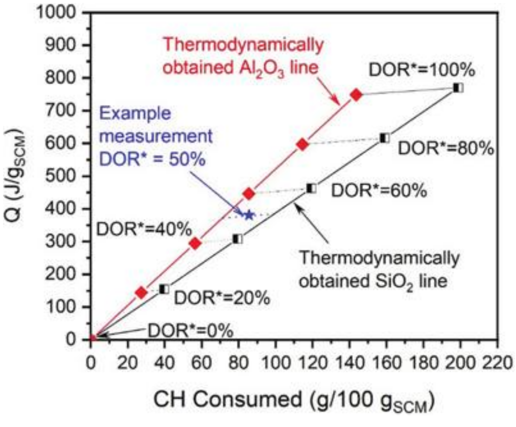

Fig. 1—Example schematic presentation of results of PRT on Q-CH consumed plot showing example experimental measurement, theoretical lines for pure SiO_2 and pure Al_2O_3, and interpolation to calculate DOR from experimental measurement.*

RESEARCH SIGNIFICANCE

This paper uses thermodynamic modeling to aid the interpretation of pozzolanic reactivity testing of SCMs. The study answers two key questions: 1) should the pozzolanic reactivity measured and/or interpreted differently for different types of SCMs based on the reaction products that form; and 2) does the presence of sulfates and/or carbonates in the system affect the measurement and/or interpretation of the pozzolanic reactivity of SCMs? The paper also makes recommendations to quantify the pozzolanic reactivity of commercial SCMs.

METHODS

Pozzolanic reactivity test (PRT) method

The PRT is a method to determine the DOR* of an SCM. The PRT is performed by reacting the SCM with an excess of CH (3:1 CH:SCM by mass) and an excess of an alkaline pore solution (0.5 N KOH solution; liquid-to-(CH+SCM) ratio is 0.90 by mass) at 50°C for 240 hours.[23,33] The test measures the Q of the reaction using an isothermal calorimeter (IC) and the CH consumed by the reaction using a thermogravimetric analyzer (TGA). For this test, only small amounts of the SCM are needed. In the standard procedure, 40 g of SCM is mixed with 120 g of CH and 144 g of 0.5 N KOH solution. Approximately 7 g of the paste is sealed in a glass ampule and loaded into the IC and the heat released is recorded for 240 hours. At the end of the 240 hours, approximately 20 mg of the reacted paste is loaded onto a platinum crucible of the TGA and the mass of CH remaining after the reaction is determined using the TGA using the approach developed by Kim and Olek.[61] The CH consumed is calculated as the difference between the initial mass of CH and the CH remaining after the reaction. In the PRT, the experimentally measured values of Q and CH consumed are plotted in the Q-CH consumed space. The theoretical Q and CH consumed of pure SiO_2 and pure Al_2O_3 are calculated using thermodynamic data and plotted as lines on the same plot. The value of DOR* is calculated by interpolating the experimental results between the theoretical SiO_2 and Al_2O_3 lines. Figure 1 is an illustration of the PRT showing an example measurement from an experiment, the theoretical lines obtained for pure SiO_2 and pure Al_2O_3, and the interpolation to obtain the DOR* of the SCM. The DOR* can also be quantified in the PRT using Eq. (1)[33]

$$\text{DOR*} = a_1Q + a_2CH_{consumed} \qquad (1)$$

where Q is measured in J/gSCM; $CH_{consumed}$ is measured in g/100g SCM; and a_1 and a_2 are constants (for the PRT, $a_1 = 1.44 \times 10^{-3}/(\text{J/g}_{SCM})$ and $a_2 = -0.54 \times 10^{-3}/(\text{g/100g}_{SCM})$, obtained from Reference 33).

Thermodynamic modeling

In this work, thermodynamic modeling is used to better interpret the PRT results by calculating the volume and compositions of the reaction products that form in the PRT as well as heat release during these reactions.[23,33,62,63] The calculations are done using GEMS3K[64] software in conjunction with the CemData v18.01[65] and PSI/Nagra[64] databases, which performs thermodynamic calculations by minimizing the Gibbs free energy of the reaction products for a given set of inputs compositions, and are used in conjunction with GEMS3K for the calculation of reaction products of cementitious systems. While all possible reaction products in cementitious systems are available in the CemData v18.01 database, the formation of some phases is blocked based on evidence from the literature that these phases do not form in significant quantities in the PRT.[65,66] The blocked phases are C_3AH_6,[66,67] Gibbsite,[65] and some AFm phases (C_4AH_{13}, C_4AH_{19}, C_4AsH_{12}). The Q is calculated by subtracting the total enthalpies of the reaction inputs from the total enthalpies of the reaction products, which are obtained from CemData v18.01 database[65] and the NIST Chemistry WebBook.[68]

RESULTS AND DISCUSSIONS

Ideal SCMs containing only SiO_2 and Al_2O_3

This section examines the phases that form, and the theoretical values of Q and CH consumed, when the proportions of SiO_2 and Al_2O_3 are varied when PRT is used to test an SCM containing only SiO_2 and Al_2O_3. Figure 2(a) shows the phases that form as the proportion of SiO_2 and Al_2O_3 is varied in an SCM that is 100% reactive when tested in the PRT. When the SCM contains only Al_2O_3, all alumina reacts to form $C_2AH_{7.5}$, releasing 748J/g_{SCM} heat and consuming 144 g of CH per 100 g SCM. As the proportion of silica in the SCM increases from 0% by weight to 36.65%, the silica and alumina preferentially react to form C_2ASH_8, and the remaining alumina (if any) reacts with the CH to form $C_2AH_{7.5}$. While it is generally considered that C_2ASH_8 and CH cannot coexist in the same system, the formation of C_2ASH_8 has been reported in experiments[69] in metakaolin+CH systems, in line with the model predictions. The Q decreases from 748 J/g_{SCM} (for 100% Al_2O_3) to 647 J/g_{SCM} (for 63.35% Al_2O_3 + 36.65% SiO_2). The CH consumed reduces from 144 g/100 g_{SCM} (for pure alumina) to 90 g/100 g_{SCM} (for 63.35% Al_2O_3 + 36.65% SiO_2). The

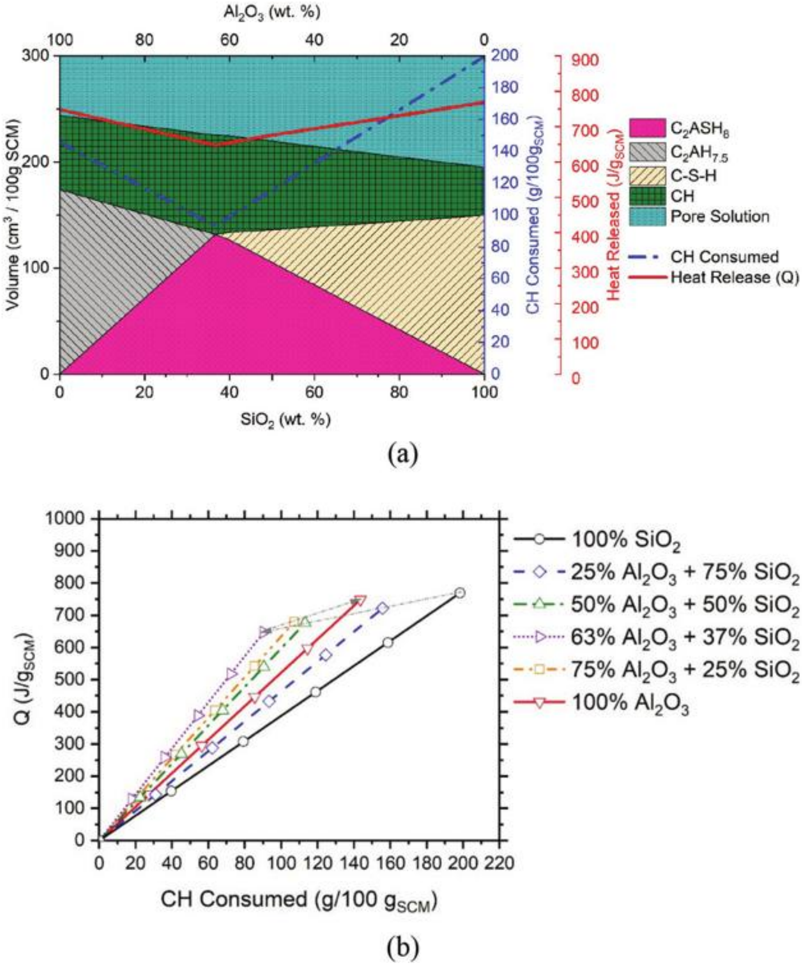

Fig. 2—(a) Phases that form as proportion of SiO_2 to Al_2O_3 is varied; and (b) reactivity lines: values of Q versus CH consumed for ideal SCMs containing varying proportions of SiO_2 and Al_2O_3.

Table 1—Reactions in PRT and their corresponding Q and CH consumed

Reaction No.	Reaction in PRT	Q, J/g_{SCM}
1	100 g SiO_2 + 198 g CH + $H_2O \rightarrow$ C-S-H	769
2	100 g Al_2O_3 + 144 g CH + $H_2O \rightarrow C_2AH_{7.5}$	748
3	100 g (Al_2O_3 + SiO_2) + 90 g CH + $H_2O \rightarrow C_2ASH_8$ (SiO_2: Al_2O_3 = 0.58 by wt.)	647
4	100g CaO + $H_2O \rightarrow$ CH	1149
5	100 g Al_2O_3 + 167 g gypsum + 215 g CH + $H_2O \rightarrow$ monosulfate	1244
6	100 g Al_2O_3 + 49 g $CaCO_3$ + 254 g CH + $H_2O \rightarrow$ hemicarbonate	1291
7	100 g Al_2O_3 + 98 g $CaCO_3$ + 218 g CH + $H_2O \rightarrow$ monocarbonate	1402

"critical composition" of 63.35% Al_2O_3+36.65% SiO_2 (when SiO_2:Al_2O_3 = 0.58) represents the minimum of Q and the minimum CH consumed for an SCM consisting of only SiO_2 and Al_2O_3 tested in the PRT, as C_2ASH_8 is the only phase formed. As the SiO_2 in the SCM increases from 36.65% to 100%, C_2ASH_8 + C-S-H forms. The Q increases from 647 J/g_{SCM} (for 63.35% Al_2O_3 + 36.65% SiO_2) to 769 J/g_{SCM} (for pure silica). The CH consumed increases from 90 g/100 g_{SCM} (for 63.35% Al_2O_3 + 36.65% SiO_2) to 198 g/100 g_{SCM} (for pure silica). The Q and CH consumed by the reactions in the PRT is summarized in Table 1. The composition of the C-S-H that is predicted to form in the PRT is uniform (C/S = 1.7), irrespective of the silica content in the SCM, as there is an excess of CH in the system. The impact of the C-S-H model used (CSHQ versus CNASH) is shown in Appendix A*; briefly, the CSHQ model is sufficient for calculating the DOR* of the SCM using the PRT.

Figure 2(b) shows the theoretical values of the Q versus the CH consumed for varying levels of reactivity for an SCM made with varying proportions of SiO_2 and Al_2O_3 plotted on the PRT-style plot. The term "reactivity line" refers to the line obtained by plotting the Q versus CH consumed obtained from thermodynamic calculations of the SCM composition. The SiO_2 reactivity line (line for an SCM made on only silica; black solid line with circle markers in Fig. 2(b)) is the rightmost line on the plot as the reaction of pure silica to form C-S-H results in the highest Q and highest CH consumed. As the mass fraction of alumina in the SCM is increased from 0 to 63.35%, the reactivity line shifts to the left (as shown in the figure with an arrow) due to a decrease in the CH consumed, and the length of the line decreases as the Q and CH consumed decrease as C_2ASH_8 forms at the expense of C-S-H. As the alumina content in the SCM is increased from 63.35 to 100% (pure alumina), the line shifts to the right (as shown in the figure with an arrow) due to an increase in the CH consumed, and the length of the line increases as the Q and CH consumed increase. The Al_2O_3 reactivity line (line for an SCM containing only alumina; red solid line with triangle markers in Fig. 2(b)) is still to the left of the SiO_2 reactivity line, as the CH consumed by the reaction of pure alumina is lower than the CH consumed by the reaction of pure silica.

The results shown in Fig. 2(b) offer insight into the typical behavior of SCMs, which do not contain significant CaO (for example, silica fume, Class F fly ashes, metakaolin calcined clays, and natural pozzolans such as pumice) in the PRT. Silica fume, which typically contains more than 85% SiO_2,[55,70,71] is expected to appear in the rightmost end of this plot as the reaction of silica to form C-S-H consumes the most CH and releases the most heat. Class F fly ashes or natural pozzolans, which typically contain 45 to 55% SiO_2 and 19 to 25% Al_2O_3,[40,55] would fall between the SiO_2 line and the 75% SiO_2 + 25% Al_2O_3 line. Metakaolin and calcined clays, which typically contain 50 to 60% SiO_2 and 30 to 45% Al_2O_3,[55] would fall on or around the 50% SiO_2 + 50% Al_2O_3 line.

Ideal SCMs containing SiO_2, Al_2O_3, and CaO

This section examines the phases that form Q and CH consumed in PRT when the proportions of CaO, SiO_2, and Al_2O_3 are varied in an ideal SCM containing only pure CaO, SiO_2, and Al_2O_3. Thermodynamic calculations predict that the reaction of CaO can be decoupled from the reaction of SiO_2 and Al_2O_3. The CaO (from the SCM) reacts with water to form CH (which is a hydraulic reaction), which can further react with the SiO_2 and Al_2O_3 to form C-S-H, C_2ASH_8, and $C_2AH_{7.5}$ depending on the SiO_2:Al_2O_3 in the SCM. Figure 3 shows the phase assemblage of an SCM containing 25% CaO with varying SiO_2 to Al_2O_3 masses. When the SCM contains only Al_2O_3 (no SiO_2), $C_2AH_{7.5}$ forms. As the mass of SiO_2 in the SCM increases from 0 to 27.5% in the SCM (the SiO_2:Al_2O_3 changes from 0 to 0.58), C_2ASH_8 forms along with $C_2AH_{7.5}$. This is associated with a corresponding decrease in Q and CH consumed. As the SiO_2 mass in the SCM increases from 27.5 to 75% (note that CaO = 25%, so the highest mass of SiO_2 in the SCM can be 75%), C-S-H phases form along with C_2ASH_8, which is associated with an increase in Q and CH consumed. The minimum of Q and CH consumed still occurs at a critical ratio of SiO_2 to Al_2O_3 in the SCM (SiO_2:Al_2O_3 = 0.58), and this value appears to be constant irrespective of the CaO content of the SCM. This is because the reaction of the SCM in the PRT when the SiO_2:Al_2O_3 = 0.58 forms only C_2ASH_8.

Figure 4(a) shows the phase assemblage of an SCM containing only SiO_2 and CaO, with an increasing CaO content. As the CaO content increases, the amount of CH in the system increases due to the reaction of CaO with water to produce CH. As the proportion of CaO in the SCM increases, the amount of SiO_2 in the SCM decreases

---

[*] The Appendix is available at **www.concrete.org/publications** in PDF format, appended to the online version of the published paper. It is also available in hard copy from ACI headquarters for a fee equal to the cost of reproduction plus handling at the time of the request.

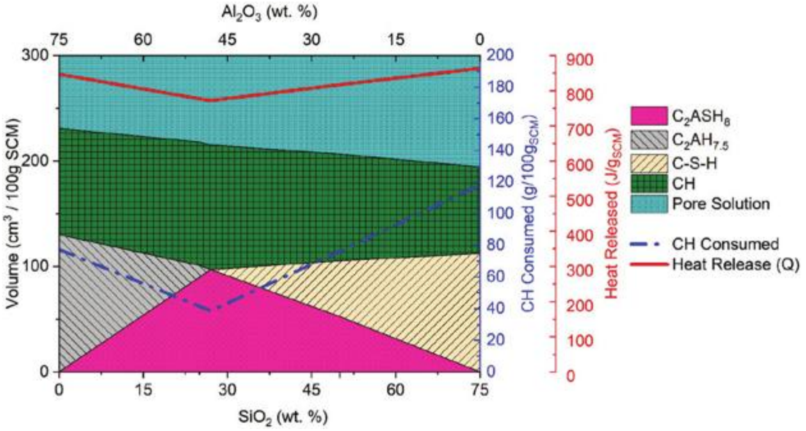

Fig. 3—Plot of phase assemblage for SCM containing 25% CaO with SiO_2:Al_2O_3 varying.

(because SiO_2 = 100% – CaO in this SCM), and the following are observed: 1) volume of C-S-H that forms at equilibrium decreases; 2) the Q increases as the reaction of CaO produces more heat than the reaction of SiO_2 in the PRT (refer to Table 1); and 3) the CH in the system increases due to the hydraulic reaction of CaO to form CH, which translates to a net reduction in CH consumed.

Figure 4(b) shows the phase assemblage of an SCM containing only Al_2O_3 and CaO, with an increasing CaO content. As the CaO content increases: 1) the volume of $C_2AH_{7.5}$ that forms decreases, as there is a lesser proportion of Al_2O_3; 2) the Q increases (the reaction of CaO that produces CH releases 401 J/g SCM more heat than the reaction of Al_2O_3 to form $C_2AH_{7.5}$; refer to Table 1); and 3) the CH in the system increases and there is a net reduction in CH consumed.

Figure 4(c) shows the phase assemblage of an SCM containing the critical mass ratio of SiO_2:Al_2O_3 = 0.58 and CaO, with an increasing CaO content. As the CaO content increases: 1) the volume of C_2ASH_8 that forms decreases due to the reduction in the amount of SiO_2+Al_2O_3 in the SCM; 2) the Q increases; and 3) the CH in the system increases due to this reaction. The Q and CH consumed by each reaction in the PRT is summarized in Table 1. Note that the Q is the cumulative heat released at complete reaction for the particular composition of SCM simulated.

Figure 5 shows a plot of how the reactivity lines vary when CaO is present in the SCM. SCMs containing 0, 25, 50, 75, and 100% wt. % CaO are shown. At each CaO content, three lines are shown: the remaining mass of SCM is SiO_2 (black solid line), the remaining mass of SCM is Al_2O_3 (red dashed line), and the remaining mass of the SCM is SiO_2 + Al_2O_3 in the critical mass ratio of SiO_2:Al_2O_3 = 0.58 (green dash-dot line) (full-color PDF can be accessed at www.concrete.org). As the CaO content of the SCM increases, the heights of all three lines increase (due to an increase in the Q) and the lines move to the left (a decrease in the CH consumed). This is because the reaction of CaO in the PRT produces more heat than the reaction of SiO_2, Al_2O_3, or a combination of SiO_2 and Al_2O_3 in the PRT. The reaction of CaO also causes a decrease in the CH consumed as the reaction of CaO results in the production of CH. This behavior is well corroborated by experiments,[55] where it is seen that SCMs containing a significant amount of CaO such as slag release 400 to 600 J/g$_{SCM}$ heat but consume only 20 to 60 g CH/100 g SCM. Note from Fig. 5 that the Q and CH consumed follow a linear behavior with respect to the CaO fraction in the SCM, which was seen in Fig. 4. If a line were to be drawn at any DOR* value (although only the 100% DOR* points are connected in Fig. 5), the Q and CH consumed plot follows a straight line from the 100% CaO to the 100% SiO_2 (thin dashed black line), 100% CaO to 100% Al_2O_3 (thin dotted red line), 100% CaO to 100% (SiO_2 + Al_2O_3) (thin dash-dot-dot green line) reactivity lines.

The practical implications of this finding are that it expands the scope of the PRT to determine the DOR* of hydraulic SCMs (such as slag) as well as pozzolans. Because the CaO reactions produce more heat than the reactions of SiO_2 and Al_2O_3 in the PRT, the reactivity lines used need to be revised when SCMs contain a significant amount of CaO. For example, slags typically contain 30 to 50% CaO, which means the Q measured in the PRT for slags will be 90 to 120 J/g SCM higher than pozzolanic SCMs such as silica fume and metakaolin for a 60% DOR*. The CH consumed by the slag of 60% reactivity would also be 40 to 80 g/100 g SCM lower than the silica fume or metakaolin of the same reactivity. If the appropriate CaO containing reactivity line is not used to determine the DOR*, and the pure SiO_2 and Al_2O_3 lines are used to determine DOR*, the reactivity would be erroneously determined to be 15 to 20% higher. Therefore, one should be careful while interpreting the Q and CH consumed from the PRT to measure the DOR* when the SCM contains CaO. This is explained later in this paper.

Influence of addition of sulfates and carbonates to pore solution

There is a debate in the literature on whether sulfates and carbonates should be added to tests when measuring the pozzolanic reactivity of SCMs.[33,37,38] The R3 test proposes the addition of sulfates and carbonates in an effort to mimic the pore solution chemistry of concrete,[37,38] while the PRT does not add sulfates and carbonates to measure only the Q and CH associated with the pozzolanic reaction.[33] This section of this paper aims to provide an insight into the changes to the reactions, Q, and CH consumed for SCMs of different chemistry when sulfates and carbonates are added

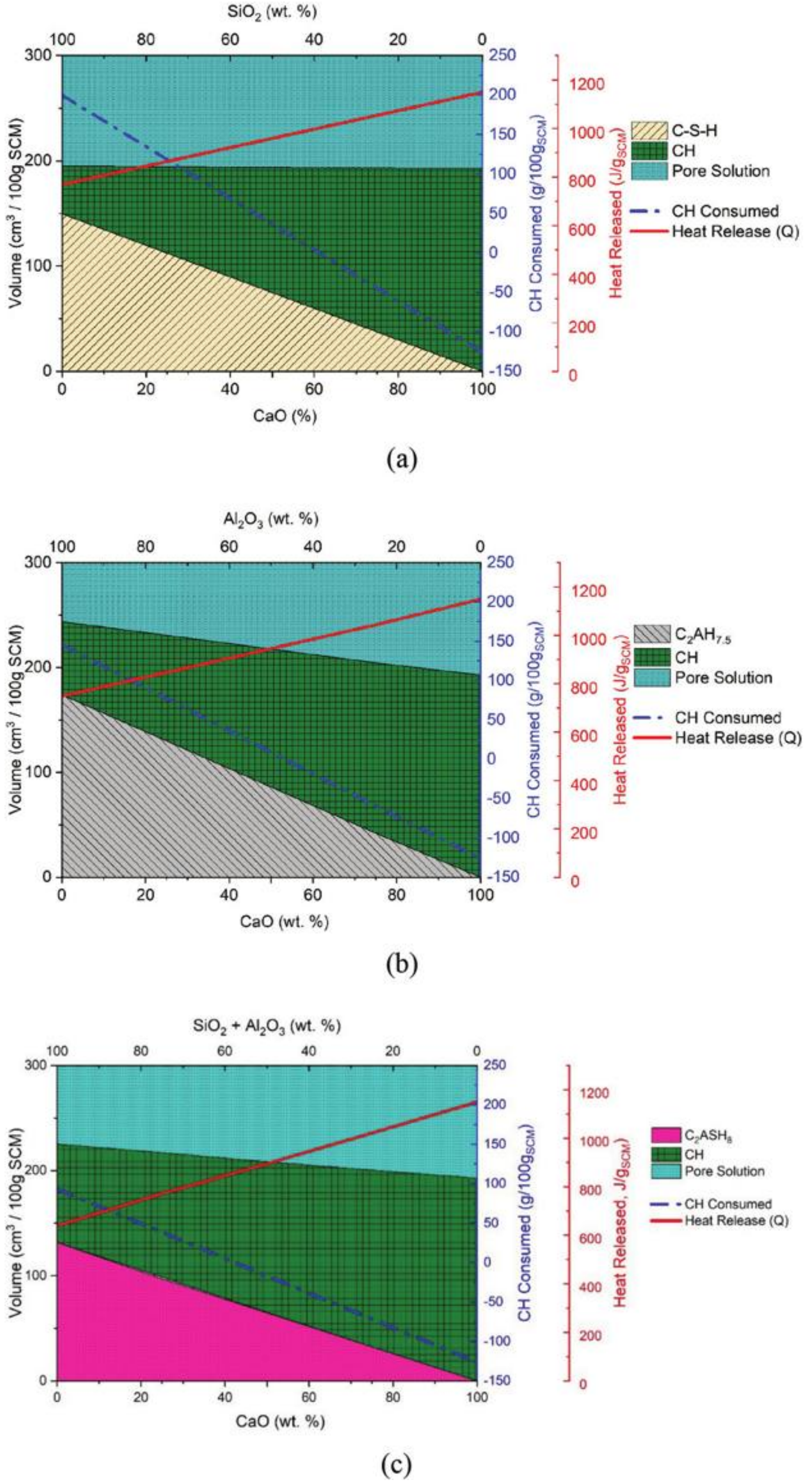

Fig. 4—Plot of phase assemblage, Q, and CH consumed for: (a) SCM containing only SiO_2 and CaO (no Al_2O_3), SiO_2:CaO varying; (b) SCM containing only Al_2O_3 and CaO (no SiO_2), Al_2O_3:CaO varying; and (c) SCM containing critical mass ratio of SiO_2:Al_2O_3 = 0.58, (SiO_2 + Al_2O_3):CaO varying.

to the pore solution in the PRT. Choudhary et al.[33] showed that the SiO_2 in the SCM does not react with the sulfates or carbonates, and the Al_2O_3 in the SCM reacts with the sulfates to form monosulfates and with carbonates to form carboaluminates preferentially at the expense of $C_2AH_{7.5}$ and C_2ASH_8. When both sulfates and carbonates are present, the compounds that form in the PRT can be a combination of monosulfate, carboaluminates, ettringite, C_2ASH_8, C-S-H, and $C_2AH_{7.5}$ phases depending on the molar ratio of sulfate to carbonate to alumina in the system[72] and the ratio of SiO_2 to Al_2O_3 in the SCM.

Figure 6(a) shows the phase assemblage of an SCM containing only SiO_2 and Al_2O_3 tested in the PRT when sulfates are added (as an example, 20 g gypsum/100 g_{SCM} addition is shown). When 100% Al_2O_3 is tested in the PRT, the Al_2O_3 preferentially reacts with the sulfates to

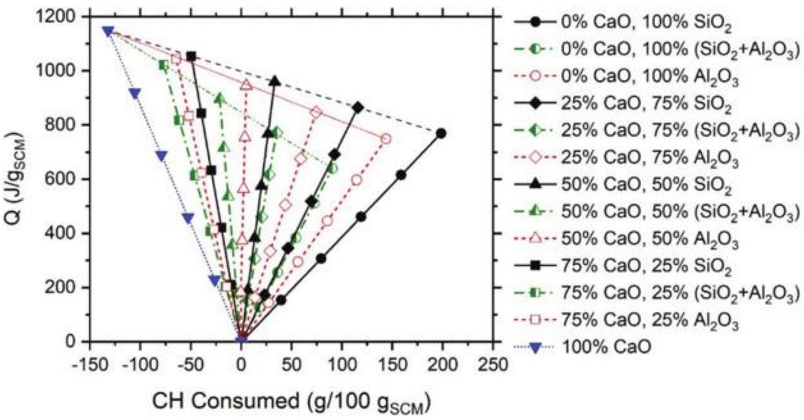

Fig. 5—Plot of Q versus CH consumed when SCMs of varying compositions are subject to PRT.

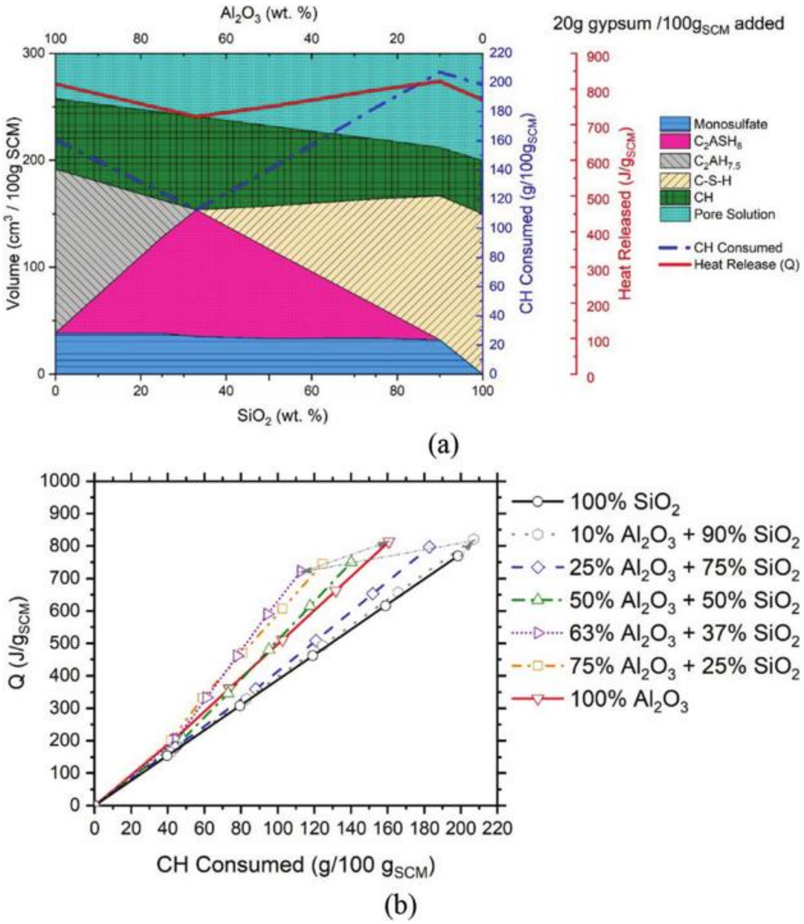

Fig. 6—(a) Plot of phases formed, Q, and CH consumed when sulfates are added to SCMs of varying compositions are subject to PRT; and (b) plot of Q versus CH consumed when SCMs of varying compositions are subject to PRT and 20 g gypsum is added.

produce monosulfates, and any remaining alumina (alumina remaining after all the sulfates are consumed) reacts pozzolanically to form $C_2AH_{7.5}$. The Q and CH consumed by alumina are higher when sulfates are present due to the formation of monosulfate.[33] As the amount of SiO_2 in the SCM increases from 0 to 33%, C_2ASH_8 forms in addition to the monosulfates and $C_2AH_{7.5}$. The volume of monosulfate formed is relatively constant as the alumina preferentially reacts with the sulfate, and only the remaining alumina reacts to form $C_2AH_{7.5}$ and C_2ASH_8. The Q and CH consumed also drop from 813 J/g$_{SCM}$ and 161 g/100 g$_{SCM}$ to 722 J/g$_{SCM}$ and 113 g/100 g$_{SCM}$, respectively, due to the formation of C_2ASH_8. The Q and CH consumed by the sulfate reaction with Al_2O_3 in the PRT is summarized in Table 1. It can also be seen that the critical point of SiO_2 + Al_2O_3 has changed from 36% SiO_2 + 64% Al_2O_3 (in a system without sulfate) to 33% SiO_2 + 67% Al_2O_3 as some of the alumina is preferentially bound in the monosulfate, and only the remaining alumina in the SCM can react with SiO_2 and CH to form C_2ASH_8. As the SiO_2 is increased from 33 to 90%, C-S-H phases form in addition to C_2ASH_8 and monosulfate. This causes an increase in the Q and CH consumed. Above a 90% SiO_2 content, all the alumina is bound in the monosulfate and there is no alumina available to react with the SiO_2 to form C_2ASH_8, so only C-S-H and monosulfate form. When the SCM is 100% SiO_2, only C-S-H forms.

The practical implications of this finding are that if sulfates are added during the measurement of reactivity, the reactions that form monosulfate need to be accounted for while determining the reactivity of the SCM using the heat released and CH consumed.[33] This can be done by determining the amount of alumina from the SCM that reacts with the sulfates. Figure 6(b) shows an example of the modification to the reactivity lines made for varying SiO_2:Al_2O_3 ratios in an SCM when 20 g gypsum/100 g SCM is added in the PRT. As expected, the 100% SiO_2 line is unaffected by the presence of sulfates. As the alumina content of the SCM increases, the top of the lines (100% DOR* point in each line) moves in the same manner as explained in the previous paragraph as shown using the arrow (Q and CH consumed increase with an increase in the sulfate added) as shown in Fig. 6(a). Some reactivity lines have kinks/bends on them. This is due to the preferential reaction of alumina with sulfate to form monosulfate, which has a higher Q/CH consumed (which is the "slope" of the line) than $C_2AH_{7.5}$. The location of the kink on a line of given composition is the point at which the reactive alumina exceeds the amount of alumina that can be consumed in the reaction that produces monosulfate—that is, for DOR* values below the kink in the line, only monosulfate forms; for the DOR* values above the kink in the line, monosulfate and $C_2AH_{7.5}$ + C_2ASH_8 form. As such, most commercial SCMs contain high levels of silica and low levels of alumina, which can pose a challenge while measuring the reactivity using the R3 test when sulfates are present due to the varying amounts of monosulfates that can form. Therefore, the addition of sulfates is not recommended while measuring the reactivity of SCMs.

Figure 7(a) shows the phase assemblage of an SCM containing only SiO_2 and Al_2O_3 tested in the PRT when carbonates are added (for illustration purposes, 5 g $CaCO_3$/100 g_{SCM} is added). Similar to sulfates, when Al_2O_3 is present in the SCM, the Al_2O_3 preferentially reacts with the carbonates to produce carboaluminates, and the remaining alumina (alumina remaining after all the carbonates are consumed) reacts pozzolanically to form $C_2AH_{7.5}$/C_2ASH_8. The Q and CH consumed by pure alumina is higher when

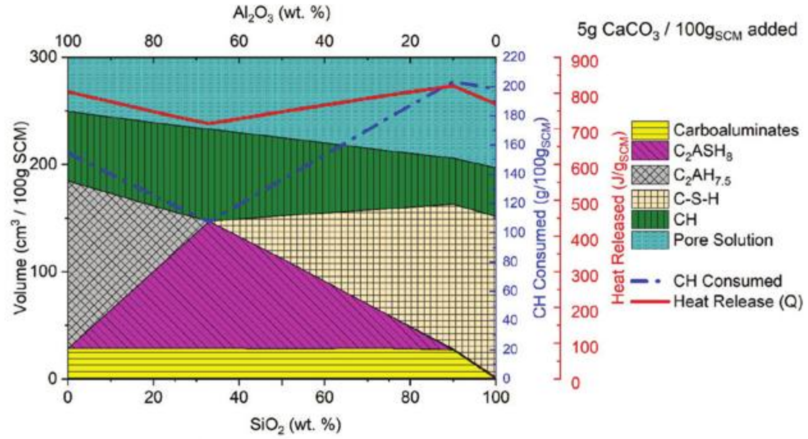

(a) Influence of carbonates on the varying SiO_2:Al_2O_3 in the SCM

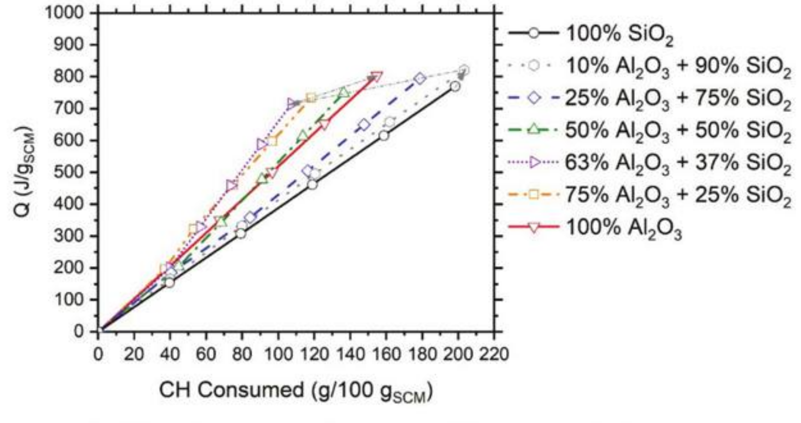

(b) Plot of the heat release and CH consumed when SCMs of varying compositions are subject to the PRT and 5g $CaCO_3$ is added

Fig. 7—(a) Plot of phases formed, Q, and CH consumed when carbonates are added to SCMs of varying compositions are subject to PRT; and (b) plot of Q versus CH consumed when SCMs of varying compositions are subject to PRT and 5 g $CaCO_3$ is added.

carbonates are present due to the formation of carboaluminates.[33] When the SCM is 100% Al_2O_3, carboaluminates + $C_2AH_{7.5}$ form. As the wt. % SiO_2 in the SCM increases from 0% to 33%, C_2ASH_8 forms in addition to the carboaluminates and $C_2AH_{7.5}$. The volume of carboaluminates formed as the SiO_2:Al_2O_3 of the SCM is varied is relatively constant as the alumina preferentially reacts with the carbonate, and only the remaining alumina reacts to form $C_2AH_{7.5}$ and C_2ASH_8 in the PRT. These changes to the reaction products result in the measured Q and CH consumed to drop from 803 to 714 J/g_{SCM} and 157 to 110 g/100 g_{SCM}, respectively. Note that the formation of different types of carboaluminate phases depends on the CO_2-SO_3-Al_2O_3 balance,[72] and this balance needs to be considered in the interpretation of the Q and CH consumed in the PRT. The Q and CH consumed by the carbonate reactions with Al_2O_3 in the PRT is summarized in Table 1. As the SiO_2 is increased from 33 to 90%, C-S-H phases form in addition to C_2ASH_8 and carboaluminate phases, which results in an increased Q and CH consumed. Above a 90% SiO_2 content, all the alumina is bound as carboaluminates and there is no alumina available to react with the SiO_2 and CH to form C_2ASH_8, and only carboaluminates and C-S-H phases form. When the SCM is 100% SiO_2, only C-S-H phases form. It can be noted that the addition of 20 g gypsum (Fig. 6(a)) and 5 g $CaCO_3$ (Fig. 7(a)) show a similar trend in the phases that form. This is because the resulting phases are both AFm phases (monosulfate forms when gypsum is added, and hemicarbonates/monocarbonates form when $CaCO_3$ is added, which both fall under the AFm family of phases).

If carbonates are added during the measurement of reactivity, as it is done in the R3 test, the reactions that form carboaluminate need to be accounted for while determining the reactivity of the SCM using the Q and the CH consumed.[33] This can be done by accounting for the mass of alumina from the SCM that reacts with the carbonates. Figure 7(b) shows an example of the modification to the reactivity lines made for varying SiO_2 to Al_2O_3 ratios in an SCM when 5 g $CaCO_3$ is added. As expected, the 100% SiO_2 line is unaffected by the presence of carbonates. As the alumina content of the SCM increases, the top of the lines (100% DOR* point in each line) moves in the same manner as explained in the previous paragraph and shown in Fig. 7(b) using the arrow. Similar to the lines when sulfates are added, it can be noted that some lines have kinks/bends on them due to the preferential reaction of alumina with carbonates to form carboaluminate. The location of the kink on a line of given composition is the point at which the reactive alumina exceeds the amount of alumina that can be consumed in the reaction that produces carboaluminates—that is, for DOR* values below the kink in the line, only carboaluminates form, for the DOR* values above the kink in the line, carboaluminates and $C_2AH_{7.5}$ + C_2ASH_8 form. As such, most commercial SCMs contain high levels of silica and low levels of alumina, which can pose a challenge while measuring the reactivity using the PRT when carbonates are present due to the varying amounts and composition of the carboaluminates that can form. Therefore, the addition of sulfates and carbonates is not recommended while measuring the reactivity of SCMs.

RECOMMENDATIONS ON CALCULATING REACTIVITY OF COMMERCIAL SCMs

This study shows that the interpretation of the reactivity test outputs to quantify reactivity can be challenging. For example, the PRT uses two theoretical reactivity lines (100% Al_2O_3 line and the 100% SiO_2 line) to interpolate and quantify the reactivity of the SCM.[23,33] It is shown in this paper that interpretation of the reactivity test outputs might need to be to be customized based on the type of SCM and its composition. It is recommended to interpret the reactivity of different classes of SCMs based on their chemical composition, using similar classifications made by standard SCM specifications and experimental data from the literature.[23,33,46,49-51,55,58-60] For PRT, in this paper, these compositional classifications are used to determine the most appropriate ways to interpret the reactivity test results for typical commercial SCMs (silica fume [SF], fly ash [FA] and natural pozzolans [NP], calcined clays [CC], and slags) for a more accurate calculation of DOR* in the PRT. Any commercial SCM tested in the PRT would fall between the bounding reactivity lines for that SCM type, shown in Table 2. The deviation in the calculated value of DOR* from the actual value of DOR* for any composition within the bounding compositions is also calculated to assess the accuracy of using these bounding lines.

The DOR* can also be quantified in the PRT using Eq. (1). In the equation, a_1 and a_2 are constants that depend on the test parameters and the chemical composition of the reactivity lines used. The values of a_1 and a_2 (shown in Table 2), therefore, will vary for each SCM, as different lines will be used for each SCM. Note that the values of a_1 and a_2 are computed from the predicted Q and CH consumed obtained in the simulations for each class of SCM.

Silica fume

Silica fume is specified to contain a minimum of 85% SiO_2 as per ASTM C1240.[71] The remaining constituents can be loss on ignition (LOI), Al_2O_3, CaO, or other impurities. Typical commercially available silica fumes contain >90% SiO_2 and have CaO or LOI as the impurity.[33,46,49,50,55] Therefore, the proposed reactivity lines to use are the 100% SiO_2 line and 85% SiO_2 + 15% CaO line. The experimental

Table 2—Typical chemical composition of commercial SCMs in this study

SCM	Left line	Right line	a_1, 1/(J/g_{SCM}))	a_2, 1/(g/100 g_{SCM}))
SF	85% SiO_2 + 15% CaO	100% SiO_2	1.00×10^{-3}	1.15×10^{-3}
FA and NP	82% SiO_2 + 18% CaO	100% SiO_2	1.00×10^{-3}	1.16×10^{-3}
CC	50% SiO_2 + 50% Al_2O_3	75% SiO_2 + 25% Al_2O_3	1.81×10^{-3}	-1.95×10^{-3}
Slags	18% SiO_2 + 50% CaO + 32% Al_2O_3	70% SiO_2 + 30% CaO	1.12×10^{-3}	1.13×10^{-4}

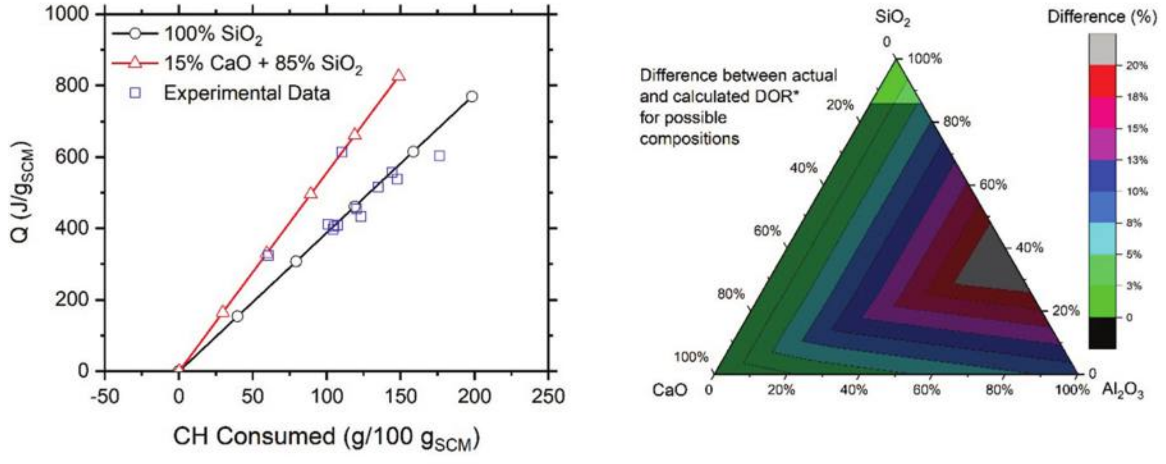

(a)

(b)

Fig. 8—(a) Reactivity lines and experimental results for silica fume; and (b) difference between actual and calculated when using reactivity lines for calculation of reactivity. Highlighted zone represents commercial silica fume compositions.

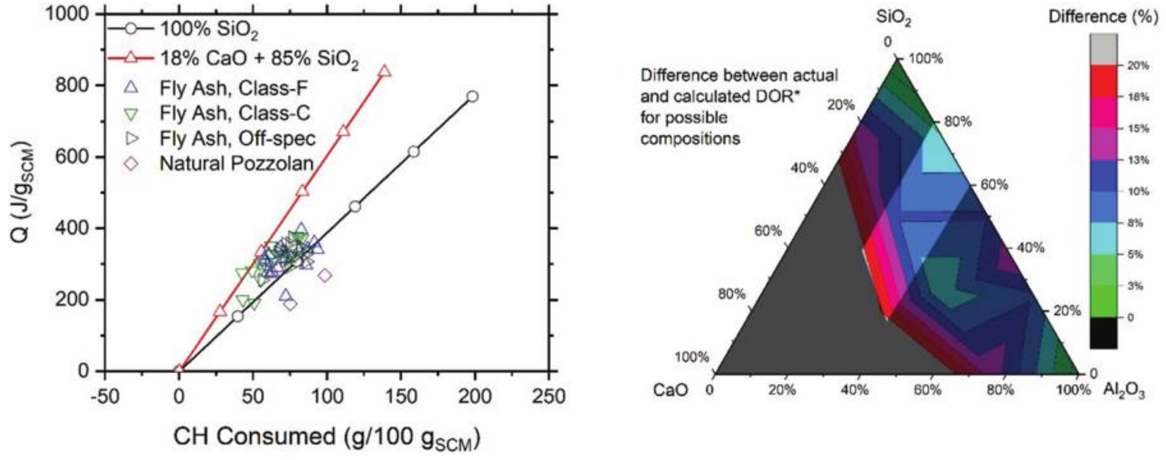

(a)

(b)

Fig. 9—(a) Reactivity lines and experimental results for fly ash; and (b) difference between actual and calculated DOR when using reactivity lines for calculation of reactivity.*

results from literature[33,46,49,50,55] are plotted, along with the recommended reactivity lines, as shown in Fig. 8(a). All the data points fall within 20 g CH consumed per 100 g_{SCM} or 50 J/g_{SCM} of the reactivity lines. Figure 8(b) shows the difference between the calculated DOR* from the actual DOR* when Eq. (2) and the constants in Table 2 are used. It should be noted from this plot that the difference in the calculated reactivity and actual reactivity for any composition is under 5%, and therefore, these lines provide an accurate measure of DOR* and should be used for the calculation of DOR* of silica fumes.

Fly ash and natural pozzolans

ASTM C618[25] specifies the chemical compositional requirements for Class F and Class C fly ashes as well as natural pozzolans. Fly ashes conforming to ASTM C618 are to contain >50% by mass of $SiO_2 + Al_2O_3 + Fe_2O_3$. Class F fly ashes are to contain less than 18% CaO and Class C fly ashes can contain more than 18% CaO. However, from the experimental data available in the literature,[33,46,49,50,55] the lines chosen for both classes of fly ash, as well as natural pozzolans, are the 100% SiO_2 line and 82% SiO_2 + 18% CaO line, as they represent the bounding cases for the experimental data. The experimental results from literature[33,46,49,50,55] are plotted along with the recommended reactivity lines, as shown in Fig. 9(a). All the data points fall within 20 g CH consumed per 100 g_{SCM} or 50 J/g_{SCM} of the reactivity lines. Figure 9(b) shows the difference in the calculated DOR* from the actual DOR* when Eq. (2) and the constants in Table 2 are used for any chemical composition of fly ash that satisfies the ASTM C618[25] requirements, which can be obtained commercially. The difference in the calculated DOR* from the actual DOR* for typical commercially available ash and natural pozzolan compositions is under 13% for CaO < 40% when the actual DOR* is 100%. It should be noted that if the DOR* is lower, the associated difference between the actual and calculated DOR* will also be proportionally lower. Because the typical DOR* of fly ashes is approximately 40%, this difference between the actual and predicted DOR* would be only approximately 5%.

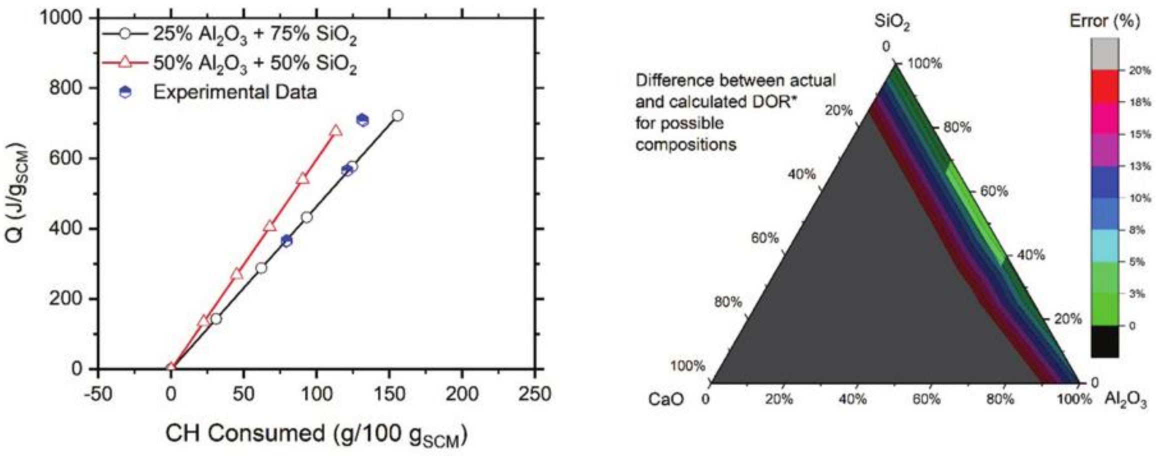

(a)

(b)

Fig. 10—(a) Reactivity lines and experimental results for calcined clays and metakaolin; and (b) difference between actual and calculated DOR when using reactivity lines for calculation of reactivity.*

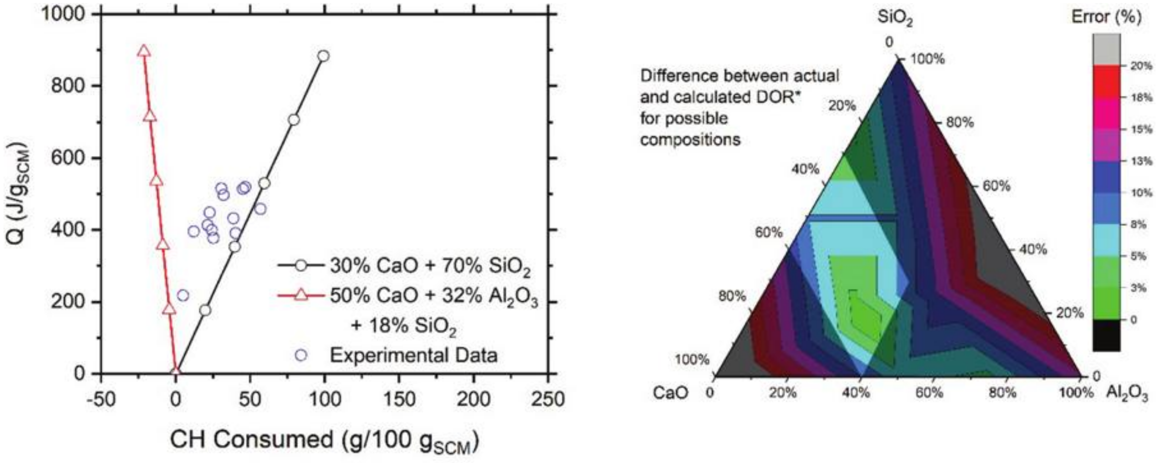

(a)

(b)

Fig. 11—(a) Reactivity lines and experimental results for slag; and (b) difference between actual and calculated DOR when using reactivity lines for calculation of reactivity.*

Calcined clays and metakaolin

Calcined clays and metakaolin typically contain high amounts of alumina (20 to 50%[55]), and high amounts of silica with negligible CaO, with the typical chemical composition obtained from the literature shown in Table 2. The lines chosen for calcined clays and metakaolin are the 75% SiO_2 +25% Al_2O_3 line and 50% SiO_2 + 50% Al_2O_3 line. The experimental results from literature[33,46,49,50,55] are plotted along with the recommended reactivity lines as shown in Fig. 10(a). All the data points fall within the bounding reactivity lines. Figure 10(b) shows the difference in the calculated DOR* from the actual DOR* when Eq. (2) and the constants in Table 2 are used for any chemical composition of fly ash that satisfies the ASTM C618[25] requirements, which can be obtained commercially. This difference between the calculated and actual reactivity for typical commercially available calcined clays and metakaolin compositions is under 5%. Therefore, for calcined clays and metakaolin, using the 75% SiO_2 + 25% Al_2O_3 line and the 50% SiO_2 + 50% Al_2O_3 line to calculate the DOR* is recommended.

Slag

ASTM C989/C989M[73] specifies the chemical compositional requirements for the use of slag (slag cements); however, the only limitation on the chemistry specified is a maximum sulfide content of 2%. Therefore, the commercially available slag compositions from the literature[33,46,49,50,55] is used to obtain the optimal reactivity lines. Typical slags available in the United States[33,46,49,50,55] contain 20 to 40% SiO_2, 10 to 15% Al_2O_3, and 30 to 50% CaO. Therefore, the reactivity lines chosen to best represent the data and calculate the reactivity is the 70% SiO_2 + 30% CaO line and 18% SiO_2 + 32% Al_2O_3 + 50% CaO line. The experimental results from the literature[33,46,49,50,55] are plotted along with the recommended reactivity lines as shown in Fig. 11(a). All but one data point fall within the bounding reactivity lines. Figure 11(b) shows the difference in the calculated DOR* from the actual DOR* when Eq. (2) and the constants in Table 2 are used for any typical slag available commercially. The difference between the calculated reactivity and actual DOR* for typical commercially available slag is under 13%

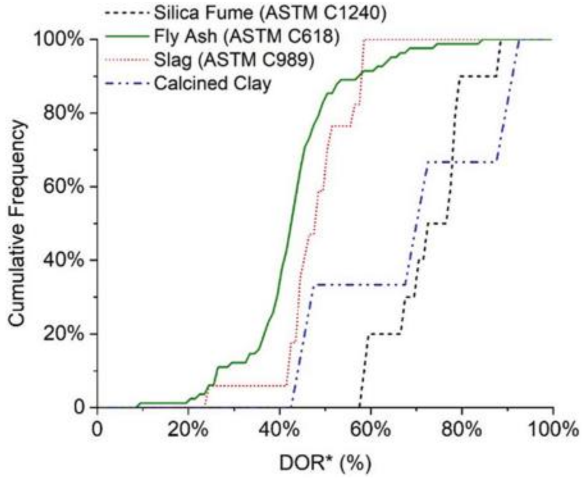

Fig. 12—Cumulative frequency plot of reactivities for commercial SCMs.

when these lines are used and, as such, the use of the 70% SiO_2 + 30% CaO line and 18% SiO_2 + 32% Al_2O_3 + 50% CaO line is recommended.

A cumulative frequency plot of the reactivities determined using experimental data in the literature[23,33,46,49,50,55,59,60] is shown in Fig. 12. This statistical distribution enables a comparison of SCMs based on their DOR* (which is a performance indicator of the SCM[39]). For example, a fly ash of 60% reactivity can be considered a highly reactive fly ash but a silica fume of 60% reactivity may be considered a low-reactivity silica fume. The range of silica fume reactivity can be seen to be from 54 to 90% (mean reactivity is 71%) while fly ash ranges from 9 to 85% (mean reactivity is 43%).

CONCLUSIONS

This paper uses thermodynamic modeling to aid the interpretation of pozzolanic reactivity testing of different classes of supplementary cementitious materials (SCMs). The following conclusions were drawn:

1. The investigation of the SCMs containing only SiO_2 and Al_2O_3 (no CaO) showed that as the ratio of SiO_2 to Al_2O_3 varies, the phase assemblage changes (pure Al_2O_3 results in the formation of $C_2AH_{7.5}$, pure SiO_2 results in the formation of C-S-H phases, and combinations of SiO_2 and Al_2O_3 result in the formation of C_2ASH_8 along with C-S-H or $C_2AH_{7.5}$). The heat release (Q) and calcium hydroxide (CH) consumed follow a response that is roughly bilinear, with the minima of heat release and CH consumed being at SiO_2:Al_2O_3 where only C_2ASH_8 forms.

2. The investigation of the SCMs containing SiO_2, Al_2O_3, and CaO showed that the presence of CaO in an SCM results in a net reduction in the measured CH consumed as the CaO in the SCM provides an internal source of Ca. The Q increases as the reaction of CaO is more exothermic than the reactions of SiO_2 and Al_2O_3.

3. The study of the influence of the presence of sulfates and carbonates during reactivity quantification indicated that both sulfates and carbonates alter the reaction of the Al_2O_3 phases. The Al_2O_3 reacts preferentially with sulfates and carbonates to form AFm phases (Al_2O_3 reacts with sulfates to form monosulfate, and with carbonates to form carboaluminates). The reaction forming these AFm phases is more exothermic than the reaction that forms $C_2AH_{7.5}$ or C_2ASH_8. As such, the addition of sulfates and carbonates in the quantification of the pozzolanic reactivity is not recommended, as it makes the interpretation of the results challenging as the reactions are altered with reactions other than pozzolanic reactions occurring.

4. Following Conclusions 1 through 3, it was shown that the reactivity of commercial SCMs should be interpreted specific to the type of SCM as described by ASTM International/AASHTO. The proposed interpretation is provided in this paper. This implies that directly comparing the Q is only applicable with SCMs of the same type.

5. The statistical data on the reactivities of commercially available SCMs using the proposed approach indicate that the mean reactivity of silica fume is 70%, the mean reactivity of fly ash + natural pozzolan is 43%, and the mean reactivity of slags is 48%.

Overall, this paper provides a fundamental understanding of the reactions that occur in the pozzolanic reactivity test (PRT), demonstrates the robustness of the PRT, extends the scope of the PRT to measure the reactivity of pozzolanic as well as hydraulic SCMs, and is intended to aid in the interpretation of the results of the PRT and allow for a more accurate determination of the degree of reactivity (DOR*).

AUTHOR BIOS

ACI member **Keshav Bharadwaj** *is a Postdoctoral Scholar at Oregon State University, Corvallis, OR, where he received his PhD in civil engineering. His research interests include thermodynamic modeling, reactivity, transport in cementitious systems, and linking the microstructure of concrete to the engineering performance of concrete.*

O. Burkan Isgor, *FACI, is a Professor in the School of Civil and Construction Engineering at Oregon State University. He is Chair of ACI Committee 222, Corrosion of Metals in Concrete, and a member of ACI Committees 236, Material Science of Concrete, and 365, Service Life Prediction. His research interests include corrosion of steel in concrete, service-life modeling, and thermodynamic modeling of cementitious systems.*

W. Jason Weiss, *FACI, is the Edwards Distinguished Professor of Engineering in the School of Civil and Construction Engineering at Oregon State University. He is Editor-in-Chief of the* ACI Materials Journal *and a member of the ACI Technical Activities Committee.*

ACKNOWLEDGMENTS

The authors gratefully acknowledge the financial support provided by ARPA-E (Advanced Research Projects Agency-Energy), EPRI (Electric Power Research Institute), CALTRANS (California Department of Transportation), and National Science Foundation (Grant No. NSF CMMI 1728358). The authors gratefully acknowledge support from the John and Jean Loosely Chair and the Edwards Distinguished Chair at Oregon State, who have supported the last two authors, respectively.

REFERENCES

1. Thomas, M., *Supplementary Cementing Materials in Concrete*, CRC Press, Boca Raton, FL, 2013, 210 pp.

2. Bredy, P.; Chabannet, M.; and Pera, J., "Microstructure and Porosity of Metakaolin Blended Cements," MRS Online Proceedings Library Archive, V. 137, 1988.

3. Bharadwaj, K.; Ghantous, R. M.; Sahan, F. N.; Isgor, B. O.; and Weiss, J., "Predicting Pore Volume, Compressive Strength, Pore Connectivity, and Formation Factor in Cementitious Pastes Containing Fly Ash," *Cement and Concrete Composites*, V. 122, Paper No. 104113, 2021.

4. Lothenbach, B.; Scrivener, K.; and Hooton, R. D., "Supplementary Cementitious Materials," *Cement and Concrete Research*, V. 41, No. 12, 2011, pp. 1244-1256. doi: 10.1016/j.cemconres.2010.12.001

5. Poon, C.-S.; Kou, S.; and Lam, L., "Compressive Strength, Chloride Diffusivity and Pore Structure of High Performance Metakaolin and Silica Fume Concrete," *Construction and Building Materials*, V. 20, No. 10, 2006, pp. 858-865. doi: 10.1016/j.conbuildmat.2005.07.001

6. Pepper, L., and Mather, B., "Effectiveness of Mineral Admixtures in Preventing Excessive Expansion of Concrete Due to Alkali-Aggregate Reaction," *American Society for Testing Materials - Proceedings*, Philadelphia, PA, 1959.

7. Thomas, M., "The Effect of Supplementary Cementing Materials on Alkali-Silica Reaction: A Review," *Cement and Concrete Research*, V. 41, No. 12, 2011, pp. 1224-1231. doi: 10.1016/j.cemconres.2010.11.003

8. Suraneni, P.; Azad, V. J.; Isgor, B. O.; and Weiss, W. J., "Calcium Oxychloride Formation in Pastes Containing Supplementary Cementitious Materials: Thoughts on the Role of Cement and Supplementary Cementitious Materials Reactivity," *RILEM Technical Letters*, V. 1, 2016, pp. 24-30. doi: 10.21809/rilemtechlett.2016.7

9. Suraneni, P.; Azad, V. J.; Isgor, O. B.; and Weiss, W. J., "Deicing Salts and Durability of Concrete Pavements and Joints," *Concrete International*, V. 38, No. 4, Apr. 2016, pp. 48-54.

10. Suraneni, P.; Azad, V. J.; Isgor, O. B.; and Weiss, W. J., "Use of Fly Ash to Minimize Deicing Salt Damage in Concrete Pavements," *Transportation Research Record: Journal of the Transportation Research Board*, V. 2629, No. 1, 2017, pp. 24-32. doi: 10.3141/2629-05

11. Whatley, S. N.; Suraneni, P.; Azad, V. J.; Isgor, O. B.; and Weiss, J., "Mitigation of Calcium Oxychloride Formation in Cement Pastes Using Undensified Silica Fume," *Journal of Materials in Civil Engineering*, ASCE, V. 29, No. 10, Paper No.04017198, 2017. doi: 10.1061/(ASCE)MT.1943-5533.00020

12. Juenger, M. C.; Snellings, R.; and Bernal, S. A., "Supplementary Cementitious Materials: New Sources, Characterization, and Performance Insights," *Cement and Concrete Research*, V. 122, 2019, pp. 257-273. doi: 10.1016/j.cemconres.2019.05.008

13. Butalia, T. S., "Beneficial Use of Ponded Fly Ash in Structural Concrete," UKIERI Concrete Congress Key Note Address, Jalandhar: Dr. B. R. Ambedkar National Institute of Technology, Jalandhar, Punjab, India, 2019.

14. Innocenti, G.; Benkeser, D. J.; Dase, J. E.; Wirth, X.; Sievers, C.; and Kurtis, K. E., "Beneficiation of Ponded Coal Ash through Chemi-Mechanical Grinding," *Fuel*, V. 299, Paper No.120892, 2021.

15. Clavier, K. A.; Paris, J. M.; Ferraro, C. C.; and Townsend, T. G., "Opportunities and Challenges Associated with Using Municipal Waste Incineration Ash as a Raw Ingredient in Cement Production—A Review," *Resources, Conservation and Recycling*, V. 160, Paper No.104888, 2020.

16. Bahurudeen, A.; Kanraj, D.; Gokul Dev, V.; and Santhanam, M., "Performance Evaluation of Sugarcane Bagasse Ash Blended Cement in Concrete," *Cement and Concrete Composites*, V. 59, 2015, pp. 77-88. doi: 10.1016/j.cemconcomp.2015.03.004

17. Bahurudeen, A.; Marckson, A.; Kishore, A.; and Santhanam, M., "Development of Sugarcane Bagasse Ash Based Portland Pozzolana Cement and Evaluation of Compatibility with Superplasticizers," *Construction and Building Materials*, V. 68, 2014, pp. 465-475. doi: 10.1016/j.conbuildmat.2014.07.013

18. Bahurudeen, A., and Santhanam, M., "Influence of Different Processing Methods on the Pozzolanic Performance of Sugarcane Bagasse Ash," *Cement and Concrete Composites*, V. 56, 2015, pp. 32-45. doi: 10.1016/j.cemconcomp.2014.11.002

19. PCA, *Design and Control of Concrete Mixtures*, Portland Cement Association, Skokie, IL, 2012, 459 pp.

20. Bharadwaj, K.; Isgor, B. O.; Weiss, J. W.; Chopperla, K. S. T.; Choudhary, A.; Vasudevan, G.; Glosser, D.; Ideker, J.; and Trejo, D., "A New Mixture Proportioning Method for Performance-Based Concrete," *ACI Materials Journal*, V. 119, No. 2, Mar. 2022, pp. 207-220.

21. Mehta, P. K., and Monteiro, P. J., *Concrete: Microstructure, Properties and Materials*, McGraw Hill Professional, New Delhi, India, 2006, 675 pp.

22. Taylor, H. F., *Cement Chemistry*, Thomas Telford, London, UK, 1997, 459 pp.

23. Glosser, D.; Choudhary, A.; Isgor, O. B.; and Weiss, W. J., "Investigation of Reactivity of Fly Ash and Its Effect on Mixture Properties," *ACI Materials Journal*, V. 116, No. 4, July 2019, pp. 193-200. doi: 10.14359/51716722

24. Glosser, D.; Suraneni, P.; Isgor, O. B.; and Weiss, W. J., "Estimating Reaction Kinetics of Cementitious Pastes Containing Fly Ash," *Cement and Concrete Composites*, V. 112, Paper No. 103655, 2020.

25. ASTM C618-19, "Standard Specification for Coal Fly Ash and Raw or Calcined Natural Pozzolan for Use in Concrete," ASTM International, West Conshohocken, PA, 2019.

26. AASHTO M 295, "Standard Specification for Coal Fly Ash and Raw or Calcined Natural Pozzolan for Use in Concrete," American Association of State Highway and Transportation Officials (AASHTO), Washington, DC, 2019.

27. EN 206-1, "Concrete—Part 1: Specification, Performance, Production and Conformity," European Committee for Standardization, Brussels, Belgium, 2000.

28. Papadakis, V. G., and Tsimas, S., "Supplementary Cementing Materials in Concrete: Part I: Efficiencya Design," *Cement and Concrete Research*, V. 32, No. 10, 2002, pp. 1525-1532. doi: 10.1016/S0008-8846(02)00827-X

29. Glosser, D.; Suraneni, P.; Isgor, O. B.; and Weiss, W. J., "Using Glass Content to Determine the Reactivity of Fly Ash for Thermodynamic Calculations," *Cement and Concrete Composites*, V. 115, Paper No.103849, 2021.

30. Durdziński, P. T.; Dunant, C. F.; Haha, M. B.; and Scrivener, K. L., "A New Quantification Method Based on Sem-Eds to Assess Fly Ash Composition and Study the Reaction of Its Individual Components in Hydrating Cement Paste," *Cement and Concrete Research*, V. 73, 2015, pp. 111-122. doi: 10.1016/j.cemconres.2015.02.008

31. EN 196-5, "Methods of Testing Cement—Part 5: Pozzolanicity Test for Pozzolanic Cement," European Committee for Standardization, Brussels, Belgium, 2011.

32. Chapelle, J., "Attaque sulfo-calcique des laitiers et des pouzzolanes," *Imprimerie Centrale de l'Ortois-Orras*, 1958, pp. 193-201.

33. Choudhary, A.; Bharadwaj, K.; Ghantous, R. M.; Isgor, B.; and Weiss, J., "Pozzolanic Reactivity Test of Supplementary Cementitious Materials," *ACI Materials Journal*, V. 119, No. 2, Mar. 2022, pp. 255-268.

34. Thorstensen, R. T., and Fidjestol, P., "Inconsistencies in the Pozzolanic Strength Activity Index (SAI) for Silica Fume According To EN and ASTM," *Materials and Structures*, V. 48, No. 12, 2015, pp. 3979-3990. doi: 10.1617/s11527-014-0457-6

35. Bentz, D. P.; Durán-Herrera, A.; and Galvez-Moreno, D., "Comparison of ASTM C311 Strength Activity Index Testing Versus Testing Based on Constant Volumetric Proportions," *Journal of ASTM International*, V. 9, No. 1, 2011, pp. 1-7.

36. ASTM C1897-20, "Standard Test Method for Measuring the Reactivity of Supplementary Cementitious Materials by Isothermal Calorimetry and Bound Water Measurements," ASTM International, West Conshohocken, PA, 2020.

37. Avet, F.; Snellings, R.; Alujas Diaz, A.; Ben Haha, M.; and Scrivener, K., "Development of a New Rapid, Relevant and Reliable (R-3) Test Method to Evaluate the Pozzolanic Reactivity of Calcined Kaolinitic Clays," *Cement and Concrete Research*, V. 85, 2016, pp. 1-11. doi: 10.1016/j.cemconres.2016.02.015

38. Snellings, R., and Scrivener, K. L., "Rapid Screening Tests for Supplementary Cementitious Materials: Past and Future," *Materials and Structures*, V. 49, No. 8, 2016, pp. 3265-3279. doi: 10.1617/s11527-015-0718-z

39. Bharadwaj, K.; Isgor, B. O.; and Weiss, J. W., "A Simplified Approach to Determine the Pozzolanic Reactivity of Commercial Supplementary Cementitious Materials," *Concrete International*, V. 44, No. 1, Jan. 2022, pp. 27-32.

40. Azad, V. J.; Suraneni, P.; Trejo, D.; Weiss, W. J.; and Isgor, O. B., "Thermodynamic Investigation of Allowable Admixed Chloride Limits in Concrete," *ACI Materials Journal*, V. 115, No. 5, Sept. 2018, pp. 727-738. doi: 10.14359/51702349

41. Bharadwaj, K.; Chopperla, K. S. T.; Choudhary, A.; Glosser, D.; Ghantous, R. M.; Vasudevan, G.; Ideker, J. H.; Isgor, B.; Trejo, D.; and Weiss, J. W., "Caltrans: Impact of the Use of Portland-Limestone Cement on Concrete Performance as Plain or Reinforced Material—Final Report," Oregon State University, Corvallis, OR, 320 pp.

42. Bharadwaj, K.; Glosser, D.; Moradllo, M. K.; Isgor, O. B.; and Weiss, J., "Toward the Prediction of Pore Volumes and Freeze-Thaw Performance of Concrete Using Thermodynamic Modelling," *Cement and Concrete Research*, V. 124, Paper No. 105820, 2019.

43. Bharadwaj, K.; Isgor, B. O.; and Weiss, J. W., "Supplementary Cementitious Materials in Portland Limestone Cements," *ACI Materials Journal*, V. 119, No. 2, Mar. 2022, pp. 141-154.

44. Choudhary, A.; Ghantous, R. M.; Bharadwaj, K.; Opdahl, O. H.; Isgor, B. O.; and Weiss, J. W., "Electrical and Transport Properties of Cement Mortar Made Using Portland Limestone Cement," *Advances in Civil Engineering Materials*, V. 11, No. 1, 2022, pp. 263-279. doi: 10.1520/ACEM20210119

45. Glosser, D.; Azad, V. J.; Suraneni, P.; Isgor, B.; and Weiss, J., "Extension of Powers-Brownyard Model to Pastes Containing Supplementary Cementitious Materials," *ACI Materials Journal*, V. 116, No. 5, Sept. 2019, pp. 205-216. doi: 10.14359/51714466

46. Suraneni, P., and Weiss, J., "Examining the Pozzolanicity of Supplementary Cementitious Materials Using Isothermal Calorimetry and Thermogravimetric Analysis," *Cement and Concrete Composites*, V. 83, 2017, pp. 273-278. doi: 10.1016/j.cemconcomp.2017.07.009

47. Glosser, D.; Isgor, O. B.; and Weiss, W. J., "Non-Equilibrium Thermodynamic Modeling Framework for Ordinary Portland Cement/

Supplementary Cementitious Material Systems," *ACI Materials Journal*, V. 117, No. 6, Nov. 2020, pp. 111-123.

48. Ramanathan, S., "Reactivity of Supplementary Cementitious Materials in Model Systems and Cementitious Pastes," PhD thesis, University of Miami, Miami, FL, 2021.

49. Ramanathan, S.; Croly, M.; and Suraneni, P., "Comparison of the Effects that Supplementary Cementitious Materials Replacement Levels Have on Cementitious Paste Properties," *Cement and Concrete Composites*, V. 112, Paper No. 103678, 2020.

50. Ramanathan, S.; Kasaniya, M.; Tuen, M.; Thomas, M. D.; and Suraneni, P., "Linking Reactivity Test Outputs to Properties of Cementitious Pastes Made with Supplementary Cementitious Materials," *Cement and Concrete Composites*, V. 114, Paper No. 103742, 2020.

51. Ramanathan, S.; Moon, H.; Croly, M.; Chung, C.-W.; and Suraneni, P., "Predicting the Degree of Reaction of Supplementary Cementitious Materials in Cementitious Pastes Using a Pozzolanic Test," *Construction and Building Materials*, V. 204, 2019, pp. 621-630. doi: 10.1016/j.conbuildmat.2019.01.173

52. Ramanathan, S.; Perumal, P.; Illikainen, M.; and Suraneni, P., "Mechanically Activated Mine Tailings for Use as Supplementary Cementitious Materials," *RILEM Technical Letters*, V. 6, 2021, pp. 61-69. doi: 10.21809/rilemtechlett.2021.143

53. Ramanathan, S.; Pestana, L. R.; and Suraneni, P., "Reaction Kinetics of Supplementary Cementitious Materials in Reactivity Tests," *Cement*, Paper No. 100022, 2022.

54. Ramanathan, S.; Suraneni, P.; Wang, Y.; Shan, H.; Hajibabaee, A.; and Weiss, J., "Combining Reactivity Test, Isothermal Calorimetry, and Compressive Strength Measurements to Study Conventional and Alternative Supplementary Cementitious Materials," *Proceedings of the International Conference of Sustainable Production and Use of Cement and Concrete*, 2020, pp. 445-454.

55. Suraneni, P.; Hajibabaee, A.; Ramanathan, S.; Wang, Y.; and Weiss, J., "New Insights from Reactivity Testing of Supplementary Cementitious Materials," *Cement and Concrete Composites*, V. 103, 2019, pp. 331-338. doi: 10.1016/j.cemconcomp.2019.05.017

56. Suraneni, P., and Ramanathan, S., "Reactivity of Tested SCMs," personal communication sent to W. J. Weiss, K. Bharadwaj, and B. O. Isgor, 2020.

57. Ramanathan, S.; Tuen, M.; and Suraneni, P., "Influence of Supplementary Cementitious Material and Filler Fineness on Their Reactivity in Model Systems and Cementitious Pastes," *Materials and Structures*, V. 55, No. 5, 2022, 25 pp. doi: 10.1617/s11527-022-01980-2

58. Moradllo, M. K.; Chung, C.-W.; Keys, M. H.; Choudhary, A.; Reese, S. R.; and Weiss, W. J., "Use of Borosilicate Glass Powder in Cementitious Materials: Pozzolanic Reactivity and Neutron Shielding Properties," *Cement and Concrete Composites*, V. 112, Paper No. 103640, 2020.

59. Burroughs, J. F., "Influence of Chemical and Physical Properties of Poorly-Ordered Silica on Reactivity and Rheology of Cementitious Materials," PhD thesis, Purdue University, West Lafayette, IN, 2019.

60. Isgor, B.; Ideker, J.; Trejo, D.; Weiss, J.; Bharadwaj, K.; Choudhary, A.; Teja, C. K. S.; Glosser, D.; and Vasudevan, G., "Development of a Performance-Based Mixture Proportioning Procedure for Concrete Incorporating Off-Spec Fly Ash," Energy Power Research Institute (EPRI), Palo Alto, CA, 78 pp.

61. Kim, T., and Olek, J., "Effects of Sample Preparation and Interpretation of Thermogravimetric Curves on Calcium Hydroxide in Hydrated Pastes and Mortars," *Transportation Research Record: Journal of the Transportation Research Board*, V. 2290, No. 1, 2012, pp. 10-18. doi: 10.3141/2290-02

62. Lothenbach, B.; Matschei, T.; Möschner, G.; and Glasser, F. P., "Thermodynamic Modelling of the Effect of Temperature on the Hydration and Porosity of Portland Cement," *Cement and Concrete Research*, V. 38, No. 1, 2008, pp. 1-18. doi: 10.1016/j.cemconres.2007.08.017

63. Lothenbach, B., and Winnefeld, F., "Thermodynamic Modelling of the Hydration of Portland Cement," *Cement and Concrete Research*, V. 36, No. 2, 2006, pp. 209-226. doi: 10.1016/j.cemconres.2005.03.001

64. Kulik, D. A.; Wagner, T.; Dmytrieva, S. V.; Kosakowski, G.; Hingerl, F. F.; Chudnenko, K. V.; and Berner, U. R., "Gem-Selektor Geochemical Modeling Package: Revised Algorithm and GEMS3K Numerical Kernel for Coupled Simulation Codes," *Computational Geosciences*, V. 17, No. 1, 2013, pp. 1-24.

65. Lothenbach, B.; Kulik, D. A.; Matschei, T.; Balonis, M.; Baquerizo, L.; Dilnesa, B.; Miron, G. D.; and Myers, R. J., "Cemdata 18: A Chemical Thermodynamic Database for Hydrated Portland Cements and Alkali-Activated Materials," *Cement and Concrete Research*, V. 115, 2019, pp. 472-506. doi: 10.1016/j.cemconres.2018.04.018

66. Gosselin, C., "Microstructural Development of Calcium Aluminate Cement Based Systems with and without Supplementary Cementitious Materials," PhD thesis, Swiss Federal Institute of Technology Lausanne, Lausanne, Switzerland, 234 pp.

67. Choudhary, A., "The Pozzolanic Reactivity Test and the Properties of Portland Limestone Cement," PhD thesis, Oregon State University, Corvallis, OR, 2021.

68. NIST, "NIST Chemistry WebBook," National Institute of Standards and Technology (NIST), Gaithersburg, MD, 2021, doi: 10.18434/T4D30310.18434/T4D303

69. de Silva, P., and Glasser, F. P., "Phase Relations in the System CaO Al_2O_3 SiO_2 H_2O Relevant to Metakaolin-Calcium Hydroxide Hydration," *Cement and Concrete Research*, V. 23, No. 3, 1993, pp. 627-639. doi: 10.1016/0008-8846(93)90014-Z

70. AASHTO M 307, "Standard Specification for Silica Fume Used in Cementitious Mixtures," American Association of State Highway and Transportation Officials, Washington, DC, 2013.

71. ASTM C1240-20, "Standard Specification for Silica Fume Used in Cementitious Mixtures," ASTM International, West Conshohocken, PA, 2020.

72. Matschei, T.; Lothenbach, B.; and Glasser, F., "The AFM Phase in Portland Cement," *Cement and Concrete Research*, V. 37, No. 2, 2007, pp. 118-130. doi: 10.1016/j.cemconres.2006.10.010

73. ASTM C989/C989M-18a, "Standard Specification for Slag Cement for Use in Concrete and Mortars," ASTM International, West Conshohocken, PA, 2018.

ACI MATERIALS JOURNAL TECHNICAL PAPER

Title No. 120-M47

Linking Concrete Rheology to Strength: Sustainability Model Approach

by Fayez Moutassem and Samir E. Chidiac

A requirement for achieving sustainable concrete structures is to develop a quantitative method for designing concrete mixtures that yields the target rheological properties and compressive strength. Toward this objective, this paper proposes a mathematical model approach to improve the sustainability of the concrete industry. A postulation that packing density, a function of the concrete mixture, provides the link between concrete mixture, rheological properties, and compressive strength was investigated. Rheological models for yield stress and plastic viscosity, and a compressive strength model were adopted with packing density as a central variable. The rheological models employ a cell description that is representative of fresh concrete. The compressive strength model is based on excess paste theory to account for the concrete mixture proportions, gradation of aggregate particles, and porosity. An experimental program was developed to calibrate and test these models. Results revealed that packing density provides a consistent and reliable link, and that the concrete mixture composition can be designed to achieve the target rheological properties and hardened properties and ensure quality control. Consequently, a new mixture proportioning methodology was developed and proposed as an improvement to the ACI 211.1 mixture design method. Furthermore, a case study was conducted to test for the applicability and adequacy of this proposed method. This research outcome, which provides a quantitative approach to design concrete mixtures to meet specific strength requirements and rheology, can also be used to ensure quality control before concrete is cast.

Keywords: packing density; rheology; strength; viscosity; yield stress.

INTRODUCTION

Improving the sustainability of structures has become a global objective over the past few decades (Moutassem and Miqdadi 2020). Sustainability of civil engineering structures encompasses effective selection of materials, which includes the use and recyclability of the material and building components, effective use of energy, and resiliency of structures. Traditionally, concrete mixture design aims to meet workability and compressive strength requirements (ACI Committee 318 2005). Research has shown that the workability of fresh concrete can be quantified using Bingham's rheological properties—namely, the yield stress and plastic viscosity (Ferraris and de Larrard 1998; Chidiac et al. 2000; de Larrard 1999). The main variables that affect these properties include the size, shape, and volume fraction of the solid particles, and method of compaction (de Larrard 1999). Different apparatuses such as the slump rate machine II (SLRM II) can be used to estimate the rheological properties of concrete (Chidiac and Habibbeigi 2005). Numerous fundamental and phenomenological rheology models have been proposed in literature. Chidiac and Mahmoodzadeh (2009, 2013) reviewed the predictive capabilities of the rheological models and concluded that the fundamental models developed based on excess paste theory and the cell method provide good and consistent predictions. Both the plastic viscosity and yield stress models employ packing density of fresh concrete as a central variable.

The strength of hardened concrete depends on its porosity and the bond strength of the hydrated cement which are function of the aggregate types, shapes and gradation, cement composition and degree of hydration, amount of entrained air, mixture proportions, and placement protocols (de Larrard 1999; Moutassem 2010). Moutassem and Chidiac (2016) reviewed the predictive capabilities of the compressive strength models proposed in literature and concluded that the comprehensive model developed by Chidiac et al. (2013) provides the highest degree of correlation to experimental data.

Research has shown that the optimum packing density of aggregates and concrete yields optimum rheology and strength by reducing concrete porosity (Johansen and Andersen 1996; Wong and Kwan 2008; Tasi et al. 2006; Shilstone and Shilstone 1993). Studies have revealed the following: rheology is a function of concrete packing density (de Larrard 1999; Chidiac and Mahmoodzadeh 2009, 2013), compressive strength is a function of aggregates packing density (de Larrard 1999; Moutassem 2010; Chidiac et al. 2013), and aggregate packing density and concrete packing density correlate (de Larrard 1999). Accordingly, packing density is a common variable that relates the mixture composition to these properties. Packing density, defined as the ratio of the volume of the solid particles to the bulk volume occupied by these particles, can be measured experimentally in accordance with ASTM C29 (1997). Moutassem and Chidiac (2008) evaluated the suitability of the packing density models proposed in the literature for concrete applications and concluded that the compressible packing model (CPM) provides the highest predictability.

Some researchers have attempted to establish a link between the rheological properties and compressive strength using experimental means (Chidiac et al. 2003; Laskar and Talukdar 2007, 2008). Chidiac et al. (2003) worked on

---

ACI Materials Journal, V. 120, No. 4, July 2023.

MS No. M-2022-319.R1, doi: 10.14359/51738818, received December 12, 2022, and reviewed under Institute publication policies. Pertinent discussion including author's closure, if any, will be published ten months from this journal's date if the discussion is received within four months of the paper's print publication.

correlating the rheological properties to the strength and durability of hardened concrete made with a mixture composed of a high water-cement ratio (*w/c*). It was observed that concrete compressive strength increases as the yield stress and plastic viscosity increase up to an optimum value. Laskar and Talukdar (2007, 2008) worked on correlating the rheological properties to the compressive strength of high-performance concrete. It was observed that the compressive strength increases with yield stress and that the increase is rapid at low values of yield stress. For the plastic viscosity, it was observed that there exists an optimum value corresponding to maximum compressive strength. These findings strongly suggest that a link exists between rheology and strength. However, they do not provide explanations, nor do they identify the common variables that permit linking these properties. Research conducted by Mehdipour and Khayat (2019) studied the effect of particle packing on rheology and strength development of dense cementitious suspensions. Particle packing was determined through altering the water content and determining the optimum water demand corresponding to maximum solid concentration and the minimum water demand required to initiate flow. The author suggests that the outcome of this study can be useful in optimizing the design of dense cementitious suspensions. However, no actual link between the mixture variables, rheology, and strength was produced to permit the design of optimum mixtures.

This paper presents an experimental program as well as an analytical methodology to demonstrate whether a link can be established between the concrete mixture, rheological properties, and compressive strength with packing density identified as the common variable.

RESEARCH SIGNIFICANCE

Current design practice is based on meeting workability and strength requirements (ACI Committee 211 1991). The slump test, which has been the standard test for workability, is not sufficient and the two rheological properties parameters—namely, yield stress and plastic viscosity—are needed to quantify workability (Tattersall and Banfill 1983; Ferraris and de Larrard 1998; Chidiac et al. 2003). For the compressive strength, current design targets the cement content and *w/c*. However, research has shown that other factors can be considered for a better prediction (de Larrard 1999). In addition, the current mixture design approach is not fundamental but is rather statistical and does not provide a link between the mixture proportions, slump, and compressive strength, which is needed to provide control over the design. Recognizing that packing density is a statistically significant variable for both strength and slump (rheology), and that it is a mixture property, it was postulated that packing density is a central variable providing a continuous link between concrete mixture, rheology, and compressive strength. On this basis, an improved version of the ACI 211.1 mixture proportioning methodology that incorporates the rheological properties and optimizes packing density of aggregates needs to be developed. This research outcome, which provides a quantitative approach to design concrete mixtures to meet specific strength requirements and rheology, can also be used to ensure quality control before concrete is cast for more sustainable structures.

EXPERIMENTAL PROGRAM

Materials

The concrete was prepared using a mixture of crushed limestone, siliceous sand, ordinary portland cement (OPC), air-entraining admixture (AEA), and water. Hydraulic Type 10 (Type GU) cement was used in this study. The chemical and physical properties are summarized in Table 1. Crushed limestone coarse aggregate (CA) with 20 and 14 mm nominal maximum aggregate sizes were used. The aggregates were obtained from a quarry located in Dundas, ON, Canada. The specific gravities, absorption values, and bulk density for the 20 mm CA are 2.75, 0.92%, and 1636 kg/m^3; and 2.74, 0.88%, and 1576 kg/m^3 for the 14 mm CA, respectively. Commercially distributed sand was obtained. The fineness modulus, specific gravities, absorption values, and bulk density for the sand are 2.72, 2.71, 1.58%, and 1812 kg/m^3, respectively. The bulk density, specific gravity, and absorption for CA and sand were obtained following ASTM C127 (2015) and ASTM C128 (2015), respectively. The particle size distribution test was carried out in accordance with ASTM C136 (2014) and was found to conform to the specification requirements. A commercial AEA meeting the requirements of ASTM C260 (2010) was used to entrain air.

Concrete mixture design

The concrete mixture was proportioned following the statistical fractional factorial design method and the ranges recommended for designing and proportioning normal concrete mixtures (Kosmatka et al. 2002). The range selected

Table 1—Chemical and physical properties of Type 10 (Type GU) hydraulic cement

SiO_2, %	19.7
Al_2O_3, %	4.9
Fe_2O_3, %	2.6
CaO, %	62.1
MgO, %	2.8
SO_3, %	3.2
Na_2O, %	1.3
Loss on ignition, %	3.1
C4AF, %	8.0
C3A, %	9.0
C3S (CSA), %	58
C2S (CSA), %	13
C3S (ASTM), %	50
C2S (ASTM), %	19
Equivalent alkalies, %	0.78
Specific surface area (Blaine), cm^2/g	4205
% Passing 325 (45 um) mesh, %	92.1
Time of setting—initial, min	113
Compressive strength—28-day, MPa	41.9

Table 2—Concrete mixture design composition

Mixture No.	w/c	Size	Water, kg/m^3	Cement, kg/m^3	Coarse aggregate (bulk volume)	Coarse aggregate, kg/m^3	Sand, kg/m^3	Air, %
1	0.40	14	193	483	0.50	794	851	5.9
2	0.60	14	193	322	0.62	971	815	5.3
3	0.40	14	205	513	0.62	971	618	4.8
4	0.60	14	205	342	0.50	794	939	5.1
5	0.40	20	184	460	0.69	1134	563	4.6
6	0.60	20	184	307	0.57	928	898	5.6
7	0.40	20	197	493	0.57	928	703	4.8
8	0.60	20	197	328	0.69	1134	641	3.1
9	0.50	14	193	386	0.504	794	934	5.7
10	0.70	14	175	250	0.504	794	1100	8.8
11	0.50	14	205	410	0.504	794	881	5.1
12	0.70	14	193	276	0.504	794	1029	7.5
13	0.50	14	193	386	0.616	971	759	5.1
14	0.70	14	175	250	0.616	971	925	8.7
15	0.50	14	205	410	0.616	971	706	4.8
16	0.70	14	193	276	0.616	971	854	5.6
17	0.50	14	199	398	0.560	883	820	5.0
18	0.50	14	199	398	0.448	706	994	7.8
19	0.50	14	199	398	0.672	1059	645	6.7
20	0.50	14	199	398	0.560	883	820	5.8
21	0.40	14	216	540	0.50	794	807	2.1
22	0.60	14	216	360	0.62	971	787	1.0
23	0.40	14	228	570	0.62	971	574	1.8
24	0.60	14	228	380	0.50	794	912	1.2
25	0.40	20	205	513	0.69	1134	542	1.6
26	0.60	20	205	342	0.57	928	892	1.5
27	0.40	20	216	540	0.57	928	692	1.4
28	0.60	20	216	360	0.69	1134	643	1.5

for w/c was from 0.4 to 0.7. The water content values ranged from 175 to 228 kg/m^3, covering the full range of slump for non-air-entrained and air-entrained concrete. The cement content ranged from 250 to 570 kg/m^3. The bulk volume of CA per unit volume of concrete, V_{CA}, ranged from 0.45 to 0.69. The CA maximum sizes were 20 and 14 mm. For the air-entrained concrete mixtures, an AEA was used to achieve 5% air content. The total number of concrete mixtures was 28 and the corresponding proportions are given in Table 2. Of the 28 concrete mixtures, 20 were air-entrained and eight were non-air-entrained.

Packing density

The maximum packing density, ϕ^*, for each mixture was computed using the compressible packing model (de Larrard 1999), which requires the dry packing densities, volume fractions, and the characteristic diameters of the particles as an input. The dry packing density of sand and CA (oven dried) were measured in accordance with ASTM C29 (1997) with rodding as the method of compaction. The test was carried out using three specimens, and both the mean value and the standard deviation are reported. The mean packing densities of sand, 14 mm maximum CA size, and 20 mm maximum CA size were measured to be 0.669, 0.575, and 0.595, respectively, and the corresponding standard deviation is 0.016, 0.011, and 0.012. The mean characteristic diameters corresponding to 63.2% passing, as recommended by Goltermann et al. (1997), were measured for sand, 14 mm maximum aggregate size, and 20 mm maximum aggregate size and found to be 1.1, 10.4, and 14.3 mm, respectively. The corresponding standard deviations are 0.05, 1.48, and 1.22 mm, respectively. The mean values of the mean diameters, corresponding to 50% passing, needed for the proposed average paste thickness (*APT*) model, were determined to be 0.74, 9.1, and 12 mm for sand, 14 mm maximum CA size, and 20 mm maximum CA size, respectively. The corresponding standard deviations are 0.06, 0.48, and 1.55 mm, respectively.

Rheological properties

Bingham material properties, namely the yield stress and plastic viscosity, were estimated using the SLRM II (Chidiac and Habibbeigi 2005). Once the mixing procedure was completed, the slump was measured in accordance with ASTM C143 (2015) and the SLRM II was used to measure the concrete slump as a function of time, the slump flow S_f, the slump S_l, and the time of slump t_{slump}. Subsequently, the rheological properties were calculated as follows

$$\tau_o = \frac{4gV\rho}{\sqrt{3}\,\pi S_f^2} = 0.0397\left(\frac{\rho}{S_f^2}\right) \tag{1}$$

$$\eta = \frac{\rho g H V}{150\pi S_l S_f^2} t_{slump} \tag{2}$$

where ρ is the concrete density; H is the height of the slump cone; V is the volume of slump cone; and g is the gravitational acceleration.

Compressive strength

For every mixture, six standard cylinders, 100 mm in diameter and 200 mm high, were cast, consolidated by rodding, and finished in accordance with ASTM C192 (2016). The cylinders were sealed for 24 hours then placed in a moist curing room, where the relative humidity was more than 95% and the temperature was 24°C. The concrete compressive strength was evaluated in accordance with ASTM C39 (2016) at 28 days. Three specimens were tested for each mixture.

ANALYTICAL MODELS

Packing density

Moutassem and Chidiac (2008) reviewed the literature and evaluated the adequacy of many models proposed for predicting the maximum packing density of aggregates. Of the nine packing density models investigated, only the CPM, modified Toufar model (MTM), and theory of particle mixtures model (TPM) were found to correctly predict the maximum packing density of aggregate used in concrete (Moutassem and Chidiac 2008). In this study, the maximum packing density of aggregates, ϕ^*_{agg}, and concrete, ϕ^*_{conc}, are predicted using the CPM (de Larrard 1999). To account for the different sizes of fine aggregate, coarse aggregate, and cement particles, a characteristic diameter concept corresponding to 63.2% passing was introduced (Goltermann et al. 1997). Given the method of compaction and knowing the following: volume fractions of cement, fine aggregate, and coarse aggregate; their characteristic diameters; and their maximum packing densities—the CPM model can be employed to calculate ϕ^*_{agg} and ϕ^*_{conc}.

Rheology

Chidiac and Mahmoodzadeh (2009, 2013) carried out a review of the models reported in the literature for predicting the plastic viscosity and yield stress of fresh concrete. They revealed that there are different types of models reported in the literature and that there are few models that can predict the properties. However, closer examination of the results revealed that the model proposed by Chidiac and Mahmoodzadeh, which is a fundamental model, yielded both good and consistent predictions.

Plastic viscosity—Chidiac and Mahmoodzadeh (2013) developed the following model for determining the plastic viscosity of fresh concrete based on the composition of the mixture

$$\eta_r \cong \eta_i y^3 \frac{4(1-y^7)}{4(1+y^{10}) - 25y^3(1+y^4) + 42y^5} \tag{3}$$

where η_i is the dynamic intrinsic viscosity and is a function of the particle shape; and y is the ratio of the radius of the cell to the radius of the particle and is given by (Frankel and Acrivos 1967)

$$y = (\phi/\phi^*)^{1/3}(1-\psi) \tag{4}$$

where ϕ and ϕ^* are the packing density of concrete (volume fraction of solids) and the maximum packing density of the concrete mixture, respectively; and ψ is a function of the concrete mixture and is defined as follows

$$\begin{cases} \psi = C_1 \times \dfrac{M_c}{M_w} \\ \psi = C_1 \times \dfrac{M_{HRWRA}}{M_c} \times \dfrac{M_W}{M_c + M_{FineSand+Sand}} \end{cases} \tag{5}$$

where M_c, M_w, M_{HRWRA}, and $M_{FineSand+Sand}$ correspond to the mass of cement, water, high-range water-reducing admixture (HRWRA), and the total sand, respectively; and C_1 is a calibration constant whose value depends on the method of compaction and method of measuring the rheological properties.

Yield stress—Chidiac and Mahmoodzadeh (2013) followed the same analogy to develop a fundamental model for yield stress and is given by

$$\tau_o \cong \tau_i y^3 \frac{4(1-y^7)}{4(1+y^{10}) - 25y^3(1+y^4) + 42y^5} \tag{6}$$

where τ_i is referred to as intrinsic yield stress and is a function of the particle shape; and y is given in Eq. (8) with ψ for yield stress model defined as

$$\psi = C_1\left(\frac{M_G}{M_w} + \rho_w \times V_{air}\right) \tag{7}$$

where M_G and M_w are the mass of gravel—that is, CA—and mass of water in the concrete mixture, respectively.

Compressive strength

Moutassem and Chidiac (2016) reviewed the literature and evaluated the adequacy of many concrete compressive strength models. The model proposed by Chidiac et al. (2013) is adopted because it provides a high degree of correlation to the experimental data and mathematically accounts for packing density. The model is given by

$$f_c'(t) = KR_{c28}\left(\frac{APT}{D}\right)^A B^{\frac{W+EA}{C}}(\alpha(t) - \alpha_{cr}) \tag{8}$$

where f_c' is the compressive strength of concrete; α is the degree of cement hydration at age t; α_{cr} is the critical degree of hydration; K is the aggregate to paste bond constant; R_{c28} is the standard cement strength at 28 days; APT is the average paste thickness; D is the mean diameter of all aggregate particles in the mixture; $(W+EA)/C$ is the ratio of the volume fractions of water + entrapped and entrained air to cement; and A and B are calibration constants. Constant A depends on the shape of the fine and coarse aggregate particles, while constant B depends on specimen shape and test conditions. APT, which is a function of aggregate gradations, mean sizes, volume fractions, and method of compaction, can be obtained as follows

$$APT \approx -\frac{1}{2}\left(D_s + \frac{\phi_{ca}D_s^2}{\phi_s D_{ca}} + \frac{\phi D_s^2(1-\phi^*)}{\phi_s\phi^* D}\right) + \frac{1}{2}\sqrt{\left(D_s + \frac{\phi_{ca}D_s^2}{\phi_s D_{ca}} + \frac{\phi D_s^2(1-\phi^*)}{\phi_s\phi^* D}\right)^2 + \frac{4}{3}\frac{(\phi^*-\phi)}{\phi^*}\frac{D_s^2}{\phi_s}} \tag{9}$$

where D_s and D_{ca} are the mean diameter of sand and CA particles, respectively; and ϕ, ϕ_s, and ϕ_{ca} are the volume fractions of the aggregates, sand particles, and coarse particles, respectively.

The degree of cement hydration, α, can be obtained using a cement hydration model such as the one proposed by Schindler and Folliard (2005) and adopted in this study. The critical degree of hydration, α_{cr}, was predicted according to Rasmussen et al. (2002). The adopted models are as follows

$$\alpha_{cr} = k \times w/c \tag{10}$$

$$\alpha = \alpha_u \cdot \exp\left(-\left[\frac{\tau}{t_e}\right]^\beta\right) \tag{11}$$

$$\tau = 66.78 p_{C3A}^{-0.154} p_{C3S}^{-0.401} \cdot \text{Blaine}^{-0.804} \cdot p_{SO3}^{-0.758} \cdot \exp(2.187 p_{SLAG} + 9.5 p_{FA} p_{FA\text{-CaO}}) \tag{12}$$

$$\beta = 181.4 p_{C3A}^{0.146} p_{C3S}^{0.227} \cdot \text{Blaine}^{-0.535} \cdot p_{SO3}^{0.558} \cdot \exp(-0.647 p_{SLAG}) \tag{13}$$

$$\alpha_u = \frac{1.031\,w/c}{0.194 + w/c} + 0.50 p_{FA} + 0.30 p_{SLAG} \leq 1.0 \tag{14}$$

$$t_e = \sum_0^t \exp\left(\frac{E}{R}\left(\frac{1}{293} - \frac{1}{T+273}\right)\right)\Delta t \tag{15}$$

where t_e is the equivalent age (hours); α_u is the ultimate degree of cement hydration; T is the concrete temperature (°C); E is the activation energy (33,500 J/mol for $T > 20°C$); R is the universal gas constant (8.3144 J/mol/K); τ and β are the hydration time parameter and hydration shape parameter, respectively; p_{C3A}, p_{C3S}, p_{SO3}, p_{FA}, p_{SLAG}, $p_{FA\text{-CaO}}$ are the weight ratios in terms of total cement content; and k is a calibration constant (0.43 for OPC concrete).

MODEL CALIBRATION AND PREDICTION

Calibration procedure

The experimental test results are used to calibrate the parameters η_i, τ_i, and C_1 in the plastic viscosity and yield stress models and the parameters K, A, and B in the compressive strength model. Model calibration was achieved using least-squares analysis. The values of the constants were selected by minimizing the model standard error (σ), which provides a global assessment of the model prediction (Montgomery and Runger 2003)

$$\sigma = \sqrt{\frac{\sum_i (Model_i - Experiment_i)^2}{n-p}} \tag{16}$$

where $Model_i$ and $Experiment_i$ are the model and experiment values corresponding to mixture i, respectively; n is the number of test points; and p is the number of model constants. In addition, the correlation coefficient (R^2), which measures the degree of correlation between the model and experiment, was also calculated.

Model prediction

The properties of the concrete mixture listed in Table 2 were evaluated. Table 3 shows the experimental and predicted values for yield stress, plastic viscosity, and compressive strength. Errors as a percent difference between experiment and model predicted values are also presented. Table 4 presents the goodness of fit—that is, σ and R^2—for non-air-entrained and air-entrained concretes. These results provide a reasonable degree of correlation to the experimental data. Figure 1 illustrates graphically the goodness of fit of the rheological properties and compressive strength prediction models for air-entrained and non-air-entrained mixtures. Because the compressive strength model accounts for air, the corresponding graph consists of both.

CORRELATION BETWEEN MIXTURE DESIGN, RHEOLOGY, AND COMPRESSIVE STRENGTH

Production and potential use of correlation nomographs

The identified models provided in this paper were used to produce correlation nomographs to illustrate graphically the postulation that packing density provides a continuous link between concrete mixture, rheology, and strength (Moutassem 2010). The input parameters include w/c, water content, air content, V_{CA}, and maximum CA size. The nomographs shown in Fig. 2 to 5 correspond to air-entrained concrete mixtures. The nomographs shown in Fig. 6 to 9 correspond to non-air-entrained concrete mixtures. Each figure contains three charts. The dashed lines in chart 1 correspond to the yield stress versus ϕ/ϕ^*_{conc}, whereas the solid lines correspond to the water content versus ϕ/ϕ^*_{conc}. Chart 2 is similar to chart 1 except that the rheological property is the plastic viscosity instead of the yield stress.

Table 3—Experimental and predicted rheological properties and compressive strength results

Mixture No.	$(\phi/\phi^*)_{agg}$	$(\phi/\phi^*)_{conc}$	τ_{oexp}, Pa	τ_{omodel}, Pa	Error, %	μ_{exp}, Pa-s	μ_{model}, Pa-s	Error, %	$f_c'{}_{exp}$	$f_c'{}_{model}$	Error, %
1	0.741	0.880	1763	1398	21	49	34	30	37.8 ± 2.3	36.5	3
2	0.803	0.863	1046	918	12	12	9	25	23.1 ± 1.2	24.3	5
3	0.716	0.883	1530	1525	0	31	40	31	36.4 ± 1.0	38.1	5
4	0.790	0.855	645	761	18	6	7	17	27.2 ± 1.1	24.9	9
5	0.752	0.895	2228	2200	1	80	84	5	35.7 ± 1.8	37.9	6
6	0.810	0.865	887	962	8	11	10	13	23.9 ± 2.0	23.7	1
7	0.721	0.885	2105	1610	23	56	45	20	38.4 ± 1.4	38.0	1
8	0.796	0.873	600	1182	97	9	13	42	23.8 ± 2.3	27.3	15
9	0.783	0.867	738	1011	37	8	13	63	30.4 ± 0.8	30.0	1
10	0.839	0.864	1391	946	32	—	—	—	14.9 ± 0.8	14.7	2
11	0.762	0.862	565	902	60	5	11	121	32.9 ± 1.0	31.1	5
12	0.815	0.850	720	680	6	8	5	34	18.4 ± 0.7	16.7	9
13	0.778	0.871	876	1103	26	9	15	66	30.7 ± 2.6	30.6	0
14	0.827	0.856	841	779	7	9	6	30	13.6 ± 0.6	14.8	9
15	0.756	0.865	864	950	10	10	12	19	32.5 ± 0.2	31.4	3
16	0.818	0.861	604	863	43	8	7	11	18.6 ± 2.0	18.7	0
17	0.770	0.867	922	1005	9	9	13	44	31.9 ± 0.6	31.0	3
18	0.761	0.844	759	592	22	7	6	13	26.3 ± 1.0	27.7	5
19	0.755	0.853	742	718	3	9	8	12	25.5 ± 1.3	28.9	13
20	0.763	0.859	794	840	6	—	—	—	33.1 ± 2.2	30.0	9
21	0.729	0.904	1208	1210	0	20	25	29	42.6 ± 1.5	41.7	2
22	0.803	0.884	607	649	7	—	—	—	31.0 ± 0.3	30.3	2
23	0.702	0.902	1464	1138	22	26	22	14	43.8 ± 3.5	42.1	4
24	0.788	0.873	728	463	36	6	5	16	29.7 ± 0.3	30.2	2
25	0.744	0.915	2131	2027	5	48	47	2	40.5 ± 2.4	42.4	5
26	0.816	0.888	679	732	8	7	8	22	31.9 ± 2.3	29.8	7
27	0.719	0.910	1134	1560	38	—	—	—	43.3 ± 1.4	42.9	1
28	0.786	0.877	597	546	8	9	5	40	27.3 ± 0.7	29.8	9

Table 4—Goodness of fit

	Plastic viscosity, Pa-s		Yield stress, Pa		Compressive strength, MPa	
Air consideration	σ	R^2	σ	R^2	σ	R^2
Air-entrained	6.1	0.92	269	0.74	1.8	0.96
Non-air-entrained	3.9	0.95	250	0.83		

The dashed lines in chart 3 correspond to ϕ/ϕ^*_{conc} versus ϕ/ϕ^*_{agg}, whereas the solid lines correspond to ϕ/ϕ^*_{agg} versus compressive strength. Following the same procedure, additional nomographs can be produced to cover a wider range of input parameters.

Applicability and adequacy of correlation nomographs

Once the mixture design is known, charts 1 and 2 can be used to determine ϕ/ϕ^*_{conc} and the corresponding yield stress and plastic viscosity values. Knowing ϕ/ϕ^*_{conc} from charts 1 or 2, the ϕ/ϕ^*_{agg} can be determined using the dashed lines shown in chart 3. With ϕ/ϕ^*_{agg} determined, the solid lines in chart 3 can be used to determine the corresponding compressive strength of concrete. To illustrate the applicability and test the adequacy of the correlation nomographs, a concrete mixture was randomly selected from Table 2 (No. 2) and the relevant nomograph was manually used to ensure that it yields rheological and strength results similar to those shown in Table 3. Entering the first chart of Fig. 4 with a water content of 193 kg/m^3 and intersecting the bold line corresponding to V_{CA} of 0.62 yields a ϕ/ϕ^*_{conc} of approximately 0.863 on the x-axis. Moving vertically upwards from this point and intersecting the dashed line corresponding to

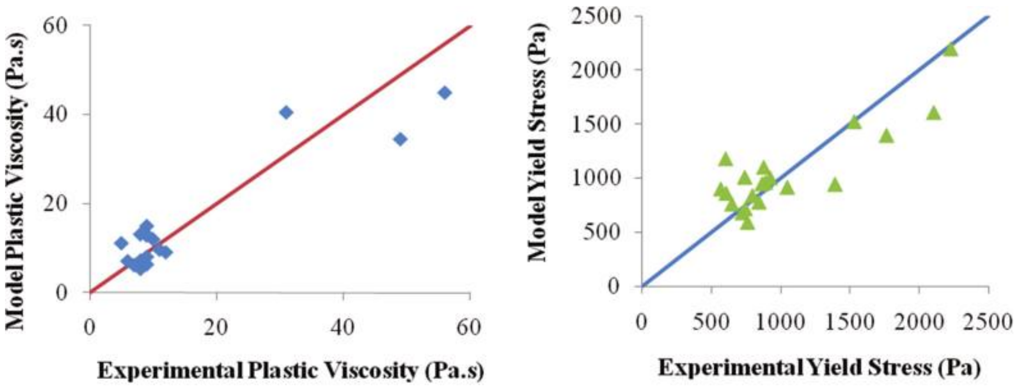

(a) Plastic Viscosity, air entrained (b) Yield Stress, air entrained

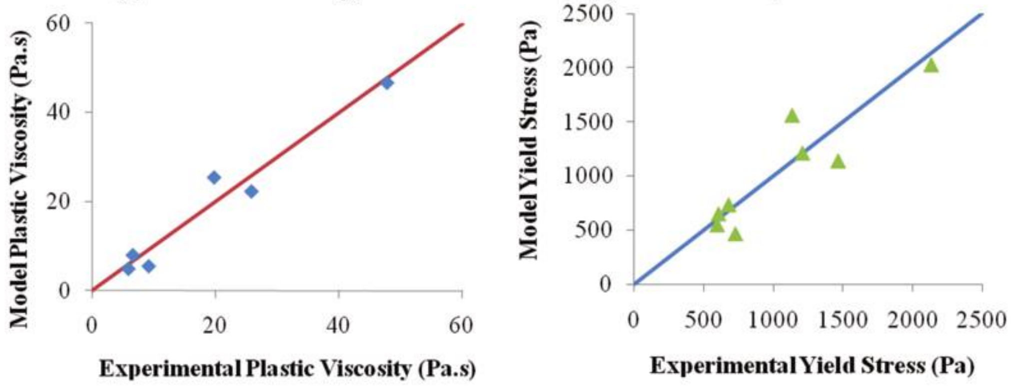

(c) Plastic Viscosity, non-air entrained (d) Yield Stress, non-air entrained

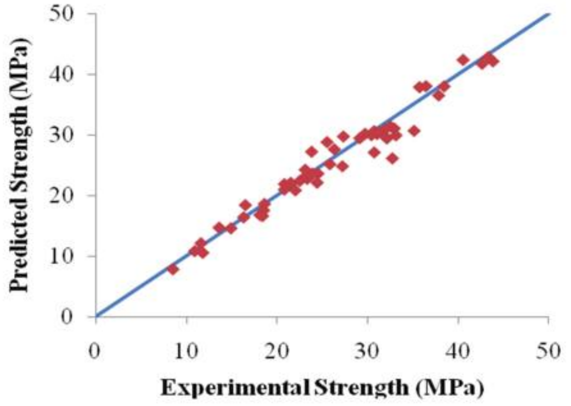

(e) Compressive Strength

Fig. 1—Prediction capability of yield stress, plastic viscosity, and strength models.

V_{CA} of 0.62 yields a yield stress of approximately 950 Pa. Entering the second chart with a water content of 193 kg/m^3 and intersecting the bold line corresponding to V_{CA} of 0.62 yields a ϕ/ϕ^*_{conc} of approximately 0.863 on the x-axis. Moving vertically upwards from this point and intersecting the dashed line corresponding to V_{CA} of 0.62 yields a plastic viscosity of approximately 9.5 Pa-s. Entering the third chart with ϕ/ϕ^*_{conc} of approximately 0.863 and intersecting the dashed line corresponding to V_{CA} of 0.62 yields a ϕ/ϕ^*_{agg} of approximately 0.805 on the x-axis. Moving vertically upwards from this point and intersecting the bold line corresponding to V_{CA} of 0.62 yields a compressive strength of approximately 24.6 MPa. Comparison reveals that these results are similar to those shown in Table 3. Hence, these nomographs demonstrate that there exists a continuous link between concrete mixture, rheology, and compressive strength through packing density. The small variability in the results is due to human error when manually using the charts, and because these nomographs for air-entrained concrete were constructed from the models by assuming a target air content of 5%, whereas the actual air content for this mixture is 5.3%.

Correlations trend

The effect of *w*/*c*, water content, V_{CA}, maximum aggregate size, and air content on the properties were investigated to verify their consistence with what is reported in literature. These figures reveal that an increase in *w*/*c* due to an increase in water content or a reduction in the cement content results in a decrease in yield stress, plastic viscosity,

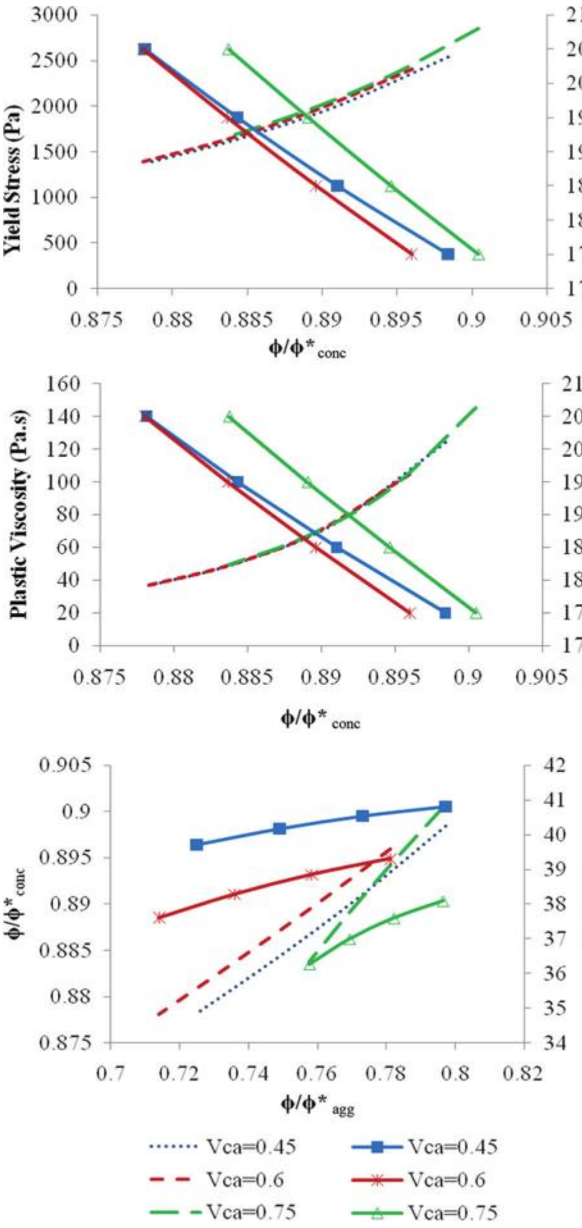

*Fig. 2—Linking rheological properties to strength: Nomograph—*w/c *= 0.40, 14 mm, air-entrained (5% air).*

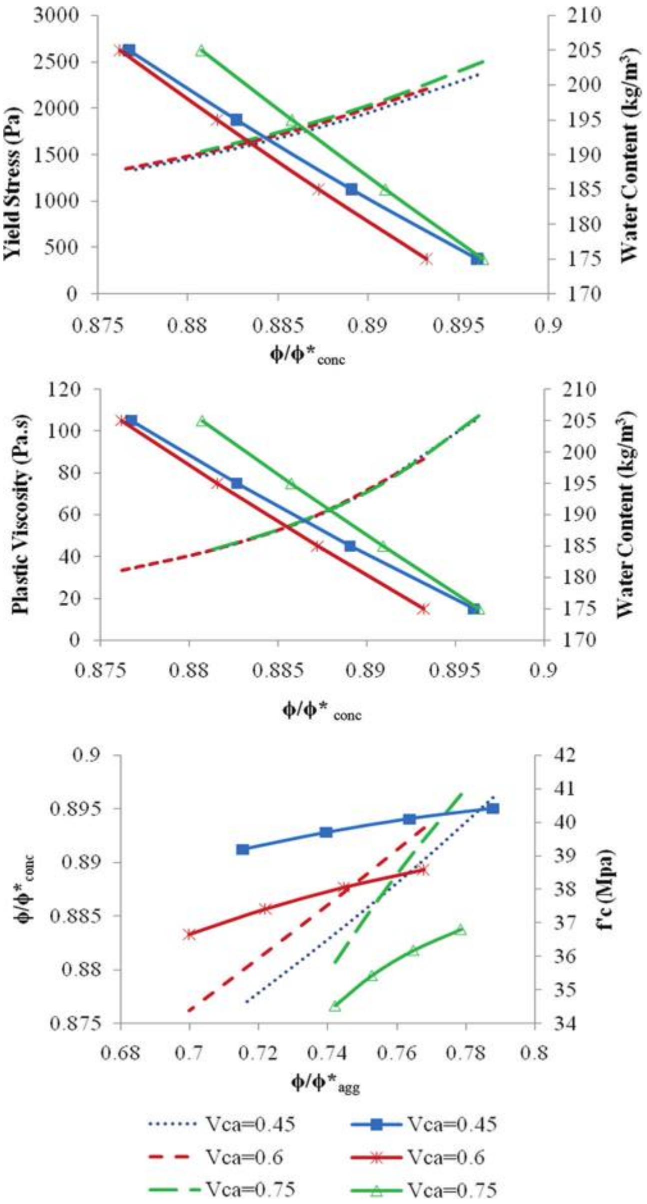

*Fig. 3—Linking rheological properties to strength: Nomograph—*w/c *= 0.40, 20 mm, air-entrained (5% air).*

and compressive strength, which is consistent with literature (Quiroga 2003). The volume fraction of solids, ϕ_{conc}, can be determined from $1–V_{air}–V_{water}$. An increase in water content or a reduction in cement content reduces ϕ_{conc} significantly relative to its effect on ϕ^*_{conc}, which depends on the mixture gradation. This results in a reduction in ϕ/ϕ^*_{conc} and a reduction in the yield stress and plastic viscosity, according to Eq. (3) and (6). In addition, an increase in *w*/*c* results in a reduction in strength due to an increase in the water-filled capillary porosity and in accordance with Eq. (8).

These figures also reveal that an increase in the water content for fixed *w*/*c* results in a reduction in yield stress, plastic viscosity, and strength, which is consistent with literature (Quiroga 2003). The reduction in yield stress and plastic viscosity is due to the presence of a larger volume of excess paste beyond what is required to fill the voids between the particles, which results in further lubrication. An increase in V_{CA} for fixed *w*/*c* and water content (that is, fixed ϕ_{agg}) influences the sand-aggregate ratio (S/A), which can result in either a decrease or increase in ϕ^*_{agg}, depending on the total aggregates gradation. Research has shown that there is an optimum S/A that equals the maximum binary packing of these elements. This optimum S/A corresponds to minimum porosity and thus maximum workability and strength (Johansen and Andersen 1996; Quiroga 2003). Comparing the figures with 14 mm maximum aggregate size to the figures with 20 mm maximum aggregate size, it is revealed that an increase in the maximum aggregate size results in an increase in workability and a slight reduction in compressive strength, which is consistent with literature (ACI Committee 318 2005; de Larrard 1999; Quiroga 2003). The figures also reveal that an increase in the air content through air entrainment for fixed mixture constituents results in a reduction in yield stress, plastic viscosity, and compressive strength, which is consistent with literature (Tattersall and Banfill

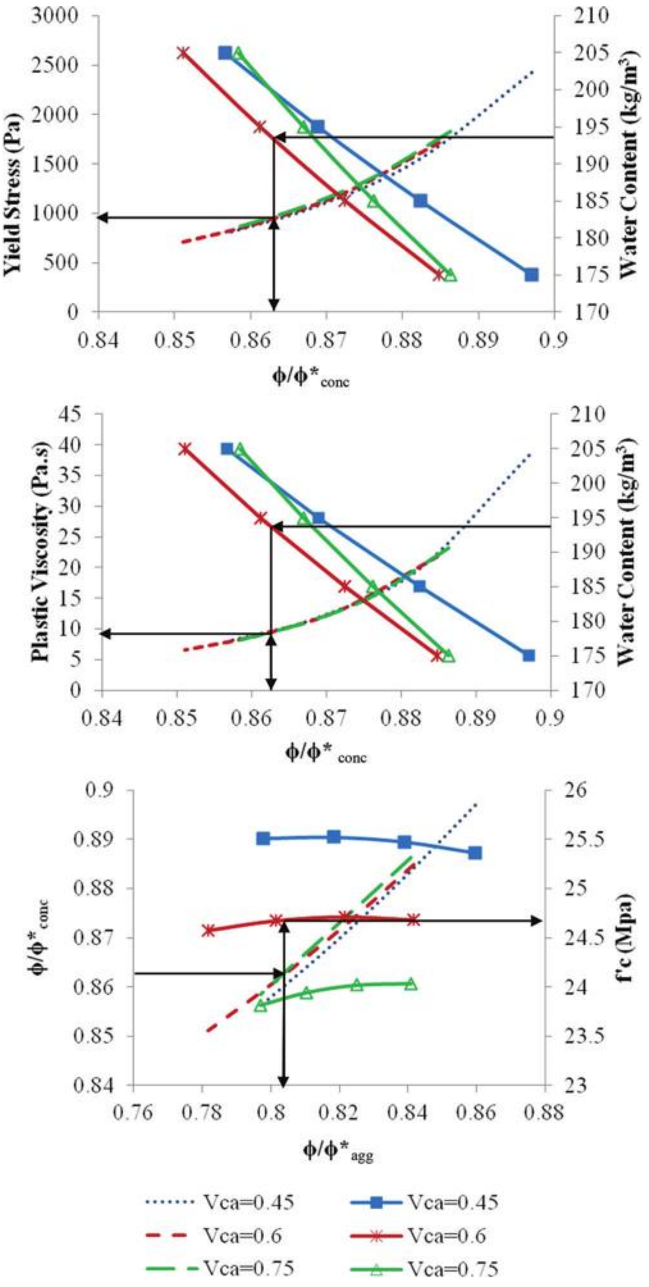

*Fig. 4—Linking rheological properties to strength: Nomograph—*w/c *= 0.60, 14 mm, air-entrained (5% air).*

1983). In the context of packing density, an increase in the amount of air results in smaller ϕ_{conc} but has no influence on ϕ^*_{conc}. Therefore, ϕ/ϕ^*_{conc} would decrease and lead to a reduction in the yield stress and plastic viscosity, according to Eq. (3) and (6). An increase in air content would increase the porosity and result in a reduction in the compressive strength of concrete (ACI Committee 318 2005).

NEW METHODOLOGY FOR CONCRETE MIXTURE DESIGN AND CASE STUDY

New concrete mixture design methodology

Recognizing that packing density is a statistically significant variable for both strength and slump (rheology), and that it is a mixture property, it was postulated and then confirmed that packing density is a central variable providing a continuous link between concrete mixture, rheology, and compressive strength. On this basis, the following methodology is proposed to integrate packing density and rheology in the design of concrete mixture:

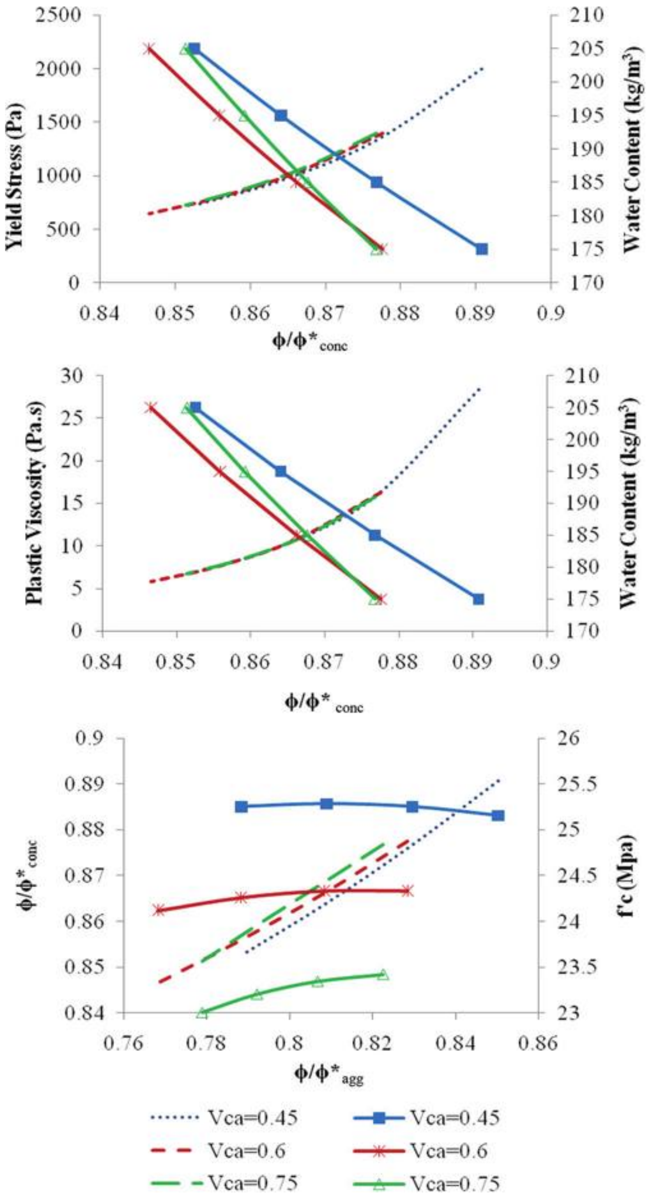

*Fig. 5—Linking rheological properties to strength: Nomograph—*w/c *= 0.60, 20 mm, air-entrained (5% air).*

Proposed methodology

- Design requirements: compressive strength, yield stress, plastic viscosity (f_c', τ_o, μ).
- From $f_c'{}_{required}$ and according to ACI 211.1 guidelines → Estimate w/c.
- From $\tau_{o\ required}$, compute slump using model (Chidiac et al. 2000; Chidiac and Habibbeigi 2005) and from ACI 211.1 guidelines → Estimate water content.
- From w/c and water content → Determine cement content.
- Determine V_{CA}/V_{agg} through optimization of ϕ^*_{agg} using a suitable packing density model such as MTM, CPM, or TPM.
- From $V_{agg} = 1 - V_w - V_c - V_{air}$ and from known V_{CA}/V_{agg} → Calculate V_{CA}.

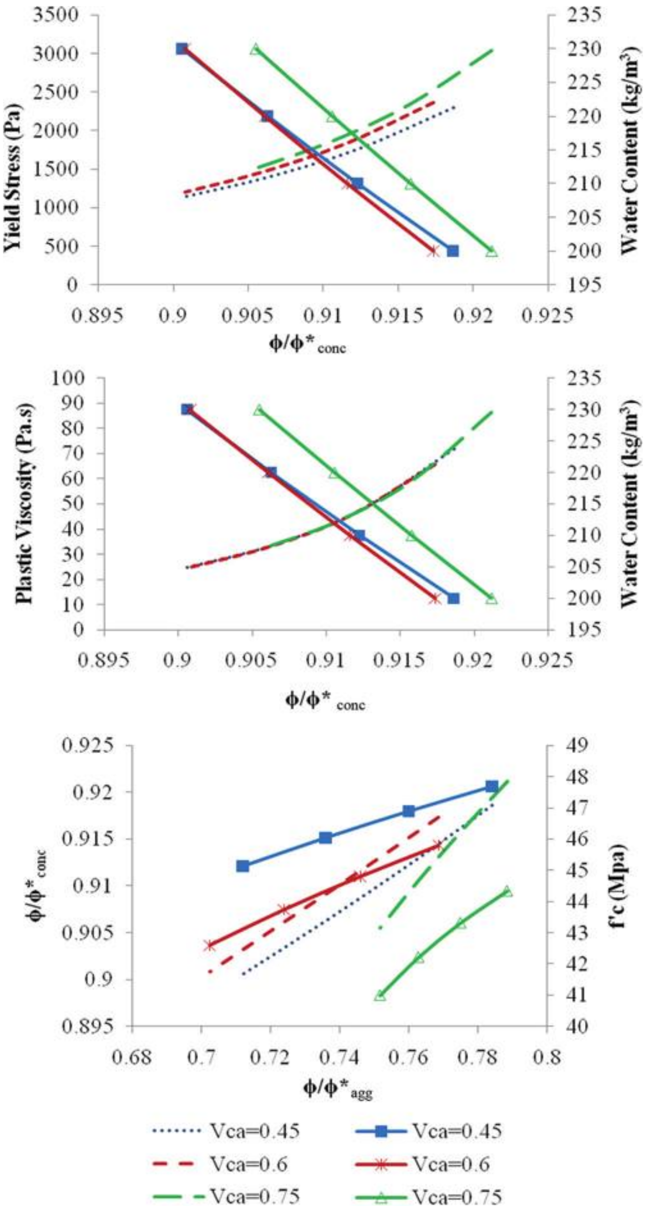

*Fig. 6—Linking rheological properties to strength: Nomograph—*w/c *= 0.40, 14 mm, non-air-entrained.*

- Determine V_s remaining and mixture proportions in kg/m^3.
- Predict f_c' using Eq. (8) or any using any other suitable f_c' model or using the nomographs, and then check that f_c' > required f_c'.
- Determine $\phi_{concrete}$ from mixture and compute $\phi^*_{concrete}$ using MTM, CPM, or TPM.
- Using rheological models such as Eq. (3) and (6) or by using the nomographs → Predict τ_o and μ and check if OK.
- If $f_c'_{predicted} < f_c'_{required}$ → adjust *w/c* and iterate.
- If predicted τ_o or μ are not as desired → adjust water content and iterate.

Case study

The following design case study demonstrates the applicability and adequacy of the proposed methodology:

Given: $f_c'_{required} > 35$ MPa, $\tau_{o,required} < 1000$ Pa, $\mu_{required} < 30$ Pa-s, 14 mm maximum aggregate size, air-entrained concrete (~5%), materials properties, and gradations.

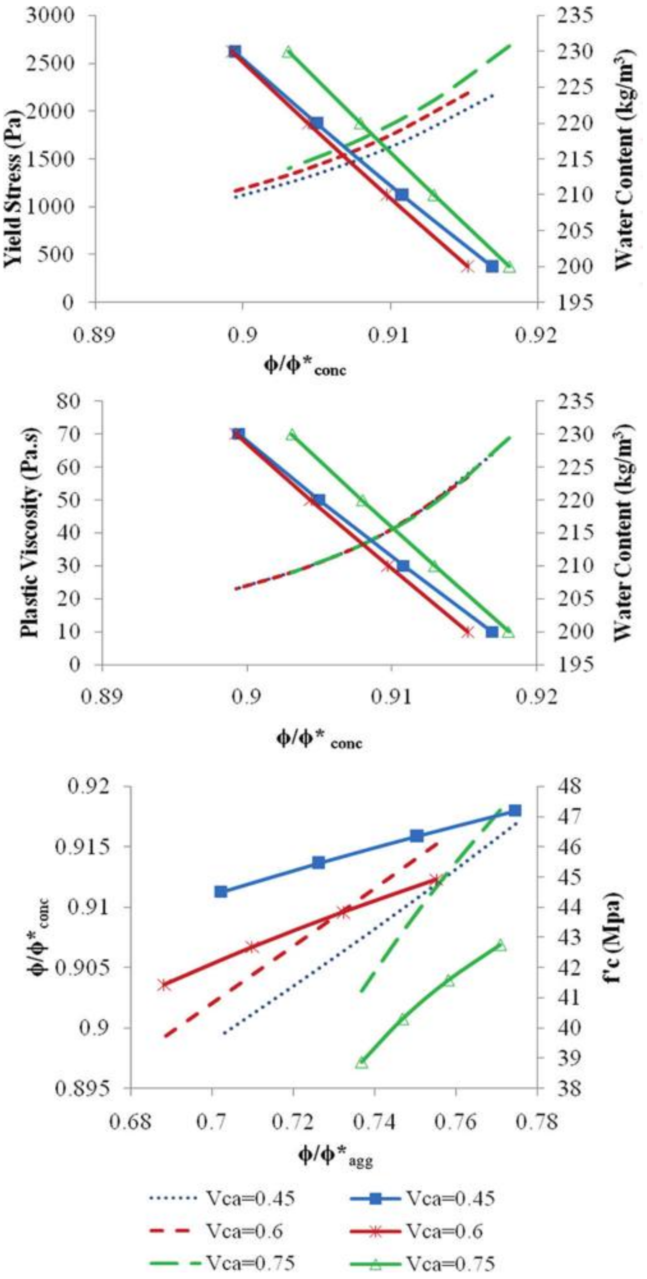

*Fig. 7—Linking rheological properties to strength: Nomograph—*w/c *= 0.40, 20 mm, non-air-entrained.*

- From ACI 211.1 guidelines → $w/c = 0.39$
- For $\tau_o = 1000$ Pa → Slump = 200 mm. From ACI 211.1 guide → W = 205 kg/m → C = 526 kg/m^3.
- Using CPM → $V_{CA} = 0.58$ and $\phi^*_{agg} = 0.816$ → CA = 914 kg/m^3 and FA = 663 kg/m^3
- Using *APT* model: *APT* = 0.208 mm
- Using f_c' model: $f_c' = 37.8$ MPa > 35 → OK
- Using rheology models: $\mu = 29.8$ Pa-s < 30 Pa-s → OK; $\tau_o = 1201$ Pa > 1000 Pa → NO → Increase water content
- Assume W = 220 kg/m^3 → C = 564 kg/m^3
- From the CPM → $V_{CA} = 0.56$ and $\phi^*_{agg} = 0.816$ → CA = 883 kg/m^3 and FA = 620 kg/m^3
- Using *APT* model: *APT* = 0.240 mm
- Using f_c' model: $f_c' = 36.3$ MPa > 35 MPa → OK
- And: $\mu = 20.9$ Pa-s < 30 Pa-s → OK; $\tau_o = 975$ Pa < 1000 Pa → OK

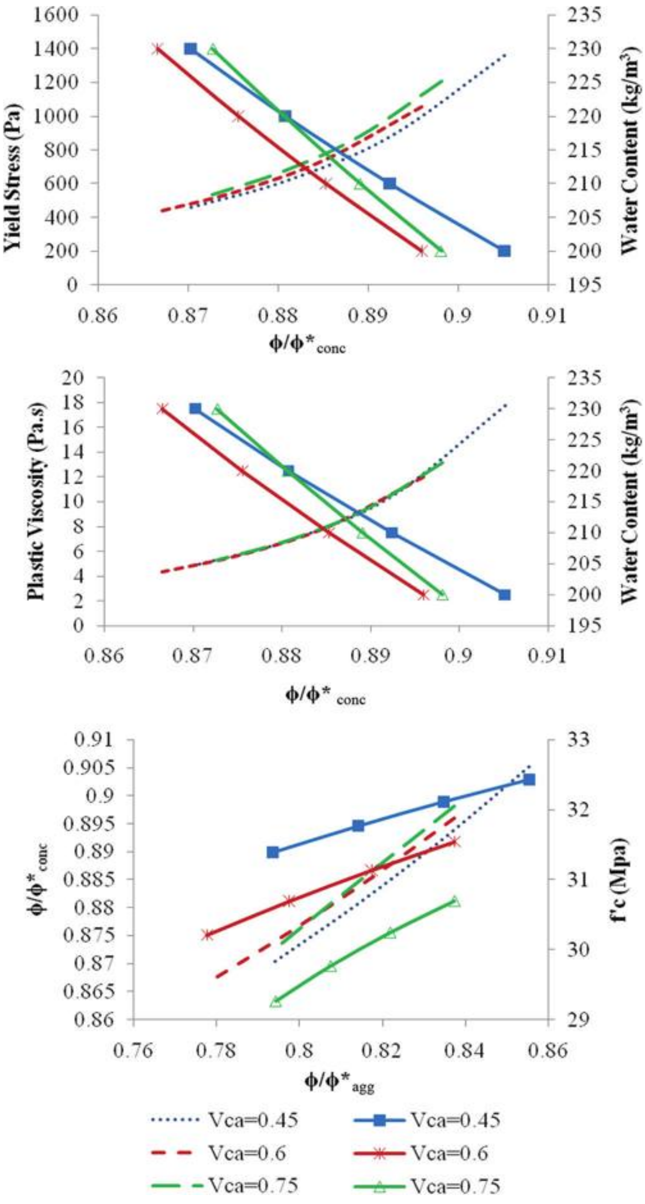

*Fig. 8—Linking rheological properties to strength: Nomograph—*w/c *= 0.60, 14 mm, non-air-entrained.*

CONCLUSIONS

The experimental and analytical study undertaken to investigate the postulation that packing density provides a link between the concrete mixture, the rheological properties, and the compressive strength has revealed the following:

1. The model analogy developed to investigate the desired link was evaluated and has shown to provide good degree of correlation to the experimental data. The correlation factors for yield stress, plastic viscosity, and compressive strength models were 0.74, 0.92, and 0.96 for air-entrained concrete and 0.83, 0.95, and 0.96 for non-air-entrained concrete, respectively.

2. The correlation nomographs demonstrate a continuous link between concrete mixture, rheology, and compressive strength through packing density.

3. The model correlation trends show that an increase in water-cement ratio (*w*/*c*), water content, maximum aggregate size, or air content through entrainment results in a reduction in the yield stress, plastic viscosity, and compressive strength whereas an increase in coarse aggregate volume can result in either a decrease or increase in the properties, depending on the corresponding maximum packing density of concrete. These trends were found consistent with what has been reported in literature.

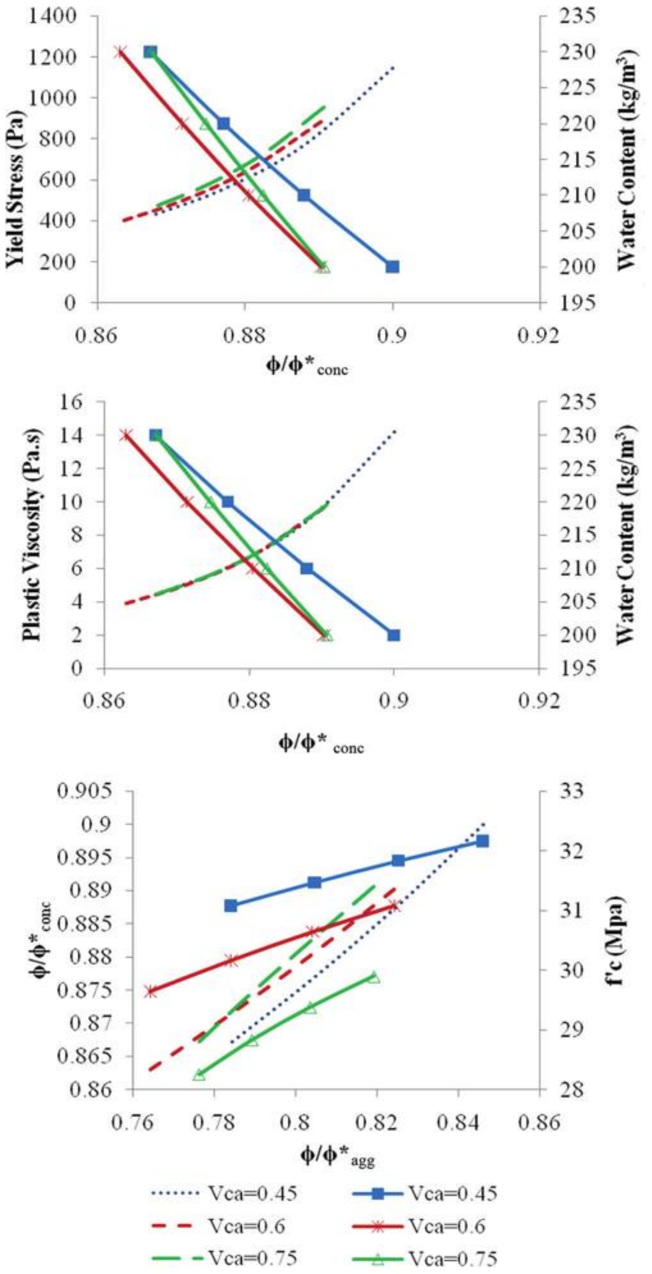

*Fig. 9—Linking rheological properties to strength: Nomograph—*w/c *= 0.60, 20 mm, non-air-entrained.*

Consequently, an improved version of the ACI 211.1 mixture proportioning methodology that incorporates the rheological properties and optimizes packing density of aggregates was proposed, and a case study was conducted to test for its applicability and adequacy. This research outcome, which provides a quantitative approach to design concrete mixtures to meet specific strength requirements and rheology, can also be used to ensure quality control before concrete is cast for more sustainable structures.

AUTHOR BIOS

Fayez Moutassem *is the Chair of the Department of Civil and Infrastructure Engineering at the American University of Ras Al Khaimah, Ras Al Khaimah, United Arab Emirates. He received his PhD in civil engineering from McMaster University, Hamilton, ON, Canada, and his MS from Texas A&M University, College Station, TX. His research interests include concrete structures and materials including precast and prestressed members, sustainability in design and construction, green buildings, quality control, and properties of structural concrete using special materials.*

ACI member **Samir E. Chidiac** *is a Professor of civil engineering and a member of the Centre for Effective Design of Structures at McMaster University, where he received his undergraduate and graduate degrees in civil engineering. His research interests include sustainability and resiliency of materials and structures.*

ACKNOWLEDGMENTS

The authors would like to thank Natural Science and Engineering Research Council of Canada and McMaster University for their support and funding. In addition, the author would like to thank the American University of Ras Al Khaimah for providing the necessary time that helped shape up the writing of the paper.

On behalf of all authors, the corresponding author states that there is no conflict of interest.

REFERENCES

ACI Committee 211, 1991, “Standard Practice for Selecting Proportions for Normal, Heavyweight, and Mass Concrete (ACI 211.1-91),” American Concrete Institute, Farmington Hills, MI, 38 pp.

ACI Committee 318, 2005, “Building Code Requirements for Structural Concrete (ACI 318-05) and Commentary (ACI 318R-05),” American Concrete Institute, Farmington Hills, MI, 430 pp.

ASTM C29-97, 1997, “Standard Test Method for Bulk Density and Voids in Aggregate,” ASTM International, West Conshohocken, PA, 4 pp.

ASTM C39-16, 2016, Standard Test Method for Compressive Strength of Cylindrical Specimens,” ASTM International, West Conshohocken, PA, 7 pp.

ASTM C127-15, 2015, “Standard Test Method for Specific Gravity and Absorption of Coarse Aggregate,” ASTM International, West Conshohocken, PA, 5 pp.

ASTM C128-15, 2015, “Standard Test Method for Specific Gravity and Absorption of Fine Aggregate,” ASTM International, West Conshohocken, PA, 6 pp.

ASTM C136-14, 2014, “Standard Test Method for Sieve Analysis of Fine and Coarse Aggregates,” ASTM International, West Conshohocken, PA, 5 pp.

ASTM C143-15, 2015, “Standard Test Method for Slump of Hydraulic-Cement Concrete,” ASTM International, West Conshohocken, PA, 4 pp.

ASTM C192-16, 2016, “Making and Curing Concrete Specimens in the Laboratory,” ASTM International, West Conshohocken, PA, 8 pp.

ASTM C260-10, 2010, “Air-Entraining Admixtures for Concrete,” ASTM International, West Conshohocken, PA, 3 pp.

Chidiac, S. E., and Habibbeigi, F., 2005, “Modelling the Rheological Behaviour of Fresh Concrete: An Elasto-Viscoplastic Finite Element Approach,” *Computers and Concrete*, V. 2, No. 2, pp. 97-110. doi: 10.12989/cac.2005.2.2.097

Chidiac, S. E.; Maadani, O.; Razaqpur, A. G.; and Mailvaganam, N. P., 2000, “Controlling the Quality of Fresh Concrete – A New Approach,” *Magazine of Concrete Research*, V. 52, No. 5, pp. 353-363. doi: 10.1680/macr.2000.52.5.353

Chidiac, S. E.; Maadani, O.; Razaqpur, A. G.; and Mailvaganam, N. P., 2003, “Correlation of Rheological Properties to Durability and Strength of Hardened Concrete,” *Journal of Materials in Civil Engineering*, ASCE, V. 15, No. 4, pp. 391-399. doi: 10.1061/(ASCE)0899-1561(2003)15:4(391)

Chidiac, S. E., and Mahmoodzadeh, F., 2009, “Plastic Viscosity of Fresh Concrete – A Critical Review of Predictions Methods,” *Cement and Concrete Composites*, V. 31, No. 8, pp. 535-544. doi: 10.1016/j.cemconcomp.2009.02.004

Chidiac, S. E., and Mahmoodzadeh, F., 2013, “Constitutive Flow Models for Characterizing the Rheology of Fresh Mortar and Concrete,” *Canadian Journal of Civil Engineering*, V. 40, No. 5, pp. 475-482. doi: 10.1139/L2012-025

Chidiac, S. E.; Moutassem, F.; and Mahmoodzadeh, F., 2013, “Compressive Strength Model for Concrete,” *Magazine of Concrete Research*, V. 65, No. 9, pp. 557-572. doi: 10.1680/macr.12.00167

de Larrard, F., 1999, *Concrete Mixture Proportioning: A Scientific Approach*, Spon Press, London, UK.

Ferraris, C. F., and de Larrard, F., 1998, “Testing and Modelling Fresh Concrete Rheology,” *NISTIR 6094*, National Institute of Standards and Technology, Gaithersburg, MD.

Frankel, N. A., and Acrivos, A., 1967, “On the Viscosity of Concentrated Suspension of Solid Spheres,” *Journal of Chemical Engineering Science*, V. 22, No. 6, pp. 847-853. doi: 10.1016/0009-2509(67)80149-0

Goltermann, P.; Johansen, V.; and Palbol, L., 1997, “Packing of Aggregates: An Alternative Tool to Determine the Optimal Aggregate Mix,” *ACI Materials Journal*, V. 94, No. 5, Sept.-Oct., pp. 435-443.

Johansen, V., and Andersen, P. J., 1996, “Particle Packing and Concrete Properties,” *Materials Science of Concrete II*, American Ceramic Society, Westerville, OH, pp. 111-147.

Kosmatka, S. H.; Kerkhoff, B.; and Panarese, W. C., 2002, *Design and Control of Concrete Mixtures*, seventh Canadian edition, Cement Association of Canada, Ottawa, ON, Canada.

Laskar, A. I., and Talukdar, S., 2007, “Correlation Between Compressive Strength and Rheological Parameters of High-Performance Concrete,” *Research Letters in Materials Science*, V. 2007, pp. 1-4. doi: 10.1155/2007/45869

Laskar, A. I., and Talukdar, S., 2008, “A New Mix Design Method for High Performance Concrete,” *Asian Journal of Civil Engineering*, V. 9, No. 1, pp. 15-23.

Mehdipour, I., and Khayat, K. H., 2019, “Elucidating How Particle Packing Controls Rheology and Strength Development of Dense Cementitious Suspensions,” *Cement and Concrete Composites*, V. 104, p. 103413. doi: 10.1016/j.cemconcomp.2019.103413

Montgomery, D. C., and Runger, G. C., 2003, *Applied Statistics and Probability for Engineers*, third edition, John Wiley and Sons Inc., New York.

Moutassem, F., 2010, “Packing Density Links Concrete Mixture, Rheology, and Compressive Strength,” PhD dissertation, McMaster University, Hamilton, ON, Canada.

Moutassem, F., and Chidiac, S. E., 2008, “Evaluation of Packing Density Models for Concrete Applications,” *2nd Canadian Conference on Effective Design of Structures*, McMaster University, Hamilton, ON, Canada.

Moutassem, F., and Chidiac, S. E., 2016, “Assessment of Concrete Compressive Strength Prediction Models,” *KSCE Journal of Civil Engineering*, V. 20, No. 1, pp. 343-358. doi: 10.1007/s12205-015-0722-4

Moutassem, F., and Miqdadi, I., 2020, “Sustainability-Model Approach for Chloride Permeability Based on Concrete Mixture,” *Structures*, V. 28, pp. 983-990. doi: 10.1016/j.istruc.2020.09.041

Quiroga, P., 2003, “The Effect of the Aggregate Characteristics on the Performance of Portland Cement Concrete,” PhD dissertation, The University of Texas at Austin, Austin, TX, 382 pp.

Rasmussen, R. O.; Ruiz, J. M.; Rozycki, D. K.; and McCullough, B. F., 2002, “Constructing High-Performance Concrete Pavements With FHWA HIPERPAV Systems Analysis Software,” *Transportation Research Record: Journal of the Transportation Research Board*, V. 1813, No. 1, pp. 11-20. doi: 10.3141/1813-02

Schindler, A. K., and Folliard, K. J., 2005, “Heat of Hydration Models for Cementitious Materials,” *ACI Materials Journal*, V. 102, No. 1, Jan.-Feb., pp. 24-33.

Shilstone, J. M. Sr., and Shilstone, J. M. Jr., 1993, “High Performance Concrete Mixtures for Durability,” *Proceedings of the Symposium on High Performance Concrete in Severe Environments*, SP-140, P. Zia, ed., American Concrete Institute, Farmington Hills, MI, pp. 281-306.

Tasi, C. T.; Li, S.; and Hwang, C. L., 2006, “The Effect of Aggregate Gradation on Engineering Properties of High-Performance Concrete,” *Journal of ASTM International*, V. 3, No. 3, pp. 1-12.

Tattersall, G. H., and Banfill, P. F. G., 1983, *The Rheology of Fresh Concrete*, Pitman Publishing, 356 pp.

Wong, H. H. C., and Kwan, A. K. H., 2008, “Packing Density of Cementitious Materials: Measurement and Modelling,” *Magazine of Concrete Research*, V. 60, No. 3, pp. 165-175. doi: 10.1680/macr.2007.00004

ACI MATERIALS JOURNAL TECHNICAL PAPER

Title No. 120-M48

Examining Effect of Printing Directionality on Freezing-and-Thawing Response of Three-Dimensional-Printed Cement Paste

by R. M. Ghantous, A. Evseeva, B. Dickey, S. Gupta, A. Prihar, H. S. Esmaeeli, R. Moini, and W. J. Weiss

The use of three-dimensional (3-D) printing with cementitious materials is increasing in the construction industry. Limited information exists on the freezing-and-thawing (FT) performance of the 3-D-printed elements. A few studies have used standard FT testing procedures (ASTM C666) to assess the FT response; however, ASTM C666 is insensitive to anisotropy caused by printing directionality. This paper investigates the FT response of 3-D-printed cement paste elements using thermomechanical analysis (TMA) to examine the influence of directionality in comparison to cast counterparts. Cement paste with a water-cement ratio (w/c) of 0.275 was used. The critical degree of saturation (DOS_{CR}) as well as the coefficient of thermal expansion (COTE) were determined for specimens with varying degrees of saturation (DOS). Micro-computed tomography (micro-CT) was conducted to quantitatively understand the heterogeneities in the pore microstructure of 3-D-printed materials. For the specimens fabricated in this study, the COTE and DOS_{CR} are independent of the 3-D-printing directionality and were comparable to conventionally cast specimens. For samples at 100% saturation, the FT damage was higher in the 3-D-printed samples as compared to the cast samples. The use of a low w/c in the 3-D-printed materials, desired from a buildability perspective, led to low capillary porosity, which thus decreased the amount of freezable pore solution and increased the FT resistance of the 3-D-printed materials. Micro-CT analysis demonstrated a significant 4.6 times higher average porosity in the interfacial regions compared to the filament cores.

Keywords: anisotropy; coefficient of thermal expansion (COTE); freezable solution; freezing-and-thawing (FT) performance; three-dimensional (3-D)-printed cement paste.

INTRODUCTION

There have been growing advancements in the fabrication of concrete elements made using additive manufacturing.[1-8] Additive manufacturing fabrication may improve productivity in the construction industry,[9,10] enable construction in remote areas using local materials,[11] reduce waste and costs associated with formwork,[12] and enable the creation of concrete components with complex architectures and novel performance.[1,13,14]

Studies have primarily focused on mixture designs and process development.[15-21] Other studies have examined the influence of processing parameters, such as speed and the time gap between the layers, on the mechanical properties of printed concrete specimens and on the interlayers' adhesion.[14,19,22-26] The durability of three-dimensional (3-D)-printed concrete structures is only recently being examined.[27-35] The layer-wise process of additive manufacturing with cement-based materials may lead to microstructural heterogeneities such as weak interfaces.[14,25,36] Further research is necessary to understand whether 3-D-printed cement-based elements can be assumed to behave as a homogenous material with an isotropic material response.

This study will focus on one aspect of durability: the freezing-and-thawing (FT) response of printed cementitious materials. The presence of cold joints, macropores, and interfaces in the printed cementitious elements may influence their FT response.[30,31,36] In addition, the quality of the entrained air (that is, shape, size, and spacing), commonly used in conventional concrete to increase its FT resistance[37,38] may be altered due to the shearing process, the processing parameters such as extrusion pressure, and the interaction of air-entraining admixtures with other admixtures typically used in the mixture design of printed materials, such as high-range water-reducing admixtures (HRWRAs) and accelerators.[35,39,40]

Few studies have investigated the FT response of printed cementitious specimens.[27,30,34,35,41,42] Das et al.[35] used protected paste volume analysis to predict similar performance for the cast and printed specimens under freezing conditions. Das et al.[30] measured the FT resistance of printed and cast specimens using ASTM C666 Procedure B and concluded that printed specimens have lower resistance to FT cycles as compared to cast specimens due to high capillary porosity at the interface between the printed filaments.[30] Zhang et al.[34] measured higher FT damage in printed specimens as compared to cast samples using the dynamic elastic modulus; they concluded that the FT-induced damage occurred along weak printed interfaces, and the aggregates were more difficult to dislodge from the surface of printed specimens than cast samples due to the extrusion pressure leading to a densely packed surface in printed materials. Assaad et al.[41] concluded that the interface between filaments is more vulnerable to FT cycles as compared to the bulk of the printed mortar filaments. They observed that the rate of decrease in the interlayer bond was two to three times higher than the rate of decrease in the compressive and flexural strengths with the FT cycles.[41] Wangler et al.[27] showed the

---

ACI Materials Journal, V. 120, No. 4, July 2023.

MS No. M-2022-381.R1, doi: 10.14359/51738808, received March 26, 2023, and reviewed under Institute publication policies. Pertinent discussion including author's closure, if any, will be published ten months from this journal's date if the discussion is received within four months of the paper's print publication.

first study on the field performance of printed cementitious materials exposed to an FT environment, where FT damage was assessed by a visual inspection of cracks development. Wang et al.[42] concluded that anisotropy influences the FT resistance of 3-D-printed mortar specimens.

The aforementioned studies evaluated the FT performance of 3-D-printed cementitious materials that were partially or fully immersed in water. However, an alternative approach, based on critical saturation theory, has been proposed to describe the FT response of conventional concrete by separately taking into account the water absorption and resistance of the specimen to freezing at a given degree of saturation (DOS).[43-46] The critical saturation theory states that concrete as a porous media is susceptible to FT damage only if its DOS is higher than a critical DOS level of saturation (that is, DOS > DOS_{CR}). The time it takes concrete to reach the critical limit state (t_{Cr}) (that is, the onset of FT damage) can be computed using Eq. (1)[47]

$$DOS_{CR} = DOS_N + \dot{S}\sqrt{t_{Cr} - t_N} \quad (1)$$

where DOS_N is the DOS where pores in the cement matrix are saturated[48]; $\dot{S}$ is the rate of water absorption in a specimen after matrix pores have been filled (that is, filling of the air voids); t_N is the duration of time needed to reach DOS_N (typically a few days); and t_{Cr} is the duration of time needed for the sample to reach critical saturation (ASTM C1585-13[49]).

For conventional concrete, it has been shown that the DOS_{CR} typically varies from 75 to 91% depending largely on the quality (the volume, size, and spacing) of the air-void system in concrete.[46,50] DOS_{CR} can be determined by measuring the FT damage in concrete at varying DOS from 100% to lower values at which no FT damage is detected.[45,51] The most common procedure consists of assessing the reduction in the dynamic modulus of elasticity by either using frequency measurements[46,52] or by using ultrasonic wave velocity measurements.[53-55] Length change can be used to assess DOS_{CR} for both cement paste and mortar specimens.[56-59] A residual change in dimension (that is, an increase in sample length) after a thermal cycle is an indicator of FT damage.[56-59] The thermomechanical analysis (TMA) measurements can be performed on specimens with various DOS and thus allow for the determination of DOS_{CR}.[56-59]

Previous TMA studies[58,59] examined cast specimens. This study investigates the influence of printing directionality on the FT response of 3-D-printed cement paste specimens, which encompass a heterogeneous microstructure with horizontal and vertical porous interfaces.[25,36] FT damage was measured using TMA in cast and printed specimens preconditioned to various DOS. This approach aims to determine whether microstructural heterogeneities and their directionality (interfaces parallel or perpendicular to the length of the specimen under investigation) influence the FT performance of printed elements at various levels of saturation. The coefficient of thermal expansion (COTE) is also extracted from this experimental data to assess any potential influence of layered heterogeneity and its directionality on the thermal expansion characteristics of 3-D-printed materials. This paper focuses on assessing "well-printed specimens" with a solid design of materials architecture (that is, "best-case scenario" specimens in which the filaments are printed close together with ~20% overlap and no intentional or few unintentional defects).

Table 1—Properties of cement used in this study

	Type I/II cement (OPC)
Cement oxides	Percentage by mass, %
Silicon dioxide (SiO_2)	19.60
Aluminum oxide (Al_2O_3)	4.40
Ferric oxide (Fe_2O_3)	2.90
Calcium oxide (CaO)	60.70
Magnesium oxide (MgO)	3.70
Sulfur trioxide (SO_3)	4.50
Equivalent alkali (Na_2O_{eq})	0.75
Loss on ignition (LOI)	2.30
Bogue phase composition	Percentage by mass, %
Tricalcium silicate (C_3S)	52.00
Dicalcium silicate (C_2S)	17.00
Tricalcium aluminate (C_3A)	7.00
Tetracalcium aluminoferrite (C_4AF)	9.00
Specific gravity	3.15

RESEARCH SIGNIFICANCE

The FT performance of 3-D-printed elements is important as they are increasingly being developed in cold climates. Previous studies have examined 3-D-printed materials using test methods (ASTM C666) designed for conventional concrete. This paper examines the influence of printing directionality on the FT response of specimens with different DOS. The TMA test method is proposed and enables the FT response to be measured with respect to the printing direction. DOS_{CR} is evaluated for potential use in the critical saturation model. The influence of 3-D-printing direction is also evaluated for the COTE.

EXPERIMENTAL PROCEDURE

Materials and mixture design

A Type I/II ordinary portland cement (OPC) (ASTM C150-07)[60] was used in this study, and its chemical composition and physical properties can be found in Table 1. The Blaine fineness of the OPC used in this study was 412 m^2/kg, and its fineness No. 325 sieve (passing) was 91.4%. An HRWRA and viscosity-modifying admixture (VMA) were used in this study (ASTM C494/C494M-08).[61] The water-cement ratio (w/c) of the cement paste was 0.275. The mixture consisted of 250 g of cement, 1.47 g of HRWRA, 2.38 g of VMA, and 65.50 g of water.

Mixture preparation, sample curing, and sample geometry

After weighing the materials, water was placed in the mixing bowl, then the VMA and HRWRA were added and dispersed using a spatula. Cement was then added to the liquid solution and mixed for 90 seconds at 400 revolutions

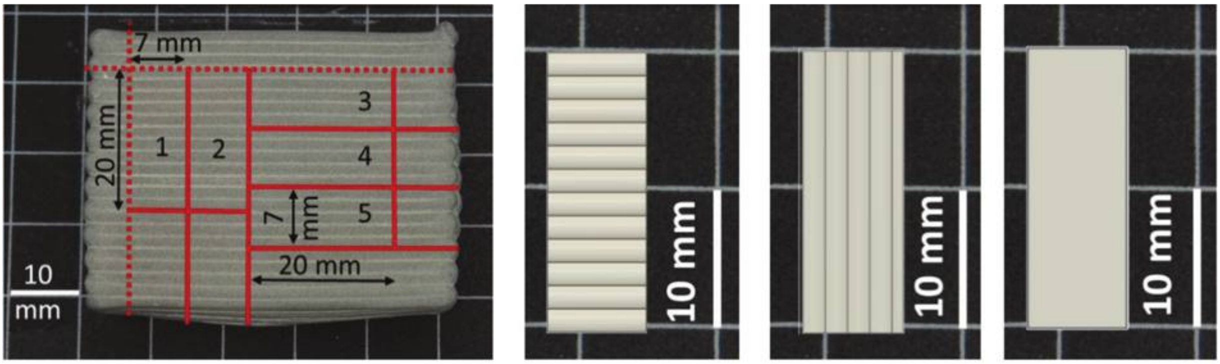

(a) (b) (c) (d)

Fig. 1—(a) Cutting sample into smaller specimens for FT damage assessment using TMA for length change measurements. Schematic representation of three geometries tested in this study: (b) 3-D-printed solid lamellar specimens with filaments perpendicular to length change measurements; (c) 3-D-printed solid lamellar specimens with filaments parallel to length change measurements; and (d) specimen obtained from cast cement paste with no filaments and interfaces. Filaments are drawn at 1:1 scale.

per minute (rpm) in a programmable vacuum mixer at a 70% vacuum level. The vacuum was stopped for 15 seconds to scrape down in the mixing bowl any paste that may have collected on the side of the bowl. The cement paste was then mixed for an additional 90 seconds at 400 rpm at a 100% vacuum level. Further details of the mixing process can be found in the earlier work of the authors.[21]

The cast cement paste was prepared in 3-D-printed polylactic acid (PLA) rectangular molds of 50 x 40 x 12 mm.

For the preparation of the 3-D-printed cement paste samples with rectilinear (lamellar) architecture, the cement paste mixture was gradually filled in a 60 mL syringe into different layers, and each layer was manually consolidated to reduce the entrapped air. The syringe was then mounted on a stepper motor-driven extrusion system, which was connected to a 3-D printer.[14] A stainless-steel nozzle with an internal diameter of 1.36 mm was used in this study and was mounted to the printer using a customized nozzle holder. A polyethylene tube with an internal diameter of 4.3 mm and length of 450 mm was used to connect the syringe and the nozzle and ensure the transfer of the paste from the syringe to the nozzle.[36] The G-code commands for the 3-D printer were generated by the commercially available slicer using the dimensions of the prismatic sample (50 x 40 x 12 mm in length, width, and height), a solid infill (100%), a lamellar filament geometry, and suitable speed and extrusion printing parameters.[25] The printing speed of 750 mm/min (corresponding to a layer deposition time of 1.6 minutes) and the filament height of 1 mm were selected. The nominal width of the filament was 1.63 mm, which is 20% larger than the internal diameter of the nozzle due to the swelling of the extrudate known as the die-swell effect, which leads to approximately a 20% overlap between the filaments.

Both the cast and printed cement paste samples were transferred immediately after preparation to a sealed curing chamber that was maintained at 93 ± 2% relative humidity (RH) using saturated solutions of potassium nitrate[62] according to the procedure introduced in Moini et al.[36] Twenty-four hours after printing, the specimens were sealed for 91 days in double bags. It is recommended for future studies to keep the specimens at an RH higher than 93 ± 2% during the first 24 hours after printing to minimize carbonation and increase hydration.

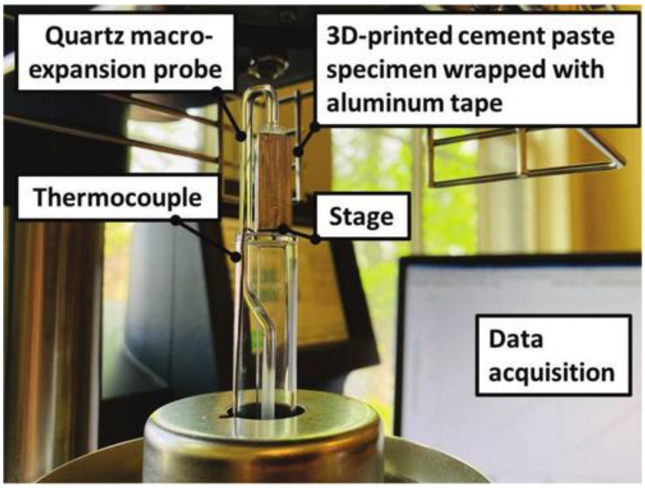

Fig. 2—Representative image of 3-D-printed specimen on glass testing stage of thermomechanical analyzer as it is prepared to be lowered into chamber.

Freezing-and-thawing damage quantification using thermomechanical analyzer

Length change measurements were collected using a thermomechanical analyzer.[58,59] After curing, five specimens were cut from each cement paste sample using a high-precision saw with a water-cooled diamond-tipped blade. First, the outer edges of the samples were cut along the dotted lines (Fig. 1(a)). Then, the specimens were cut along the solid lines as illustrated in Fig. 1(a). The dimensions of the cut prismatic specimens were 7.2 ± 0.3 mm wide, 11.6 ± 0.3 mm deep (corresponding to 12 3-D-printed layers), and 20.3 ± 0.5 mm tall. These dimensions were selected to capture several filaments in each specimen and based on the requirements of the TMA stage illustrated in Fig. 2.

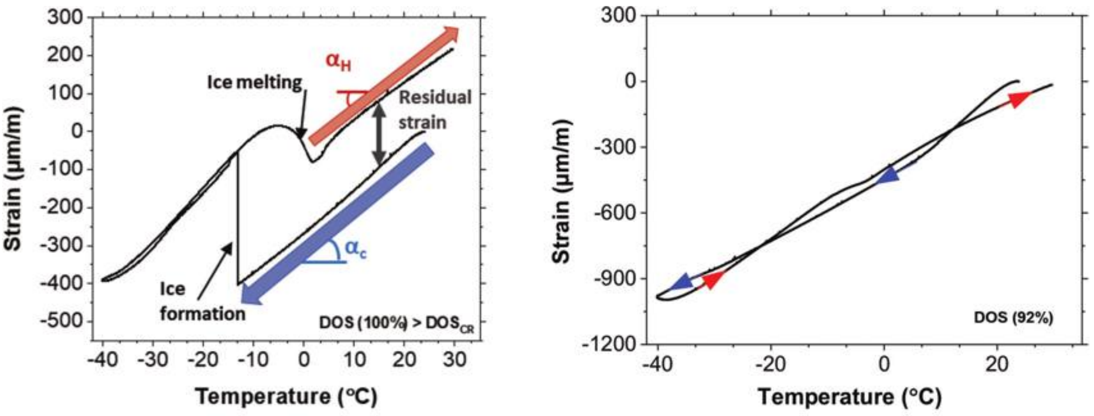

(a) (b)

Fig. 3—Strain evolution with respect to temperature in 3-D-printed specimen at: (a) 100% DOS; and (b) 92% DOS.

The 3-D-printed specimens with two different filament orientations (relative to the length change testing direction) and cast specimens were prepared for TMA as follows:

- Prismatic specimens with 3-D-printed filaments and interfaces perpendicular to the direction of the length change measurements (Fig. 1(b)).
- Prismatic specimens with 3-D-printed filaments and interfaces parallel to the direction of length change measurements (Fig. 1(c)).
- Prismatic specimens that do not contain filaments and interfaces that are obtained from the conventional casting of cement paste (Fig. 1(d)).

A comparison between the measurements collected from these three types of specimens was performed to determine the influence of printing and printing directionality on the FT response and the COTE.

For the three geometries illustrated in Fig. 1, specimens with DOS varying from 100 to 91% were prepared to be tested for FT damage using TMA. Upon cutting, the specimens were vacuum saturated according to the procedure described in AASHTO TP 135-20.[63,64] After saturation, the specimens intended to be tested at 100% DOS were taken out of the solution, saturated surface-dried, and their vertical sides were sealed with aluminum tape, as illustrated in Fig. 2, to minimize moisture loss during the test. Immediately thereafter, the specimens were placed in the thermomechanical analyzer for FT damage measurement. The samples prepared to be tested at lower DOS values were left out of the solution at room temperature until reaching the targeted DOS for testing, which was determined by continuously tracking their mass. Immediately after reaching the targeted DOS, the specimens were wrapped in shrink wrap and sealed in double bags at 23 ± 1°C for 7 days to allow for an equilibrium of moisture distribution inside the specimen. After 7 days, the specimens were taken out of the bags for a final mass measurement, sealed with aluminum tape on their vertical sides, and placed in the thermomechanical analyzer to measure their FT damage.

Upon mounting the specimen in the TMA chamber, a temperature ramp—cooling from 24 to –40°C followed by heating back up to 30°C at a 1°C/min cooling and heating rate—was applied.[59] The test was performed under a 50 mL/min nitrogen purge rate. A high-precision linear variable differential transformer (LVDT) was used to continuously measure the length change of the specimen. This was done by measuring the movement of the quartz macro-expansion probe that is touching the upper surface of the specimen (Fig. 2).[59] Figure 3(a) illustrates the length change (reported as strain evolution in the longitudinal direction) with respect to temperature obtained from the TMA for a specimen at 100% DOS. During the cooling cycle (from 24 to –40°C), the specimen initially decreases in length as anticipated. However, when ice formation occurs (at approximately –14.5 ± 2.4°C), there is an increase in the specimen length. The specimen then continues to shrink as the temperature is further reduced. After reaching a temperature of –40°C at the initiation of the heating cycle, the specimen is heated and expanded. As the temperature increases, the ice begins to melt, leading to a decrease in specimen length, as observed in Fig. 3(a). After the ice has completely thawed (that is, at approximately 0.5 ± 1.9°C), the specimen continues to expand until the heating cycle is complete (at 30°C).

In specimens where the DOS is either below the DOS_{CR} or close to DOS_{CR}, the length change of the specimens as they heat and cool follows a similar path, with no ice formation and melting during the cooling and heating (Fig. 3(b)). In contrast, and as illustrated in Fig. 3(a), in DOS higher than DOS_{CR} where ice forms and FT damage occurs, the specimen will not return to its original length at the end of the first FT cycle. As such, a residual strain remains in the specimen and serves as a direct indication of the FT damage (Fig. 3(a)).[59,65] The COTE during cooling (α_C) can be determined by calculating the slope of strain-temperature obtained during cooling and before ice formation (Fig. 3(a)). The COTE during heating (α_H) can also be determined by calculating the slope of measurements obtained after ice melting (Fig. 3(a)). While the COTE is generally thought of as linear, a local nonlinearity in the COTE is observed immediately at the end of the ice melting (Fig. 3(a)) and is further discussed later in this paper.

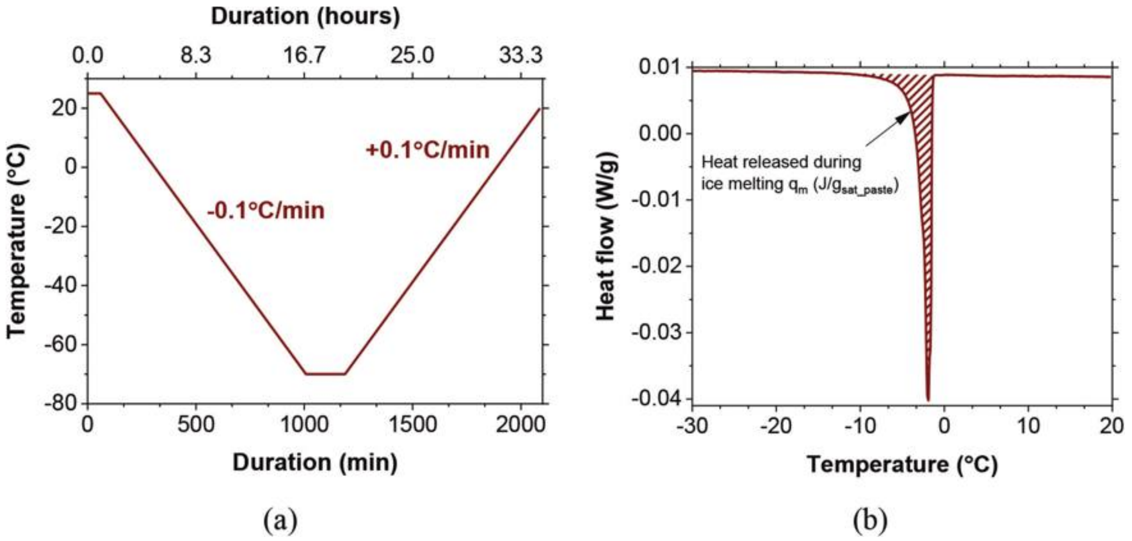

Fig. 4—(a) Temperature ramps during FT cycle in LT-DSC; and (b) ice quantification using heat flow, released during ice melting normalized with respect to gram of saturated cement paste.

Ice quantification using low-temperature differential scanning calorimetry

The percentage of freezable pore solution was quantified for both the 3-D-printed and cast cement paste specimens with the various DOS ranging from 100 to 75% using a low-temperature differential scanning calorimeter (LT-DSC). Slab-shaped specimens (48.5 ± 2.3 mg) were extracted from both the 3-D-printed and cast cement paste samples and immersed in saturated lime solution for a duration of 48 ± 2 hours. The slab-shaped specimens contained two interfaces. The slab-shaped specimens were then removed from the lime solution, saturated surface-dried, and sealed in a high-volume platinum pan after reaching the targeted DOS. For the tests that were intended to be performed at 100% DOS, the slab-shaped specimens were sealed immediately inside the pan after being saturated surface-dried, while for lower DOS, the specimens were kept at room temperature until reaching the targeted DOS per continuous mass measurements. The sealed pan was then loaded in the LT-DSC equipment, followed by a cooling ramp from 25 to –70°C at a 0.1°C/min cooling rate. The specimen was then kept at –70°C for 3 hours before following a heating ramp up to 24°C at 0.1°C/min (Fig. 4(a)). The test was performed under a 50 mL/min nitrogen purge rate. The percentage of freezable pore solution that developed in the cement paste was then quantified using Eq. (2)

$$I = \frac{q_m}{q_i} \tag{2}$$

where I is the gram of ice that was measured per gram of saturated paste ($g_{ice}/g_{saturated\_paste}$); q_m is the heat released during the ice melting per gram of paste (J/$g_{satuarted\_paste}$) and was quantified by calculating the area under the peak corresponding to ice melting (Fig. 4(b)); and q_i is the latent heat of ice equal to 334 J/g_{ice} (that is, the energy required to melt 1 g of ice at 0°C).

Pore-size distribution using dynamic vapor sorption

The influence of the presence of interfaces in the 3-D-printed specimens on the pore-size distribution was determined by comparing the pore-size distribution of the 3-D-printed cement paste specimens with that of the conventionally cast specimens. Slab-shaped specimens (110.2 ± 4.6 mg) were extracted from both the 3-D-printed cement paste and the cast samples at the end of the curing period. The slab-shaped specimen extracted from the 3-D-printed sample contained three interfaces. The specimens were then vacuum saturated in saturated lime simulated pore solution according to AASHTO TP 135-20.[63] After 48 hours of immersion in the lime simulated pore solution, the slab-shaped specimens were removed from the saturated solution, saturated surface-dried, and placed in a tared quartz pan that was immediately loaded in the environmental chamber of the dynamic vapor sorption (DVS) analyzer to assess the desorption response of the specimens. The specimen mass was continuously monitored during the desorption while the specimens were exposed to the following RH points until the equilibrium point was reached: 97.5, 95, 92.5, 90, 87.5, 85, 82.5, 80, 76, 70, 60, 50, 40, 30, 20, 11, and 0%. The specimens were considered at equilibrium for each RH step when the weight change was less than 0.001% for a duration of 15 minutes or when the RH value was maintained for 98 hours. The measurements were performed at a constant temperature of 23°C and 10 mL/min nitrogen purge rate.

The pore radius corresponding to each RH step is estimated as the sum of the Kelvin radius, calculated using the Kelvin-Laplace equation[66,67] and the absorbed water film thickness (that is, the *t*-curve determined for each RH value).[68-70] The details of the pore-radius calculation can be found in Qiao et al.[71] For each RH, the DOS of the specimens was calculated at equilibrium using Eq. (3)

$$DOS_i = \frac{m_i - m_0}{m_{100} - m_0} \tag{3}$$

where DOS_i is the DOS of the specimen at each RH step; m_0 is the mass of the specimen at an RH of 0%; and m_{100} is the saturated surface-dry mass of the specimen at the beginning of the desorption test.

This test quantifies the percentage of capillary pores as well as gel pores for both the 3-D-printed and cast cement paste specimens. This is an important parameter to assess, as based on the Gibbs-Thomson equation, the smaller the pore size, the lower the temperature needed for ice to begin forming.[72] The results obtained from this measurement were correlated with the percentage of freezable pore solution measurements and FT damage measurements.[72]

Pore characteristics and size distribution using micro-computed tomography

Micro-computed tomography (micro-CT) was used to capture a series of two-dimensional (2-D) X-ray images by rotating the specimen at various angles and reconstructing the images into 2-D slices that can be further analyzed to represent the interior volume of the material.[73,74] The variation in the grayscale intensities assists in the identification of the 3-D spatial distribution of distinct microstructural phases in the specimen.

In this study, an X-ray microscope was used to conduct the microstructural investigations. A wide field of view (FOV) at 0.4× geometric magnification technique was used to allow for scanning the entire 3-D-printed sample (40 x 50 x 12 mm), which involved the suitable relative positioning of the source, sample, and detector. The 0.4× magnification corresponded to a resolution of 36.25 μm (per 1 pixel); thus, the quantification of the percentage of larger capillary pores, with a radius greater than the resolution, present in either the filaments or the interfaces of the 3-D-printed cement paste materials, could be performed. The technique provided a suitable bridge to characterize the capillary pore sizes (in the orders of tens of micrometers) that are not captured by DVS (in the orders of tens of nanometers). The beam energy of 140 keV, power of 10 W, the exposure period of 1 second, and complete 360-degree rotation were employed. The data was post-processed using Avizo 2016[75] to obtain the 3-D reconstructions as well as the 2-D-sliced images.

Binary segmentation of the 2-D slices of the pore and solid phases was conducted by manual thresholding of grayscale intensities using ImageJ software.[76] The binary segmentation was chosen over segmentation with a higher number of phases given the coarse resolutions at 0.4× magnification. The tangent-slope method was employed to determine the upper threshold intensity limit of pores, which is the intersection point of the tangents at the initial region of the grayscale histogram and the upper region of the hydrated product peak.[77] The binary segmented image was converted to a matrix using MATLAB 2022,[78] where each element corresponded to the grayscale value of each pixel. This matrix is further used to produce the spatial distribution of phases in the 2-D slices.

RESULTS AND DISCUSSION

Freezing-and-thawing damage and coefficient of thermal expansion

The length change over the cooling-and-heating cycle, reported as strain evolution with respect to temperature, is illustrated in Fig. 5 for the three types of cement paste specimens tested at 100% DOS. Figures 5(a) and (b) represent the results collected on the 3-D-printed cement paste specimens with the filaments perpendicular and parallel to the longitudinal direction of length change measurements, respectively. Figure 5(c) demonstrates the results obtained on a conventionally cast cement paste specimen with no filaments and interface. The residual strain, as the direct indicator of FT damage,[58,59,65,79] was determined for each of the plots in Fig. 5. In addition, the COTE of the three types of specimens (perpendicular filaments, parallel filaments, and cast specimens without discrete filaments) were determined during both cooling and the heating cycles.

The residual strain measured on the cast cement paste specimen is lower than the values measured on the 3-D-printed cement paste specimens in both the parallel and perpendicular directions (Fig. 5). However, at 100% DOS, this difference between cast specimens and specimens with filaments parallel to the longitudinal direction does not appear to be significant based on the *t*-test. At this DOS of 100%, the specimens tested with filaments perpendicular to the longitudinal direction (Fig. 5(a)) showed the highest residual strain value as compared to the other two types of specimens (Fig. 5(b) and (c)), which is in accordance with the findings of Wang et al.[42] This could be due to the fact that FT damage is primarily localized along the weak interfaces, as stated in the literature,[30,34,41] which are perpendicular to the length change measurements for this type of specimen (Fig. 5(a)). However, more data points are required to confirm if the difference observed in residual strain values recorded on specimens with perpendicular filaments direction and the other two types of specimens is significant, and this is due to the inherent statistical variability in the FT response of cementitious materials at full saturation (that is, 100% DOS).[58]

The difference observed between the 3-D-printed and cast values of α_C and α_H are insignificant and within the statistical variation (that is, a standard deviation of 1.3 μm/(m·°C) and 0.7 μm/(m·°C), respectively). It should be noted that these observations are valid for the specimens tested in this study, with a 0.275 *w/c* and no printing defects (that is, 20% overlap between filaments[31]). Further work is in progress to investigate the effect of interfacial and layered heterogeneities on the FT response and COTE for specimens with unintentional printing defects (that is, processing parameters that lead to lower overlap or ultimately macroscopic gaps between filaments).

The evolution of the residual strain (that is, FT damage) with respect to the range of DOS (91 to 100%) of specimens for the three types of geometries tested in this study is illustrated in Fig. 6. It can be noted that the DOS_{CR} for both the cast and 3-D-printed specimens is approximately 91% and appears to be generally independent of the printing directionality. In addition, based on the statistical analysis

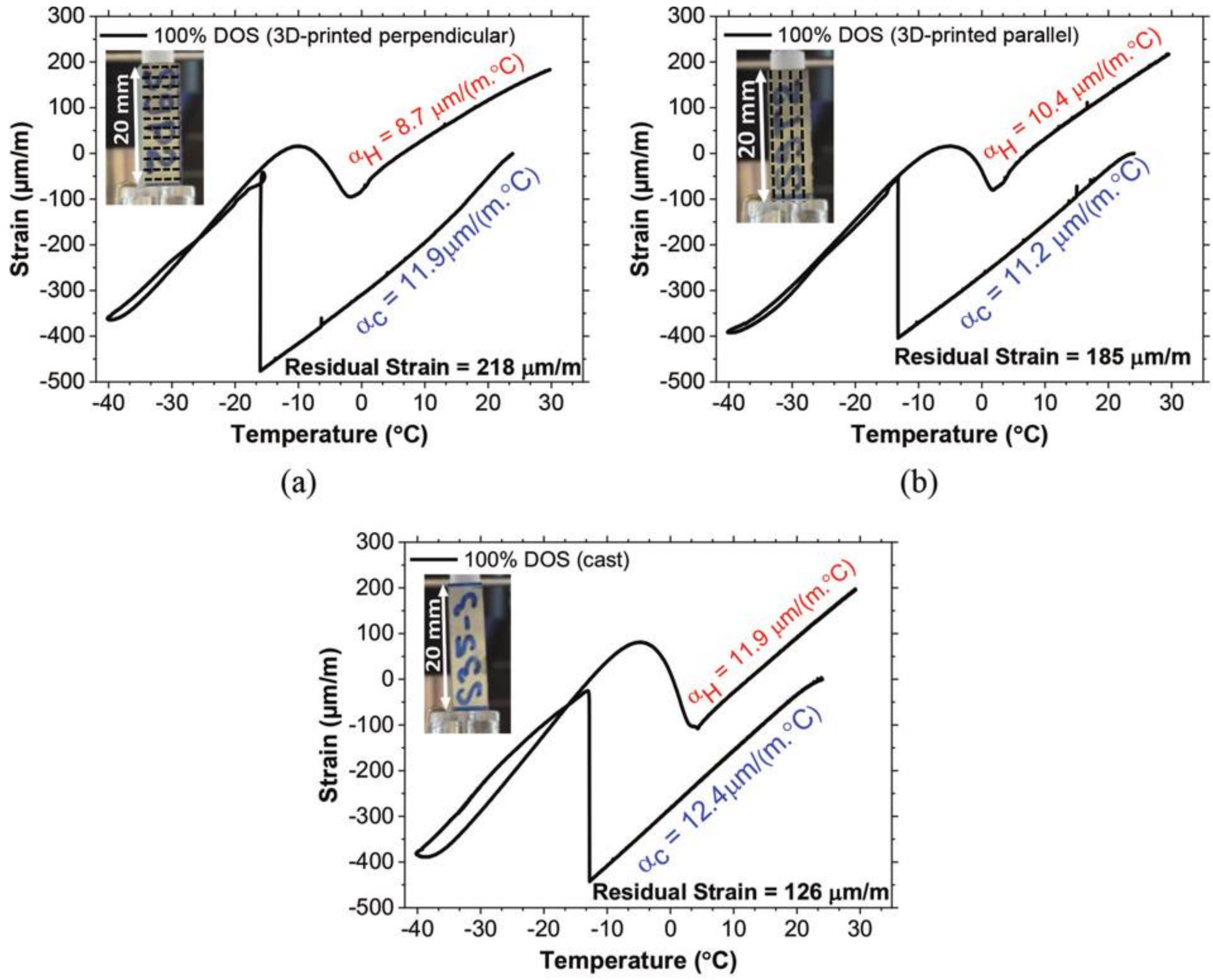

(a) (b)

(c)

Fig. 5—Strain evolution with respect to temperature for cement paste specimens at 100% DOS with: (a) printed filaments perpendicular to length change measurements; (b) printed filaments parallel to length change measurements; and (c) cast specimen with no filaments.

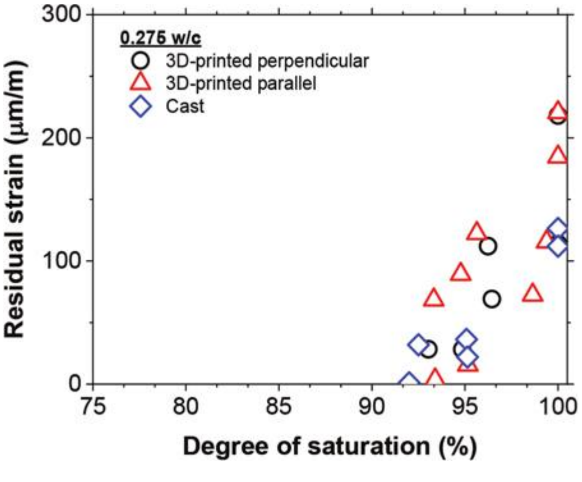

Fig. 6—Residual strain measurements with respect to DOS for three various geometries tested in this study.

of variance (ANOVA) single factor and Tukey test, there is no significant difference in the FT response of the cast and 3-D-printed specimens independent of the printing directionality.

Figures 7(a) and (b) demonstrate the measured COTE (α) based on the cooling and heating phases during the TMA test according to the approach illustrated in Fig. 3(a). The linear fitted lines are with an average coefficient of determination, R^2, of 0.992 ± 0.005 and 0.995 ± 0.005 during cooling and heating, respectively. The observed nonlinearity immediately at the end of the ice melting phase, commented on in Fig. 3(a), is local and does not significantly influence the R^2 values of the linear fitted lines. It can be noted that both α_C and α_H increase with the decrease in the DOS for both the cast and 3-D-printed cement paste specimens. The COTE of all the specimens tested in this study fall within the range of values measured on mature cement paste in the literature (that is, range between 8×10^{-6}°C^{-1} and 22×10^{-6}°C^{-1}).[80-85] No significant difference can be noted between the COTE values measured on the cast specimens as compared to the printed specimens independent of the printing directionality.

Based on the results of Fig. 6 and 7, it can be concluded that for this mixture design (0.275 *w/c*), and for specimens with no printing defects (that is, 20% overlap between filaments[31]), the printing directionality does not influence the DOS_{CR} of these specimens or FT response at DOS below

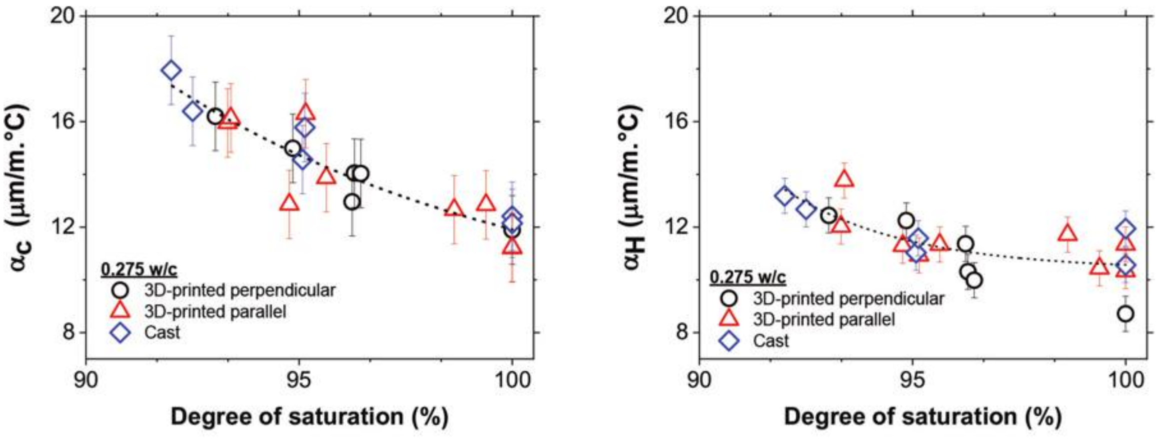

(a) (b)

Fig. 7—Coefficient of thermal contraction and expansion from cooling-and-heating cycles of TMA test, plotted with respect to DOS for three types of geometries under: (a) contraction; and (b) expansion.

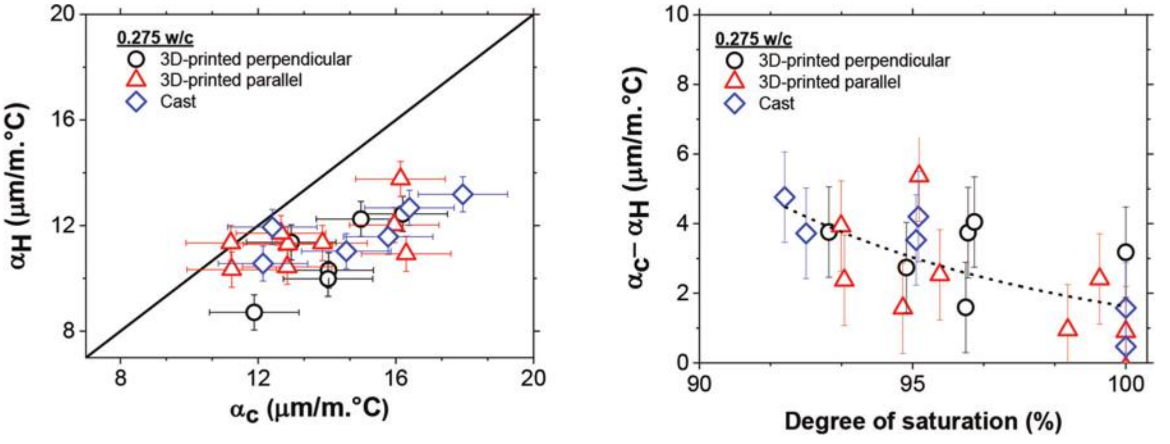

(a) (b)

Fig. 8—(a) Coefficient of thermal expansion of 3-D-printed and cast cement paste specimens during heating compared to coefficient of thermal expansion during cooling; and (b) comparison of difference between coefficients of thermal expansion during cooling and heating with respect to DOS.

100%. As such, well-printed specimens have isotropic COTE and DOS_{CR} values. Ongoing work is underway examining the influence of printing defects by varying filament overlap. 3-D-printed samples with 100% DOS appear to have a higher FT damage as compared to their cast counterpart samples; however, due to the inherent variability in the FT damage at 100% DOS, additional data points are needed to confirm if this observed difference is statistically significant.

For all specimens, α_H values are either similar to or lower than α_C, as illustrated in Fig. 8(a), and the difference between α_H and α_C increases with the decrease in the DOS of the specimen (Fig. 8(b)).

A typical nonlinearity in the strain evolution response was observed, immediately at the end of the ice melting phase and before the linear temperature up-ramp (Fig. 9(a)). To more clearly illustrate this, Fig. 9(b) illustrates the derivative of the strain evolution (that is, the COTE) with respect to the temperature during the entire cooling-and-heating cycle. The derivative of the strain evolution with temperature highlights the ice formation point (Fig. 9(c)), ice melting, and nonlinear after-melting points (Fig. 9(d)). This nonlinear response at the end of the ice melting phase, magnified in Fig. 9(d), can be explained by the redistribution of water inside the pores of the cementitious matrix.[86,87] During the cooling phase, water moves from the smaller to larger pores.[86,87] During the heating phase, water moves from larger to smaller pores,[86] explaining differences between α_H and α_C (α_H being lower than α_C, as shown in Fig. 8(a)).

In this study, for specimens at full saturation (100% in this study), cracks can form due to FT damage, which would decrease the COTE[88] (that is, during the heating cycle). This explains the decrease in the difference between α_C and α_H with the increase in DOS (that is, an increase in FT damage) (Fig. 8(b)).

Influence of interface on ice formation and pore-size distribution

Figure 10 illustrates the percentage of freezable pore solution (obtained from LT-DSC) with respect to the DOS of both

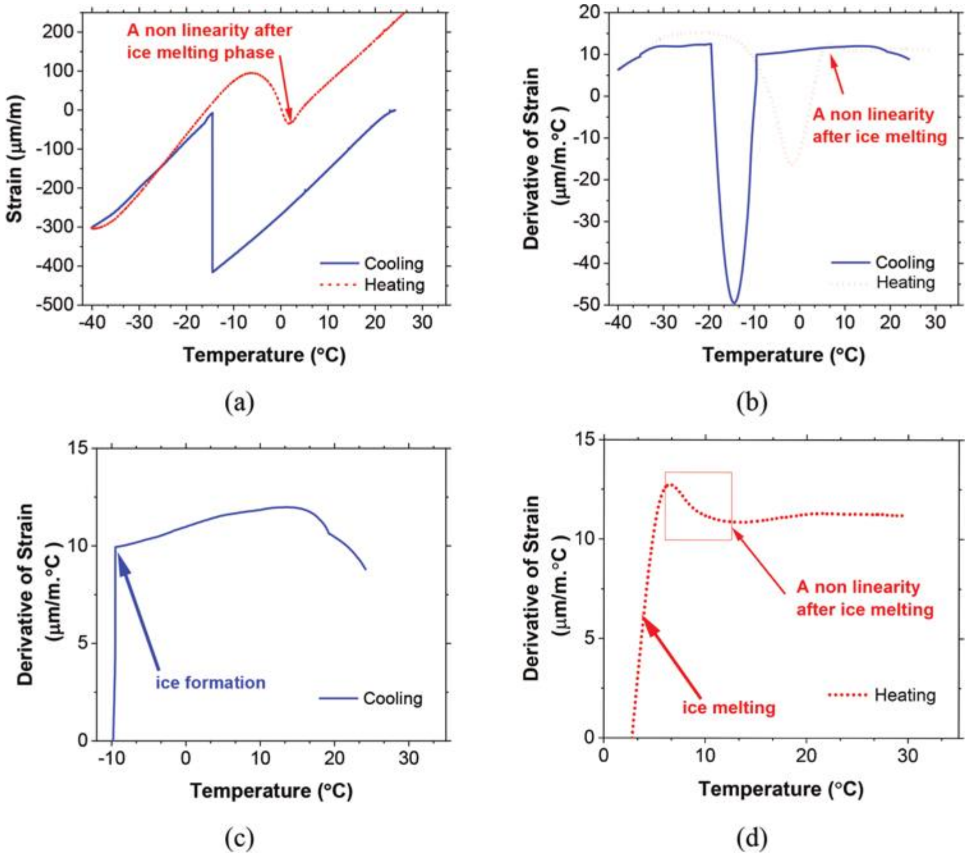

(a) (b)

(c) (d)

Fig. 9—(a) Strain evolution with respect to temperature (100% DOS); and derivative of strain with respect to temperature: (b) for entire FT cycle; (c) before ice formation; and (d) after ice melting.

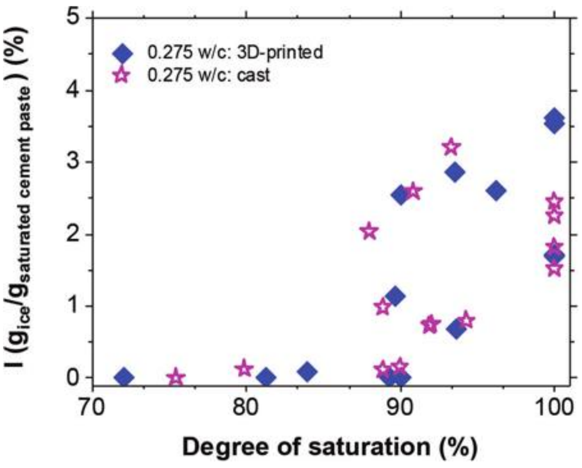

Fig. 10—Percentage of freezable pore solution with respect to DOS.

the 3-D-printed and cast cement paste specimens with a *w/c* of 0.275. It can be noted based on Fig. 10 that the percentage of freezable pore solution in the 3-D-printed and cast specimens is closely comparable. The statistical ANOVA single factor and Tukey test confirmed that there is no significant difference between these two data sets. In addition, the percentage of freezable pore solution decreases with the decrease in the DOS in all specimen types, as expected. This is in accordance with the correlation observed between the DOS and the residual strain values (that is, FT damage), as illustrated in Fig. 6.

Pores with a pore radius greater than 5 nm correspond to large pores such as capillary pores, air voids, and directional interfacial pores in the case of 3-D-printed samples. Pores with a pore radius below 5 nm can be filled with gel water, surface water, and phase water.[89] Water in capillary pores can freeze during an FT cycle, while only a portion of gel pores solution is able to freeze.[90,91] The desorption curves and pore-size distribution curves measured in this study for both the 3-D-printed cement paste and cast specimens are illustrated in Fig. 11(a) and (b), respectively. A coarser pore structure is measured for the 3-D-printed cement paste specimens, which may be related to the interface porosity. For the cast cement paste specimens, only 13% of the pores have a pore radius above 5 nm, and this percentage explains the low percentage of freezable pore solution in Fig. 10. The 3-D-printed specimens showed a higher percentage of coarser pores (>5 nm), equal to 28% of the pores (Fig. 11). However, the total porosity of the samples tested in this study with a *w/c* of 0.275 is low (that is, ~27% of the specimen volume obtained from Powers' model[48]).

In summary, using a low *w/c* in the mixture design of 3-D-printed cement paste may be beneficial for increasing the FT resistance of the materials by decreasing the percentage of freezable pore solution.

Influence of interfacial heterogeneity of 3-D-printed materials on FT response

Reconstructions of the 3-D-printed cement paste specimens and the representative 2-D slices in two different

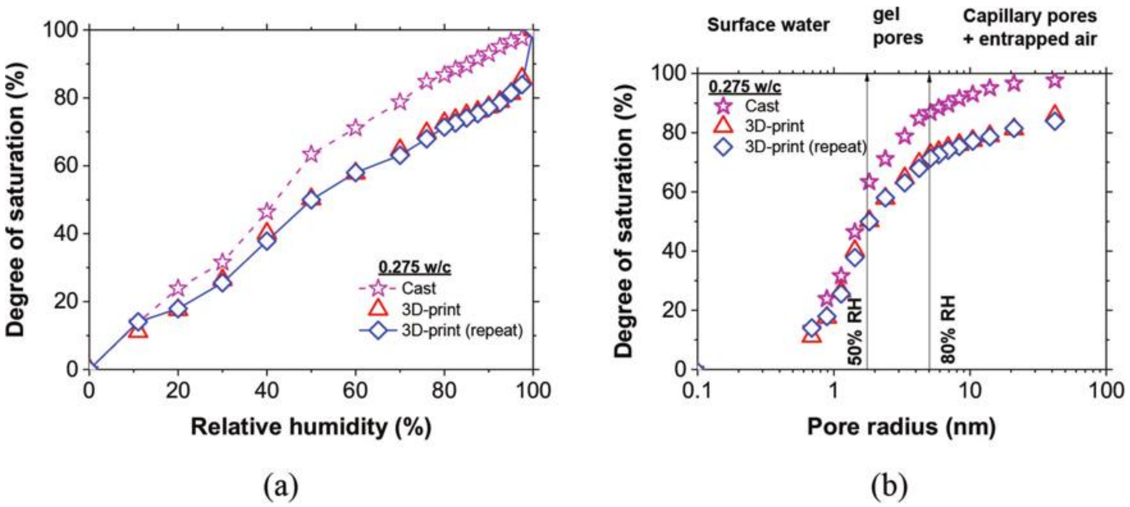

Fig. 11—(a) Sorption isotherm collected on 3-D-printed and conventionally cast cement paste specimens; and (b) pore-size distribution of 3-D-printed and conventionally cast cement paste specimens.

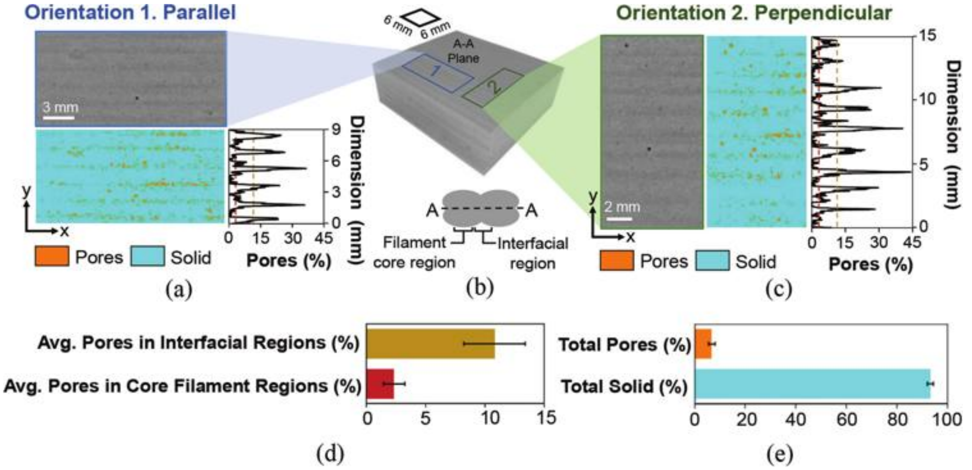

Fig. 12—(a) 2-D-micro-CT raw and segmented images in parallel direction; (b) 3-D-micro-CT rendering of additively manufactured cement paste; (c) 2-D-micro-CT raw and segmented images in perpendicular direction; (d) comparison of pore phase in interfacial region and core filament region; and (e) percentages of total pore and solid phases in 3-D-printed materials.

orientations along with their binary segmented images are presented in Fig. 12(a) to (c). The 2-D slices of the specimen in the parallel (orientation 1) and perpendicular (orientation 2) are shown in Fig. 12(b) in rectangular boxes and illustrated in Fig. 12(a) and (c), respectively. These raw 2-D slices are obtained from the horizontal interface between the two 3-D-printed layers, as presented in Plane A-A in Fig. 12(b). In the raw 2-D slices in both orientations, the pore phase is demonstrated by the darker gray regions, and the solid phase (that is, hydrated and unhydrated cement) is represented as brighter gray regions. These darker regions qualitatively illustrate the presence of pores at the filament interfaces, highlighting the concentration of pores surrounding the filaments (that is, interfacial regions around the filament cores). Using binary segmentation, the 2-D distribution of the pore phase versus the solid phase is plotted in Fig. 12(a) and (c) to quantitatively capture the heterogeneous characteristics of 3-D-printed materials. In these segmented images, the pore phase and solid phases are represented by the orange and cyan colors, respectively. The cumulative distribution of the pore phase as the phase of interest is shown along the x-direction as a function of distance from the bottom of the segmented images in the y-direction. (Fig. 12(a) and (c)) The amount of porosity in the 2-D-sliced images alters quite significantly from as high as 45% in the interfacial regions to as low as 0.2% in the core filament regions. This is a frequent heterogeneity that is commensurate with the qualitative observations of the frequency of darker regions in the raw sliced images. This spatial variation in the pore heterogeneity was found to be nearly uniform given the pore peaks were located at a relatively constant spacing of 1.64 mm (ranging from 1.56 to 1.7 mm) corresponding to the nominal filament width used in slicing (1.63 mm). This pore peak spacing associated with the (cumulative) porosity at the interfacial regions corroborates well with the pore plateau spacing of the (cumulative) porosity associated with the core filament regions.

To better capture the microstructural heterogeneity, the average pore phase in the interfacial region versus the core filament region is quantified and plotted in Fig. 12(d). The values plotted in Fig. 12(d) are also shown as brown and red dashed lines in Fig. 12 (a) and (c). The interfacial and filament core regions of equal width (along the y-axis) were assumed based on the cumulative distribution of porosity along the 2-D-sliced images, with the peaks in the pore distribution plots taken as the center of the interfacial region. Using the moving averages of the data in Fig. 12(a) and (c), it was observed that the average porosity in the interfacial region is 10.8% compared to the 2.3% average porosity at the filament core regions. The 4.6 times higher average interfacial porosity additionally indicated significant heterogeneity in the bulk-layered microstructure of the 3-D-printed cement paste materials. Such a significant heterogeneity in the pore microstructure of the 3-D-printed materials is exacerbated by the underlying nonuniform distributions observed in Fig. 12(a) and (c) and can directly impact the characteristics of FT response compared to the cast counterparts with a homogeneous microstructure. This finding confirms that the coarser pore-size distribution in the 3-D-printed specimens observed using the DVS at the nanoscale is related to the interfacial porosity.

The total porosity based on the 2-D-sliced images is characterized and presented in Fig. 12(e). The total bulk pore phase was quantified as 6.7%, which closely corresponds to 6.6% as the mean of the two average data points for the interfacial and core filament regions presented in Fig. 12(d). It should be noted that the resolution of the 0.4× magnification limits the size of quantifiable pores at 36.25 μm, and imaging at higher magnification is a subject of ongoing research to better capture the smaller spatial pore distribution.

CONCLUSIONS

This paper examined the influence of the printing directionality on the freezing-and-thawing (FT) response, critical degree of saturation (DOS_{CR}), and coefficient of thermal expansion (COTE) of three-dimensional (3-D)-printed cement paste specimens with various degrees of saturation (DOS) in comparison with conventionally cast specimens. The FT response measurements were performed using thermomechanical analysis (TMA) on a mixture design with a water-cement ratio (w/c) of 0.275. The pore microstructure was characterized by using micro-computed tomography (micro-CT).

For the mixtures tested (0.275 w/c), the DOS_{CR}, COTE, and FT response of the 3-D-printed cement paste specimen with a DOS less than 100% were independent of the printing directionality and were comparable to the conventionally cast cement paste. The DOS_{CR} was approximately 91% for all specimens tested, which is at the upper end of various types of conventional concrete.

The COTE of both the 3-D-printed and cast cement paste specimens increased with a decrease in the DOS from 100 to 91%. The COTE values measured during the heating phase of the specimens were lower than the values measured during the cooling. This is likely caused by the redistribution of water inside the pores.

The 3-D-printed specimens with a 100% DOS appear to have higher FT damage as compared to the cast specimens. The 3-D-printed specimens with perpendicular filaments showed the greatest FT damage at 100% DOS as compared to the other two types of specimens (that is, filaments in the parallel direction and cast specimens). However, due to the inherent variability in the FT damage at 100% DOS, additional data points are needed to confirm if this observed difference is statistically significant.

The percentage of freezable pore solution with respect to the DOS was measured to be comparable for both the cast and 3-D-printed cement paste specimens. This percentage of freezable pore solution was small (~$4g_{ice}/100g_{paste}$ at 100% DOS), mainly due to the low w/c of the mixture design. Consequently, the low w/c in the mixture designs of the 3-D-printed cement paste can be beneficial in increasing the FT resistance due to a reduction in the capillary porosity and the percentage of freezable pore solution.

The 3-D-printed specimens showed a coarser pore-size distribution as compared to conventionally cast specimens (mainly due to the presence of interfacial porosity).

The micro-CT analysis demonstrated that the amount of porosity in the two-dimensional (2-D)-sliced images significantly alters from 45% in the interfacial regions to 0.2% in the core filament regions, with a nonuniform pore distribution but a rather uniform filament spacing in each region. This is a frequent heterogeneity in 3-D-printed material and is commensurate with the observations of the frequency of darker interfacial regions in the raw sliced images. Such a significant heterogeneity in the pore microstructure of 3-D-printed materials can directly impact their FT response. The uniform spatial variation of the pore phase was found at a relatively constant frequency of 1.64 mm corresponding to the nominal filament width used in slicing. Moving averages indicated that the mean porosity in the interfacial region is 10.8% compared to the 2.3% average porosity at the filament core regions. The 4.6 times higher average interfacial porosity additionally supports the significant heterogeneity in the bulk-layered microstructure of 3-D-printed cement paste materials.

In conclusion, 3-D-printed cement paste specimens with a low w/c (0.275) and no visible printing defects (20% overlapping between printed filaments) have a similar DOS_{CR} to conventionally cast specimens. The performance of the 3-D-printed specimen was independent of the printing directionality for DOS below 100%. However, the anisotropy in the FT performance of the layered fabrication process and printing-induced interfaces and defects is an area of ongoing study. In addition, the influence of filament porosity on the rate of water absorption is still being studied.

AUTHOR BIOS

Rita Maria Ghantous *is a Research Associate in the School of Civil and Construction Engineering at Oregon State University, Corvallis, OR. She received her MS from the École Centrale de Nantes, Nantes, France, and her PhD in civil engineering from the Institut National des Sciences Appliquées (INSA) Toulouse, Toulouse, France. Her research interests include carbonation, durability, and sustainability of concrete and cementitious materials.*

Anastasiia Evseeva *is an Undergraduate Research Assistant in the School of Civil and Construction Engineering at Oregon State University.*

Brandon Dickey *is an Undergraduate Research Assistant majoring in business administration in international business. His research interests include three-dimensional (3-D) construction printing and sustainable communities.*

ACI member **Shashank Gupta** *is a PhD Student in the Department of Civil and Environmental Engineering at Princeton University, Princeton, NJ. He received his BE (Hons) in civil engineering from the Birla Institute of Technology & Science (BITS) Pilani, Pilani, Rajasthan, India, and his MSc in civil engineering from Politecnico di Milano, Milan, Italy.*

ACI member **Arjun Prihar** *is an MSE Student in the Department of Civil and Environmental Engineering at Princeton University. He received his BSc in civil engineering from The University of British Columbia, Vancouver, BC, Canada.*

Hadi Shagerdi Esmaeeli *is an Associate Research Scholar in the Department of Civil and Environmental Engineering at Princeton University. He received his BSc in civil engineering from the University of Tabriz, Tabriz, Iran, and his MSc and PhD in civil engineering from Purdue University, West Lafayette, IN. He is a member of ACI Committees 201, Durability of Concrete; 236, Material Science of Concrete; and 564, 3-D Printing with Cementitious Materials. His research interests include additive manufacturing and computational mechanics toward developing resilient infrastructure.*

ACI member **Reza Moini** *is an Assistant Professor of civil and environmental engineering at Princeton University. He received his BSc from Qom University, Qom, Iran, and his MSc from the University of Wisconsin-Milwaukee, Milwaukee, WI, both in civil and environmental engineering, and his PhD from Purdue University Lyles School of Civil Engineering. He is Secretary of ACI Subcommittee 211-M, Aggregate Packing Model, and a member of ACI Committee 564, 3-D Printing with Cementitious Materials. His research interests include the mechanics of resilient and multifunctional architected materials enabled by automated and robotic manufacturing techniques.*

W. Jason Weiss*, FACI, is the Edwards Distinguished Chair at Oregon State University. He received his BAE from The Pennsylvania State University, University Park, PA, and his MS and PhD from Northwestern University, Evanston, IL, in 1995, 1997, and 1999, respectively. He is Editor-in-Chief of the* ACI Materials Journal*, and a member of the ACI Technical Activities Committee (TAC).*

ACKNOWLEDGMENTS

The authors gratefully acknowledge support for this work from the National Science Foundation (Award Numbers 2129566 and 2129606) and the U.S. Endowment. The authors are grateful to the MBCC Group and Buzzi Unicem for providing materials for this research work.

REFERENCES

1. Gosselin, C.; Duballet, R.; Roux, P.; Gaudillière, N.; Dirrenberger, J.; and Morel, P., "Large-Scale 3D Printing of Ultra-High Performance Concrete – A New Processing Route for Architects and Builders," *Materials & Design*, V. 100, June 2016, pp. 102-109. doi: 10.1016/j.matdes.2016.03.097

2. Buswell, R. A.; Soar, R. C.; Gibb, A. G. F.; and Thorpe, A., "Freeform Construction: Mega-Scale Rapid Manufacturing for Construction," *Automation in Construction*, V. 16, No. 2, Mar. 2007, pp. 224-231. doi: 10.1016/j.autcon.2006.05.002

3. Buswell, R. A.; Leal de Silva, W. R.; Jones, S. Z.; and Dirrenberger, J., "3D Printing Using Concrete Extrusion: A Roadmap for Research," *Cement and Concrete Research*, V. 112, Oct. 2018, pp. 37-49. doi: 10.1016/j.cemconres.2018.05.006

4. Khoshnevis, B., "Automated Construction by Contour Crafting—Related Robotics and Information Technologies," *Automation in Construction*, V. 13, No. 1, Jan. 2004, pp. 5-19. doi: 10.1016/j.autcon.2003.08.012

5. Delgado Camacho, D.; Clayton, P.; O'Brien, W. J.; Seepersad, C.; Juenger, M.; Ferron, R.; and Salamone, S., "Applications of Additive Manufacturing in the Construction Industry – A Forward-Looking Review," *Automation in Construction*, V. 89, May 2018, pp. 110-119. doi: 10.1016/j.autcon.2017.12.031

6. Mechtcherine, V.; Bos, F. P.; Perrot, A.; Leal da Silva, W. R.; Nerella, V. N.; Fataei, S.; Wolfs, R. J. M.; Sonebi, M.; and Roussel, N., "Extrusion-Based Additive Manufacturing with Cement-Based Materials – Production Steps, Processes, and Their Underlying Physics: A Review," *Cement and Concrete Research*, V. 132, June 2020, Article No. 106037.

7. Khan, M. S.; Sanchez, F.; and Zhou, H., "3-D Printing of Concrete: Beyond Horizons," *Cement and Concrete Research*, V. 133, July 2020, Article No. 106070.

8. Wangler, T.; Lloret, E.; Reiter, L.; Hack, N.; Gramazio, F.; Kohler, M.; Bernhard, M.; Dillenburger, B.; Buchli, J.; Roussel, N.; and Flatt, R., "Digital Concrete: Opportunities and Challenges," *RILEM Technical Letters*, V. 1, 2016, pp. 67-75. doi: 10.21809/rilemtechlett.2016.16

9. Biernacki, J. J.; Bullard, J. W.; Sant, G.; Brown, K.; Glasser, F. P.; Jones, S.; Ley, T.; Livingston, R.; Nicoleau, L.; Olek, J.; Sanchez, F.; Shahsavari, R.; Stutzman, P. E.; Sobolev, K.; and Prater, T., "Cements in the 21st Century: Challenges, Perspectives, and Opportunities," *Journal of the American Ceramic Society*, V. 100, No. 7, July 2017, pp. 2746-2773. doi: 10.1111/jace.14948

10. Barbosa, F.; Woetzel, J.; Mischke, J.; João Ribeirinho, M.; Sridhar, M.; Parsons, M.; Bertram, N.; and Brown, S., "Reinventing Construction: A Route to Higher Productivity," McKinsey Global Institute, 2017, 168 pp.

11. Schuldt, S. J.; Jagoda, J. A.; Hoisington, A. J.; and Delorit, J. D., "A Systematic Review and Analysis of the Viability of 3D-Printed Construction in Remote Environments," *Automation in Construction*, V. 125, May 2021, Article No. 103642.

12. Allouzi, R.; Al-Azhari, W.; and Allouzi, R., "Conventional Construction and 3D Printing: A Comparison Study on Material Cost in Jordan," *Journal of Engineering*, V. 2020, 2020, Article No. 1424682.

13. De Schutter, G.; Lesage, K.; Mechtcherine, V.; Nerella, V. N.; Habert, G.; and Agusti-Juan, I., "Vision of 3D Printing with Concrete—Technical, Economic and Environmental Potentials," *Cement and Concrete Research*, V. 112, Oct. 2018, pp. 25-36. doi: 10.1016/j.cemconres.2018.06.001

14. Moini, M.; Olek, J.; Youngblood, J. P.; Magee, B.; and Zavattieri, P. D., "Additive Manufacturing and Performance of Architectured Cement-Based Materials," *Advanced Materials*, V. 30, No. 43, Oct. 2018, Article No. 1802123.

15. Marchon, D.; Kawashima, S.; Bessaies-Bey, H.; Mantellato, S.; and Ng, S., "Hydration and Rheology Control of Concrete for Digital Fabrication: Potential Admixtures and Cement Chemistry," *Cement and Concrete Research*, V. 112, Oct. 2018, pp. 96-110. doi: 10.1016/j.cemconres.2018.05.014

16. Roussel, N., "Rheological Requirements for Printable Concretes," *Cement and Concrete Research*, V. 112, Oct. 2018, pp. 76-85. doi: 10.1016/j.cemconres.2018.04.005

17. Ma, G., and Wang, L., "A Critical Review of Preparation Design and Workability Measurement of Concrete Material for Largescale 3D Printing," *Frontiers of Structural and Civil Engineering*, V. 12, No. 3, Sept. 2018, pp. 382-400. doi: 10.1007/s11709-017-0430-x

18. Kazemian, A.; Yuan, X.; Cochran, E.; and Khoshnevis, B., "Cementitious Materials for Construction-Scale 3D Printing: Laboratory Testing of Fresh Printing Mixture," *Construction and Building Materials*, V. 145, Aug. 2017, pp. 639-647. doi: 10.1016/j.conbuildmat.2017.04.015

19. Tay, Y. W.; Panda, B.; Paul, S. C.; Tan, M. J.; Qian, S. Z.; Leong, K. F.; and Chua, C. K., "Processing and Properties of Construction Materials for 3D Printing," *Materials Science Forum*, V. 861, 2016, pp. 177-181. doi: 10.4028/www.scientific.net/MSF.861.177

20. Rodriguez, F. B.; Olek, J.; Moini, R.; Zavattieri, P. D.; and Youngblood, J. P., "Linking Solids Content and Flow Properties of Mortars to Their Three-Dimensional Printing Characteristics," *ACI Materials Journal*, V. 118, No. 6, Nov. 2021, pp. 371-382.

21. Moini, R.; Olek, J.; Zavattieri, P. D.; and Youngblood, J. P., "Open-Span Printing Method for Assessment of Early-Age Deformations of Additively Manufactured Cement-Based Materials Using an Isosceles Triangle," *ASTM Symposium on Standards Development for Cement and Concrete Used in Additive Construction*, S. Z. Jones and E. L. Kreiger, eds., 2021, pp. 1-12.

22. Sanjayan, J. G.; Nematollahi, B.; Xia, M.; and Marchment, T., "Effect of Surface Moisture on Inter-Layer Strength of 3D Printed Concrete," *Construction and Building Materials*, V. 172, May 2018, pp. 468-475. doi: 10.1016/j.conbuildmat.2018.03.232

23. Tay, Y. W. D.; Ting, G. H. A.; Qian, Y.; Panda, B.; He, L.; and Tan, M. J., "Time Gap Effect on Bond Strength of 3D-Printed Concrete," *Virtual and Physical Prototyping*, V. 14, No. 1, 2019, pp. 104-113. doi: 10.1080/17452759.2018.1500420

24. Van Der Putten, J.; De Schutter, G.; and Van Tittelboom, K., "The Effect of Print Parameters on the (Micro)structure of 3D Printed Cementitious Materials," *First RILEM International Conference on Concrete and Digital Fabrication – Digital Concrete 2018*, T. Wangler and R. J. Flatt, eds., Zurich, Switzerland, Springer, Cham, Switzerland, 2019, pp. 234-244.

25. Moini, R.; Baghaie, A.; Rodriguez, F. B.; Zavattieri, P. D.; Youngblood, J. P.; and Olek, J., "Quantitative Microstructural Investigation of 3D-Printed and Cast Cement Pastes Using Micro-Computed Tomography and Image Analysis," *Cement and Concrete Research*, V. 147, Sept. 2021, Article No. 106493.

26. Wolfs, R. J. M.; Bos, F. P.; and Salet, T. A. M., "Hardened Properties of 3D Printed Concrete: The Influence of Process Parameters on Interlayer Adhesion," *Cement and Concrete Research*, V. 119, May 2019, pp. 132-140. doi: 10.1016/j.cemconres.2019.02.017

27. Wangler, T.; Aguilar Sanchez, A. M.; Anton, A.; Dillenburger, B.; and Flatt, R. J., "Two Year Exposure of 3D Printed Cementitious Columns in a High Alpine Environment," *Third RILEM International Conference on Concrete and Digital Fabrication: Digital Concrete 2022*, R. Buswell, A. Blanco, S. Cavalaro, and P. Kinnell, eds., Loughborough, UK, Springer, Cham, Switzerland, 2022, pp. 182-187.

28. Mohan, M. K.; Rahul, A. V.; De Schutter, G.; and Van Tittelboom, K., "Salt Scaling Resistance of 3D Printed Concrete," *Third RILEM International Conference on Concrete and Digital Fabrication: Digital Concrete 2022*, R. Buswell, A. Blanco, S. Cavalaro, and P. Kinnell, eds., Loughborough, UK, Springer, Cham, Switzerland, 2022, pp. 188-193.

29. Aguilar Sanchez, A. M.; Wangler, T.; Stefanoni, M.; and Angst, U., "Microstructural Examination of Carbonated 3D-Printed Concrete," *Journal of Microscopy*, V. 286, No. 2, May 2022, pp. 141-147. doi: 10.1111/jmi.13087

30. Das, A.; Aguilar Sanchez, A. M.; Wangler, T.; and Flatt, R. J., "Freeze-Thaw Performance of 3D Printed Concrete: Influence of Interfaces," *Third RILEM International Conference on Concrete and Digital Fabrication: Digital Concrete 2022*, R. Buswell, A. Blanco, S. Cavalaro, and P. Kinnell, eds., Loughborough, UK, Springer, Cham, Switzerland, 2022, pp. 200-205.

31. Rodriguez, F. B.; Garzon Lopez, C.; Wang, Y.; Olek, J.; Zavattieri, P. D.; Youngblood, J. P.; Falzone, G.; and Cotrell, J., "Evaluation of Durability of 3D-Printed Cementitious Materials for Potential Applications in Structures Exposed to Marine Environments," *Third RILEM International Conference on Concrete and Digital Fabrication: Digital Concrete 2022*, R. Buswell, A. Blanco, S. Cavalaro, and P. Kinnell, eds., Loughborough, UK, Springer, Cham, Switzerland, 2022, pp. 175-181.

32. Schröfl, C.; Nerella, V. N.; and Mechtcherine, V., "Capillary Water Intake by 3D-Printed Concrete Visualised and Quantified by Neutron Radiography," *First RILEM International Conference on Concrete and Digital Fabrication – Digital Concrete 2018*, T. Wangler and R. J. Flatt, eds., Zurich, Switzerland, Springer, Cham, Switzerland, 2019, pp. 217-224.

33. Van Der Putten, J.; De Smet, M.; Van den Heede, P.; De Schutter, G.; and Van Tittelboom, K., "Influence of the Print Process on the Durability of Printed Cementitious Materials," *Third RILEM International Conference on Concrete and Digital Fabrication: Digital Concrete 2022*, R. Buswell, A. Blanco, S. Cavalaro, and P. Kinnell, eds., Loughborough, UK, Springer, Cham, Switzerland, 2022, pp. 194-199.

34. Zhang, Y.; Zhang, Y.; Yang, L.; Liu, G.; Chen, Y.; Yu, S.; and Du, H., "Hardened Properties and Durability of Large-Scale 3D Printed Cement-Based Materials," *Materials and Structures*, V. 54, No. 1, Feb. 2021, Article No. 45. doi: 10.1617/s11527-021-01632-x

35. Das, A.; Song, Y.; Mantellato, S.; Wangler, T.; Lange, D. A.; and Flatt, R. J., "Effect of Processing on the Air Void System of 3D Printed Concrete," *Cement and Concrete Research*, V. 156, June 2022, Article No. 106789.

36. Moini, M.; Olek, J.; Magee, B.; Zavattieri, P.; and Youngblood, J., "Additive Manufacturing and Characterization of Architectured Cement-Based Materials via X-Ray Micro-computed Tomography," *First RILEM International Conference on Concrete and Digital Fabrication – Digital Concrete 2018*, T. Wangler and R. J. Flatt, eds., Zurich, Switzerland, Springer, Cham, Switzerland, 2019, pp. 176-189.

37. Powers, T. C., and Willis, T. F., "The Air Requirement of Frost Resistant Concrete," *Highway Research Board Proceedings*, V. 29, 1950, pp. 184-211.

38. Smith, S. H.; Kurtis, K. E.; and Tien, I., "Probabilistic Evaluation of Concrete Freeze-Thaw Design Guidance," *Materials and Structures*, V. 51, No. 5, Oct. 2018, Article No. 124. doi: 10.1617/s11527-018-1259-z

39. Du, L., and Folliard, K. J., "Mechanisms of Air Entrainment in Concrete," *Cement and Concrete Research*, V. 35, No. 8, Aug. 2005, pp. 1463-1471. doi: 10.1016/j.cemconres.2004.07.026

40. Tunstall, L. E.; Scherer, G. W.; and Prud'homme, R. K., "Studying AEA Interaction in Cement Systems Using Tensiometry," *Cement and Concrete Research*, V. 92, Feb. 2017, pp. 29-36. doi: 10.1016/j.cemconres.2016.11.005

41. Assaad, J. J.; Hamzeh, F.; and Hamad, B., "Qualitative Assessment of Interfacial Bonding in 3D Printing Concrete Exposed to Frost Attack," *Case Studies in Construction Materials*, V. 13, Dec. 2020, Article No. e00357.

42. Wang, L.; Xiao, W.; Wang, Q.; Jiang, H.; and Ma, G., "Freeze-Thaw Resistance of 3D-Printed Composites with Desert Sand," *Cement and Concrete Composites*, V. 133, Oct. 2022, Article No. 104693. doi: 10.1016/j.cemconcomp.2022.104693

43. Fagerlund, G., "The Critical Degree of Saturation Method of Assessing the Freeze/Thaw Resistance of Concrete," *Matériaux et Constructions*, V. 10, No. 4, July 1977, pp. 217-229.

44. Fagerlund, G., "A Service Life Model for Internal Frost Damage in Concrete," Report TVBM, V. 3119, Division of Building Materials, LTH, Lund University, Lund, Sweden, 2004, 138 pp.

45. Todak, H.; Lucero, C.; and Weiss, W. J., "Why Is the Air There? Thinking about Freeze-Thaw in Terms of Saturation," *Concrete InFocus*, 2015, pp. 3-7.

46. Li, W.; Pour-Ghaz, M.; Castro, J.; and Weiss, J., "Water Absorption and Critical Degree of Saturation Relating to Freeze-Thaw Damage in Concrete Pavement Joints," *Journal of Materials in Civil Engineering*, ASCE, V. 24, No. 3, Mar. 2012, pp. 299-307. doi: 10.1061/(ASCE)MT.1943-5533.0000383

47. Weiss, W. J.; Ley, M. T.; Isgor, O. B.; and Van Dam, T., "Toward Performance Specifications for Concrete Durability: Using the Formation Factor for Corrosion and Critical Saturation for Freeze-Thaw," Transportation Research Board 96th Annual Meeting, Washington, DC, 2017, 20 pp.

48. Powers, T. C., "A Discussion of Cement Hydration in Relation to the Curing of Concrete," *Highway Research Board Proceedings*, V. 27, 1948, pp. 178-188.

49. ASTM C1585-13, "Standard Test Method for Measurement of Rate of Absorption of Water by Hydraulic-Cement Concretes," ASTM International, West Conshohocken, PA, 2013, 6 pp.

50. Vuorinen, J., "On Use of Dilation Factor and Degree of Saturation in Testing Concrete for Frost Resistance," *Nordisk Betong*, 1970, pp. 37-64.

51. Barde, V.; Radlinska, A.; Cohen, M.; and Weiss, W. J., "Relating Material Properties to Exposure Conditions for Predicting Service Life of Concrete Bridge Decks in Indiana," Report No. FHWA/IN/JTRP-2007/27, Joint Transportation Research Program, Purdue University, West Lafayette, IN, 2009, 218 pp.

52. Todak, H. N., "Durability Assessments of Concrete Using Electrical Properties and Acoustic Emission Testing," MSCE thesis, Purdue University, West Lafayette, IN, 2015.

53. Farnam, Y.; Bentz, D.; Hampton, A.; and Weiss, W. J., "Acoustic Emission and Low-Temperature Calorimetry Study of Freeze and Thaw Behavior in Cementitious Materials Exposed to Sodium Chloride Salt," *Transportation Research Record: Journal of the Transportation Research Board*, V. 2441, No. 1, Jan. 2014, pp. 81-90. doi: 10.3141/2441-11

54. Todak, H.; Tsui Chang; M., Ley, M. T.; and Weiss, J., "Freeze-Thaw Resistance of Concrete: The Influence of Air Entrainment, Water to Cement Ratio, and Saturation," *Proceedings*, 11th International Symposium on Brittle Matrix Composites, Warsaw, Poland, 2015, pp. 101-109.

55. Kawamoto, S., and Williams, R. S., "Acoustic Emission and Acousto-Ultrasonic Techniques for Wood and Wood-Based Composites: A Review," General Technical Report No. FPL-GTR-134, United States Department of Agriculture, Washington, DC, 2002, 18 pp.

56. Tao, J.; Ghantous, R. M.; Jin, M.; and Weiss, J., "Influence of Silica Fume on Freezing-and-Thawing Resistance of Cement Paste at Early Age," *ACI Materials Journal*, V. 118, No. 2, Mar. 2021, pp. 107-116.

57. Jin, M.; Ghantous, R. M.; Tao, J.; and Weiss, J., "Freezing-and-Thawing Behavior of Cementitious Materials Containing Superabsorbent Polymers at Early Ages," *ACI Materials Journal*, V. 117, No. 6, Nov. 2020, pp. 243-252.

58. Ghantous, R. M.; Khanzadeh Moradllo, M.; Hall Becker, H.; Ley, M. T.; and Weiss, W. J., "Determining the Freeze-Thaw Performance of Mortar Samples Using Length Change Measurements during Freezing," *Cement and Concrete Composites*, V. 116, Feb. 2021, Article No. 103869.

59. Ghantous, R. M.; Madland, H.; Kwong, J.; and Weiss, W. J., "Examining the Influence of the Degree of Saturation on Length Change and Freeze-Thaw Damage," *Advances in Civil Engineering Materials*, V. 8, No. 1, 2019, pp. 365-374. doi: 10.1520/ACEM20190001

60. ASTM C150-07, "Standard Specification for Portland Cement," ASTM International, West Conshohocken, PA, 2007, 8 pp.

61. ASTM C494/C494M-08, "Standard Specification for Chemical Admixtures for Concrete," ASTM International, West Conshohocken, PA, 2008, 10 pp.

62. Greenspan, L., "Humidity Fixed Points of Binary Saturated Aqueous Solutions," *Journal of Research of the National Bureau of Standards, Section A: Physics and Chemistry*, V. 81A, No. 1, Jan.-Feb. 1977, pp. 89-96. doi: 10.6028/jres.081A.011

63. AASHTO TP 135-20, "Standard Method of Test for Determining the Total Pore Volume in Hardened Concrete Using Vacuum Saturation," American Association of State Highway and Transportation Officials, Washington, DC, 2020, 7 pp.

64. Bu, Y.; Spragg, R.; and Weiss, W. J., "Comparison of the Pore Volume in Concrete as Determined Using ASTM C642 and Vacuum Saturation," *Advances in Civil Engineering Materials*, V. 3, No. 1, 2014, pp. 308-315. doi: 10.1520/ACEM20130090

65. Trofimov, B. Y.; Kramar, L. Y.; and Schuldyakov, K. V., "On Deterioration Mechanism of Concrete Exposed to Freeze-Thaw Cycles," *IOP Conference Series: Materials Science and Engineering*, V. 262, 2017, Article No. 012019. doi: 10.1088/1757-899X/262/1/012019

66. Radlinska, A.; Rajabipour, F.; Bucher, B.; Henkensiefken, R.; Sant, G.; and Weiss, J., "Shrinkage Mitigation Strategies in Cementitious

Systems: A Closer Look at Differences in Sealed and Unsealed Behavior," *Transportation Research Record: Journal of the Transportation Research Board*, V. 2070, No. 1, Jan. 2008, pp. 59-67. doi: 10.3141/2070-08

67. Henkensiefken, R.; Bentz, D.; Nantung, T.; and Weiss, J., "Volume Change and Cracking in Internally Cured Mixtures Made with Saturated Lightweight Aggregate under Sealed and Unsealed Conditions," *Cement and Concrete Composites*, V. 31, No. 7, Aug. 2009, pp. 427-437. doi: 10.1016/j.cemconcomp.2009.04.003

68. Barrett, E. P.; Joyner, L. G.; and Halenda, P. P., "The Determination of Pore Volume and Area Distributions in Porous Substances. I. Computations from Nitrogen Isotherms," *Journal of the American Chemical Society*, V. 73, No. 1, Jan. 1951, pp. 373-380. doi: 10.1021/ja01145a126

69. Rajabipour, F., and Weiss, J., "Electrical Conductivity of Drying Cement Paste," *Materials and Structures*, V. 40, No. 10, Dec. 2007, pp. 1143-1160. doi: 10.1617/s11527-006-9211-z

70. Leão, T. P., and Tuller, M., "Relating Soil Specific Surface Area, Water Film Thickness, and Water Vapor Adsorption," *Water Resources Research*, V. 50, No. 10, Oct. 2014, pp. 7873-7885. doi: 10.1002/2013WR014941

71. Qiao, C.; Ni, W.; and Weiss, J., "Transport due to Diffusion, Drying, and Wicking in Concrete Containing a Shrinkage-Reducing Admixture," *Journal of Materials in Civil Engineering*, ASCE, V. 29, No. 9, Sept. 2017, p. 04017146. doi: 10.1061/(ASCE)MT.1943-5533.0001983

72. Esmaeeli, H. S.; Farnam, Y.; Bentz, D. P.; Zavattieri, P. D.; and Weiss, W. J., "Numerical Simulation of the Freeze–Thaw Behavior of Mortar Containing Deicing Salt Solution," *Materials and Structures*, V. 50, No. 1, Feb. 2017, Article No. 96. doi: 10.1617/s11527-016-0964-8

73. de Wolski, S. C.; Bolander, J. E.; and Landis, E. N., "An *In-Situ* X-Ray Microtomography Study of Split Cylinder Fracture in Cement-Based Materials," *Experimental Mechanics*, V. 54, No. 7, Sept. 2014, pp. 1227-1235. doi: 10.1007/s11340-014-9875-1

74. Landis, E. N., and Keane, D. T., "X-Ray Microtomography," *Materials Characterization*, V. 61, No. 12, Dec. 2010, pp. 1305-1316. doi: 10.1016/j.matchar.2010.09.012

75. Nguyen, T. T.; Yvonnet, J.; Bornert, M.; Chateau, C.; Bilteryst, F.; and Steib, E., "Large-Scale Simulations of Quasi-Brittle Microcracking in Realistic Highly Heterogeneous Microstructures Obtained from Micro CT Imaging," *Extreme Mechanics Letters*, V. 17, Nov. 2017, pp. 50-55. doi: 10.1016/j.eml.2017.09.013

76. Schneider, C. A.; Rasband, W. S.; and Eliceiri, K. W., "NIH Image to ImageJ: 25 Years of Image Analysis," *Nature Methods*, V. 9, No. 7, July 2012, pp. 671-675. doi: 10.1038/nmeth.2089

77. Scrivener, K. L.; Patel, H. H.; Pratt, P. L.; and Parrott, L. J., "Analysis of Phases in Cement Paste Using Backscattered Electron Images, Methanol Adsorption and Thermogravimetric Analysis," *MRS Online Proceedings Library*, V. 85, No. 1, Dec. 1986, Article No. 67.

78. McAndrew, A., "An Introduction to Digital Image Processing with MATLAB: Notes for SCM2511 Image Processing 1: Semester 1, 2004," School of Computer Science and Mathematics, Victoria University, Melbourne, VIC, Australia, 2004, 233 pp.

79. Beaudoin, J. J., and MacInnis, C., "Dimensional Changes of Hydrated Portland Cement Paste during Slow Cooling and Warming," *Cement and Concrete Research*, V. 2, No. 2, Mar. 1972, pp. 225-240. doi: 10.1016/0008-8846(72)90044-0

80. Meyers, S. L., "Thermal Expansion Characteristics of Hardened Cement Paste and of Concrete," *Highway Research Board Proceedings*, V. 30, 1951, pp. 193-203.

81. Mitchell, L. J., "Thermal Expansion Tests on Aggregates, Neat Cements, and Concretes," *ASTM International Proceedings*, V. 53, 1953, pp. 963-977.

82. Dettling, H., "Die Wärmedehnung des Zementsteines, der Gesteine und der Betone [Thermal Expansion of the Cement Paste, the Aggregates, and the Concretes]," thesis, Technische Hochschule Stuttgart, Stuttgart, Germany, 1962. (in German)

83. Emanuel, J. H., and Hulsey, J. L., "Prediction of the Thermal Coefficient of Expansion of Concrete," *ACI Journal Proceedings*, V. 74, No. 4, Apr. 1977, pp. 149-155.

84. Grasley, Z. C., and Lange, D. A., "Thermal Dilation and Internal Relative Humidity of Hardened Cement Paste," *Materials and Structures*, V. 40, No. 3, Apr. 2007, pp. 311-317. doi: 10.1617/s11527-006-9108-x

85. Sellevold, E. J., and Bjøntegaard, Ø., "Coefficient of Thermal Expansion of Cement Paste and Concrete: Mechanisms of Moisture Interaction," *Materials and Structures*, V. 39, No. 9, Nov. 2006, pp. 809-815. doi: 10.1617/s11527-006-9086-z

86. Powers, T. C., and Helmuth, R. A., "Theory of Volume Changes in Hardened Portland-Cement Paste during Freezing," *Highway Research Board Proceedings*, V. 32, 1953, pp. 285-297.

87. Coussy, O., *Poromechanics*, John Wiley & Sons, Inc., Hoboken, NJ, 2004.

88. Wang, Z. D.; Yao, Y.; and Wang, L., "Research on the Apparent Thermal Expansion Coefficient of Concrete Subject to Freeze-Thaw Cycles and Chloride Salt Attack," *Advanced Materials Research*, V. 446-449, 2012, pp. 3304-3310.

89. Powers, T. C., and Brownyard, T. L., "Studies of the Physical Properties of Hardened Portland Cement Paste," *ACI Journal Proceedings*, V. 43, No. 9, Nov. 1946, pp. 249-336.

90. Cai, H., and Liu, X., "Freeze-Thaw Durability of Concrete: Ice Formation Process in Pores," *Cement and Concrete Research*, V. 28, No. 9, Sept. 1998, pp. 1281-1287. doi: 10.1016/S0008-8846(98)00103-3

91. Scherer, G. W., and Valenza, J. J. II, "Mechanisms of Frost Damage," *Materials Science of Concrete VII*, F. Young and J. P. Skalny, eds., John Wiley & Sons, Inc., Hoboken, NJ, 2005, pp. 209-246.

CALL FOR ACTION

ACI Invites You To...

Share your expertise

Do you have EXPERTISE in any of these areas?

- BIM
- Chimneys
- Circular Concrete Structures Prestressed by Wrapping with Wire and Strand
- Circular Concrete Structures Prestressed with Circumferential Tendons
- Concrete Properties
- Demolition
- Deterioration of Concrete in Hydraulic Structures
- Electronic Data Exchange
- Insulating Concrete Forms, Design, and Construction
- Nuclear Reactors, Concrete Components
- Pedestal Water Towers
- Pipe, Cast-in-Place
- Strengthening of Concrete Members
- Sustainability

Then become a REVIEWER for the *ACI Structural Journal* or the *ACI Materials Journal*.

Become a Reviewer for the ACI Journals

How to become a Reviewer:

1. Go to: **http://mc.manuscriptcentral.com/aci**;
2. Click on "Create Account" in the upper right-hand corner; and
3. Enter your E-mail/Name, Address, User ID and Password, and Area(s) of Expertise.

Update your Manuscript Central user account information

Did you know that the database for MANUSCRIPT CENTRAL, our manuscript submission program, is separate from the ACI membership database?

How to update your user account:

1. Go to **http://mc.manuscriptcentral.com/aci**;
2. Log in with your current User ID & Password; and
3. Update your E-mail/Name, Address, User ID and Password, and Area(s) of Expertise.

QUESTIONS?

E-mail any questions to Journals.Manuscripts@concrete.org.

aci®

American Concrete Institute

Always advancing

ACI MATERIALS JOURNAL

The American Concrete Institute (ACI) is a leading authority and resource worldwide for the development and distribution of consensus-based standards and technical resources, educational programs, and certifications for individuals and organizations involved in concrete design, construction, and materials, who share a commitment to pursuing the best use of concrete.

Individuals interested in the activities of ACI are encouraged to explore the ACI website for membership opportunities, committee activities, and a wide variety of concrete resources. As a volunteer member-driven organization, ACI invites partnerships and welcomes all concrete professionals who wish to be part of a respected, connected, social group that provides an opportunity for professional growth, networking, and enjoyment.

aci®
American Concrete Institute